Image registration in quantitative inversion recovery MRI and applications in heart and lungs

Laura Saunders

University of Sheffield

This dissertation is submitted for the degree of
Doctor of Philosophy

January 2019

Acknowledgements

I would like to thank The Medical School at The University of Sheffield for awarding me a funding scholarship for my PhD. I would like to thank my supervisors, Professor Jim Wild and Dr Andy Swift. They gave me their academic guidance during my PhD, they enabled me to attend international academic conferences, encouraged me to write my own publications and gave me the freedom to pursue the research areas I found most interesting. Most of all, I would like to thank them both for believing in me.

I would also like to acknowledge my husband, Adam, for being there for me throughout my physics studies. At every point, from my physics A-level to writing my PhD thesis, he has been encouraging and supporting me, and I could not have done it without him by my side for the past 10 years.

Finally, I would like to thank my parents for their support, and for encouraging me to do what makes me happy. I would like to thank my friends, Marion and Graham, who were always around to cook food for me, craft with me and watch plenty of TV with throughout my PhD.

Abstract

The aims of this thesis are to develop fast, accurate and clinically applicable motion-correction solutions in T_1 mapping acquisitions in cardiac and lung imaging. In order to maximise clinical applicability, this thesis focuses on using automated post processing solutions which minimise the time-cost to patients, clinical staff and MRI scanner scheduling.

This has been achieved in 4 separate but related original pieces of work:

- Chapter 3: A novel method for correcting accidental respiratory motion in Modified Look Locker Inversion Recovery (MOLLI) sequences for cardiac T_1 mapping is presented and compared to an established, alternative method. The method presented produces synthetic images via an inversion recovery model. It is shown that both methods successfully improve image registration, but that the method presented here uses less post-processing time.

- Chapter 4: The method discussed in Chapter 3 is implemented and evaluated in a large cohort of patients with pulmonary hypertension to assess the diagnostic and prognostic value of T_1 mapping in this patient cohort. Although myocardial T_1 was found to be significantly elevated in patients with pulmonary hypertension, the diagnostic and prognostic value of myocardial T_1 was found to be limited.

- Chapter 5: The method discussed in Chapter 3 was extended to free breathing lung T_1 mapping, and implemented in patients with idiopathic pulmonary fibrosis (IPF) and healthy volunteers. The method is shown to register free breathing Look-Locker lung

images successfully. The results show that free breathing lung T_1 can discriminate between patients with IPF and healthy volunteers. Free breathing lung T_1 is significantly lower and more heterogeneous in patients with IPF compared to healthy volunteers.

- Chapter 6: The method discussed in Chapter 5 is extended to free breathing cardiac MOLLI sequences, and is implemented in healthy volunteers. It is shown that the images are successfully motion corrected in the short axis plane, though the results are likely to be less precise due to out of plane motion. The myocardial T_1 is shown to be significantly affected by oxygen enhanced imaging, and is significantly higher during free breathing, compared to breath hold.

Table of contents

List of figures

List of tables

Chapter 1

Introduction

1.1 Context

The concept of using magnetic resonance to categorise tissue properties was first used to assess the relaxation properties of normal and cancerous tissues by Raymond Damadian in 1971, before the first magnetic resonance image [3]. Damadian measured longer T_1 and T_2 relaxation times in cancerous tissues using nuclear magnetic resonance. Two years after Damadian published his work on the relaxation properties of cancerous and normal tissues, Paul Lanterbur published the first magnetic resonance image, followed in 1977 by the first images of a living alive subject - a clam [4]. 30 years later, Lauterbur was jointly awarded the 2003 Nobel prize in physiology or medicine with Sir Peter Mansfield, for his contributions to the invention of magnetic resonance imaging (MRI). By this time MRI was established for diagnostic and prognostic clinical investigations worldwide. The use of measurement of magnetic resonance times in research continues, however nowadays usually focusing on measurement derived from 2D or 3D images. Despite initial indications that relaxation times may be useful in identifying and characterising diseased tissues, it has become clear that relaxation times are non-specific and changes in relaxation times may be caused by a wide variety of mechanisms, such that a single measurement is not able to identify or characterise a tissue. Nevertheless, interest in relaxation times and their use in understanding tissue changes continues, with the caveat that multiple information sources or circumstantial data are needed to contextualise and interpret the relaxation time changes. The use of imaging allows parametric mapping: pixel by pixel visualisation of tissue relaxation times. This can identify regional changes in tissues, such as the presence of fibrosis or oedema. In order to be clinically useful, these methods need to be accurate and reproducible, a particular challenge in areas significantly affected by motion such a cardiac and respiratory systems. The use of breath hold and cardiac gating can compensate for motion to some degree. However, not all patients are able to maintain the breath holds required for longer sequences - such as 17s for cardiac T_1 mapping sequences. This has lead to the development of motion-correction algorithms to compensate for unintended motion [5] [6], and free breathing acquisitions which side-step the restriction of breath hold all together, and increase patient comfort [7] [8]. Patients with pulmonary hypertension may benefit greatly from motion correction in their imaging. These patients have elevated pressure in the pulmonary arteries leading to cardiac remodelling and reduced cardiac function. Cardiovascular MRI is now an established imaging technique for the assessment of patients with pulmonary hypertension, allowing direct visualisation and accurate analysis of cardiac structure (mass, size and shape of the ventricles) and function (volume and flow of blood within the ventricles). The use of contrast agents (such as gadolinium) allow enhancement of areas of myocardial fibrosis and scarring via late gadolinium enhancement imaging (LGE). However, T_1 mapping may allow tissue changes in these patients to be identified without the use of contrast agents, and may also allow diffuse myocardial changes to be detected. In addition, this patient group may struggle to maintain the breath hold needed for a traditional cardiac or pulmonary MRI, and therefore free breathing image acquisition would significantly improve image accuracy and patient comfort. The aim of this work was to investigate the use of motion-corrected T_1 mapping sequences. This would establish whether T_1 mapping can produce accurate, useful and clinically applicable measurements of cardiac and lung tissue changes. This work investigates patients with pulmonary hypertension (cardiac) and idiopathic pulmonary fibrosis (lung).

1.2 Objectives

The objective of this thesis is to work towards fast, accurate, clinically applicable free breathing solutions to T_1 mapping of both the cardiac and respiratory systems. This will be achieved by addressing four specific aims:

1. To develop a method to correct unwanted respiratory motion in cardiac T_1 mapping images.
2. To robustly assess the diagnostic and prognostic utility of cardiac T_1 mapping in patients with pulmonary hypertension.
3. To develop a free breathing motion correction method for cardiac and lung T_1 mapping applications.
4. To assess the impact of free breathing on cardiac and lung T_1 values.

1.3 Overview

Chapter 2 provides the necessary information to understand the work described in this thesis. It provides an introduction to MRI theory including imaging principles and T_1 relaxation principles, an introduction to T_1 mapping sequences and methods, an introduction to pulmonary hypertension - the main patient population considered in this thesis, and an introduction to idiopathic pulmonary fibrosis.

Chapters 3-6 describe four separate pieces of original research, which are linked thematically by the concept of motion correction in T_1 mapping and through which a novel method for motion correction in T_1 mapping is developed.

Chapter 3 describes a novel method for image registration to correct unwanted respiratory or cardiac motion in a MOLLI (MOdified Look-Locker Inversion recovery) T_1 mapping sequence. The method is implemented and compared to an alternative motion correction method from Xue et al [5]. The two methods are compared in a cohort of patients with pulmonary hypertension.

Chapter 4 uses the method described in Chapter 3 and implements it in a large pulmonary hypertension cohort to assess the utility of cardiac T_1 mapping in these patients, including the diagnostic and prognostic utility of T_1.

Chapter 5 modifies the method described in Chapter 3 for free breathing lung T_1 mapping. The method is tested on a small cohort of patients with idiopathic pulmonary fibrosis and healthy volunteers. The method is also used for oxygen enhanced lung T_1 mapping during free breathing on a subset of the healthy volunteers.

Chapter 6 modifies the method described in Chapter 5 for free breathing cardiac T_1 mapping. The method is tested in a small cohort of healthy volunteers, and the feasibility of oxygen enhanced cardiac T_1 mapping during both breath hold and free breathing is tested on a subset of the healthy volunteers. The challenges and potential for free breathing cardiac T_1 mapping and the role that oxygenation plays in myocardial T_1 values are discussed.

Chapter 7 summarises the work described in chapters 3-6 and discusses areas of future work to further validate the free breathing method described, it discusses the method's potential potential for future clinical studies evaluating cardiac and lung changes due to disease, without the need for breath hold.

1.4 Publications resulting from this thesis

The contents of Chapter 4 have been published in the Journal of Cardiovascular Magnetic Resonance: **L Saunders**, C Johns, N Stewart, C Oram, D Capener, V Puntmann, C Elliot, D Kiely, M Graves, J Wild and A Swift. "Diagnostic and prognostic significance of cardiovascular magnetic resonance native myocardial T1 mapping in patients with pulmonary hypertension", 2018, vol. 20, no.78.

The contents of Chapters 3, 5 and 6 have not yet been published in the form of a manuscript, however preliminary results have been submitted to ISMRM 2019 and the work is intended to be published as manuscripts in the near future.

In addition, the work in this thesis has also been presented at the following conferences:

- "Accurate T1 mapping using automated image registration in patients with pulmonary hypertension and aged matched volunteers", **Hutchison, L.***, Hammerton, C., Stewart, N., Capener, D., Graves, M., Kiely, D., Swift, A., Wild, J. In Proceedings of the European Society for Magnetic Resonance in Medicine and Biology (ESMRMB) meeting, Edinburgh, 2015. Oral lightning talk and E-Poster.

- "Myocardial T1 mapping MRI in patients with PH and age-matched healthy volunteers." **Hutchison, L.****, Hammerton, C., Stewart, N., Graves, M., Kiely, D., Wild, J., Swift, A. In European Respiratory Society (ERS) meeting, Amsterdam, 2015. Poster presentation.

- "Native myocardial T1 correlates with invasive catheter measurement in patients with pulmonary hypertension" **Saunders, L.****, Hammerton, C., Stewart, N., Graves, M., Kiely, D., Wild, J., Swift, A. In International Society for Magentic Resonance in Medicine (ISMRM) Meeting, Singapore, 2016. E-poster presentation.

- "Accurate T1 mapping in patients with pulmonary hypertension and age matched volunteers using synthetic image based registration" **Saunders, L.***, Hammerton, C., Stewart, N., Graves, M., Kiely, D., Swift, A., Wild, J. In International Society for Magentic Resonance in Medicine (ISMRM) Meeting, Singapore, 2016. Oral power-pitch talk and E-poster.

- "Native myocardial T1 correlates with right ventricular remodelling in patients with pulmonary hypertension" **Saunders, L.***, Stewart, N., Hammerton, C., Capener, D., Puntmann, V. Kiely, D., Graves, M., Wild, J., Swift, A. In European Respiratory Society (ERS) meeting, London, 2016. Poster presentation.

- "Myocardial T1 mapping MRI in patients with PH and age-matched healthy volunteers." **Hutchison, L.***, Hammerton, C., Stewart, N., Graves, M., Kiely, D., Wild, J., Swift, A. In European Cardiovascular Magnetic Resonance (EuroCMR) meeting, Florence, 2016. Poster presentation.

- "Validation of non-iterative model for synthetic image based registration of cardiac MOLLI T1 mapping images." **Saunders, L.***, Hammerton, C., Stewart, N., Graves, M., Kiely, D., Swift, A., Wild, J. In International Society for Magentic Resonance in Medicine (ISMRM) Meeting, Honolulu, 2017. E-poster presentation.

- "Diastolic Septal Angle Is An Independent Predictor Of Right Ventricular Insertion Point T1 In Pulmonary Hypertension " **Saunders, L.***, Hammerton, C., Stewart, N., Graves, M., Kiely, D., Wild, J., Swift, A. American Thoracic Society (ATS) meeting, San Diego, 2018. Poster presentation.

- "Prognostic Value Of T1 Mapping In Pulmonary Arterial Hypertension" **Saunders, L.***, Hammerton, C., Stewart, N., Graves, M., Kiely, D., Wild, J., Swift, A. American Thoracic Society (ATS) meeting, San Diego, 2018. Poster presentation.

- "Prognostic value of cardiac T1 mapping in Pulmonary Arterial Hypertension" **Saunders, L.***, Hammerton, C., Stewart, N., Graves, M., Kiely, D., Swift, A., Wild, J. In

International Society for Magentic Resonance in Medicine (ISMRM) Meeting, Paris, 2018. E-poster presentation.

* note L. Hutchison is the maiden name of the author of this thesis L. Saunders.

Chapter 2

Theory

This chapter outlines the relevant MR (magnetic resonance) theory and background information to aid understanding of the work described in the experimental chapters of this thesis. Unless otherwise referenced, section 2.1 is informed by the two text books [9] and [10].

2.1 MRI theory

2.1.1 Introduction to basic magnetic resonance imaging

2.1.1.1 Spin basics

In a magnetic field, stationary particles that possess a property known as spin have angular momentum, and an associated magnetic moments, μ. In classical mechanics this is analogous to an object physically rotating around an axis. However, over small distances (objects on an atomic scale), classical mechanics breaks down and other models - such as quantum mechanics - better describe and predict particle behaviour at this scale. In quantum mechanics, spin is understood to be an inherent property of a particle - much like mass or charge. However, spin is quantised, only existing in increments of $\frac{n}{2}$, where n is an integer. A classically rotating object has angular momentum with a direction - either up or down with respect to its axis of rotation. Similarly, in quantum mechanics, spin can be parallel to the static magnetic field (spin up) or anti-parallel to the magnetic field (spin down). A nucleus will have an overall magnetic moment arising from the combined effect of its nuclear spins. The maximum projection of nuclear spin is represented by **I**, which in the case of a fermion (such as a proton, neutron or electron) is equal to $\frac{1}{2}$. MRI manipulates the spin state of a nucleus (usually a hydrogen proton) to obtain information about nuclear density and position. As illustrated in Figure 2.1, in the presence of a static magnetic field (B_0), nuclear spin can align parallel or anti-parallel with the magnetic field. The alignment of a spin with respect to the field alters its energy state. For a nucleus with spin quantum number **I**, there are a number of discrete energy levels, due to the alignment of spins, with values given by m, where m can take $2I+1$ values. For example, for ^{1}H the spin quantum number is $\frac{1}{2}$ and therefore spin can be either $\frac{+1}{2}, \frac{-1}{2}$. The energy levels due to the spin alignment of a proton take the values $\pm\gamma\hbar I\dot{B}_0$, where γ is the gyromagnetic ratio (the ratio of a particle's magnetic moment to its angular moment). The energy difference between spin states which lie parallel and anti parallel alignment with the field is $\delta E = \gamma\hbar B_0$, this is illustrated in Figure 2.1. This splitting of nuclear energy levels in the presence of a magnetic field is known as the Zeeman

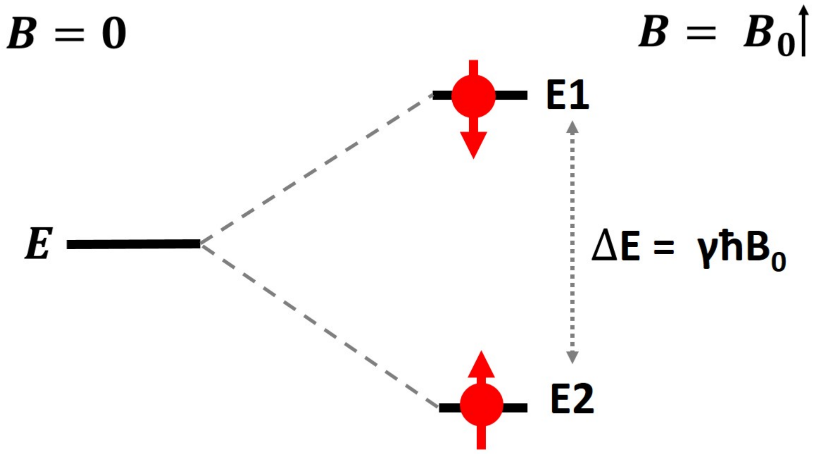

Fig. 2.1 Schematic drawing showing the energy difference between $spin = -\frac{1}{2}$ (E_1) and $spin = \frac{1}{2}$ (E_2) energy levels, where E is energy, B is static magnetic field, γ is gyromagnetic ratio and $\hbar$ is the reduced Planck's constant.

effect. The lower-energy state is the most stable, so protons can only transition from the lower-energy state ($spin = +\frac{1}{2}$) to the higher-energy state ($spin = -\frac{1}{2}$), if they absorb exactly quantum δE of energy (see Figure 2.1).

The behaviour of a particle's spin in the presence of a static magnetic field can be understood using both quantum mechanics and a semi classical model. For the purpose of this thesis, a semi classical model will be used where spin exists in a quantised form creating a net magnetisation but the behaviour of particles is described using classical mechanics. For a single nucleus in a static magnetic field, its spin due to its magnetic moment (μ) experiences a torque (rate of change of angular momentum) given by $\tau = dJ/dt = \mu \times B$, where J is the nuclear angular momentum. As $\mu = \gamma J$ and the net magnetisation of N spins is given by $M = V^{-1} \sum n = jn = N\mu_j$ this can be rewritten as:

$$\frac{dM}{dt} = \gamma M \times B \tag{2.1}$$

Where M is the net magnetisation. This is the equation of motion for a group of non-interacting spins in the laboratory frame.

Statistical mechanics describes the behaviour of a population of spins at a macroscopic level and can be used to describe the behaviour of a population of spins which can transition between Zeeman energy levels by absorbing or emitting discrete amounts of energy (equal to the energy difference between states) in the form of photons. A spin system will have a resonance frequency - a frequency which corresponds to the photon absorption energy required to excite proton spins from the lower energy level (spin $\frac{1}{2}$) to the higher energy level (spin $-\frac{1}{2}$). This frequency is known as the Larmor frequency and is defined as:

$$\omega_0 = \frac{\nu}{2\pi} = \gamma B_0 \tag{2.2}$$

Where ω_0 is the Larmor frequency, ν is frequency, γ is the gyromagnetic ratio and B_0 is the externally applied static magnetic field strength.

Within a spin population, some spins will be in the lower energy level (N_α) and some will be in the higher energy level (N_β). When in equilibrium, the spin population (N_α N_β) can be described using statistical mechanics as a Boltzmann energy population similar to heat transfer within a reservoir. This is expressed as:

$$\frac{N_{-1/2}}{N_{+1/2}} \propto e^{\frac{-\gamma\hbar B_0}{KT}} \tag{2.3}$$

Where K is the Boltzmann constant and T is the temperature. The thermal equilibrium of spins in a static magnetic field will be reached at a time characterised by T_1, which is a characteristic relaxation time defined, in part, by the temperature of the system (the Boltzmann lattice). Spins change energy level by interacting with the surrounding molecular environment (known as the lattice). Interactions with the lattice provide mechanisms for energy loss and gain, and the properties of the molecular environment (i.e. the probability of interactions occurring which provide energy at the frequency required for absorption) characterise how quickly the system can reach equilibrium. The properties of the molecular environment therefore characterise to the overall relaxation time, T_1.

In an MR experiment, the net magnetisation is perturbed by an external energy source (known as a radio-frequency or RF pulse) and the magnetisation relaxes back to equilibrium in time characterised by T_1. The behaviour of a spin system in this environment are described phenomenologically by a set of equations known as the Bloch equations [11].

The evolution of a macroscopic magnetisation $\mathbf{M(t)} = (M_x(t), M_y(t), M_z(t))$ in a magnetic field $\mathbf{B(t)} = (B_x(t), B_y(t), B_z(t))$ is described by the Bloch equations in the following way:

$$\frac{M_x(t)}{dt} = \gamma(\mathbf{M}(t) \times \mathbf{B}(t))_x - \frac{M_x(t)}{T_2} \tag{2.4}$$

$$\frac{M_y(t)}{dt} = \gamma(\mathbf{M}(t) \times \mathbf{B}(t))_y - \frac{M_y(t)}{T_2} \tag{2.5}$$

$$\frac{M_z(t)}{dt} = \gamma(\mathbf{M}(t) \times \mathbf{B}(t))_z - \frac{M_z(t) - M_0}{T_1} \tag{2.6}$$

Where M_0 is the equilibrium magnetisation.

Equation 2.6 refers to the z plane and is governed by relaxation time T_1. Equations 2.4 and 2.5 are governed by the relaxation time T_2, which describes the relaxation in the xy plane. Both relaxation mechanisms are described in more detail in section 2.1.2.1 and 2.1.2.2.

If we consider a magnetic field which is static in the longitudinal plane, and another applied rotating field in the transverse plane: $B_x = B_1 cos(\omega t)$, $B_y = B_1 sin(\omega t)$, $B_z = B_0$ and apply an RF pulse along the +x axis, such that $M_x(0) = M_z(0) = 0$ and $M_y(0) = M_0$ the equations 2.4, 2.5 and 2.6 can be solved to show:

$$M_x(t) = M_0 sin(\omega_0 t)) \cdot e^{\frac{-t}{T_2}} \tag{2.7}$$

$$M_y(t) = M_0 cos(\omega_0 t)) \cdot e^{\frac{-t}{T_2}} \tag{2.8}$$

$$M_z(t) = M_0(1 - e^{\frac{-t}{T_1}}) \tag{2.9}$$

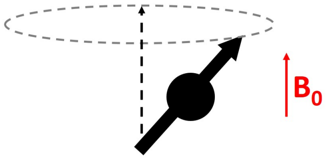

Fig. 2.2 Schematic drawing showing a spin precessing about its axis due to the presence of an external magnetic field.

An example of a simple MRI experiment is the observation of free induction decay (FID). During FID, an object is placed in a static magnetic field (B_0). The static magnetic field causes the spin to precess around its axis. Then, a 90° radio-frequency (RF) pulse is applied which transiently polarises (aligns) the spins in the protons in a different plane. The net magnetisation is rotated from the z plane into the xy plane. Once the RF pulse is removed, the polarised dipoles gradually begin to dephase, due to small differences in the magnetic field they experience (T_2 decay). The acquired phase difference increases with magnetic field difference and time. Over time, the acquired phase differences result in the spin isochromats becoming incoherent, see Figure 2.3, so that the overall magnetisation decreases with a characteristic time, T_2, see Figure 2.4. The application of a 180° RF pulse (or a suitable gradient) will reverse the phase angle of each spin, leading the spins to come back into phase as the spins precession re-aligns and a second coherence occurs. This is known as a spin echo (SE) experiment.

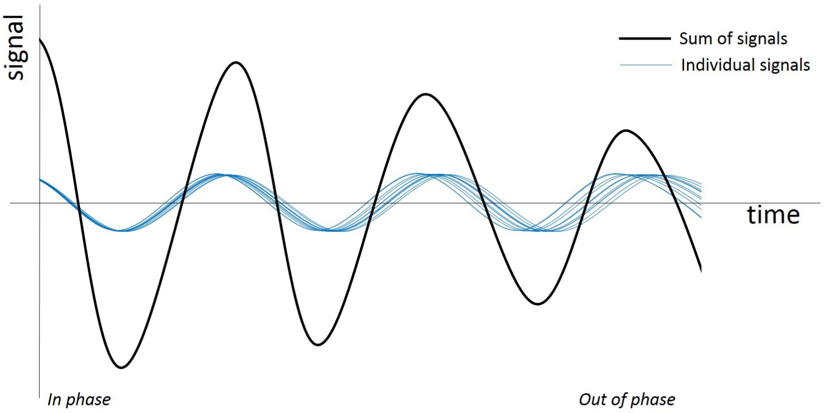

Fig. 2.3 Schematic drawing of the concept of dephasing and free induction decay showing a series of waves which start in phase and gradually become incoherent, leading to a reduction of the overall summed waveform.

2.1.1.2 Imaging basics

The basic principle of nuclear magnetic resonance (NMR) is that a changing magnetic field will cause magnetic induction. A wire in the presence a changing magnetic field caused by the precession of spins in the xy plane will experience a current, due to the effect of the varying magnetic field on the free electrons, which can be measured. In the presence of a resonant coil (i.e. tuned to the Larmor frequency), this precession will induce a voltage in a coil, which will be damped as the spins dephase (T_2 decay).

An RF pulse perturbs the net magnetisation vector out of equilibrium (aligned with the static magnetic field) and into the xy plane, see Figure 2.5. In a rotating frame of reference (rotating at the same frequency of spin precession) the spin behaviour is simplified and can be described as the magnetisation flipping from the longitudinal (z) plane into the transverse plane (xy) when manipulated with either a 90 degree radio-frequency pulse or an appropriate magnetic field gradient. The "RF pulse" itself is an oscillating field, B_1, which is orthogonal to B_0.

Spatial information is encoded by magnetic field gradients $G_{x,y,z} = \frac{dB_z}{d_{x,y,z}}$. To obtain spatial information, an MRI pulse sequence requires three basic components: an RF pulse with a simultaneous slice selective gradient (in this work, depicted in the in the z axis, G_z); a frequency encoding gradient (in this work, depicted in the x axis, G_x) and a phase encoding gradient (in this work, depicted in the y axis, G_y). These three components combine to enable spin spatial location to be resolved in three dimensions. The MRI signal is then received in frequency (k) space and is transformed into real space using a Fourier transform:

$$f(r) = \frac{1}{2\pi} \int_{-\infty}^{\infty} s(k) e^{i2\pi k \cdot r} \, dk \tag{2.10}$$

Where r is radial distance, s is signal, and k is frequency.

$$\omega_0(x) = \gamma(B_0 + G_x x) \tag{2.11}$$

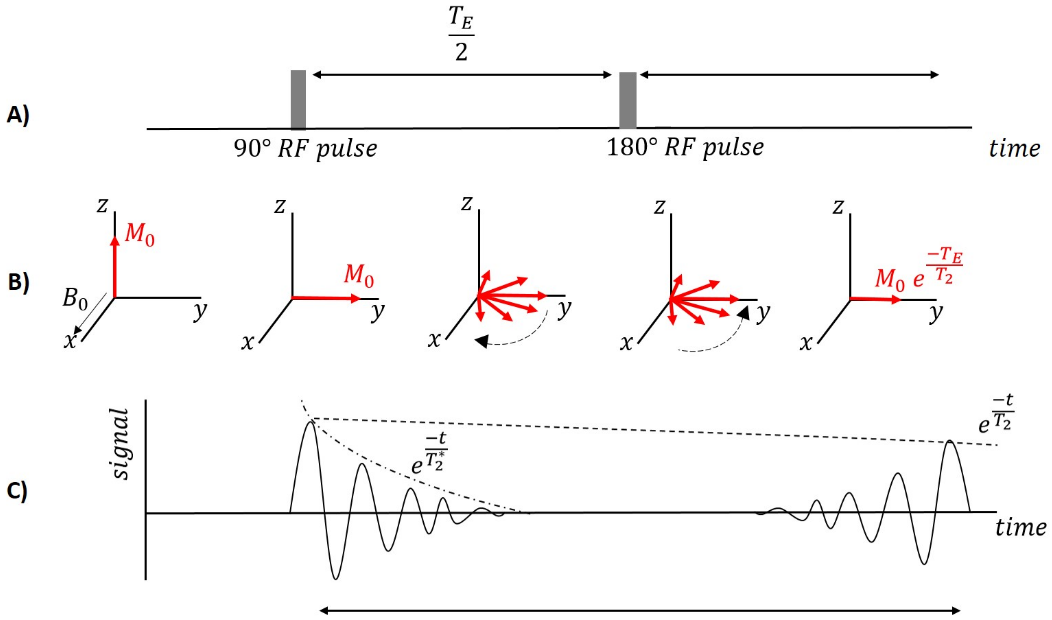

Fig. 2.4 Schematic drawing showing a spin echo experiment. A) Shows the RF pulse sequence over time, B) shows the magnetisation behaviour of the spin system and C) shows the measured signal over time in response to A). All panels share a time axis.

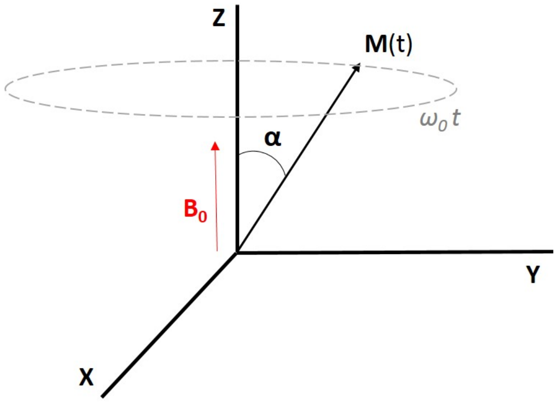

Fig. 2.5 Schematic drawing showing the net magnetisation of a spin, with angular frequency ω_0 about the z axis, being flipped from the z plane into the y plane by an angle of α.

To achieve frequency encoding an additional magnetic field that varies spatially is applied to the system. For example, a linear gradient G_x in the x axis could be applied such that the overall magnetic field experienced by a spin would be $B_x = B_0 + G_x x$. The precession frequency of that spin will depend on its location along the x axis.

Which, in the rotating frame of reference which rotates at γB_0 can be written as:

$$\omega(x) = \gamma G_x x \tag{2.12}$$

If an image of a certain field of view (FOV) is desired in the x direction, with a resolution $\Delta x = FOV_x / N_x$ where N_x is number of pixels, the gradient required is given by:

$$G_x = \frac{\omega}{\gamma x} = \frac{\omega N_x}{\gamma FOV_x} \tag{2.13}$$

As a gradient requires a finite time to turn on and off (ramp up and down), the shape of the magnetic field with time is trapezoidal, as depicted in pulse sequence diagrams in Figure 2.6. Frequency encoding cannot be used in both the x and y directions, as some points in space will have overlapping frequencies. Therefore, phase encoding is used in the y plane to determine spatial information. When a spatially varying field gradient is applied to a set of spins, they precess at a different frequency and acquire a phase shift which depends on their spatial location. When the gradient is turned off, they return to precessing at their original frequency but the phase shift remains. This allows a location-dependant phase shift to be applied to the spins in the y-plane prior to the image acquisition window.

The phase encoding gradient must be repeated for each step in frequency Δk_y where the time between repetitions is known as T_R. Therefore for number of phase encoding steps N_y, with image resolution $\Delta y = \frac{FOV}{N_y}$ there is a total time cost of:

$$t_{acquisition} = N_y T_R \tag{2.14}$$

For this reason, increased spatial resolution in the phase encoded direction results in a longer acquisition time, whereas the spatial resolution in the frequency encoding direction can be increased by simply decreasing the gradient amplitude.

The slice selection gradient, G_z, is applied to obtain information from a specific image plane (or slice). G_z is applied at the same time as the RF pulse such that only spins in the selected spatial plane are perturbed. The RF pulse has bandwidth (range of frequencies it excites) $BW = 2\pi\delta\omega$ which are centred around ω_0. The simultaneous field gradient G_z is placed such that the desired slice corresponds to the frequencies $\omega_0 \pm \frac{\delta\omega}{2}$.

Therefore:

$$G_z = \frac{\omega}{\gamma\Delta z} = 2\pi\frac{BW}{\Delta z} \tag{2.15}$$

Where Δz is slice thickness.

When combined, as in Figure 2.6, a 2D spatially resolved image can be obtained. Figure 2.6 shows an RF pulse applied for duration τ where:

$$f(\omega) = \int_{-\infty}^{\infty} f(t)e^{i\omega t}\,dt \tag{2.16}$$

However, if T_R is smaller than T_1, the longitudinal relaxation (z plane) does not fully recover at the end of acquisition. Over time, the residual longitudinal relaxation will reach a steady state as the transverse magnetisation, which can be fed back into the spin system and when the system is re-excited. Similarly, if T_R is smaller than T_2 there will also be residual magnetisation in the transverse magnetisation (xy) plane. This can either be eliminated with a spoiling gradient, or preserved for the next iteration of the sequence.

If the transverse magnetisation is spoiled (removed), it is known as a SPGR (spoiled gradient) sequence, whereas if it is recovered it is known as a SSFP (steady state free precession) sequence. An example of a SSFP sequence is a balanced steady state free precession sequence - bSSFP - where all three axes (transverse and longitudinal magnetisation) are in a steady state, as shown in Figure 2.7.

An alternative to a gradient echo sequence is a spin echo sequence, which uses a second 180° RF inversion pulse (rather than a gradient) to reverse the individual phase angles of the spins, creating a second coherence in the transverse plane, as shown in Figure 2.8.

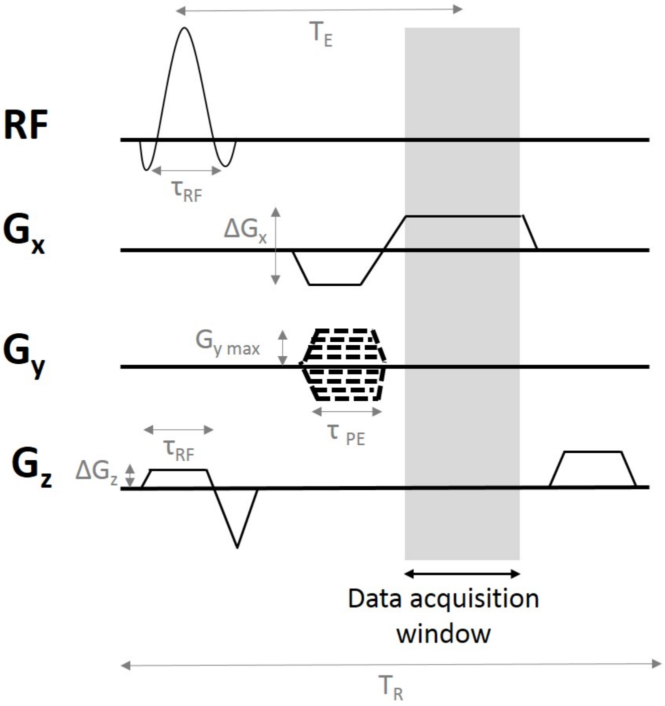

Fig. 2.6 Schematic drawing showing a pulse sequence timing diagram, with an RF pulse and simultaneous slice selection gradient on the z axis, a frequency encoding gradient on the x axis, and a phase encoding gradient on the y axis (depicted as a number of gradient amplitudes on top of one another).

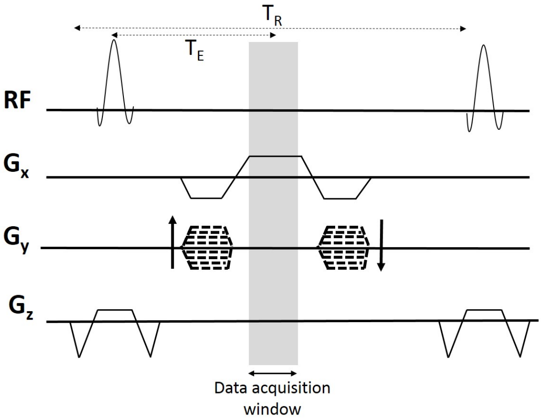

Fig. 2.7 Schematic drawing showing a pulse sequence timing diagram for a bSSFP sequence.

In general, for T_1 weighted imaging gradient echo sequences (which are usually acquired with a large flip angle (α) and a short echo time (TE) result in much faster image acquisition. This is particularly important in breath-held chest imaging such as cardiac and lung imaging, where acquisition time is restricted to that of a single breath hold. T_1 weighted gradient echo images also result in high SNR (signal to noise ratio) and image resolution. T_1 weighted imaging results in good contrast between tissue, fluid and fat, with fluid such as blood appearing darker than tissue and fat due to its short T_1 (the reasons for this will be discussed further in section 2.1.3). For imaging the lungs or the myocardium, this can be particularly useful because the signal from the blood in the heart and lungs is low and signal from tissue is high.

2.1.2 T_1 relaxation principles

The relaxation times T_1 and T_2 have already been described in reference to the Bloch equations: eq (2.7), eq (2.8) and eq (2.9). Particular molecular environments and lattice temperatures have characteristic relaxation times. The times represent how efficiently a set of spins reach their equilibrium population states. For the longitudinal relaxation time, T_1, the relaxation mechanisms arise from interactions with the surrounding environment (the lattice), see section 2.1.2.1. For the transverse relaxation, T_2, interactions with other spins drive the relaxation mechanisms, see section 2.1.2.2.

2.1.2.1 Longitudinal relaxation - T_1

Protons (spin $\frac{1}{2}$) can absorb or emit energy, resulting in transfer between the lower energy state ($+\frac{1}{2}$)and the higher energy state ($-\frac{1}{2}$). Protons absorb or emit energy at the frequency that corresponds to the energy difference between energy levels, as mentioned in section 2.1.1. The speed of this process depends on the molecular interactions that can occur at this frequency (i.e. interactions that result in the emission or absorption of energy that corresponds to this frequency). The more mechanisms, and the more energy available to the system, the faster the system will reach equilibrium.

For the proton, T_1 relaxation primarily occurs due to intra-molecular dipole-dipole interactions, which occur at the energies required for longitudinal relaxation, see Figure 2.1.

$$\delta E = \hbar \gamma B_0 \tag{2.17}$$

The energy required for transitions depends on B_0; at higher magnetic fields, more energy is needed for a transition to take place. Therefore, the resultant relaxation time (T_1) is dependent on the energy is available to the system (i.e. the spins' local environment) and the energy required to transition (i.e. the Zeeman energy which is determined by the magnetic field strength).

Each individual spin fluctuates over time, but overall there is a small net alignment with the magnetic field. This is known as spontaneous magnetisation. This magnetisation is described by

$$M_z(t) = M_{equilibirum}(1 - e^{-\frac{t}{T_1}}) \tag{2.18}$$

Where T_R is the time between RF pulses, and T_1 is the longitudinal relaxation time T_1 [9]. In an MRI experiment where spins are manipulated out of their equilibrium energy states using RF pulses or gradients, T_1 will also characterise the time it takes for the system to return back to its equilibrium position, losing energy to the surrounding environment (or "lattice") in the process. During this process longitudinal magnetisation can be described by:

$$M_z(t) = M(0)(1 - e^{\frac{-T_R}{T_1}})e^{\frac{-T_E}{T_2^*}} \tag{2.19}$$

The primary mechanism for longitudinal relaxation, intra-molecular dipole-dipole interactions, occur due to the magnetic dipoles (i.e. the spins) creating small local changes to the magnetic field. These local magnetic field changes create small localised energy changes, and these energy fluctuations can cause protons to transition between spin states [1]. Two spins in the presence of one another have four possible alignment combinations, with four different associated energies, see Figure 2.9, and moving between these states allows energy emission/absorption in the frequencies associated with longitudinal relaxation. Transfers between the energy states are shown in Figure 2.9. Each of the energy levels has an associated transition rate, i.e. the probability of these interactions occurring has an associated rate of transfer. These interactions are the dominant mechanism for spin-lattice relaxation.

The strength of the interaction between two dipoles depends upon the type of spins (electrons have a larger gyromagnetic ratio than protons and therefore a proton-electron interaction is stronger than a proton-proton interaction), the distance between the spins (with interactions stronger between closer spins), the angle between the spin vectors, and other properties such as the relative motion of the spins. The thermal motion of molecules leads to fluctuations of the field experienced at the site of the nuclear spin. As a molecule tumbles in its environment, the strength and direction of the local field experienced changes. The magnetic field experienced by nuclei can be described as a combination of an approximately static magnetic field in the z direction (B_o) and a fluctuating transverse field due to the thermal motion of molecules leading to fluctuating interactions between spins ($B_x(t)$) which changes with time.

For each spin, $B_x(t)$ (the local magnetic field each spin experiences in the transverse plane) is different and fluctuates with time. $B_x(t)$ is assumed to have a mean of 0, but $B_x^2(t) > 0$. The mean magnitude value of the field is assumed to be the same for all spins. The fluctuations of $B_x(t)$ can be described using an autocorrelation function, $\mathbb{G}$. At some point in time, $t + \tau$, the field's behaviour is independent of its behaviour at a previous point in time t, and so the system "loses it's memory". This occurs when τ is much greater than the size of the fluctuations in $\mathbb{G}$.

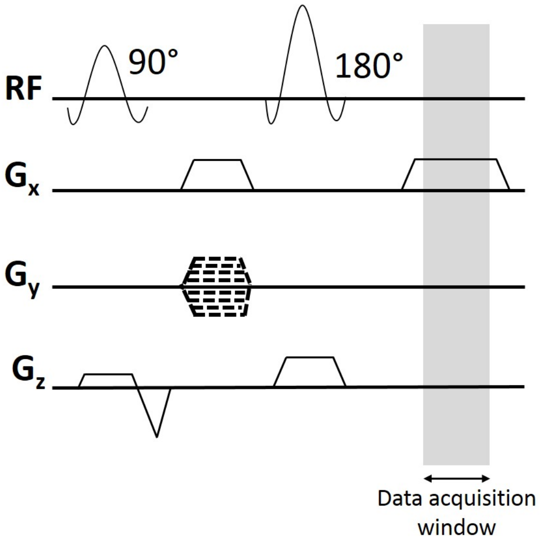

Fig. 2.8 Schematic drawing showing a pulse sequence timing diagram for a spin echo sequence.

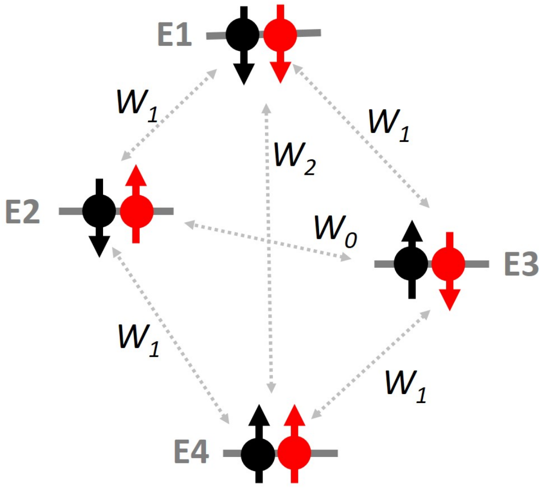

Fig. 2.9 Schematic drawing showing the four energy levels between two dipoles. W_0 indicates a zero-quantum transition, W_1 indicates a single-quantum transition and W_2 indicates a double-quantum transition.

Although not based in theory, qualitatively $\mathbb{G}$ may be assumed to be equal to:

$$\mathbb{G} = < B_x(t)B_x(t+\tau) > \neq 0 \tag{2.20}$$

Correlation time (τ_c), is a constant that characterises the loss of correlation in the system - rapid fluctuations have a small τ_c and slow fluctuations have a large τ_c. The dependence of T_1 and T_2 on τ_c is shown in Figure 2.10. Relaxation is most efficient when the tumbling rate, $\frac{1}{\tau_c}$, occurs approximately at the Larmor frequency (ω_0) (i.e. $\omega_0 \sim \frac{1}{\tau_c}$). This can be seen at the minimum of the T_1 dependence line on Figure 2.10 [1]. Therefore, although at low fields dipole-dipole interactions are the dominant relaxation mechanism, as B_0 increases chemical shift ansiotropy (CSA) plays an increasingly important role in longitudinal relaxation for spin $\frac{1}{2}$ nuclei. CSA interactions occur at a higher frequency and are the result of electrons in the molecules causing submolecular magnetic field fluctuations. Electrons within the molecule itself create fields due to their movement through the magnetic field. As field strength increases, the relative importance CSA to dipole-dipole coupling to longitudinal relaxation mechanisms changes, with CSA interactions contributing more to longitudinal relaxation as field strength increases.

2.1.2.2 Transverse relaxation - T_2

T_2 relaxation describes the dephasing of spins over time due to interactions with other spins. Local field inhomogeneities occur due to two processes: 1) inhomogeneities in the main magnetic field, and 2) inhomogeneities caused by nearby spins own magnetic moments. Each spin has an associated magnetic moment, which causes a local perturbation of the magnetic field. Therefore, the location of other spins effects the magnetic field experienced by a given spin, causing spin precession to occur at slightly different frequencies, due to experiencing slightly different magnetic fields.

Two protons experiencing a slightly different field, $\pm\delta B_0$ will precess at slightly different frequencies:

$$\omega_1 = \gamma(B_0 + \delta B_0) \tag{2.21}$$

$$\omega_2 = \gamma(B_0 - \delta B_0) \tag{2.22}$$

The two different frequencies result in the two protons acquiring a phase difference in the rotating frame:

$$\delta\theta = \theta_1 - \theta_2 = \omega_1 t - \omega_2 t = t\gamma(B_0 + \delta B_0 - B_0 + \delta B_0) = 2\delta B_0 \gamma t \tag{2.23}$$

The acquired phase difference therefore increases with magnetic field difference and time. Over time, the acquired phases differences result in the spins becoming incoherent so that the overall magnetisation decreases, as described in section 2.1.1.1.

2.1.3 Longitudinal relaxation times in the body

T_1 relaxation time of a spin depends upon how it interacts with its surroundings, as discussed in section 2.1.2.1 and the dominant mechanism for this is magnetic dipole-dipole interactions. The rate at which relaxation occurs depends on the rate of interactions between the proton (the spin) and its local environment (the lattice) as well as the static magnetic field strength B_0. As discussed in section 2.1.2.1, this rate can be described by using a time scale, τ_c, which corresponds to the average time between interactions with the environment. The random motion of surrounding particles produces random fluctuations in the magnetic field experienced by a spin. Generally, solids have long τ_c, as the protons move slowly, and liquids have shorter τ_c values as the protons are move quickly, although this is not always the case. For example lipids have a very short T_1, due to the large size of unbound lipid molecules. Different tissues will be differently affected by an increase in static magnetic strength, in general protons in solids have less freedom of movement (are "bound") and therefore at higher field strengths the fraction of molecules able to tumble at the resonance frequency decreases, resulting in reduced energy transfer and thus increase in relaxation time. Liquids and gases, in general, are less affected by a change in field strength as they are more mobile and so a higher proportion of protons within the gas or liquid are able to interact at higher frequencies.

This behaviour can be understood as a proton interacting with a heat reservoir (where the heat reservoir describes the thermal motion of atoms and the energy available due to those interactions), where the final equilibrium population of spins is described using a Boltzmann distribution:

$$\frac{N_-}{N_+} = \exp\frac{-\gamma\hbar B_0}{KT} \tag{2.24}$$

Where N_- and N_+ are the number of spins with spin $-\frac{1}{2}$ and $\frac{1}{2}$ respectively. K is the Boltzmann constant, and T is temperature in Kelvin. The thermal equilibrium population is therefore defined by the reservoir (lattice) temperature (how much energy is available to the system) and the static magnetic field, B_0. The static magnetic field defines the energy levels between spin states, see equation (2.17) and Figure 2.9, and therefore the probability of a transition between energy levels occurring.

However, few tissues within the body are a solid (bound protons) or liquid (freely moving protons). Rather, most can be described as "structured" (somewhere in between). Therefore, their behaviour falls on a continuum between predictions for a solid or liquid object. There are exceptions to this - blood and cerebrospinal fluid are MRI relevant liquids. In general though, most tissues contain a range of proton binding levels, which are exchanged between environments.

In a water or fluid environment, such as blood, the presence macromolecules (e.g. proteins) shorten T_1 by providing additional relaxation pathways for water molecules, for

Table 2.1 Normal blood T_1 values. *MOdified Look Locker Inversion recovery

	N	**Sequence**	**Field strength (T)**	**Sex (% female)**	**mean age (years)**	**Region**	**T_1 (ms)**
Zhang et al [13]	6	Look-Locker	1.5T	50%	31±6	sagittal sinus	1480 ± 61
Zhang et al [13]	6	Look-Locker	3T	50%	31±6	sagittal sinus	1480 ± 61
Zhang et al [13]	6	Look-Locker	1.5T	50%	31±6	sagittal sinus	1649 ± 68
Zhang et al [13]	6	Look-Locker	3T	50%	31±6	sagittal sinus	2087 ± 131
Reiter et al [14]	40	MOLLI*	1.5T	50%	24±3	left ventricle	1586 ± 103

example, through proton exchange between water molecules and macromolecules. Blood contains several macromolecules, such as albumin in the blood plasma, and haemoglobin in red blood cells, and increases in the blood macromolecule content will shorten blood T_1 [2]. Paramagnetic substances can also affect T_1. Examples include macromolecules such as deoxyhaemoglobin in the blood. Therefore blood T_1 will vary with oxygenation and the hematocrit (the ratio of the volume of red blood cells to the total volume of blood). Hematocrit also varies with age and sex [12] with women typically having lower hematocrit levels and a higher blood T_1 [13] [14]. Typical blood T_1 values are shown in Table 2.1.

The measured T_1 will always occur due to a combination of processes, and usually the multiple, complex anatomical mechanisms responsible for changes to tissue T_1 cannot be understood through an MRI examination or image alone. However, in general, changes to tissue composition due to disease alter the atomic environment, which may lead to T_1 changes. For example, the existence of oedema (an abnormal build up of fluid) results in an increased T_1, as does fibrosis - a thickening and scarring of connective tissue in the body. Similarly, the presence of fat in a tissue will cause a decrease in T_1. Combining T_1 measurement with other data, either MRI (such as T_2) or other medical information (such as tissue samples), can help determine how T_1 changes relate to pathology and what T_1 changes indicate in the context of certain patient groups or pathologies.

When calculating T_1 from a region of interest drawn on a T_1 map, or set of images, it is necessary to avoid tissue boundaries in order to avoid partial volume effects and measure the

T_1 of a single tissue. Including pixels corresponding to more than one tissue into a regional T_1 calculation leads to a weighted combination of T_1s being measured according to:

$$\frac{1}{T_{1observed}} = \frac{N_1}{N_{tot}T_{1(1)}} + \frac{N_2}{N_{tot}T_{1(2)}} .... + \frac{N_n}{N_{tot}T_{1(n)}} \tag{2.25}$$

Where N is the number of protons corresponding to a given T_1, and N_{tot} is the total number of protons. Which, if interpreted as a the T_1 for a single tissue which lead to inaccuracies in calculating T_1.

2.1.4 Effect of oxygenation on T_1

Molecular oxygen contains two unpaired electrons (i.e. two electrons which do not occupy an orbit with a paired electron of opposite spin). Each oxygen molecule therefore has a magnetic moment of 2.8 Bohr Magnetons [15]. This makes oxygen paramagnetic; it has a permanent magnetic moment in a magnetic field. Paramagnetic ions provide a mechanism for dipole-dipole coupling, as the gyromagnetic ratio of the electrons is much larger than that of another proton, so it can interact with a proton's spin over longer distances. The presence of oxygen in an object will increase relaxation rate, in terms of both T_1 (by providing a dipole-dipole relaxation mechanism) and T_2 (by perturbing the local magnetic field and causing additional precession dephasing).

Oxygen is both present in the body naturally, due to respiration of air (21% O_2), and can be used at higher inhaled concentrations as an additional contrast agent. In the body, molecular oxygen can effect blood T_1 via two methods: 1) by attaching to the paramagnetic deoxyhaemoglobin, reducing the amount of deoxyhaemoglobin present and thus increasing T_1 relaxation time and 2) by dissolving in the plasma, thus decreasing T_1 by promoting relaxation in nearby protons [16]. Lung T_1 measurements when using 100% oxygen as a contrast agent demonstrate a decrease in T_1 due to the presence of oxygen dissolved in the blood plasma

[17]. $Ex-vivo$ and $in-vivo$ blood measurements show that blood T_1 is dependent on both haematocrit levels and oxygenation state. Blood with oxygenation levels between 5% and 95% demonstrate a decrease in T_1 as blood becomes less oxygenated, and deoxyhaemoglobin increases. This effect is stronger with higher levels of haematocrit. However, at high levels of oxygenation (>95%) T_1 decreases with increased oxygenation due to the presence of dissolved oxygen in the blood plasma [2], see Figure 2.11. Deoxygenated venous blood is typically $60-70\%$ oxygenated, whereas oxygenated arterial blood is typically $95-100\%$. The T_1 of deoxygenated right ventricular and oxygenated left ventricular blood at 1.5T are $1535 \pm 76ms$ and $1515 \pm 76ms$ respectively [18].

Oxygen enhanced T_1 maps have been performed to visualise and calculate the transfer of oxygen to the lung, by using 100% inhaled oxygen. The T_1 shortening can be measured with T_1 weighted MRI sequences providing information on oxygen absorption by blood and tissue. This is considered to indirectly measure pulmonary function. As oxygen passively diffuses from the alveoli to the blood capillaries in the lung (due to the partial pressure gradient that exists between them) the dissolved oxygen lowers overall lung T_1, demonstrating regions that have been ventilated and subsequently perfused [19]. The wash-in and wash-out of O_2 over time can be visualised using rapidly acquired lung T_1 maps. By not waiting for magnetisation to fully recover before subsequent inversions, T_1 maps can be acquired quickly enough to visualised the uptake (and wash out) of oxygen in the lung via T_1 mapping. Oxygen was found to have a wash-in time of 52.20 ± 15.53s and a wash-out time of 43.90 ± 10.47s in healthy volunteers [17].

2.2 T_1 mapping methods and MR sequences

A T_1 map is an image where each pixel represents the T_1 value of the corresponding real-space image. It shows pixel-by-pixel T_1 differences in a single slice of the object or anatomy being imaged, allowing regional variations in T_1 to be visualised. Measuring an objects T_1 can

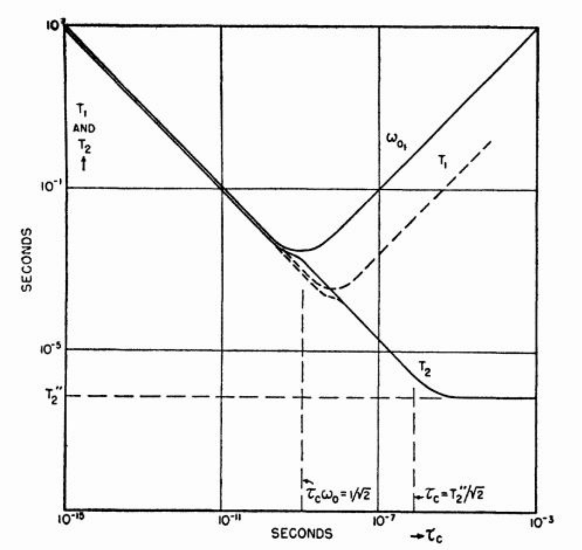

Fig. 2.10 Variation of T_1 and T_2 with τ_c according to the simplified theory where all interactions are assumed to have the same τ_c. Note: Reprinted with permission from [1].

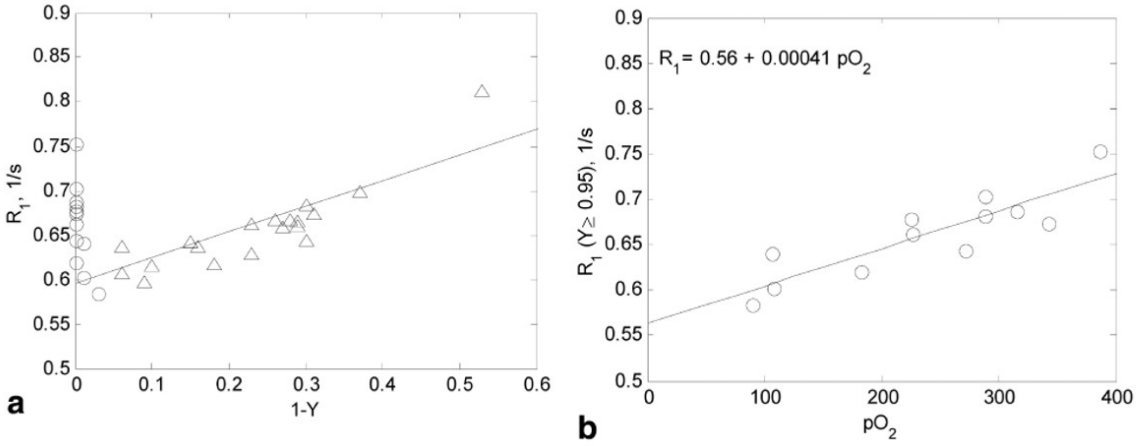

Fig. 2.11 a) Longitudinal relaxation rate (R_1) in bovine blood at haematocrit 0.41 as a function of deoxygenation (1-Y) at 4.7T. Open circles show hyperoxygenated blood (Y>0.95). b) hyperoxygenated blood as a function of partial pressure of oxygen at 4.7T. Note: Reprinted with permission from Magnetic Resonance in Medicine [2].

be achieved in several ways, including: saturation recovery sequences, inversion recovery sequences and signal ratio sequences. To implement a saturation recovery sequence, a spin echo experiment is repeated with a variable recovery time (T_R) or flip angle (α). This varies the amount of magnetisation in the longitudinal plane. The intensity change of the images depends on T_1. A spoiling mechanism must be used to eliminate remnant transverse (xy) magnetisation prior to each RF pulse. For a low T_R and variable flip angle sequence, a small angle approximation can be used and the signal is approximately given by:

$$S(\alpha) = \frac{S_0 sin(\alpha)(1-E)e^{\frac{T_E}{T_2^*}}}{1-Ecos(\alpha)} \tag{2.26}$$

Where S_0 is the initial magnetisation and E is: $E = exp(-\frac{T_R}{T_1})$. The maximum signal (which occurs at maximum transverse magnetisation) occurs at:

$$\frac{dS(\alpha)}{d\alpha} = \frac{-(Esin^2(\alpha) - Ecos^2(\alpha) + cos(\alpha))S_0(1-E)e^{-\frac{T_E}{T_{2^*}}}}{(1-Ecos(\alpha))^2} = 0 \tag{2.27}$$

To which the solution for maximum magnetisation is:

$$cos(\alpha) = E \tag{2.28}$$

Therefore, the an angle which maximises transverse magnetisation is given by:

$$\alpha = cos^{-2}(E) \tag{2.29}$$

This is known as the Ernst angle [20].

An inversion recovery sequence uses a 180° RF pulse to invert magnetisation prior to magnetisation being flipped into the transverse plane. The initial magnetisation is $-M_0$. This creates a T_1 dependence of magnetisation and signal over time:

$$S(t) = S_0(1 - 2e^{\frac{-t}{T_1}}) \tag{2.30}$$

The equation (2.30) is only true if it is assumed that there is a perfectly inverted set of spins. In reality, spin inversion is imperfect in practice due to the pulse profile being finite, and off-resonance effects. To take these into account, the following equation is used during data fitting:

$$S(t) = S_0(1 - Ae^{(\frac{-t}{T_1})}) \tag{2.31}$$

Where S_0, A and T_1 are parameters to be fit [10].

This creates a 3 parameter fitting technique. However, if the images are magnitude images, the signal polarity of the images is not known. Signal polarity can be restored by a multi-fitting approach, where the signal is inverted for each TI, per pixel, and fit to Equation 2.31. This creates pixel sets with different signal polarity, the first with all positive pixel values, the second with the first pixel signal inverted, the third with the first two pixels signal inverted, and so on. By choosing the set of pixels which minimises the residual between a fitted value and the data, polarity can be restored to the images, on a pixel by pixel basis.

An alternative to this is to fit to a magnitude equation:

$$S(t) = |S_0(1 - Ae^{\frac{-t}{T_1}})| \tag{2.32}$$

Which may result in quicker computation but at the expense of a poor estimation of signal at the zero crossing point, see Figures 2.12 and 2.13. In addition, a magnitude fitting has been found to be more sensitive to initial conditions than a multi-fitting approach [21],

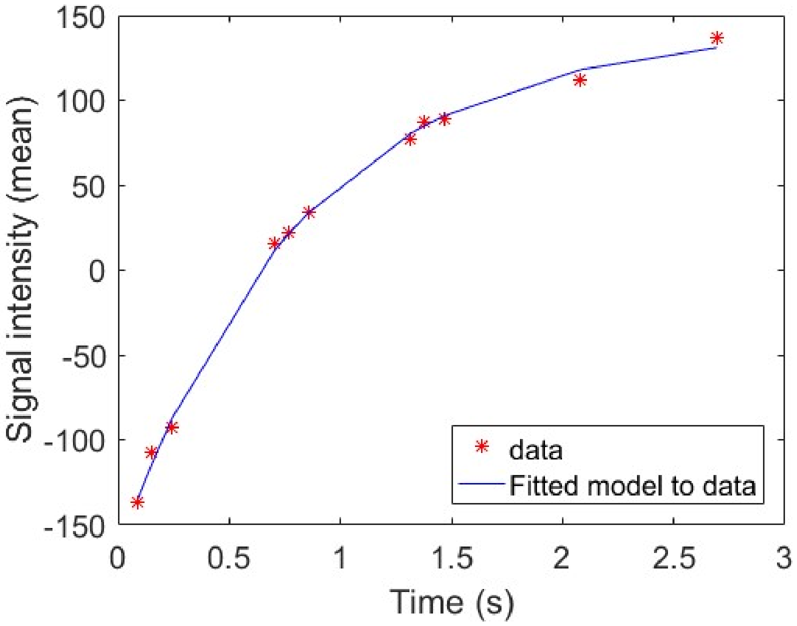

Fig. 2.12 Examples of fitting to a 3 parameter inversion recovery equation from a MOdified Look-Locker Inversion recovery sequence (MOLLI) acquisition, where signal polarity has been restored via a multi-fitting approach.

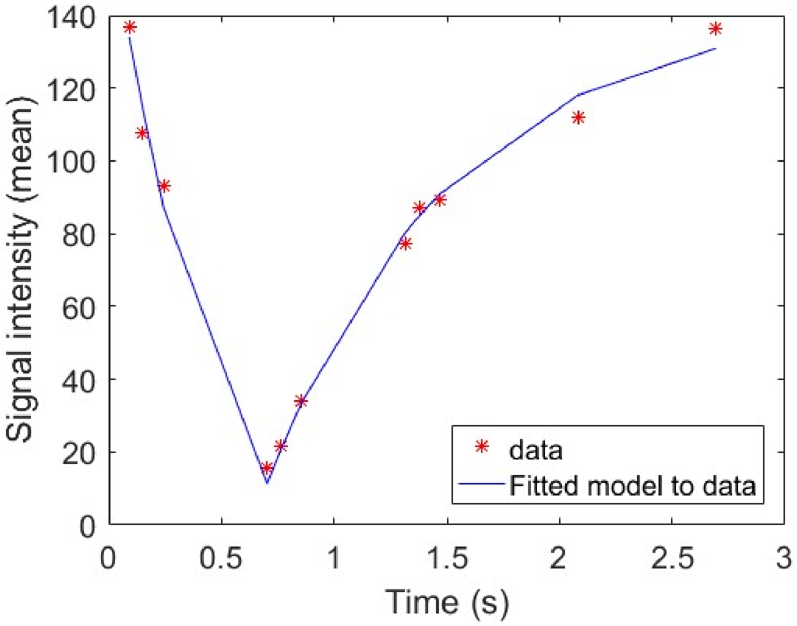

Fig. 2.13 Examples of fitting to a magnitude fit to the inversion recovery equation from a MOdified Look-Locker Inversion recovery sequence (MOLLI) acquisition.

An alternative method to saturation and inversion recovery techniques is to use the ratio of T_1 weighted and proton density weighted images to calculate T_1.

$$\frac{S_{T_1}}{S_{PD}} = \frac{M_0(1-e^{\frac{-T_R}{T_1}})}{M_0} = 1-e^{\frac{-T_R}{T_1}} \tag{2.33}$$

Where S_{T1} is the signal from the T_1 weighted image and S_{PD} is the signal from the proton density weighted image. This method automatically eliminates T_2 weighting and does not require model fitting. T_1 can be directly calculated from the ratio of signal intensities:

$$T_1 = \frac{T_R}{ln(1-\frac{S_{T_1}}{S_{PD}})} \tag{2.34}$$

[10].

2.2.1 Cardiac T_1 mapping

The MOdified Look-Locker Inversion Recovery sequence (MOLLI) adapted the inversion recovery Look-Locker sequence [22] for cardiac imaging. The sequence is gated to cardiac motion and combines acquisitions from three inversion recovery sweeps in order to sample the beginning of the inversion recovery curve more thoroughly. The original Look-Locker sequence uses a correction factor based on using a spoiled gradient echo readout (SPGR). A spoiled readout eliminates any transverse magnetisation, ensuring there is no magnetisation in the transverse plane, such that a steady state of transverse magnetisation cannot develop. Under this condition, the following equation and correction can be used:

$$S(t) = A(1-Be^{\frac{-t}{T_1*}}) \tag{2.35}$$

Where T_1 is given by

$$T_1 = T_1^*(\frac{B}{A}-1) \tag{2.36}$$

However, MOLLI uses single-shot steady-state free-precession (SSFP) readout. Instead of eliminating transverse magnetisation, an SSFP readout allows the system to reach a steady-state in the transverse plane (i.e. an equilibrium of non-zero transverse magnetisation develops). This makes the above correction inapplicable and gives the sequence a slight T_2 weighting. The correction in equation (2.36) is technically invalid, and leads to an underestimation in resultant T_1 due to longitudinal magnetisation recovering faster than it would with an SPGR readout. Nonetheless, the correction factor has been found to be reasonably affective at low read-out excitation flip angles [21].

The MOLLI sequence consists of three inversion recovery sweeps, see Figure 2.14. The original version of the sequence has 11 image acquisitions in 17 heartbeats [23]. The signal intensity from each MOLLI image is plotted against the time of data acquisition, showing a signal recovery curve. From this, curve fitting can determine the value of T_1 as the signal recovers according to equation 2.35.

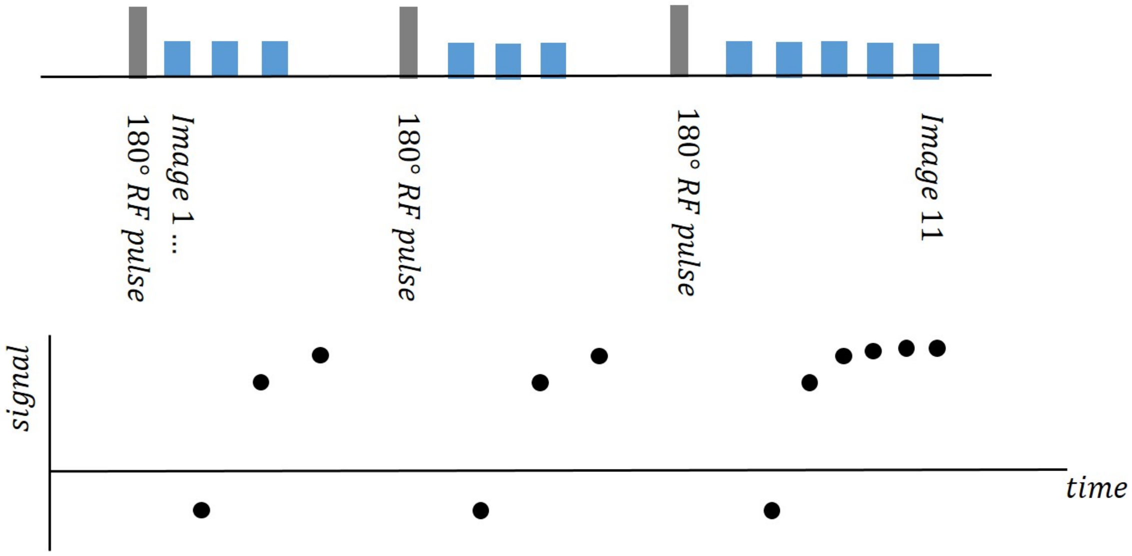

Fig. 2.14 Schematic drawing of a MOLLI sequence and subsequent inversion recovery curve.

Studies comparing MOLLI T_1 values in phantoms have shown that T_1 values are less accurate but more reproducible when compared to saturation recovery based techniques

[24] with phantom spin-echo acquisitions used as reference T_1 data. Magnetisation transfer comprises a significant component of MOLLI underestimation, as the RF inversion pulse does not fully invert the bound pool of spins (spins that are bound to molecules, but which are continually exchanging with free spins). This leads to an accelerated impression of inversion recovery. Saturation recovery techniques, such as SASHA [25] acquire cardiac gated saturation recovery images which do saturate the bound pool and are not effected by magnetisation transfer. However, in inversion recovery images the effect of the un-inverted bound pool is largely due to physiological parameters rather than acquisition parameters and is found to be reproducible. This results in an inaccurate but reproducible T_1 measurement. SASHA has been found both through simulations and phantom experiments to be less precise and less reproducible than MOLLI [21].

The precision of T_1 measurement when using a MOLLI sequence also depends on the method of curve-fitting employed to determine T_1 from the acquired images. Resultant T_1 accuracy depends on how signal-polarity is determined (restored) from magnitude images. Signal polarity can be determined from magnitude images using curve-fitting to equation (2.35). Though time consuming a final fitting process to equation (2.35) results in a more precise fitting than a fit to magnitude data, as shown in Figures 2.12 and 2.13.

Phantom studies show that the MOLLI sequence is heart-rate dependent as the time interval between inversions and SSFP readout is determined by heart rate. Heart rate dependence can be reduced by acquiring just 7-8 images over 11 heartbeats, using two inversions (5-3), or (4-3). In this there is a trade-off between increasing heart-rate dependence versus acquiring less data with shorter sequences which may effect curve-fitting precision. An alternative method is to reverse the order of sampling, so that 5 images are acquired in the first inversion, followed by 3 images after the subsequent inversions (5-3-3), reducing average time between inversions and therefore heart rate dependence without acquiring less images [26, 27]. However, an in vivo study on 20 healthy volunteers and a separate study of 60 healthy volunteers showed no measurable T_1 heart rate dependence within the group [28, 29], which may indicate heart rate dependence contributes less to variability than normal physiological variation.

The shMOLLI sequence was designed to overcome the heart rate dependence of MOLLI. The shMOLLI sequence uses three inversions, but acquires 5 images after the first inversion, followed by 1 image after the subsequent inversions (5-1-1) as well as using conditional fitting [30]. In phantom and in-vivo based experiments (10 patients and 8 controls) shMOLLI showed greater underestimation of T_1 compared to MOLLI and less precise measurement. However, the shMOLLI acquisition still resulted in more precise T_1 measurements than SASHA acquisition [24]. In a larger, in-vivo experiment characterising normal T_1 variation (342 subjects) shMOLLI T_1 was found to be heart-rate independent – once corrected for age and sex. However, the use of conditional fitting results in less precise measurement if T_1 due to the discarding of data, with no corresponding gain in accuracy [21].

Overall, despite alternative sequences being developed, such as saturation recovery (SASHA) and combined saturation and inversion recovery based techniques (SAPPHIRE [31]) MOLLI sequences remain widely used for their advantages in reproducibility and precision. Many of the accuracy-based disadvantages are reproducible and do not necessarily effect the clinical usefulness of the sequence, especially when centre-specific normal T_1 values are well established and understood. Examples of normal myocardial T_1 values are presented in Table 2.2.

2.2.2 Lung T_1 mapping

The gold-standard MRI technique for measuring T_1 is a cardiac-gated inversion recovery sequence with a spin echo readout, however long scan times are required for this sequence. Faster sequences have been developed using faster readout and with a larger number of images acquired enabling more robust curve fitting. Acquiring 16 low flip angle (α) gradient

Table 2.2 Normal cardiac myocardial T_1 values, measured using MOLLI sequences.

	N	**Sequence**	**Field strength (T)**	**Sex (% male)**	**mean age (years)**	**Region**	**T_1 (ms)**
Dabir et al [32]	102	MOLLI 3-3-5	1.5T	41	52	entire myocardium	950 ± 21
Bulluck et al [33]	101	MOLLI 5-3-3	1.5T	51	46	inferior septum	1013 ± 27
Reiter et al [14]	40	shMOLLI 5-1-1	1.5T	50	46	mean myocardium	984 ± 28
Dabir et al [32]	102	MOLLI 3-3-5	3T	41	52	entire myocardium	1052 ± 23
Rosmini et al [34]	94	shMOLLI 5-1-1	3T	50	52	mid septum	957±30
Rosmini et al [34]	94	MOLLI 3-3-5	3T	50	52	mid septum	1028±38
Roy et al [35]	75	MOLLI 3-3-5	3T	56	54	entire myocardium	1122 ± 57
Roy et al [35]	75	MOLLI 3-3-5	3T	56	54	mid septum	1162 ± 81

echo images with short effective echo times after an inversion pulse was proposed [22], see Figure 2.15 for a pulse sequence diagram. This creates a set of images using breath hold to suppress respiratory motion. These images can be processed in much the same way as cardiac T_1 mapping images, using equations (2.35) and (2.36) but in this instance the correction factor remains valid as the sequence uses a SPGR readout.

A modified version of the approach by Jakob et al., [36] uses an ultra-short TE (UTE) of $750\mu s$ and an asymmetric readout to compensate for the short T_2^* of the lung parenchyma. This sequence was implemented in the lung in volunteers and resulted in a breath hold of less than 5 seconds. However this method used an image resolution of 64x128, due to acquisition time limitations. There is a limit on the resolution of the images, as multiple images at short TIs need to be acquired in order to sample the beginning of the inversion recovery curve well and ensure an accurate curve fitting. Therefore, increasing spatial resolution of the images increases the time between subsequent image acquisitions which may lead to inaccurate T_1, especially for tissues with a short T_1, see Figure 2.16.

A free breathing UTE sequence has been developed which is sensitive to both T_1 and T_2^* changes from which two parameter maps can be calculated from one sequence. The technicalities of the motion correction of this sequence is described in the next section of this thesis. The sequence uses TE of $70\mu s$ [7] and is based on a Look-Locker sequence, but is segmented into blocks. Each block contains an inversion pulse, a set of radial k-space projections and a delay time to allow the magnetisation to fully relax between segmentations.

A 3D, UTE saturation recovery sequence which maps both T_1 and T_2 named ITSR-DUTE (interleaved saturation recovery with dual echo ultra short echo time) has also been published [37]. In this method T_1 is calculated from two images, one with and one without a saturation pulse:

$$T_1 = -T_S/(ln(1-\beta S(T_S)/S_0))/\eta) \tag{2.37}$$

Where T_S is the saturation delay time, S_0 is the signal from the image without a saturation pulse. η is the saturation efficiency. During Bloch simulations of the excitation profile of the saturation pulse used in the ITSR-DUTE sequence, the saturation efficiency was measured to be $\eta \approx 1$ for lung and muscle tissue [37]. β is a correction term, for which the derivation is shown in [37]. A 3D stack acquisitions (acquired with a radial k-space acquisition scheme) result in two sets of images: one which follows a saturation pulse and one which does not. There is a minimum delay of 4 seconds between each acquisition to allow the saturated signal to recover.

Lung T_1 mapping is often used with oxygen enhancement to demonstrate regions of poor ventilation and/or perfusion as well as any native T_1 changes due to disease processes [19] [38]. A meta-analysis of published data of MR measurements of the human lung at 1.5T found the average, healthy T_1 of the lung to be distributed around 1200±150ms with a reduction of around 10% upon inhalation of 100% oxygen [39]. Oxygen enhancement T_1 mapping has been described in more detail in section 2.1.4.

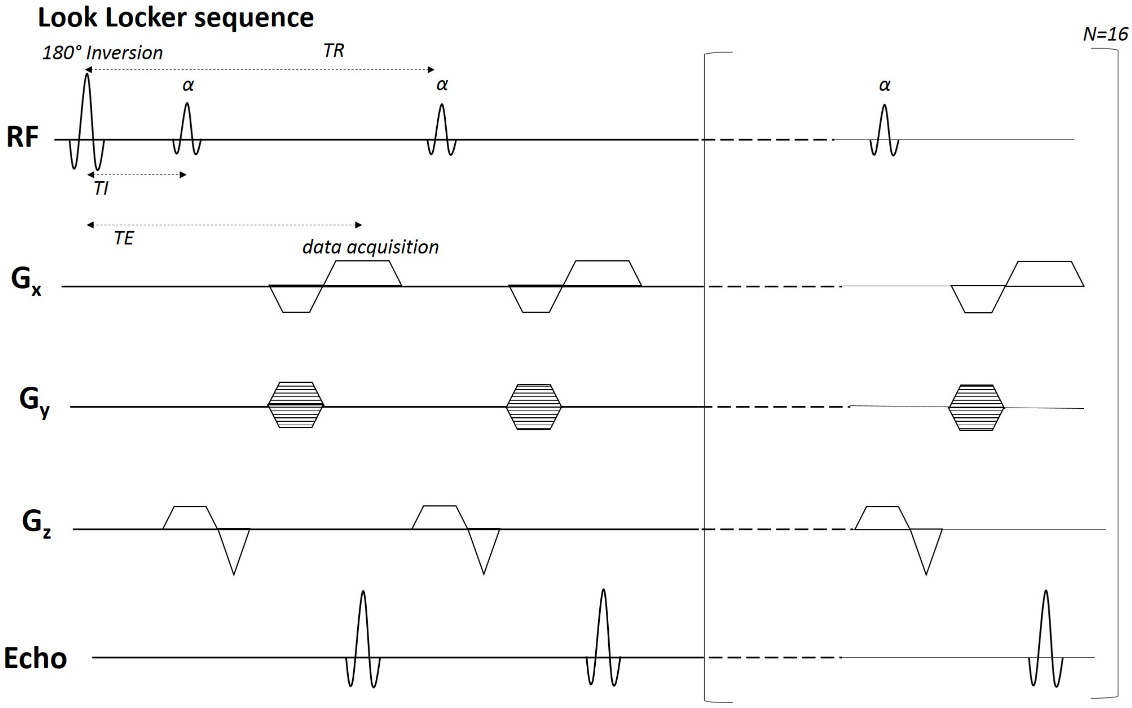

Fig. 2.15 Diagram of a Look-Locker inversion recovery acquisition. A 180 degree inversion pulse is followed by 16 low flip angle (α) gradient echo image acquisitions.

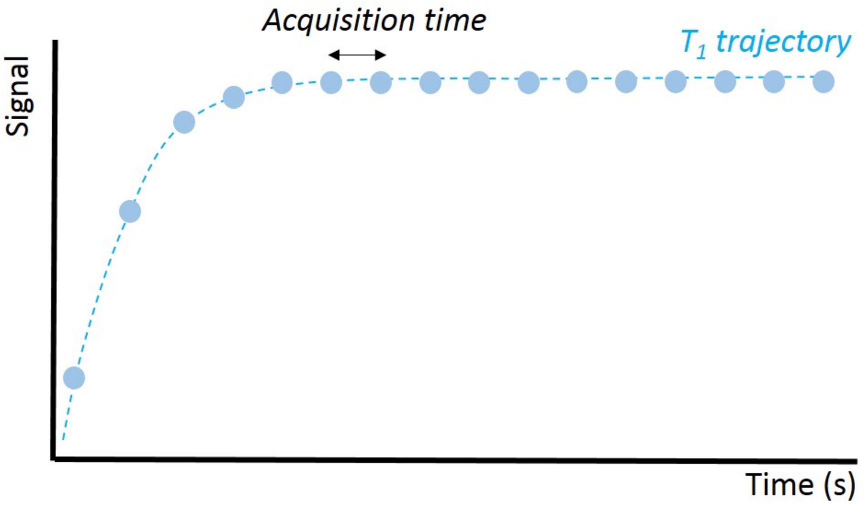

Fig. 2.16 Diagram of a Look-Locker inversion recovery curve to demonstrate the increased sampling at the beginning of the recovery curve when a shorter acquisition time is used.

2.3 T_1 mapping and motion correction

2.3.1 Image registration background

Image registration is the process of spatially aligning images. In medical imaging, it can be necessary to spatially align images: when the subject has moved; when combining images that occur at different times; when images are acquired with different modalities; or when images originate from different patients. There are a wide variety of image registration techniques that have been developed to solve these varied problems. A registration algorithm itself has four basic components which are shown Figure 2.17. Two images will usually be used - a reference (fixed) image and a target (moving) image and the moving image is spatially aligned to the fixed image.

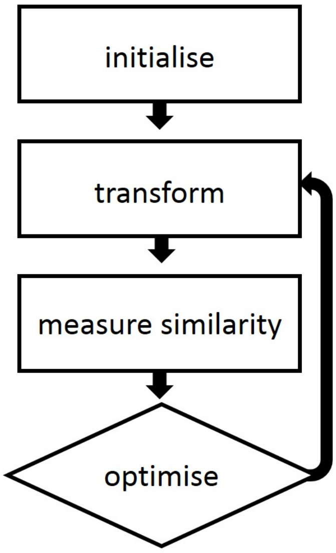

Fig. 2.17 Diagram showing the basic registration algorithm.

The transformation applied to an image can take one of four forms: rigid, affine, projective or curved/deformable. The different transformations have different degrees of freedom available to them. Rigid transformations have rotational and translational degrees of freedom; affine transformations have rotational, translational, skew and scaling degrees of freedom; projective transforms allow straight lines to be transformed to straight lines, and curves to be transformed to curves; deformable transformations can be considered free-form and allow straight lines to be mapped to curves, see Figure 2.18 for examples [40].

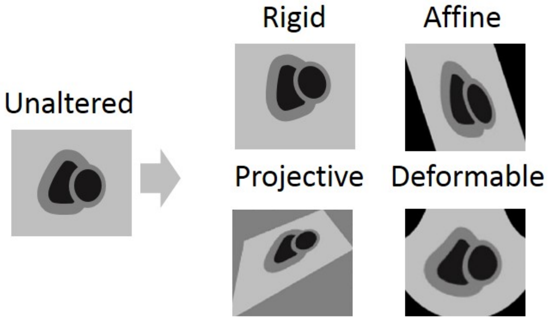

Fig. 2.18 Diagram showing the four basic transformation descriptions.

A similarity measure will calculate the likeness of two images using a criteria based on either feature matching (e.g. matching landmarks of segmentations) or pixel properties (e.g. cross correlation coefficient). The similarity measured used will evaluate how well the images align during the optimisation process, and the registration algorithm will iterate until the similarity measure meets a specified criteria (e.g. is minimised).

For inversion recovery images with respiratory motion, image registration may be able to correct both accidental and free breathing respiratory motion without extending scan-time or requiring additional equipment during the MRI scan (such as bellows or optical tracking) to monitor motion or for a radiographer to segment an image or identify landmarks. Alternative methods of dealing with motion in inversion recovery images are discussed in Section 2.3.2 and 2.3.3, and usually require greatly extended scan times for patients or manual input from the radiographer analysing the data. In contrast, image registration may offer a fully automated method of motion correction without any extension in scan time.

In the cases discussed in this thesis, the images are from the same modality (monomodal), patient (intrasubject) and image slice. This thesis will only consider 2D imaging problems, as a single 2D slice is the most common situation in cardiac and lung T_1 mapping as 3D imaging increases scan time. There are a wide variety of choices theoretically available when

2D registering inversion recovery images, see Figure 2.19 [41] [40]. However, to create fast, efficient and clinically-applicable image registration, an intrinsic, automated method is preferable. Moreover, in the case of inversion recovery images, some images will have poor contrast due to signal-nulling and tissue contrast changing with TI, making it difficult to segment or landmark the images. Pixel-property based methods are most suited to an automated work-flow and are theoretically the most flexible similarity measure as they are not specific to a certain anatomic region (or even anatomy at all), however they generally have a larger computational cost [41].

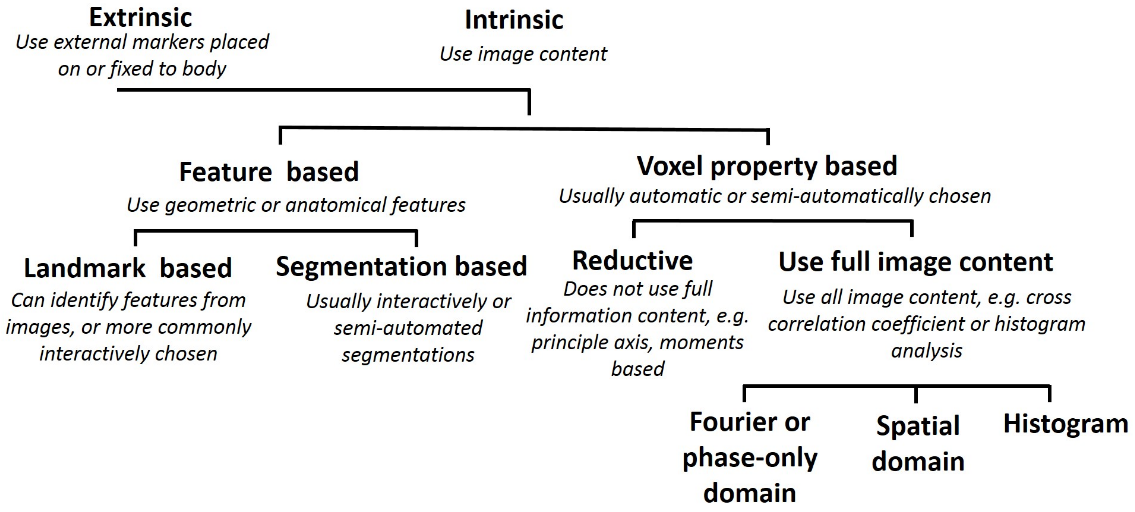

Fig. 2.19 Diagram showing the key registration choices available in approaching a monomodal intrasubject registration problem.

A common pixel-property based similarity measure is the sum of square differences (SSD), which uses the pixel intensity differences between the fixed image, **f**, and target image, **m**, as a measure of image similarity. This can be written as:

$$SSD = \sum (\mathbf{f} - \mathbf{m^T}(\mathbf{a}))^2 \tag{2.38}$$

Where parameter **a** is a set of vectors which define the deformation between **f** and **m**. Thus **a** is optimised via minimising SSD. A common alternative to the sum of square differences is mutual information, as it does not rely on image intensity, instead looking at similarities in the histogram distribution of signal between the fixed and target image. However mutual information can be very computationally costly.

In the work described in this thesis, a pre-existing image registration toolkit called ShIRT was used [42] [43]. The ShIRT toolkit is written in C and for this work ran from Matlab. The image space is described using a finite mesh (grid) which is then warped by the mapping functions $u(x,t)$ and $v(x,t)$ to result in the moved (registered) image. The transformation is described by the mapping between the registered and unregistered images, such that if the co-ordinates of a region on the fixed image are x, y and the co-ordinates of the same region on the target image are x', y', the mapping is described by functions $u(x,y)$ and $v(x,y)$ such that:

$$x' = u(x,y) + x, y' = v(x,y) + y \tag{2.39}$$

ShIRT uses a diffeomorphic transformation, which is applicable to this work as the cardiac and respiratory system may exhibit large non-rigid motion. The deformation is non linear uses one-to-one (the image cannot fold back on itself) and continuous (an object cannot be bisected or torn) mapping. The smoothness of the deformation can be controlled via a user-defined input.

Image similarity is measured using the sum of square differences with an additional modification which reduces the methods sensitivity to variations in signal intensity. This is described in [43] as the following cost function:

$$Q = \sum (\mathbf{f} - \mathbf{m}^{\mathbf{T}}(\mathbf{a}))^{\mathbf{2}} + \lambda \mathbf{a}'\mathbf{L}'\mathbf{L}\mathbf{a} \tag{2.40}$$

Where the second term is a weighting function which acts as a smoothing constraint, $\mathbf{L}$ is the discrete second derivative (Laplacian) and the coefficient λ corresponds to the degree of smoothing. Therefore λ controls the relative importance of the first term (sum of squares) and the second term (smoothing constraint). λ is halved iteratively from its starting value until mutual information between the images decreases. This works to balance image registration and image smoothness. The starting value of λ is chosen based on empirical findings to minimise $\mathbf{T^TT} + \lambda\mathbf{LL^T}$ where $\mathbf{T}$ is a function of $m(a)$ which is derived in the work of Barber and Hose [42].

The node spacing (the space between the grid nodes on the mesh) starts at one quarter of the image size and is similarly iteratively optimised until there is no improvement in mutual information between images. The minimum node spacing (the distance between nodes on the grid that describes the image transformation) can be chosen by the user. A smaller node spacing will warp finer details but at an increased computational (and therefore time) cost. The transformation applied to pixels between nodes is interpolated. The mapping solution is therefore found iteratively until $(\mathbf{a})$ falls below 0.1 pixels.

Although the ShIRT toolkit is robust to intensity differences between the fixed and target image due to the additional smoothing term in the cost function in Equation 2.40, the dramatically changing contrast as well as signal intensity across images in an inversion recovery series cannot be overcome using ShIRT alone. Existing registration methods which have been developed to overcome this additional problem in T_1 mapping (of drastic contrast changes and signal inversion), as well as non-registration based motion correction alternatives, are described in the following sections 2.3.2 and 2.3.3.

2.3.1.1 Evaluation of image motion using Dice Similarity Coefficient

Dice Similarity Coefficient measures how well two segmented areas overlap (DSC) and therefore can be used to assess global alignment of segmented areas on MR images [44]:

$$DSC = \frac{2area(\mathbf{M} \cap \mathbf{N})}{area(\mathbf{M}) + area(\mathbf{N})} \tag{2.41}$$

Where M and N are two segmented areas. An example of the process of segmenting cardiac images and calculating DSC is shown in Figure 2.20.

For each segmentation ‘M’, ‘N’ corresponded to the segmentation for the first image, such that the DSC value corresponds to how well each image is registered to the first image. If image registration has been applied to the image set, DSC is calculated as a metric of how well each image corresponds to the first registered image (not the unregistered first image). Although DSC is a global metric which does not provide precise information on spatial alignment, it is a robust and well established method which gives a basic indication of image alignment. An example of DSC calculated before and after image registration are shown in Figure 2.21.

2.3.2 Cardiac T_1 mapping and motion correction

Cardiac T_1 mapping relies upon pixel-by-pixel calculations across a set of images acquired at different times, see Figure 2.14, therefore image sets must be spatially aligned. Spatial misalignment leads to the same pixels in different images corresponding to different anatomical space, which results in erroneous T_1 calculations. The problem of motion-induced artefact or misalignment can be overcome in several ways: restricting motion (e.g. breath hold or sedation); reducing sensitivity to motion (e.g. using sequence acquisitions with less vulnerability to motion artefact); detecting motion and acquiring data in line with it (e.g. gating or triggering); detecting motion and correcting for it (e.g. using an external sensor or image data itself to navigate image acquisition); minimising the time in which motion can occur (e.g. using shorter sequences); or correcting motion post-acquisition using image registration.

In cardiac T_1 mapping, image alignment is usually achieved by combining breath hold and cardiac gating. Cardiac gating synchronises image acquisition with cardiac motion, and breath hold suppresses respiratory motion. The original MOLLI sequence requires 17 heartbeats, which with a 60bpm heart rate results in a 17 second breath hold. For some patient groups this may be a struggle: 40% - 48.3% of some patient cohorts have been reported to

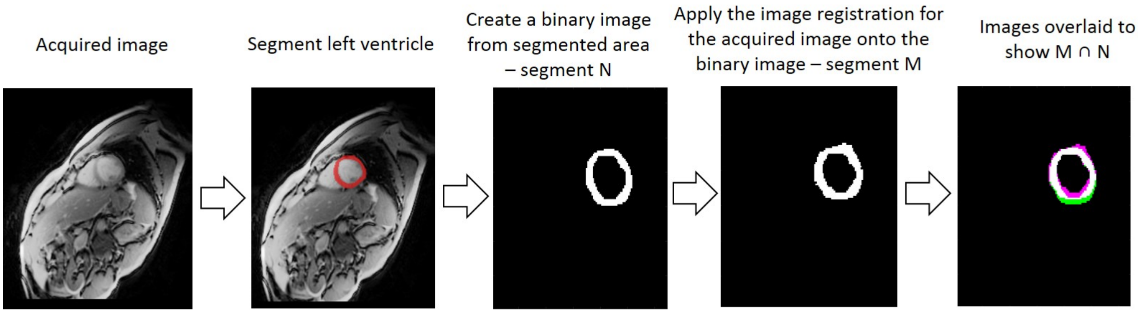

$$DSC = \frac{2\,area\,(M \cap N)}{area(M) + area(N)}$$

Fig. 2.20 An example of the process of segmenting cardiac images and calculating DSC. Pink segment corresponds to ’M’, green segment corresponds to ’N’.

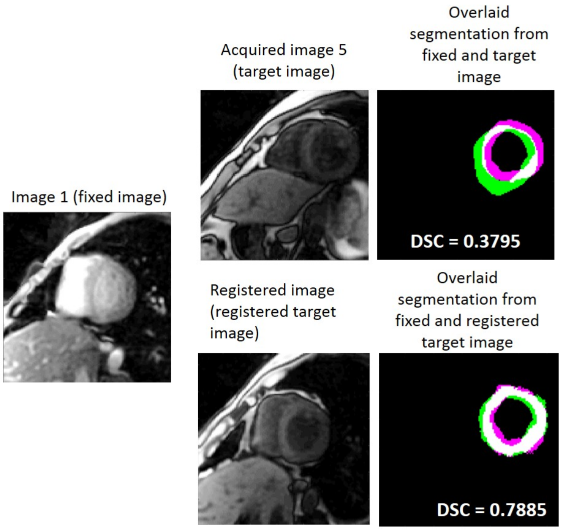

Fig. 2.21 An example of the process of segmenting cardiac images and comparing DSC before and after image registration. The pink segments correspond to the fixed image (image 1) and the green segments to target images (image 5).

display motion [5, 45]. Cardiac gating difficulties or irregular heart beats can also result in cardiac motion regardless of respiration.

Studies using MOLLI sequences have responded to cardiac motion in different ways, including:

- Discarding images which show motion [46],
- Manually segmenting or correcting each image [28, 47, 48],
- Automated image registration [5, 45],
- Shortening image acquisition time [30].

The shMOLLI sequence reduces problems with breath-holding in patients (as well as reducing heart rate dependence) by shortening the sequence. However, the shortened sequence acquires less data which results in a loss of precision in the resultant T_1 measurement [24].

Several different image registration algorithms to correct motion MOLLI images have also been suggested. These algorithms have been developed specifically for cardiac T_1 mapping images, which pose additional challenges for image registration due to the contrast differences between images. Areas such as the blood pool and myocardium may have no relative contrast in some images and considerable contrast in others. Traditional image registration techniques which use signal intensity to align images are therefore unsuccessful. Similarly, though images adjacent in TI (the time between image acquisition and the most recent inversion pulse) have similar contrast, attempts to register each image to the previous or next image are also unsuccessful as the image contrast differences still are too severe. The existing motion-correction methods include:

- Creating synthetic images using an iterative energy minimisation algorithm. This method creates an initial T_1 map estimate to calculate synthetic images. The synthetic images are iteratively improved to produce a spatially aligned set of images with similar contrast to the acquired images. Acquired images are then co-registered to their corresponding synthetic images, creating an aligned set of acquired images [5].

- Acquiring phase-sensitive images and using an estimated background phase removal to remove contrast changes between inversion recovery images. This method allows a more simplistic registration process by removing phase-based signal intensity changes [45].
- A group-wise image registration method based on principle component analysis which registers all of the images as a group [6].

An alternative approach to respiratory motion is to remove the breath hold and acquire images during free breathing. This improves patient comfort and allows for the possibility of acquiring 3D data in cases where breath-hold length would otherwise be prohibitive. Cardiac free-breathing methods usually involve selectively acquiring data or selectively discarding data such that you only acquire or use data within the same respiratory phase. Navigator images known as NAV-echos are commonly used in cardiac MR imaging to automatically determine the state of respiration of the patient and then choose whether to acquire the following image based upon a pre-determined respiratory window. NAV-echos can be either spin echo or gradient echo RF pulses which acquire a fast image (known as a "scout image") across the right hemi-diaphragm. A common scout image is a rapid, cylindrical, 1D image through the liver known as a pencil beam. The signal from the scout image is reconstructed prior to acquisition of the following image. Over time the reconstructed pencil beam images form a respiratory curve with peaks and troughs corresponding to expiration and inspiration. Therefore, the diaphragm position in the reconstructed 1D data can be used to determine respiratory state. If the scout image occurs within the pre-defined respiratory window, the following image is acquired, otherwise it is not. The linear relationship between the diaphragm motion and the resultant cardiac motion means that the motion tracked at the diaphragm can indirectly select aligned cardiac images (in the superior-inferior plane) [49]. However, due to the large amount of discarded data, free breathing navigated acquisitions can result in long scan times.

One example of this has been demonstrated in a cardiac T_1 mapping sequence, which used NAV respiratory gating (using a rapid 1D image acquisition to track the position of the diaphragm) for central k-space, and both NAV respiratory gating and prospective slice tracking to acquire outer k-space. This method produces 3D T_1 maps, with a 9 minute scan time for five component 2D images [8]. A similar method using a 1D NAV respiratory gating and the SASHA image acquisition sequence resulted in a 5-10 minute scan time [50]. In contrast, a 2D breath hold MOLLI sequence allows a scan time of around 17 seconds for the patient per slice.

2.3.3 Lung T_1 mapping and motion correction

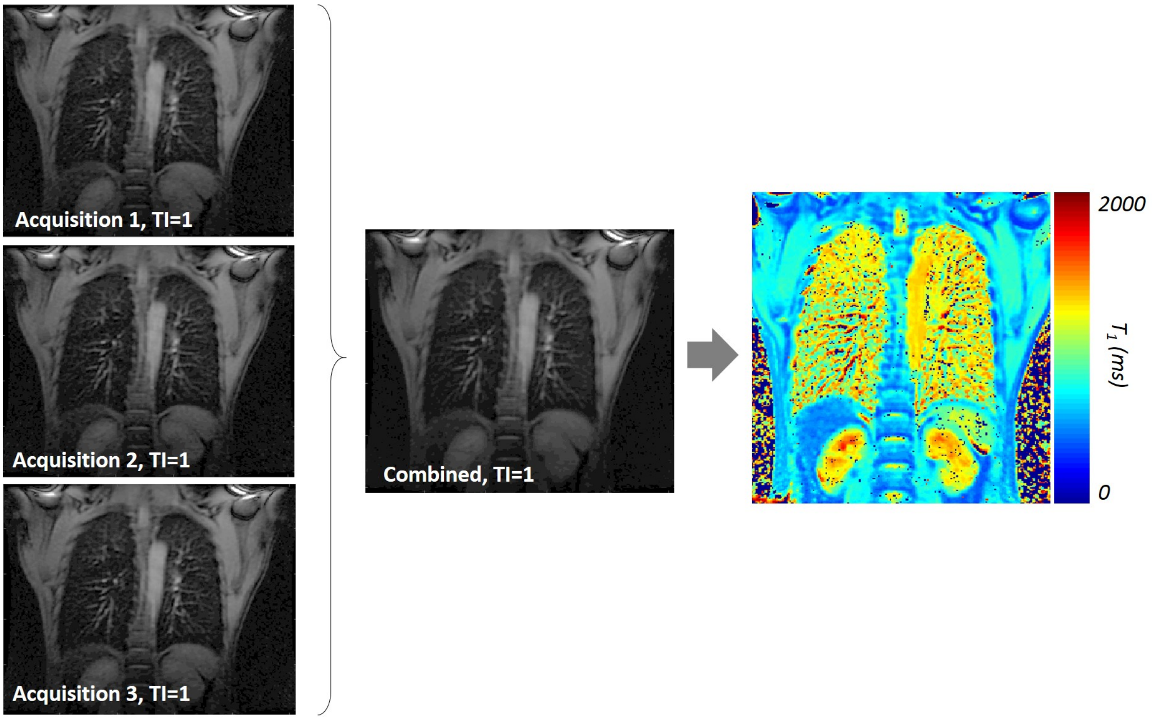

Fig. 2.22 Example of a lung T_1 map from a healthy volunteer, with three images averaged prior to T_1 map calculation, acquired matrix size 128 x 128.

Lung T_1 maps are usually acquired during breath hold. Due to the low proton-density in the lung resulting in a poor signal to noise ratio (SNR), which may be improved with image averaging, see Figure 2.22. In healthy subjects, expiration breath hold produces a significantly higher T_1 than those acquired in inspiration [51]. It is known that in expiration breath hold pulmonary perfusion significantly increases to over 200% of inspiration breath hold levels, which would substantially increase the relative contribution of blood to mean lung T_1 values [52].

Lung inversion recovery images require breath hold which patients may struggle to maintain. As with MOLLI images, contrast varies significantly throughout an image series. In particular, the liver, stomach, body fat and blood vessels vary in T_1 posing a challenge to lower lung registration. Like cardiac T_1 mapping, navigated free-breathing acquisitions can be used to remove the restrictions of breath hold. Free breathing datasets increase patient comfort and allow for longer sequences. An external navigator may be used to track respiratory motion. A data acquisition window is defined, and images are acquired within a certain respiratory range, such that they are aligned without the need for breath hold. However, this means only a fraction of the acquisition time results in useful imaging, leading to a much longer scan times with around 10 minutes for a 3D acquisition [37]. In addition, external respiratory triggering devices may provide poor gating resolution and if a large acquisition window is chosen there will still be some mis-registration in the images.

As well as external navigators, MR data itself can provide the information for respiratory monitoring and triggering. This can lead to more accurate respiratory triggering, although scan times are still much longer than a breath hold sequence. One example of this is navigator echoes (NAV-echoes) where respiration is tracked by acquiring a "pencil" imaging band at the diaphragm and automated software detects signal peaks and troughs due to respiration. The imaging sequence also uses a radial readout which reduces motion corruption in free breathing images. Images are acquired following several inversions occur and are interleaved after acquisition according to *TI*. However, this method requires around 2 minutes for a single 2D slice [7].

2.4 Clinical applications of T_1 mapping applications

2.4.1 Introduction to pulmonary hypertension

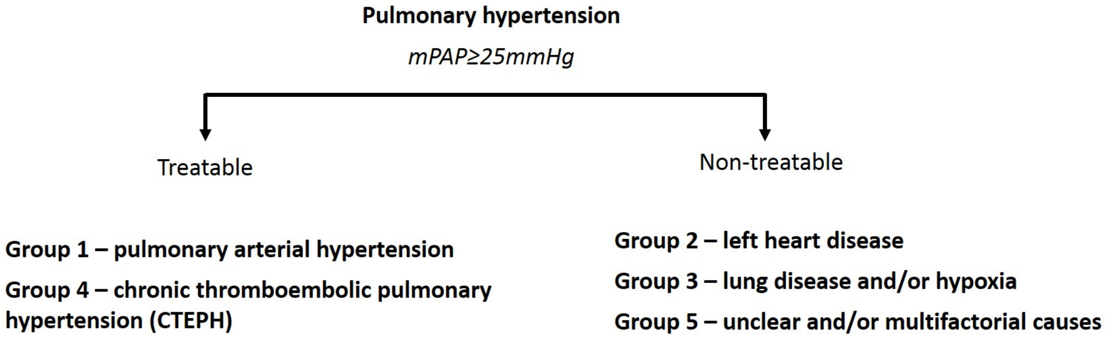

Fig. 2.23 Pulmonary hypertension subcategories.

Pulmonary hypertension a condition where blood pressure is increased in the pulmonary artery with a threshold for diagnosis of mean pulmonary artery pressure (mPAP) $\geq$25mmHg as measured by right heart catheter (RHC) [53]. RHC is an invasive procedure where a catheter is inserted into the pulmonary artery via a vein, commonly in the neck or groin, to allow measurement of blood pressures within the pulmonary artery. The RHC allows multiple quantitative measures, described in Table 2.3.

Pulmonary hypertension is a complex heterogeneous condition, with 5 diagnostic subcategories and a variety of causes, see Figure 2.23 [54]. Pulmonary arterial hypertension (group 1, see Figure 2.23), is the result the small pulmonary artery branches stiffening or thickening which restricts blood flow through the arteries. The restricted flow in the arteries then results in a build up of pressure in the main pulmonary artery. The prolonged elevated pressure in the right ventricle (RV) in patients with pulmonary hypertension leads to the RV adapting by thickening (RV hypertrophy) and dilating see Figure 2.24. There may be no known cause of the stiffening and/or thickening of the pulmonary artery branches (known as idiopathic pulmonary arterial hypertension - IPAH), however, it is more common for pulmonary hypertension to be the result of an associated cardiac or respiratory disease.

Pulmonary hypertension occurs in around 2.6% of the population and is more predominant in older individuals, with 59% of the PH population being female [55]. Diagnosis often occurs late with patients waiting up to two years after first experiencing symptoms to be diagnosed [56]. The median survival of patients with pulmonary hypertension without treatment is 2.8 years [57], although survival of patients with pulmonary hypertension depends on the form of the condition. For patients with pulmonary hypertension caused by another medical condition, treatment is primarily for the underlying medical condition which causes pulmonary hypertension. Patients with pulmonary arterial hypertension (group 1) or CTEPH (group 4) may receive treatment targeted at managing the condition specifically.

Table 2.3 Typical cardiac parameters obtained in a right heart catheterisation examination.

Parameter	**description**	**Calculation**	**Units**
PCWP	pulmonary capillary wedge pressure	-	$mmHg$
sPAP	systolic pulmonary artery pressure	-	$mmHg$
dPAP	diastolic pulmonary artery pressure	-	$mmHg$
mRAP	mean right arterial pressure	-	$mmHg$
svO_2	mixed venous oxygen saturation	-	%
saO_2	mixed arterial oxygen saturation	-	%
CO	cardiac output	estimated based on thermodilution	L/min
CI	cardiac index	CO/BSA	$L/min/m^2$
mPAP	mean pulmonary arterial pressure	dPAP + (sPAP - dPAP)/3	$mmHg$
PVR	pulmonary vascular resistance	(mPAP - PCWP)/CO	$dyn/s/cm^3$
PVRI	pulmonary vascular resistance index	(mPAP - PCWP)/CO	$dyn/s/cm^5$

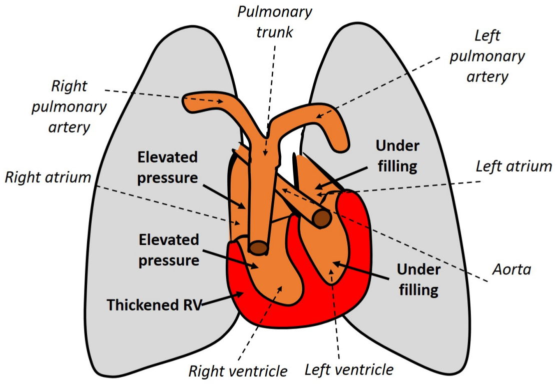

Fig. 2.24 Schematic drawing of the effects of pulmonary hypertension on the cardiovascular system.

Table 2.4 Typical cardiac parameters obtained in a cardiac exam for patients with suspected pulmonary hypertension measured from a cardiac cine MR image (bSSFP). BSA: body surface area.

Parameter	Description	Calculation	Units
RVEDVI	Right ventricular end diastolic volume index	RVEDV/BSA	ml/m^2
RVESVI	Right ventricular end systolic volume index	RVESV/BSA	ml/m^2
RVSVI	Right ventricular end stroke volume index	RVESV/RVEDV	ml/m^2
RVEF	Right ventricular ejection fraction	RVESV/RVEDV	%
LVEDVI	Left ventricular end diastolic volume index	LVEDV/BSA	ml/m^2
LVESVI	Left ventricular end systolic volume index	LVESV/BSA	ml/m^2
LVSVI	Left ventricular end stroke volume index	LVESV/LVEDV	ml/m^2
LVEF	Left ventricular ejection fraction	LVESV/LVEDV	%
RV mass index	Right ventricular mass index	Estimated from myocardial slice volumes assuming density of 1.05 / BSA	g/m^2
LV mass index	Left ventricular mass index	Estimated from myocardial slice volumes assuming density of 1.05g/cm^2 / BSA	%
VMI	Ventricular mass index	RV mass / LV mass	-
Septal angle diastolic	-	-	degrees
Septal angle systolic	-	-	degrees

2.4.2 Introduction to imaging modalities used in patients with pulmonary hypertension

Although pulmonary hypertension is diagnosed and characterised by elevated mPAP and pulmonary vascular resistance (PVR), it is failure of the RV to function that causes mortality in this condition. Therefore, visualising and measuring the structure, function and changes in the RV via imaging plays a key role in diagnosing and managing pulmonary hypertension. Imaging can aid in the identification of the cause of pulmonary hypertension which will guide treatment options and prognosis.

Transthoracic 2D Doppler echocardiography is a cheap and efficient way to estimate systolic pulmonary arterial pressure. However, for a more detailed assessment of RV volume, mass and function MRI or CT can be used [57–62]. MRI can provide both structural and functional information of the cardiac system without exposing the patient to ionising radiation. Analysis of a cardiac short axis cine MRI can provide volumetric, functional and mass metrics which describe cardiac adaptations and functionality see Table 2.4. In addition, cardiac flow measurements provide information on cardiac function and stiffness. The use of contrast agents (such as gadolinium) allow pulmonary perfusion to be visualised, as well as enhancement of areas of fibrosis and scarring via late gadolinium enhancement imaging in the myocardium (LGE).

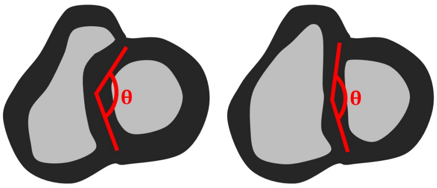

Fig. 2.25 Schematic drawing of two examples of interventricular septal angle measurements - the angle made between the interventricular insertion points and the centre of the interventricular septum.

To obtain ventricular volumetric measures the endocardial and epicardial surfaces on a short axis cine image are manually traced. Measurements are typically divided by body surface area (BSA) resulting in a volume index, see Table 2.4 [63]. High pressures in the RV may result in the interventricular septum bowing or deviating due to the pressure difference between the right and left ventricles. This can be characterised by a measurement of interventricular septal angle, see Figure 2.25 [64].

Cardiac MRI allows non-invasive investigation of the cardiac system and how it is adapting and changing due to the elevated pulmonary artery and right ventricular pressures. Multiple parameters can be calculated from a cardiac MRI scan, many of which have diagnostic and prognostic utility. VMI, septal eccentricity and pulmonary arterial velocity have been found to be of diagnostic value in pulmonary hypertension [56] and prognostic markers include RVEDVI, RVESVI, LVEDVI, RVEF, RVSVI and pulmonary arterial coupling [58, 60, 62, 65], see Table 2.4.

2.4.3 T_1 mapping applications in patients with pulmonary hypertension

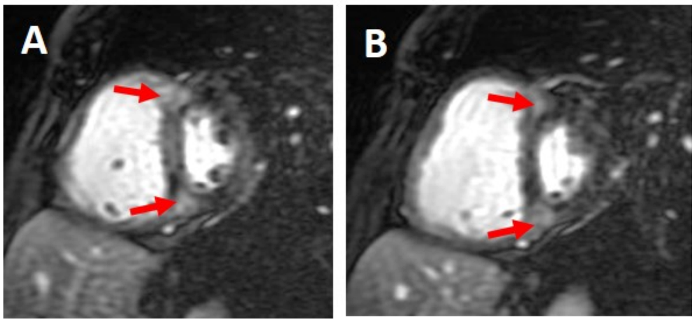

Fig. 2.26 Example images of LGE patterns in patients with pulmonary hypertension. A) LGE is shown in the RV insertion points extending into the interventricular septum. B) LGE is shown in the RV insertion points only. Arrows indicate regions of enhancement.

Cardiovascular magnetic resonance has become an established imaging technique in the evaluation of patients with pulmonary hypertension, as it allows direct visualisation and accurate analysis of the cardiac structure and function. MRI can also be used to assess myocardial tissue changes during disease. In late gadolinium enhanced (LGE) imaging, gadolinium accumulated in the extrocellular space in the myocardium is visualised using T_1 weighted imaging, due to the paramagnetic properties of the gadolinium contrast agent. In patients with pulmonary hypertension, LGE tends to present in the RV insertion points and septum in a distinctive pattern [66, 67], see Figure 2.26. The gadolinium contrast agent cannot pass through intact cell membranes, and therefore accumulates in the extra cellular space and damaged cells. An increase of gadolinium enhancement in the myocardium therefore indicates pathology. In addition, gadolinium enhanced imaging may be used to calculate Extracellular Volume Fraction (ECV) measurement, where the ratio of gadolinium uptake in the blood pool and myocardium is used as a measure of myocardial interstitial volume (i.e. extracellular volume) due to the accumulation of gadolinium in the interstitial area but not the myocyctes, see Figure 2.27. Native T_1 will also change to reflect a change in interstitial volume, as the component of overall T_1 which originates from the interstitial volume T_1 will increase accordingly.

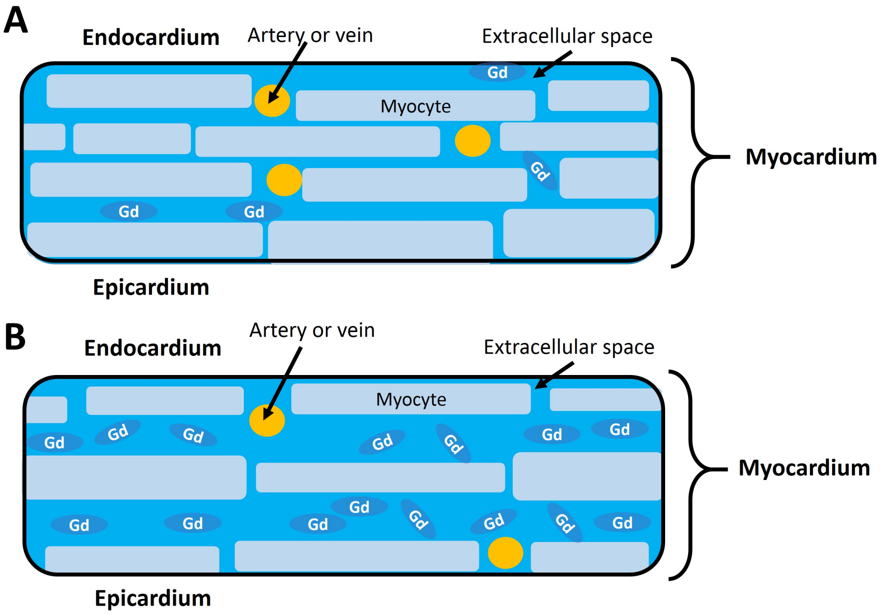

Fig. 2.27 Diagram showing how gadolinium uptake in the myocardium is increased when extra cellular volume is increased, (A) shows a healthy myocardium and (B) shows myocardium with increased extra cellular volume.

The specific mechanism responsible for accumulation of gadolinium (and associated native T_1 changes) in the myocardium in pulmonary hypertension is unclear. The myocardium is comprised of myocytes (long tubular cells which form muscle and lie in striated bands), blood vessels and blood (which is supplied by the coronary circulation), nerves and extracellular space (molecules which exist outside of the cells, including structural proteins such as collagen). Interstitial thickening is known as fibrosis and causes a stiffening of the cardiac muscle and may lead to functional deterioration [68]. This is known as replacement fibrosis, if the fibrosis replaces myocytes after damage to the myocytes occurs. If fibrosis occurs due to myocardial stress or inflammation, it is known as reactive fibrosis and is diffuse rather than localised [68].

Studies into tissue composition in pulmonary hypertension have shown that 2 patients with PAH show fibrosis at the RV insertion points [69]. However, a different study found a patient with IPAH and LGE present during MRI who did not have replacement fibrosis on autopsy, but the patient did have increased collagen and fat between fibre bundles [70]. Histological analysis of two porcine models of pulmonary hypertension showed the RV insertion points were found to have increased interstitial collagen associated with fibre disarray compared to controls [71]. Fibre disarray occurs where cardiac myocytes lie irregularly, rather than parallel which increases extracellular space, see Figure 2.28. Overall, it seems that while increased extracellular space and associated collagen is present in pulmonary hypertension, the presence

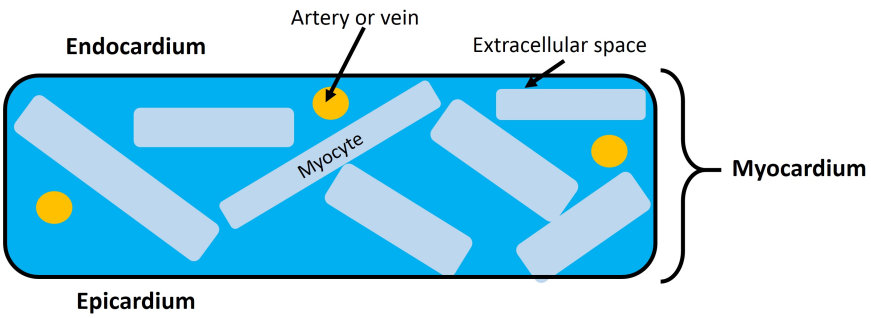

Fig. 2.28 Diagram showing how myocyte disarray results in increased extra cellular volume.

of replacement fibrosis does not seem to be. This may indicate that the myocardial changes present in pulmonary hypertension occur due to strain or inflammation, i.e. diffuse fibrosis, rather than replacement fibrosis due to cell damage.

It has been shown that RV dysfunction and remodelling is associated with worse prognosis in the presence of septal myocardial changes visualized by LGE [66, 72], however it has also been shown that myocardial changes visualised by LGE do not provide additive value over existing markers of prognosis in pulmonary hypertension [61, 66]. The prognostic significance of LGE in pulmonary hypertension therefore remains unclear.

An increase in extra cellular volume is expected to change native T_1 due to the tissue comprising a different ratio of cellular to extracellular space. In addition, native T_1 is also expected to change due to any changes in the composition of the extra cellular space, for example an increase of lipid molecules or collagen. T_1 mapping may provide a contrast-free alternative to visualising and quantifying myocardial changes in pulmonary hypertension without the side effects and risks associated with gadolinium. Porcine models and CTEPH patients show that native T_1 is significantly higher in subjects with LGE compared to those without LGE, and in addition, in pulmonary hypertension models and CTEPH patients without LGE native T_1 is significantly higher than control models - indicating that native T_1 may be a more sensitive marker to tissue changes [71, 73].

Elevated T_1 in the RV insertion points has been identified in porcine models [71] as well as patients with pulmonary hypertension [73] [74] [75] at both 1.5T and 3T, with one study finding elevated T_1 across the entire myocardium [75], see Table 2.5. Although these studies show promise, the number of patients considered are between 18-70 patients and do not evaluate diagnostic or prognostic significance. Therefore, it remains unclear whether the visualisation of myocardial changes via T_1 mapping is clinically beneficial for pulmonary hypertension patients.

Table 2.5 Scope of the current literature on native T_1 mapping in patients with pulmonary hypertension.

	Subjects	**Sequence**	**N**	**Field strength (T)**	**Patient groups**	**T_1 elevated?**
García-Álvarez et al [71]	porcine model	MOLLI 3-5	38	3	porcine model of chronic PH	insertion points elevated
Spruijt [74]	patients	MOLLI 3-3-5	70	1.5	mixed IPAH, PAH-SSc and CTEPH	insertion points elevated
Roller et al [73]	patients	MOLLI 3-3-5	24	1.5	CTEPH	septal and insertion points elevated
Reiter [75]	patients	MOLLI 5-1-1	35	3	groups 1 3 4 and 5	septal, lateral, global and insertion points elevated
Wang et al [76]	patients	MOLLI 3-5-5	19	1.5	PAH	insertion points elevated

2.4.4 Introduction to idiopathic pulmonary fibrosis (IPF)

Idiopathic pulmonary fibrosis (IPF) is a condition where the lung contains heterogeneous regions of fibrosis, inflammation and cysts known as honeycombing. Patients with IPF often have traction bronchiectasis - a widening of the airways leading to a build up of excess mucus which increases the likelihood of infection. The condition normally presents in patients in their 60-70s with men being almost twice as likely to develop IPF as women [77]. The cause of IPF is unknown, however it is overrepresented in patients who have worked with woodwork, metalwork, agriculture or who have been regularly exposed to cigarette smoke and therefore it may be that long term exposure to dust particles plays a role in causing or aggravating this condition [78]. Around $32\% - 50\%$ of patients with advanced IPF also develop pulmonary hypertension. IPF is fatal and prognosis is poor with a median survival of 2-3 years [79].

The symptoms of IPF are unspecific, with patients experiencing the following: breathlessness; a dry cough; tiredness; aching; clubbing of fingers and toes. Due to the unspecific nature of symptoms diagnosis often occurs late in these patients. The prevalence of IPF in the UK has increased in recent years to 15-25 people per 100,000 of the UK population [80]. Assessment of the condition can include X-ray or CT imaging, lung function tests and biopsy [81], however predicting prognosis remains difficult in patients with IPF. Some patients with IPF experience exacerbations and/or a rapid deterioration of disease and others a much slower disease progression with few symptoms many years after diagnosis. However differentiating those patients from one another is challenging [81].

The presence of fibrosis in the lung causes the lung to lose elasticity in the affected areas. This results in a decrease of lung volume, as the lung cannot stretch to accommodate large volumes of air. For this reason IPF is termed a restrictive lung disease and the clinical gold standard for assessment is the Forced Vital Capacity (FVC). In addition, the presence of fibrosis in the lung thickens the tissue between the airspace and blood, which inhibits oxygen exchange within the effected regions of tissue. This is assessed clinically with the carbon monoxide gas transfer test (DLCo). Both loss of lung elasticity and increase in lung fibrosis limit lung function, and there is currently no way to reverse the fibrosis present in the lung. The fibrosis is often distributed in the periphery and base of the lung, and can only be visualised using imaging methods such as CT and UTE MR imaging see Figure 2.29.

The clinical gold standard methods currently available to assess patients with IPF lack sensitivity. Pulmonary function tests (PFTs) provide easy to perform measurement of lung volume and function, but are unable to visualise tissue changes or regional variation within the lung. FVC has been shown to be an indication of mortality [82] however its longer term value is limited and can only predict short-term mortality, not future exacerbations [83]. Furthermore, a reduction in airway elasticity associated with emphysema may also

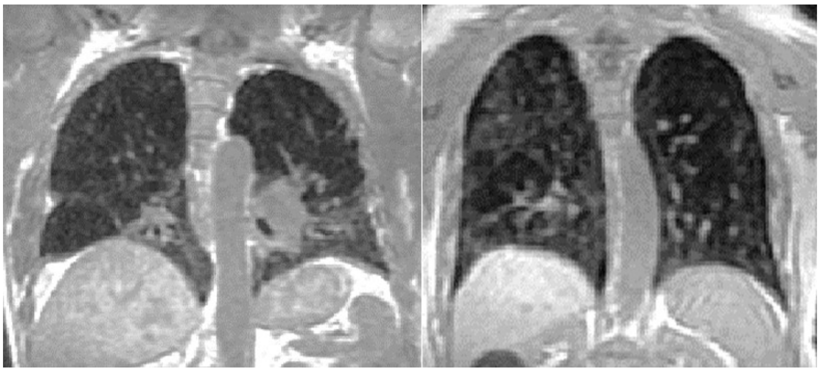

Fig. 2.29 Two coronal UTE images from patients with IPF demonstrating heterogeneous honeycombing in the lung.

occur within patients with IPF. This reduction in airway elasticity may appear as an increase in lung volume and obscure the severity of disease. X-ray allows some visualisation of fibrosis but with limited sensitivity to honeycombing (where cystic regions within the lung are small and widespread) and traction bronchiectasis (widened airways). CT imaging allows greater sensitivity to these features, however both X-ray and CT imaging expose the patient to ionising radiation. Therefore, there remains an urgent need for novel markers to help visualise the effect and progression of the condition, monitor treatment and to assess prognosis.

2.4.5 Lung T_1 mapping in patients with IPF

IPF is a condition characterised by changes to the lung tissue which limit the volume, oxygen exchange and function of the lung. Therefore, MRI methods which could characterise the tissue changes within the lung and evaluate lung function and oxygen exchange may be able to assist in diagnosing and characterising the condition without the use of invasive biopsy or ionising radiation.

T_1 mapping is used to assess tissue changes, including fibrosis, within the myocardium, and therefore may be able to assess pulmonary tissue changes too. T_1 mapping is also sensitive to oxygenation changes within the lung [39] and maybe be able to visualise regions of poor oxygenation in the lungs of patients with IPF. Due to the heterogeneous nature of tissue and oxygen exchange within the lung, it is possible that T_1 mapping may be able to demonstrate regional changes in tissue and oxygenation due to IPF in patients with the condition.

To date, two studies have performed lung T_1 mapping in patients with IPF [84] [85] which have found significant differences in lung T_1 compared to healthy volunteers, and significant correlations with measures of lung function such as lung capacity and lung residual volume. Fibrotic regions of lung in patients with IPF were found to have significantly different T_1 when compared to non-fibrotic lung regions within the same patients when CT was used to locate fibrotic areas [85]. These studies provide promising indications that lung T_1 mapping could be of use in the assessment and characterisation of IPF, however both studies had small patient numbers (7 IPF patients [85] and 10 IPF patients [84]). Before possible clinical benefits of lung T_1 mapping in patients with IPF can be explored, it is necessary to:

- Characterise the changes in lung T_1 in patients with IPF in larger numbers.
- Understand cause of changes in lung T_1 and the extent to which they arise from tissue, perfusion and oxygenation changes.

In addition, as patients with IPF experience breathlessness, the breath holds associated with conventional lung T_1 mapping may be a challenge for this patient cohort and development of free breathing techniques for lung T_1 mapping would improve patient comfort and clinical applicability [7]. Therefore assessing the practicality of a free breathing T_1 mapping sequence would be of particular benefit for this patient group.

Chapter 3

Image Registration method for Cardiac T_1 Mapping

This chapter describes a novel method for image registration to correct unwanted respiratory or cardiac motion in a MOLLI T_1 mapping sequence. The method is implemented and compared to an alternative motion correction method from Xue et al [5]. The two methods are compared in a cohort of patients with suspected pulmonary hypertension [1].

3.1 Background

T_1 mapping and extracellular volume imaging (ECV) are emerging tools for assessing the myocardium in multiple cardiac pathologies [86] and can detect myocardial changes such as fibrosis, inflammation or oedema. Both native T_1 and ECV imaging methods require the acquisition of accurate T_1 maps, which traditionally combine cardiac gating and breath hold to eliminate cardiac and respiratory motion. However, this also limits the number of

---

[1] The contents of Chapters 3 has been written in the form of a manuscript which is intended to be submitted for publication in the near future by: **Saunders, L.**, Stewart, N.J., Kiely, D.G, Graves., M.J, Swift., A.J. Wild., J.M.

longitudinal recovery images which can be acquired to one image per cardiac cycle, and limits time duration to that of a comfortable breath hold.

As seen in equation (2.25), if a pixel contains two tissues, the overall T_1 will be a weighted combination of the individual T_1s of the two tissues. This is particularly important in cardiac T_1 mapping where the typical myocardial thickness in a short axis plane is $5.3 \pm 0.9mm$ and $6.3 \pm 1.1mm$ for women and men respectively [87]. This results in pixels around the edges of the myocardium corresponding to a mixture of signal from the myocardium and blood pool, see Figure 3.1. In order to visualise the myocardium, good spatial resolution is therefore required. However, as spatial resolution increases, so does the inversion time interval (TI) and the resultant scan time. The spatial resolution of the acquired images will determine the extent to which the myocardium is affected by partial volume, see Figure 3.1. With decreased spatial resolution, a higher proportion of pixels which make up the myocardium correspond to a mixed signal. When drawing a region of interest on the myocardium, including these pixels results in an artificially elevated T_1 due to the inclusion of signal from the blood pool, resulting ultimately in a less precise T_1 measurement and potentially poorer reproducibility as mean T_1 will depend on the extent to which signal from the blood pool is included in regions of interest. Awareness of the issue of partial volume effects in T_1 mapping has led to suggestions of standardising methods of drawing regions of interest when assessing myocardial T_1 measurements, to minimise inclusion of the blood pool and increase reproducibility in T_1 measurements [88]. For this reason, unless otherwise specified, regions of interest are drawn conservatively and centrally, to avoid the blood-myocardium boundary throughout the work in this thesis.

Although T_1 mapping is becoming established as a tool for understanding myocardial changes in multiple pathologies, to utilise the full potential of T_1 mapping and ECV the methods used need to be reproducible, accurate and precise. This can be particularly challenging in patients who exhibit respiratory motion which leads to inaccuracies, or

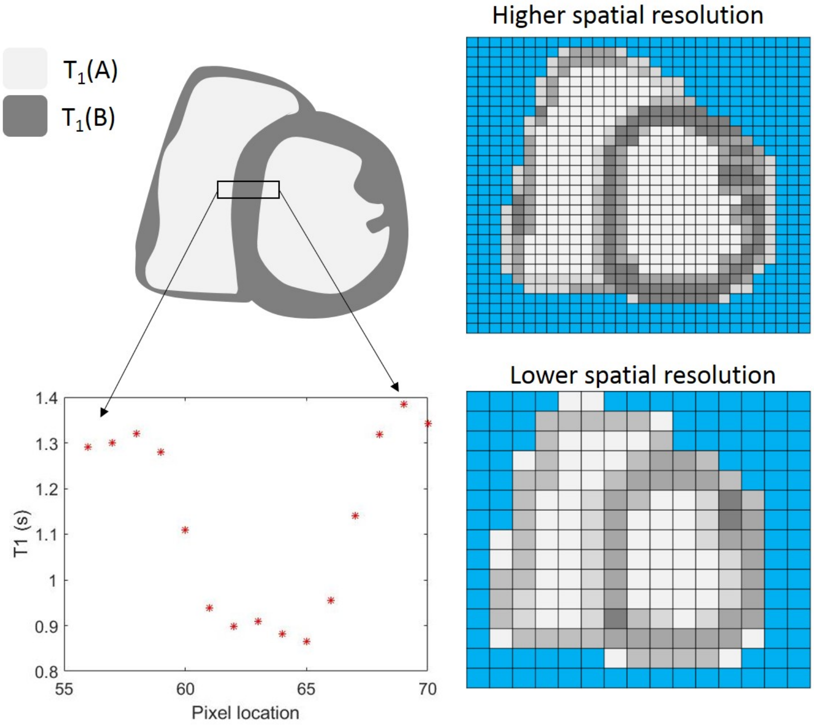

Fig. 3.1 Schematic diagram to show how with decreased spatial resolution, partial volume effects increase as a higher proportion of pixels in an image correspond to signal which corresponds to more than one tissue.

demonstrate heterogeneous myocardial T_1 where it can be difficult to determine where the myocardial boundaries lie.

Patients with pulmonary disease can struggle to maintain breath hold, leading to motion in acquired images and inaccuracy in resultant T_1 maps. Previous studies have reported 40% [45] and 48.3%[5] of patients National Heart, Lung and Blood Institute (Maryland, USA) displaying some motion in acquired images when using a MOLLI 3-5 protocol. The matter of respiratory motion has resulted in both the development of sequences with a shortened acquisition time and image registration based motion correction solutions. Shortened sequences, such as shMOLLI which uses a 5-1-1 sequence with conditional fitting, are intended to reduce respiratory motion by acquiring the majority of the images at the beginning of acquisition when breath-hold is more likely to be maintained, as well as reducing overall breath-hold time. However, as shMOLLI collects less data than the original 3-3-5 sequence, this is at the expense of SNR. Motion correction solutions aim to eliminate unintended respiratory motion after acquisition using image registration techniques designed to overcome the intensity and contrast differences in inversion (or saturation) recovery images. However, it has not been established the extent to which these solutions overcome the problem of motion in cardiac T_1 mapping, and whether both are required to optimally reduce motion.

Motion correction has been demonstrated with a variety of approaches: using pair-wise image registration to synthetic images [5]; using phase-sensitive motion correction [45] and using a group-wise algorithm to solve a combined motion problem [6]. These three methods are summarised in Table 3.1 and described below.

3.1.1 Synthetic Images

Using synthetic images to register MOLLI images was suggested by Xue et al. [5] using **synthetic images created via iterative energy minimisation**. The method creates a set of spatially aligned images with similar signal contrast and intensity to the acquired images using an energy minimisation algorithm. The method defines energy as a function of the acquired MOLLI images ($I(x,y,t)$), the inversion recovery images calculated from the initial T_1 parameter fitting ($S(x,y,t)$), the synthetic images ($M(x,y,)$) and a weighting parameter ($\omega(x,y)$) to preserve edge sharpness based on a pixel's correlation coefficient, such that:

$$E(M,I,S,\omega) = \int [((I(x,y,t) - M(x,y,t))^2 + \alpha \cdot \omega(x,y) \cdot (M_x^2 + M_y^2) + \beta \cdot (|S(x,y,t)| - M(x,y,t))^2] dxdydt \tag{3.1}$$

Were M_x and M_y are the first order partial derivatives of M with respect to x and y, and α and β are constants. The partial differential equation in equation 3.1 can be discretized, leading to a direct solution. $I(x,y,t)$, $S(x,y,t)$ and $M(x,y,t)$ are reformatted as a 1 dimension vectors, $\tilde{\mathbf{I}}$, $\tilde{\mathbf{S}}$ and $\tilde{\mathbf{M}}$:

$$\tilde{\mathbf{I}} = [I(1,1,1), I(2,1,1) ... i(N_x,1,1) ... I(N_x,N_y,1) ... I(N_x,N_y,N)] \tag{3.2}$$

Such that the energy function can be rewritten:

$$\tilde{E}(\tilde{\mathbf{I}},\tilde{\mathbf{M}},\tilde{\mathbf{S}},\omega) = (\tilde{\mathbf{I}}-\tilde{\mathbf{M}})\cdot(\tilde{\mathbf{I}}-\tilde{\mathbf{M}})' + \alpha\sum_{d=1}^{4}(\tilde{\mathbf{M}}\cdot\mathbf{D_d})\cdot\omega_{\mathbf{d}}\cdot(\tilde{\mathbf{M}}\cdot\mathbf{D_d}) + \beta(\tilde{\mathbf{s}}\mathbf{M})\cdot\tilde{\mathbf{s}}\mathbf{M})' \tag{3.3}$$

Where the four-neighbourhood of every pixel, D_1 to D_4 are first order derivative operators which form a sparse matrix of size $N_xN_yN_Z$ for four neighbouring pixels. Minimising equation 3.3 leads to a linear equation:

$$\tilde{\mathbf{M}}[(1+\beta)\cdot\mathbf{Ind}+\alpha\sum_{\mathbf{d=1}}^{\mathbf{4}}\mathbf{D_d}\cdot\omega(\mathbf{x},\mathbf{y})_{\mathbf{d}}\cdot\mathbf{D'_d}] = \tilde{\mathbf{I}}+\beta\cdot\tilde{\mathbf{S}} \tag{3.4}$$

Where **Ind** is the identity matrix.

Solving the minimisation problem given in equation 3.4 produces a set of synthetic images, which are then used to register the acquired images and produce a T_1 map. The registered images and T_1 map are then re-input into the energy minimisation problem, creating an iterative process where the synthetic images, registration and resultant T_1 map are improved upon. An initial registration step is undertaken prior to the energy minimisation process between the first and last images in the sequence. Image registration is performed using a fast variational non-rigid image registration framework which is an extension of the classical optical flow method, using cross correlation as the similarity measure and estimating the deformation field as a solution to a calculus of variation problem. The choice of the coefficients α, β and number of iterations was not specified by Xue et al., [5].

Phase-sensitive inversion recovery registration removes the contrast inversion which occurs in MOLLI images due to different T_1s in the myocardium and blood pool. However, misregistration in acquired images will lead to phase estimation errors, and this is overcome with a pre-registration step between the last image of the first inversion and the last image of the sequence (i.e. in a 3-3-5 sequence, between the third and last acquired images), the deformation field from this registration is then applied to all other images of the first

Table 3.1 Scope of current literature on motion-correction for T_1 mapping sequences.

	Year published	**Implemented on**	**Method**
Xue et al [5]	2012	MOLLI 3-5	synthetic images via iterative energy minimisation
Xue et al [45]	2013	MOLLI 3-5	phase-sensitive inversion recovery registration
Tao et al [6]	2017	MOLLI 3-3-5	group-wise registration

inversion. This method uses the same image registration framework as the method using synthetic images via energy minimisation. This method assumes that the MOLLI image with the longest TI has fully recovered magnetisation, and therefore uses the phase of this image to restore signal polarity for the MOLLI series. In addition, the use of phase-sensitive reconstruction results in eliminating the need to undergo multiple fitting to restore signal polarity, which results in a high computational cost. Phase-sensitive motion correction has been found to achieve similar accuracy to registration to synthetic images, but to be more computationally efficient.

Both synthetic image registration and phase-sensitive registration are pair-wise methods. An alternative is **group-wise motion correction**. Group wise motion correction optimises a transformation for two sets of T_1 mapping images pre and post contrast in a unified registration strategy with 22 frames. The method measures the alignment of all frames together, the more aligned the images are, the more that the signal time course of each pixel across images $1...N$ is similar.

Both phase-sensitive inversion recovery and group-wise registration techniques were compared to the iterative synthetic image based registration method in the publications of Xue et al., [5] and Tao et a., [6]. Both methods were found to be of similar registration robustness and quality to the synthetic-image registration method, but faster in terms of post-processing. Phase-sensitive inversion recovery was found to be 3.2x faster than their implementation of the iterative synthetic image based method [45], and group-wise registration was found to be 3.1x faster than their implementation of the iterative synthetic image based method.

To summarise, three methods of registration have been described in the literature, which compare equally well in terms of registration quality. All three methods are implemented on a single MOLLI sequence. All three methods are shown to correct accidental patient motion, but have not been applied to free breathing, as the authors state the methods either may not be capable of dealing with large through plane motion [5] [45], or, in the case of group-wise registration which was only trialled in patients who were reasonably good at breath holding, that more work is warranted in patients with "larger motion" [6]. Shorter sequences may also help reduce the amount of motion acquired. It is not clear whether sequences with shorter acquisition time such as shMOLLI eliminate the need for motion correction, and whether they improve overall registration when combined with motion correction.

3.2 Objectives

The objectives of this chapter are to

- Establish whether shortened sequences successfully eliminate the need for motion correction,
- Present a novel motion correction method and evaluate its success against an implementation of the published synthetic image based motion correction method of Xue et al [5].

3.2.1 Quantifying the need for image registration in cardiac T_1 mapping

It has been established that significant levels of motion are present in MOLLI 3-3-5 sequences when applied to a patient population, and that a clinically relevant solution to motion-correction is required to produce accurate T_1 maps. The shortened MOLLI sequence shMOLLI minimises breath-hold whilst maintaining three inversions, acquiring 7 images across three inversions in a 5-1-1 manner across 9 heart beats [30], see Figure 3.2. However, it has not been established whether this completely eliminates motion in patient populations with respiratory disease or breath hold difficulty. It is therefore of interest to establish the extent to which motion is significantly reduced or removed using a shorter sequence in a pulmonary patient population and which images are most significantly affected.

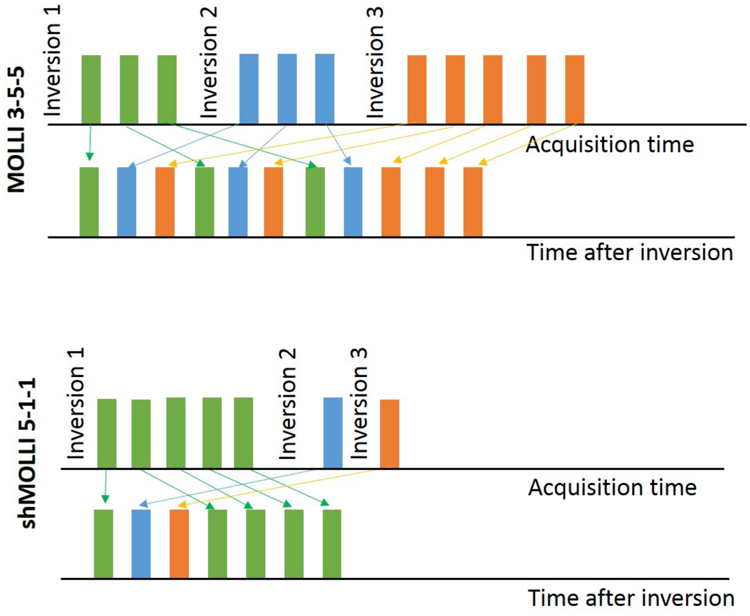

Fig. 3.2 Schematic diagram of MOLLI 3-3-5 and shMOLLI 5-1-1 acquisition schemes, and how those images are later interleaved into one signal recovery curve. Colours are added to show which inversion each acquisition follows, with green images following the first acquisition, blue the second and orange the third.

3.2.2 Quantifying the efficacy of registration

Additionally, it is of interest to develop an accurate, robust, fast and automated method for creating synthetic images. A novel method has been developed, which will be compared to an established iterative energy minimisation method for motion correction [5] and post-processing speed to validate the accuracy and robustness of both methods.

3.3 Methods

3.3.1 Registration algorithm and implementation

The use of synthetic images which are spatially aligned with similar contrast to the acquired MOLLI images was proposed by Xue et al., as a method of overcoming the contrast differences between acquired MOLLI images [5]. Acquired images can be registered to a corresponding synthetic image, consequentially aligning the acquired images to the aligned synthetic image spatial frame. In this chapter, synthetic images were created by two methods, A and B for each subject. Method A is based on the work of Xue et al., [5]. Method B was developed in-house to provide a faster and more robust solution to synthetic image creation. All image-processing was performed using custom functions written on Matlab 2016b. Images underwent signal polarity restoration by a multi-fitting approach. Subsequently, T_1 maps were produced by pixel-wise fitting of the signal [23]. All images were automatically centrally cropped. Matlab-based non-rigid registration toolkit ShIRT [42] was integrated into the custom Matlab pixel-wise T_1 mapping algorithm for both the initial and final registrations. All computation was performed on a 64 bit Windows 10 workstation with 16GB RAM and 4 X Intel® Core™ 3.6GHz processors.

The left ventricle on each image was segmented and image registration was quantified using the Dice similarity coefficient (DSC) as discussed in section 2.3.1.

3.3.1.1 Synthetic image creation Method A

Method A used an energy minimisation algorithm based on the direct implementation of the algorithm outlined in the work of Xue et al. [5], see Figure 3.3, which corrects motion and calculated T_1 maps as one combined process. This method iteratively solves an energy minimisation problem using partial differential equations to produce synthetic images by solving the equation .

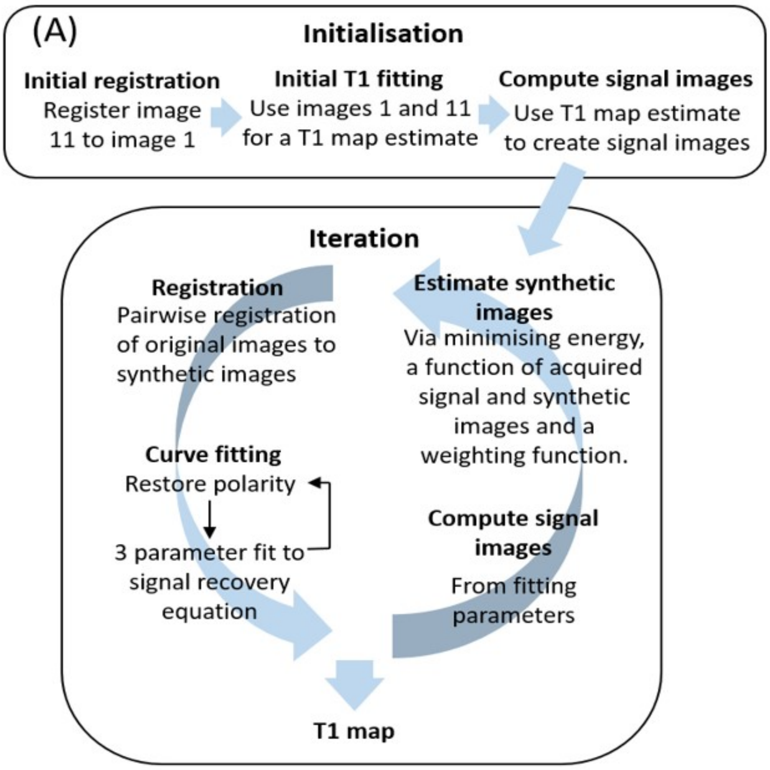

Fig. 3.3 Diagram demonstrating image registration using method A.

The implementation in this chapter discretised the energy minimisation problem using vector solutions to find $\tilde{\mathbf{M}}$.

Acquired images are then co-registered to the synthetic images, followed by the production of estimated T_1 maps. The estimated T_1 maps are then used in the energy minimisation process during the next iteration, using the equation (3.1). This implementation was written in Matlab and all common features (e.g. multi-fitting to correct signal polarity) between this implementation and method B used identical functions in order to create a fair comparison. The registration algoirthm was optimised using 5 randomly chosen sets of patient data, 3 pre contrast and 2 post contrast. Coefficients α and β were both varied between 0.5 and 2 in 0.1 increments while the other had a value of 1. Number of iterations, N, was varied between 5 and 100 iteration. DSC was used as a similarity measure, and mean DSC across the group was found to be optimal at α=1 and β=1.2. Number of iterations was chosen to be 10, after which it was found that improvement in registration plateaued whilst time-cost increased. Coefficients α and β were undefined in the original paper.

3.3.1.2 Synthetic image creation - Method B

Method B produces synthetic images via an inversion recovery signal model, see Figure 3.4. The relevant code and accompanying flow charts can be found in appendix A.1. This is an empirically derived method developed to efficiently produce synthetic images for registration of inversion recovery images. The method fits to a 1-parameter model to allow robust estimation of synthetic images based on three pre-registered input images, eliminating the need for time-costly iterations. The three input images are chosen via an algorithm described below. The images may undergo initial registration, depending on which images are chosen (see appendix A.1.3). The images are then input into an inversion recovery equation model which has been simplified such that it has a single free parameter. This enables a robust curve fitting based upon three spatially aligned images, from which a set of spatially aligned synthetic images can be produced. The algorithm proceeds as follows, see Figure 3.4:

1. Input images for the synthetic model are selected: the first image, the last image, and the image with the lowest overall signal from tissue (see appendix A.1.1).

2. Initial registrations: the input images are registered to an image acquired in the first 5 seconds (based on the assumption patients typically hold their breath during the first 5 seconds of imaging) if the images have similar contrast (determined by whether they occur at similar TI) (see appendix A.1.2).

3. The three input images are then fit to a simplified inversion recovery model of: $S(t) = S(l) - 2S(l)e^{\frac{-t}{T_1}}$. Where $S(l)$ is the last image (image with the longest TI) of the three input images (see appendix A.1.5).

4. The T_1 map calculated by the model is then used to create a set of synthetic images corresponding to each time point in the inversion recovery series (see appendix A.1.7).

The inversion recovery model makes two assumptions:

i. Spins are perfectly inverted,

ii. The last time point represents the fully recovered signal intensity.

These simplifications create a single-parameter fitting model. The inversion recovery equation (2.35), had three free parameters: the fully recovered signal S_0, the coefficient A which takes into account imperfect spin inversion, and T_1*. This can be used to create an equation with one free parameter (T_1), from which a T_1 for each pixel can be produced from fitting pixel information from the three input images. The estimated T_1 is then used to produce spatially aligned synthetic images for all time points on a pixel by pixel basis. The simplified inversion recovery signal model allows a robust set of synthetic images to be produced. The predominant reason for this is the inclusion of an image which occurs in the middle of the inversion recovery curve (the second input image) as it provides information on curve steepness. This additional information allows a robust set of synthetic images to be produced without iterative processing.

3.3.1.3 Key differences between the methods

Key differences between this implementation of method A and method B are that method B is iterative and using an energy minimisation process to refine the synthetic images. In contrast, method A creates a robust set of synthetic images in the first instance, avoiding the need for time costly iterations. This is achieved by fitting to a simplified inversion recovery model and using an additional image input into the synthetic image creation to provide information on curve steepness. These differences are highlighted in Figure 3.5.

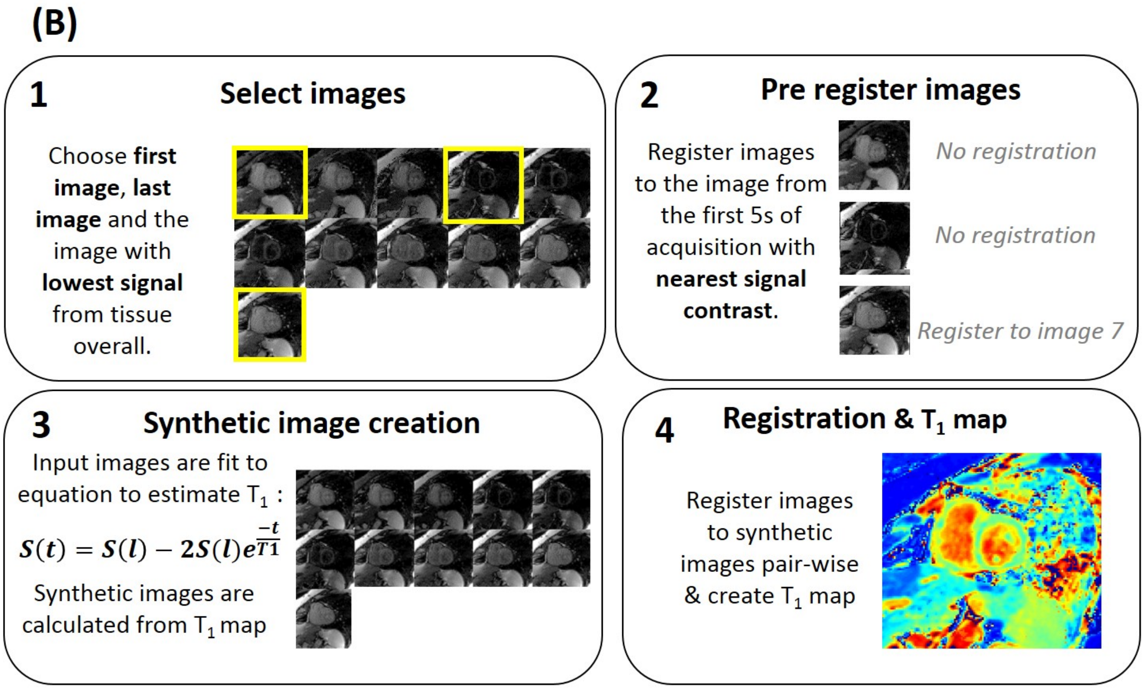

Fig. 3.4 Diagram demonstrating image registration using method B. Method B has been written to work for any MOLLI or shMOLLI sequence (including post contrast sequences). S(l) is the last image input into the synthetic image model.

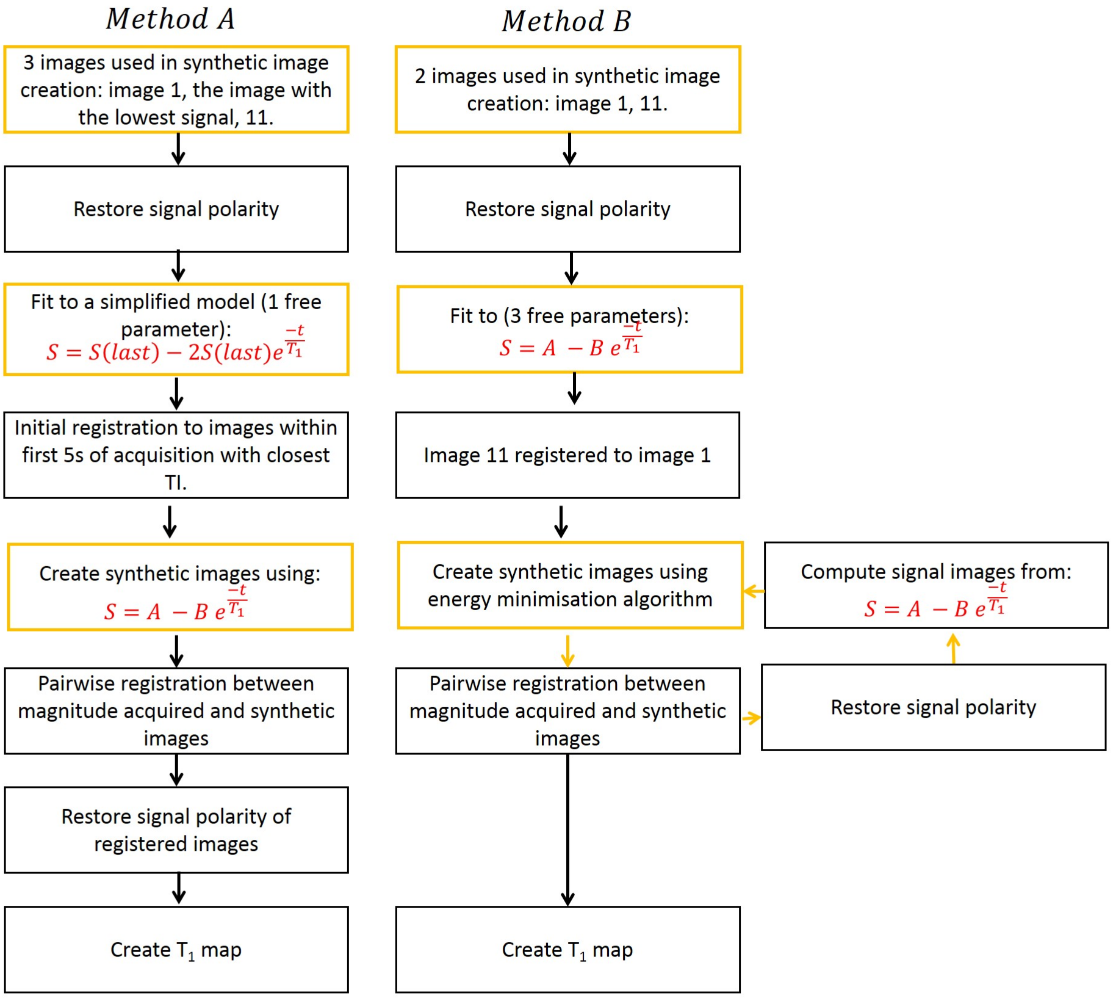

3.3.2 Registration

Pair-wise registration is performed between each unregistered magnitude acquired image and its corresponding magnitude synthetic image. Registration was performed using pre-existing ShIRT Matlab registration toolkit [42]. For method B, signal polarity is restored to the registered images, after which T_1 mapping is performed. ShIRT was integrated into the custom Matlab pixel-wise T_1 mapping algorithm for both the in initial and final registrations. A finer minimum node spacing of 1 pixel was used for the final registrations, whereas a larger node spacing of 4 pixels was used for the initial registrations. Image registration was performed without a mask, to fully automate the procedure. Further details of ShIRT are given in section 2.3.1. All computation was performed on a 64 bit Windows 10 workstation wiht 16GB RAM and 4 X Intel Core^{TM} 3.6GHz processors.

3.3.3 Assessing image alignment

The left ventricle on each image was segmented and image registration was quantified using the Dice similarity coefficient, described in section 2.3.1. The left ventricular myocardium was segmented for every subject in all images.The DSC was calculated for each subject pre-registration and after applying the corresponding registration maps. Each set of unregistered images were also viewed as a video for qualitative visual inspection of respiratory motion. Each image set was rated as either containing motion or not containing motion by a radiographer with 10 years' experience blind to DSC or other data. Motion was considered to be present if any noticeable movement of the left ventricular myocardium was observed across the time series of images.

3.3.4 Clinical data

MOLLI image registration techniques were implemented on MRI scans from two cohorts of consecutive patients who underwent a MOLLI sequence as part of their clinical assessment at a tertiary pulmonary hypertension referral centre between 01.10.2015-30.11.2015 (n=41) and 22.11.2017-13.12.2017 (n=17) [6]. Approval for analysis of imaging data was granted by the local research ethics committee and consent was waived for this retrospective study.

3.3.5 Image acquisition

A whole body, 1.5 T GE HDx scanner (GE Healthcare, Waukesha, WI) and 8-channel cardiac coil were used during MOLLI image acquisition. Patients were positioned supine with ECG gating. Of the first cohort, all 41 patients underwent a 3-3-5 MOLLI sequence pre contrast at a resolution of 128x128 and 14 of those patients also underwent a 3-3-5 MOLLI sequence post contrast at a resolution of 128x128. Of the second cohort, 17 underwent a 3-3-5 MOLLI imaging at resolution 192x192, 16/17 underwent 2 sets of 3-3-5 MOLLI images at resolution 128x128 and 256x256 in the short axis slice and 1 set of 5-1-1 shMOLLI images at resolution 192x192. 15/17 of the second cohort also underwent one 3-3-5 MOLLI image 192x192 in the long axis slice. All images were acquired during inspiration breath hold. In total there were 136 sets of MOLLI images. Imaging parameters were: 35 degree flip angle, parallel imaging factor 2, TE: 0.92, TR: 2.82, FOV $400mm^2$, slice thickness $10mm$. The image acquisition time for a heart rate of 60bpm at resolution 192x192 for the MOLLI sequence was 17s, and for shMOLLI was 9s.

3.3.6 Statistics

Statistical analysis was performed and presented using SPSS 21 (SPSS, Chicago, IL). Data is presented as mean ± standard deviation. Unregistered DSC and qualitative motion scoring was compared between the shortened MOLLI 5-1-1 sequence and all pre-contrast short axis MOLLI sequences to establish whether the sequence sufficiently supresses motion in this patient population.

DSC values before and after registration, as well as between both registration methods, was compared using a paired t-test and the mean DSC value for all the images in the dataset, unless otherwise stated. Mean values were plotted using a box plot diagram. The performance of method A and method B were compared in terms of registration success using a Bland-Altman diagram.

Registration computation timings were compared in 3 pre-contrast and 2 post-contrast randomly selected datasets. T_1 maps were produced pre-registration, as well as post-registration for both registration methods. T_1 measurement was evaluated in T_1 maps which underwent registration using both method A and method B, by applying a LV mask to the T_1 map and evaluating mean T_1 in the entire LV. Statistical differences between T_1 mean were measured using a paired t-test. A value of $P<0.05$ was considered statistically significant. The effect of pixel size and sequence choice on resultant T_1 was determined using an ANOVA with post-hoc Bonferroni test or an independent t-test (depending on number of variables) for both global myocardial T_1 values and standard deviation of T_1 values within the whole myocardium.

3.3.7 T_1 analysis

A global mean T_1 measure were calculated using the segmented left ventricle that the images are registered to. This was compared between the two methods to evaluate whether they produce consistent myocardial tissue T_1, using a paired t-test for differences.

3.4 Results

3.4.1 Respiratory motion

Table 3.2 Presence of motion in patient population. Motion score is a binary score of whether the diaphragm moves (yes=1, no=0) due to respiration during the acquired images.

Sequence type	**Phase x Frequency**	**Contrast (Y/N)**	**Imaging plane**	**Number of datasets**	**Motion score**	**Unregistered DSC**
3-3-5	128x128	N	SA	56	28/56	0.71 ± 0.09
3-3-5	128x128	Y	SA	16	3/16	0.76 ± 0.06
3-3-5	192x192	N	SA	16	7/16	0.77 ± 0.09
3-3-5	256x256	N	SA	17	9/17	0.73 ± 0.14
5-1-1	192x192	N	SA	16	3/16	0.80 ± 0.07
3-3-5	192x192	N	LA	15	10/15	0.69 ± 0.12
All data sets				136	60/136	0.74 ± 0.10

An example of a motion corrected dataset is shown in Figure 3.6. Motion was found after inspection in 44% of patient datasets. See Table 3.2. Pre-contrast short axis MOLLI 3-5-5 image datasets (n=89) had significantly more motion than shMOLLI 5-1-1 datasets (n=16) when measured by DSC ($p<0.001$) and observer motion scoring ($p<0.001$). However, motion was still observed in 19% of shMOLLI sequences. Examples of a motion corrupted T_1 map and subsequent motion corrected T_1 map are shown in Figure 3.7.

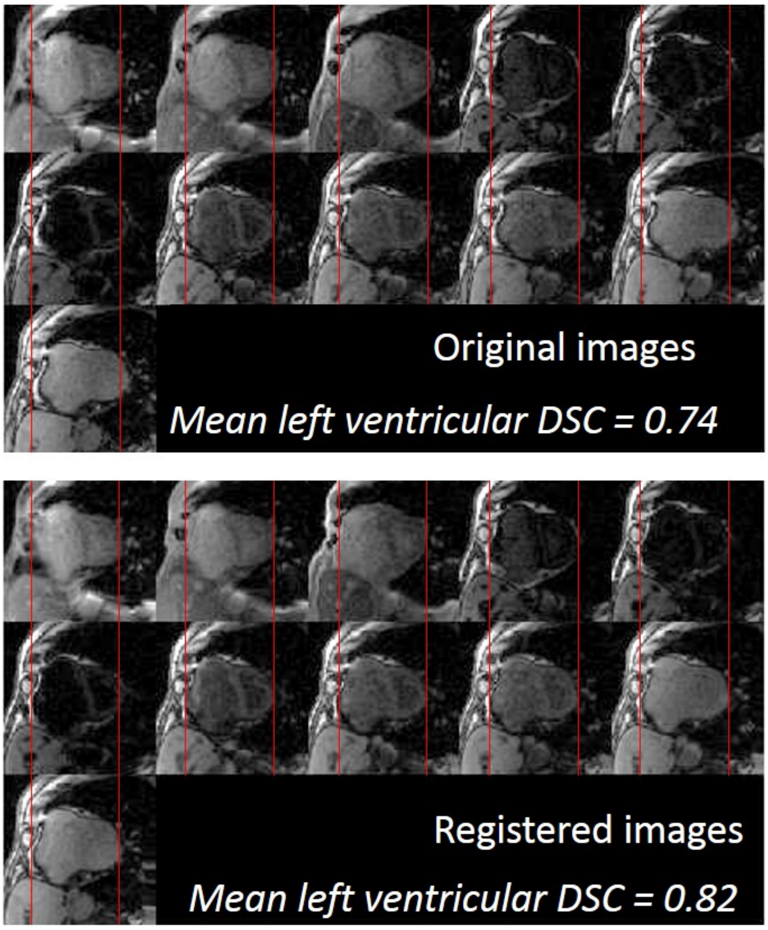

Fig. 3.6 An example of an image data set registered using method B. Vertical red lines correspond to the edges of the RV free wall and LV free wall in the first image of the sequence. In the original images, it can be seen that the LV free wall is to the left of this line in some images and to the right of this line in others - which would result in both blood and myocardium pixels being combined into the T1 estimate for the LV free wall. The registered images show the LV free wall being consistently to the left of this line.

Figure 3.8 confirms the assumption that overall image alignment deteriorates with increase in time after the breath hold, with overall poorest alignment seen in image 10, and best seen in the 2nd and 3rd images acquired. Figure 3.9 shows overall improved unregistered image alignment compared to MOLLI images in Figure 3.8. Figure 3.10 shows two datasets, one where respiratory motion was not observed and one where respiratory motion was observed. The time course of a lower LV myocardial pixel is shown over time, demonstrating how when

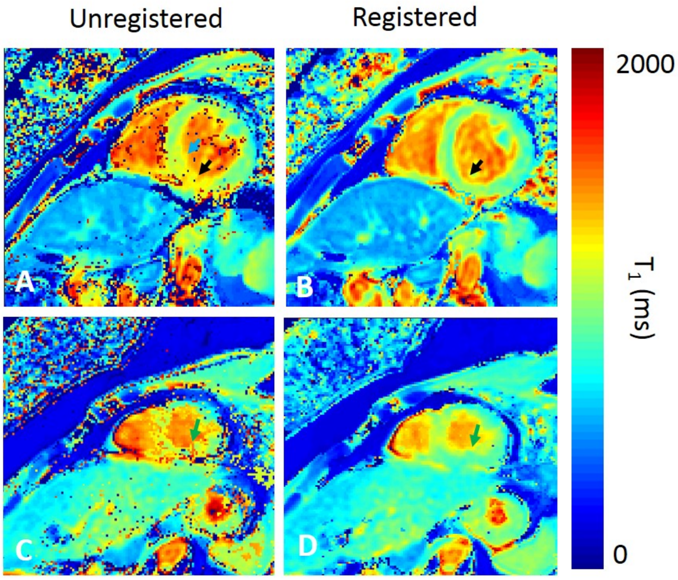

Fig. 3.7 T_1 map created without image registration and with image registration. Blue arrows show the LV free wall is unresolved in the unregistered image and resolved in the registered image. Black arrows show areas of elevated myocardial T_1 in the unregistered image that may be misinterpreted as tissue T_1 changes. Green arrow shows some pixels are still resulting in erroneous T_1 even though the overall T_1 accuracy is improved.

motion is present pixel signal does not follow the expected signal recovery time course due to motion misaligning the pixels. This misalignment will lead to inaccurate resultant T_1. When compared with native MOLLI sequences of the same image resolution, using a shMOLLI sequence was not shown to significantly decrease motion in acquired images (p=0.292). Of all 16 shMOLLI images, 3 datasets still showed motion which requires registration (19%).

3.4.2 Registration accuracy

DSC was significantly improved in images after registration to synthetic images created via method A (p<0.001) and method B (p<0.001). An example of images registered using method B that resulted in DSC improvement is shown in Figure 3.6. Overall there was no significant difference between the two registration techniques (p=0.611), see Figure 3.13. Both methods significantly improved image registration pre and post contrast. All sequences

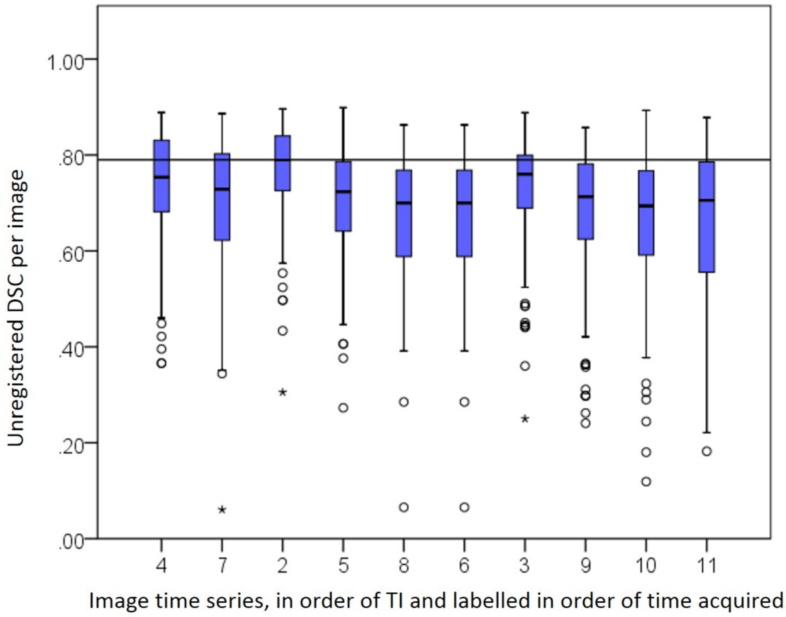

Fig. 3.8 A box plot to show mean DSC for all datasets analysed across all MOLLI images per time frame, compared to time frame 1. A horizontal guide line is plotted at y=0.79, the highest mean DSC. Images are show in the order of acquisition, and labelled in order of TI.

except shMOLLI demonstrated an improvement in mean DSC, however not all sequence groups showed significance between pre and post registration mean DSC, see Table 3.3.

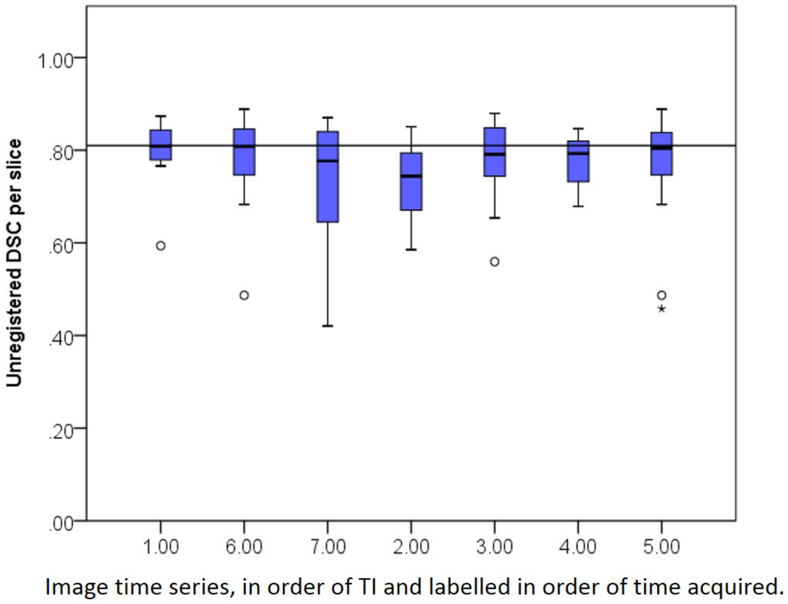

Fig. 3.9 A box plot to show mean DSC across all shMOLLI images per time frame, compared to time frame 1. A horizontal guide line is plotted at x=0.81, the highest mean DSC. Images are shown in the order of acquisition, and labelled in order of TI.

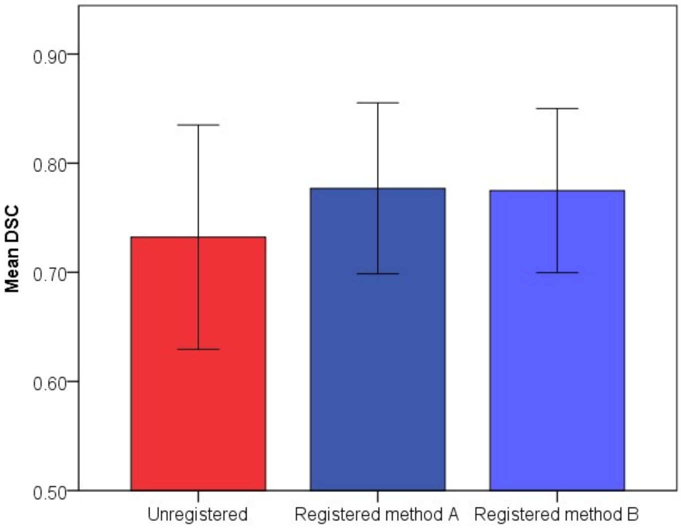

Fig. 3.11 Mean DSC averaged over all inversion times over all datasets without registration, with registration using synthetic images produced by method A, and with registration using synthetic images produced by method B. DSC is average DSC for each image set, for all images in this study. P values are given for the difference between registered and unregistered DSC values (method A: $p<0.001$; method B: $p<0.001$).

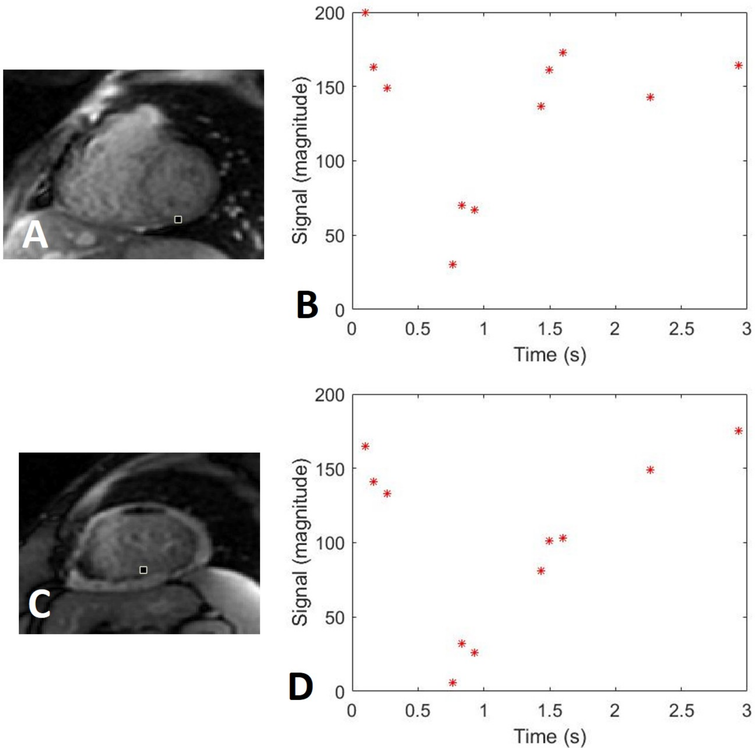

Fig. 3.10 Examples of pixel signal changes over time in the lower myocardium of a patient without motion (B) and with motion (D).

Image sets where respiratory motion was not observed nonetheless had significantly higher DSC post-registration, see Figure 3.12. For the three patients with shMOLLI scans which were identified as containing respiratory motion, the mean DSC for each data set is 0.61 to 0.75, 0.82 to 0.83 and 0.82 to 0.87.

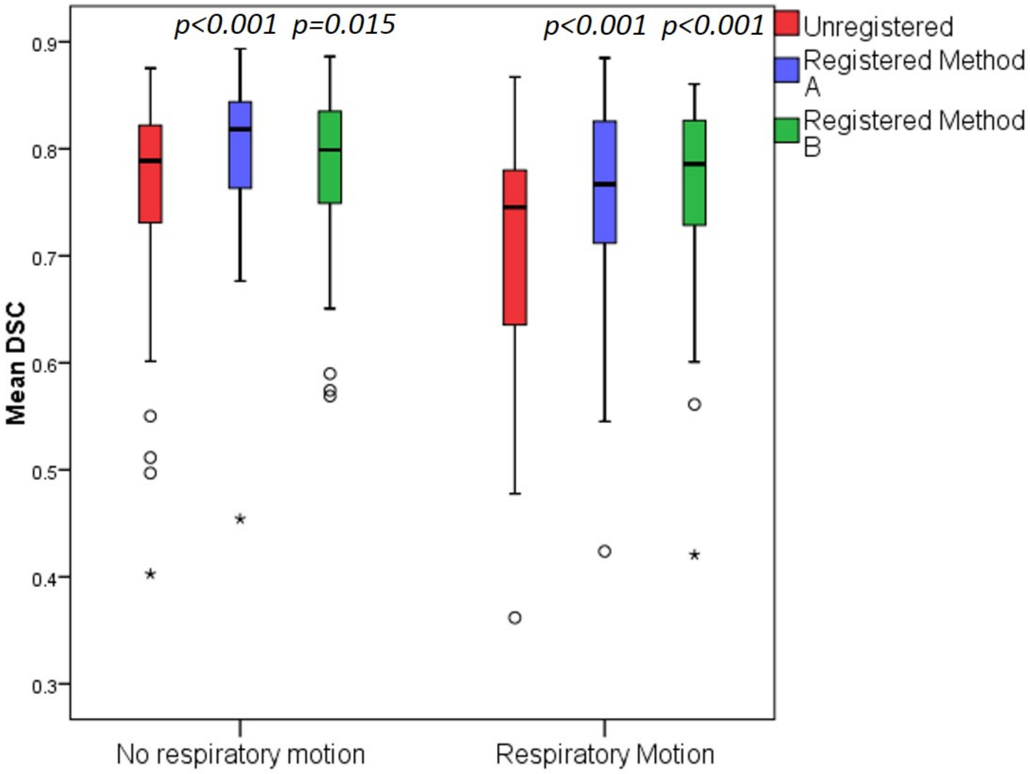

Fig. 3.12 Mean DSC without registration, with registration using synthetic images produced by method A, and with registration using synthetic images produced by method B. DSC is the mean DSC for each image set, for all images in this study. Images are split into those with observed respiratory motion and those without. P values are given for the difference between registered and unregistered DSC values.

Table 3.3 Post registration DSC.

Imaging parameters	**Unregistered DSC**	**DSC method A**	**P Value**	**DSC method B**	**P value**
Sequence:3-5-5; Matrix: 128x128; No Contrast; Short Axis; N=56	0.71 ± 0.09	0.80 ± 0.06	p<0.001**	0.80 ± 0.05	p<0.001**
Sequence:3-5-5; Matrix: 128x128; Contrast; Short Axis; N=16	0.71 ± 0.09	0.71 ± 0.09	p=0.037*	0.80 ± 0.05	p=0.003**
Sequence:3-5-5; Matrix: 192x192; No Contrast; Short Axis; N=16	0.77 ± 0.10	0.77 ± 0.08	p=0.166	0.82 ± 0.06	p=0.007**
Sequence:3-5-5; Matrix: 256x256; No Contrast; Short Axis; N=16	0.72 ± 0.14	0.78 ± 0.08	p=0.307	0.82 ± 0.06	p=0.052
Sequence:5-1-1; Matrix: 192x192; No Contrast; Short Axis; N=16	0.80 ± 0.07	0.80 ± 0.07	p=0.898	0.80 ± 0.06	p=0.896
Sequence:3-5-5; Matrix: 192x192; No Contrast; Long Axis; N=15	0.69 ± 0.13	0.72 ± 0.12	p=0.058	0.72 ± 0.03	p=0.333
All cases combined, N=136	0.73 ± 0.10	0.77 ± 0.07	p<0.001**	0.78 ± 0.08	p<0.001**

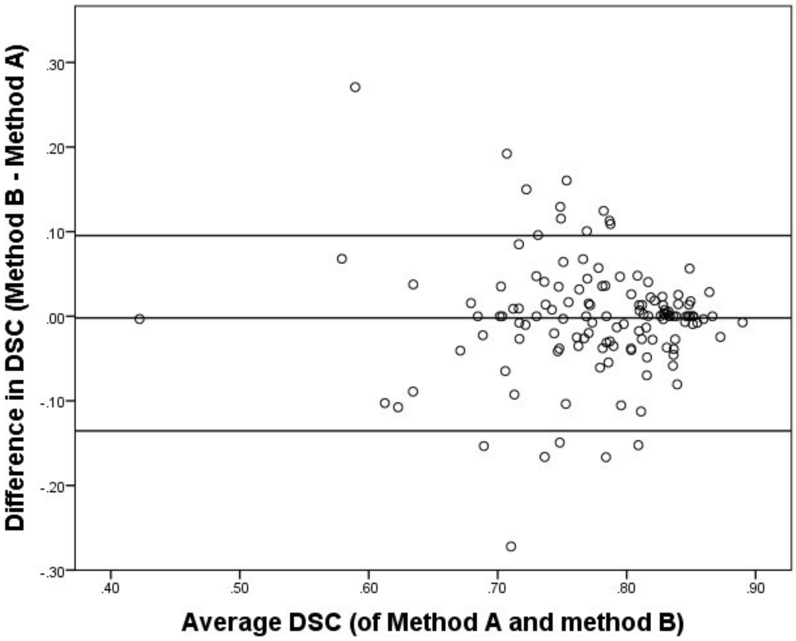

Fig. 3.13 Bland Altman plot comparing DSC measurement following registration, using method A and method B. Positive y-values correspond to method B resulting in a higher DSC, whereas negative y-values correspond to method A resulting in a higher DSC.

3.4.3 Breakdown of computational timings

A breakdown of computational timings for post-processing is given in Table 3.4. The most time costly process in both methods was restoring signal polarity via multi-fitting. Overall, method B was 6 times faster than method A, primarily because it does not iterate over time-costly curve fitting for signal polarity restoration.

Table 3.4 Breakdown of computational post-processing timings.

	Method A (minutes)	Method B (minutes)
Intial registration step(s)	<0.1	<0.1
Initial curve fitting	8.1	N/A
Signal polarity restoration		34.4
Creation of synthetic images	0.03	2.25
Final registration	0.42	0.42
Signal polarity restoration 2	32.4	26.3
T_1 map creation	7.14	4.21
Number of iterations	10	N
Total time	405	67.5

3.4.4 Accuracy of resultant T_1

A paired t-test showed no significant differences between T_1 measured by method A when compared to T_1 measured by method B (p=0.735). Intra class correlation coefficient for absolute agreement was calculated using Cronbach's Alpha which was 0.981 p<0.001 between the two methods. Mean LV T_1 calculated from T_1 maps created using method A was 890±27ms, and mean LV T_1 calculated from T_1 maps created using method B was 900±27ms. There was no significant difference in global T_1 or pixel-wise T_1 standard deviation in the myocardium with a change in matrix size (matrix sizes: 128, 129 and 256 considered using MOLLI 3-3-5 sequences) (T_1: p=0.173l; SD: p=0.104). There was no significant difference between mean T_1 in the short or long axis in this cohort (p=0.982), although the long axis showed a significantly higher standard deviation of T_1 values (p=0.003). There was not a significant difference in T_1 or standard deviation between shMOLLI and MOLLI 3-5-5 sequences (T_1: p=0.846; SD: p=0.127).

3.5 Discussion

A time frame consideration of mean DSC for each inversion recovery time point showed that misalignment between images increases with time after the beginning of the acquisition, see Figure 3.8, which is consistent with the assumption that misalignment due to release of breath-hold later into the image acquisition is responsible for the majority of motion in images. Both registration methods A and B show significant improvement in overall DSC when compared to unregistered images. The two methods did not result in an overall significant difference in DSC. Figure 3.13 shows a mean difference of -0.020 in DSC. The two farthest outliers with a registration difference of -0.27 and 0.27 show cases where one method was more successful than the other during image registration. In the case of the outlier with a lower DSC when registered using method B compared to method A, the patient is breathing from the beginning of the exam and therefore the assumption that breath is held in the first 5s of imaging did not hold, resulting in corrupted synthetic images and a poor image registration. In the case where method B was more successful than method A there is not a clear reason why one method performed a more successful image registration than the other. In both cases there was a large amount of fat surrounding the myocardium, which due to its low T_1 has a large contrast difference in images with a low T_I, further work would be warranted to establish if this is a contributing factor for inconsistent image registration and how it could be resolved.

A breakdown of the registration results for different T_1 mapping sequences is given in Table 3.3. Post-contrast data DSC was significantly improved using both methods. Neither method resulted in significantly higher DSC in the long-axis orientation, however both data sets were small (n=15) and greater numbers would be required to fully establish the significance of results in this orientation.

Using a shMOLLI sequence was shown to significantly decrease motion in acquired images. There was not an overall statistical difference between unregistered and registered

DSC for shMOLLI scans, however, in the three image sets that did have motion, the mean DSC for the image set increased after registration. This demonstrates that the use of a shMOLLI scan can reduce the amount of respiratory induced motion present in images, however motion remains present in around 19% of cases and in these cases image alignment does improve the registration. Both registration methods improved image registration even when respiratory motion was not observed. This may be due to a combination of factors, including motion due to poor cardiac gating and diaphragm drift. This indicates that even in patients where respiration is not observed, motion correction may still be of benefit, and does not show detrimental warping of images.

Both registration methods resulted in significantly higher resultant T_1 in the LV myocardium. This confirms that unregistered images do lead to inaccurate resultant T_1 and emphasises the need for correcting motion prior to T_1 mapping to prevent erroneous T_1 measurement. Both registration methods led to resultant T_1s which were not significantly different from one another, however method B required only 15% of the post-processing time of method A. The most time costly part of both registration processes was the restoration of signal polarity, as it requires several curve fitting processes for each pixel. As method B eliminates the need for iterations over this time-costly process the method is intrinsically faster. The curve fitting process used a Matlab 2016b curve fitting function. During restoration of signal polarity, 128x128 pixels were fit multiple times in each data set, resulting in 20-30 minute of computing time. If this process was implemented using parallel processing and an alternative programming language and fitting process, this could be significantly reduced. As both methods were implemented on the same processors with identical code for common processes other implementations of these methods which may be more computationally efficient are expected to maintain similar relative processing speeds.

The need to restore signal polarity could also be overcome by using phase sensitive image reconstruction and registration [45], which estimates background phase from the MOLLI image with the longest TI. This method still requires initial motion correction to remove error in the phase sensitive images, nonetheless it remains an alternative option for fast, accurate image registration in inversion recovery imaging. There was no significant difference found in measured T_1 or the pixel wise standard deviation of T_1 values in the myocardium with changes in matrix size, or with whether a MOLLI or shMOLLI sequence was used. There was a higher standard deviation of T_1 values in the long axis orientation, but no change in measured mean T_1 values for the LV myocardium.

One of the limitations of this study is that not all patients underwent all of the sequences analysed. Larger patient numbers would be required to fully investigate the robustness of the registration methods in the long axis and in shMOLLI sequences with motion present. Nonetheless the overall data shows that both methods are successful at improving image registration, in various MOLLI permutations including post-contrast, short axis and shMOLLI sequences.

3.6 Conclusion

This work demonstrates the necessity for image registration in patient populations who struggle to maintain breath hold, even when using a shortened sequence, and shows that when motion occurs in a sequence with reduced acquisition time it can be successfully corrected using this method. A model-based method of image registration for inversion recovery images is described, which produces robust image registration without the need for time-costly iterations and is successful in correcting motion in pre contrast MOLLI and shMOLLI images as well as post-contrast MOLLI images. This work demonstrates that shortened T_1 mapping sequences can reduce image motion due to respiration in patients considerably, however image registration may still be needed to correct respiratory motion in some cases. The method described produces robust image registration without the need for time-costly iterations which is 6 times faster than the iterative synthetic image creation method described by Xue et al., [5] and is successful in correcting motion in pre contrast MOLLI and shMOLLI images as well as post-contrast MOLLI images.

Chapter 4

Application of motion corrected T_1 mapping to patients with pulmonary hypertension

This chapter implements the method described in Chapter 3 in a large pulmonary hypertension cohort to assess the utility of cardiac T_1 mapping in these patients, including the diagnostic and prognostic utility of T_1. [1]

4.1 Introduction

Chapter 3 showed how patients who undergo MRI assessment at a pulmonary hypertension referral centre were unable to maintain breath hold in 44% of MOLLI sequences and 19% of shMOLLI sequences. In order to assess myocardial T_1 accurately in these patients, post-

---

[1] The contents of Chapter 4 have been published in the Journal of Cardiovascular Magnetic Resonance: **L Saunders**, C Johns, N Stewart, C Oram, D Capener, V Puntmann, C Elliot, D Kiely, M Graves, J Wild and A Swift. "Diagnostic and prognostic significance of cardiovascular magnetic resonance native myocardial T1 mapping in patients with pulmonary hypertension", 2018, vol. 20, no.78.

processing registration was required. In this chapter[2], the method that was developed and evaluated in chapter 3 was used to register all images in a cohort of patients with suspected pulmonary hypertension and age and sex matched healthy volunteers. The aim of this study was to accurately assess myocardial changes in these patients with pulmonary hypertension, and whether changes to myocardial T_1 visualised by T_1 mapping have diagnostic or prognostic significance in these patients.

4.1.1 Motivation for quantification of myocardial changes in pulmonary hypertension

Myocardial tissue changes have been visualised in patients with pulmonary hypertension using T_1 mapping, T_2 mapping and late gadolinium enhanced MRI. Native myocardial changes measured using native T_1 mapping have been shown to have clinical applications across a range of cardiac diseases [89, 90]. It has been shown that in patients with pulmonary hypertension, RV insertion point T_1 is elevated. Several studies also found elevated T_1 in the interventricular septum and, in one case, the LV free wall [73–75].

Patients with pulmonary hypertension have been shown to have worse prognosis in the presence of myocardial changes visualized by late gadolinium enhancement (LGE) at the RV insertion point [59] and in the septal myocardium [61], although the independent prognostic significance of the myocardial changes in pulmonary hypertension remains unclear [66]. Elevated T_1 at the insertion point occurs in a similar location and shape to LGE, and both patients and animal models with pulmonary hypertension exhibiting LGE have been found to have higher T_1 in this region than those without. Native T_1 mapping has been found to be a more reproducible marker in healthy volunteers than post contrast T_1 with good long-term stability of native myocardial T_1 [91]. The co-occurrence of LGE and elevated T_1 implies that

---

[2] **Laura C. Saunders**, Chris S. Johns, Neil J. Stewart, Charlotte J. E. Oram, David A. Capener, Valentina O. Puntmann, Charlie A. Elliot, Robin C. Condliffe, David G. Kiely, Martin J. Graves, Jim M. Wild, Andy J. Swift, "Diagnostic and prognostic significance of cardiovascular magnetic resonance native myocardial T1 mapping in patients with pulmonary hypertension", *Journal of Cardiovascular Magnetic Resonance*, vol. 20, no. 1, Page 1

they may have common mechanistic causes. However, studies in both patients and animal models have reported higher native T_1 in the RV insertion points than in controls, despite no LGE being seen in this region, which indicates that native T_1 may be a more sensitive marker than the presence of LGE [66, 73]. Therefore, T_1 mapping may provide a contrast-free, robust and sensitive marker to myocardial tissue changes in pulmonary hypertension, and there is reason to suspect that, like LGE, T_1 changes may have prognostic relevance.

Pulmonary hypertension is a heterogeneous condition with 5 diagnostic subcategories: pulmonary arterial hypertension; pulmonary hypertension due to left heart disease (PH LHD) pulmonary hypertension due to lung disease and/or hypoxia; chronic thromboembolic pulmonary hypertension (CTEPH) and pulmonary hypertension with unclear or multifactorial causes. To date T_1 mapping studies have used relatively small populations, with only one report wherein diagnostic subcategories of pulmonary hypertension were considered separately [74] and therefore it is unclear whether myocardial T_1 changes in patients with pulmonary hypertension are homogeneous across patient subtypes.

RV remodelling and failure occur as a result of prolonged elevations of RV afterload. Elevated mean pulmonary artery pressure (mPAP) and pulmonary vascular resistance (PVR) are characteristic features of the condition, however it is the failure of the RV that is the key determinate of adverse outcome [57–61, 92]. Early markers of adverse cardiac remodelling may be able to guide treatment strategies, predicting therapy response and failure. It is unclear whether elevated myocardial T_1 is associated with prognostic features in pulmonary hypertension, and whether it can provide additive information to patient outcome.

4.2 Objectives

To accurately acquire native T_1 maps in patients with pulmonary hypertension, using image registration methods developed in Chapter 3 to provide more accurate T_1 maps produced from aligned images, and to determine whether elevation of T_1 exists in the LV myocardial tissue in patients with pulmonary hypertension:

- varies according to pulmonary hypertension subtype,
- is related to adverse outcome independent of RV size and function,
- is associated with biventricular remodelling and function as described by functional cardiac MRI metrics.

4.3 Methods

4.3.1 Study population

Approval for analysis of imaging data was granted by the local research ethics committee and consent was waived for this retrospective database study. Patients were consecutive with suspected pulmonary hypertension who underwent MRI including a MOLLI cardiac MRI sequence as part of their clinical assessment at a tertiary pulmonary hypertension referral centre between 01.01.2015 and 31.12.2015. Exclusion criteria were applied to all subjects according to standard criteria for undergoing MRI. A total of 490 patients were identified. 369 patients had a diagnosis of pulmonary hypertension without left heart disease as specified below, 39 patients were identified with pulmonary hypertension associated with left heart disease, and 82 did not have a diagnosis of pulmonary hypertension – mean pulmonary arterial pressure (mPAP) < 25mmHg – and were used as a control group, see Figure 4.1. 25 healthy volunteers with no current cardiac or respiratory symptoms and no history of cardiac disorders were also recruited as an additional control group. Patients with a mean pulmonary arterial pressure $\geq$ 25mmHg and pulmonary capillary wedge pressure (PCWP) > 15mmHg were considered to have a diagnosis of pulmonary hypertension due to left heart disease, and patients with a mean pulmonary arterial pressure < 25mmHg were considered to

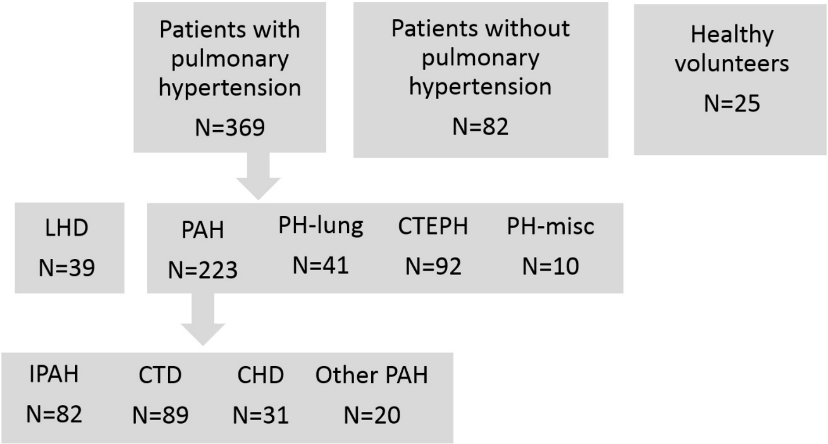

Fig. 4.1 Patients were grouped for statistical analysis as indicated. Patients with pulmonary hypertension were compared to two control groups: patients without pulmonary hypertension and healthy volunteers. Patients with left heart disease (LHD), pulmonary arterial hypertension (PAH), pulmonary hypertension due to lung disease and/or hypoxia (PH-lung), chronic thromboembolic pulmonary hypertension (CTEPH) and pulmonary hypertension with unclear or multifactorial causes (PH-misc) were compared using ANOVA. Patients with idiopathic pulmonary arterial hypertension (IPAH), connective tissue disease (CTD), chronic heart disease (CHD) and other types of PAH were compared using ANOVA. Patients with PAH were assessed for independent prognostic value of T_1.

have a diagnosis of no pulmonary hypertension. Subtypes of pulmonary hypertension were defined as previously described [93]. The patients with pulmonary hypertension included the following sub-group diagnoses: Group 1 pulmonary arterial hypertension; Idiopathic PAH (IPAH), n=83; PAH heritable, n=5; PAH associated with connective tissue disease (PAH-CTD), n=89; PAH associated with congenital heart disease (CHD), n=31; PAH associated with portal hypertension, n=9; PAH drug/toxin induced, n=3; PAH other, n=3. Group 2 left heart disease (LHD), n=39 (note these patients were considered separately – see Figure 1). Group 3 PH associated with lung disease, n=41. Group 4, chronic thromboembolic pulmonary hypertension CTEPH n=92; group 5, sarcoidosis, n=10; patients without diagnosis: 3. All patients with PAH (n=223) were treated with PAH therapy with 22±28 months of treatment prior to MRI. 49% of patients with PAH were undergoing therapy with combined oral therapy (phosphodiesterase 5 inhibitor and endothelin receptor antagonist), 27% were taking an oral monotherapy (phosphodiesterase 5 inhibitor or endothelin receptor antagonist or calcium channel blocker), and 24% were taking prostanoid therapy. A summary of all subject characteristics is shown in Table 4.1.

Table 4.1 Demographic data for patients with pulmonary hypertension (PH) patients with pulmonary hypertension due to left heart disease (PH LHD) and patients without PH. Abbreviations described in Tables 2.3 and 2.4.

	Patients with PH	**Patients with PH LHD**	**P value**	**Patients without PH**	**P value**	**Healthy volunteers**	**P value**
N	369	39		82		24	
Age (years)	58.2±15.0 (18-85)	68.1±12.7 (19-88)	p<0.001**	55.4±18.3 (16-83)	0.218	58.1±3.88 (50-63)	0.972
Sex (%)	66.			67.1	0.856	50.9	0.966
Heart Rate (bpm)	72.17±14.4	69.81±3.8	p=1.000	67.9±10.3	p=0.002**4		
RVEDV Index (ml/m^2)	87.2±34.1	81.9±31.7	p=0.978	68.0±20.4	p<0.001**		
RVESV Index (ml/m^2)	51.7±29.0	45.4±23.1	p=0.479	31.1±11.6	p<0.001**		
RVSV Index (%)	35.6±14.2	36.5±12.1	p=1.000	36.9±12.9			
RVEF (%)	43.1±13.6	46.8±11.2	p=0.295	54.4±10.0	<0.001**		
LVEDV Index (ml/m^2)	58.5±16.1	68.9±21.2	p=0.001**	66.6±16.1	p<0.001**		
LVESV Index ml/m^2)	19.2±8.2	26.1±16.6	P<0.001**	21.3±8.2	p=0.037*		
LVSV Index (%)	39.2±11.9	42.8±13.4	p=0.060	45.3±10.8	p<0.001**		
LVEF (%)	67.3±9.7	63.8±14.5	p=0.128	68.3±7.6			
Systolic septal angle (^{o})	165.5±23.9	145.9±15.5	p=0.061	150.5±108.4	p=0.016*		
Diastolic septal angle (^{o})	143.34±11.0	138.3±10.3	p=0.014**	134.9±7.9	p<0.001**		
RV mass index (g/m^2)	21.9±12.5	14.4±5.5	p<0.001**	11.9±5.8	<p0.001**		
LV mass index (g/m^2)	48.0±12.3	57.2±21.1	P<0.001**	47.7±10.7			
VMI average	0.47±0.27	0.28±0.13	p<0.001**	0.26±0.18	<0.001**		
RV insertion point T_1 (ms)	1065±86	1074±103	p=1.000	1017±69	<0.001**	943±52	p<0.001**
Septal T_1 (ms)	975±67	986±073	p=1.000	976±75	p=0.606	940±56	p=0.011*
LV free wall T_1 (ms)	965±68	982±81	p=0.818	961±66	p=0.694	913±55	p<0.001**
LV blood T_1 (ms)	1473±121	1515±147		1505±127	p=0.031*	1471±88	p=0.930
RV blood T_1 (ms)	1483±128	1546±164		1525±125	p=0.007**	1482±102	p=0.972

RHC data	**Patients with PH**	**Patients with PH LHD**	**P value**	**Patients without PH**	**P value**
N	237	39		37	
mRAP (mm Hg)	10.31±5.50	14.95±5.46	p<0.001**	6.55±3.35	<0.001**
mPAP(mm Hg)	44.36±13.49	40.23±11.96	p=0.471	19.4±2.7	<0.001**
PCWP (mm Hg)	11.85±3.87	23.68±6.89	p<0.001**	10.9±3.8	
PVR (dyne/s/cm^3)	611±402	379±81	p=0.004**	183±97	<0.001**

4.3.2 MRI acquisition

Cardiac MRI was performed on a whole body 1.5T GE HDx scanner (GE Healthcare, Waukesha, WI), using an 8-channel cardiac coil. Subjects were scanned in the supine position with ECG gating. Short axis cine images were acquired using a multi-slice balanced steady state free precession (bSSFP) sequence with: temporal phases per cardiac cycle: 20; field of view: 480mm; matrix: 256x256; bandwidth: 125KHz/pixel; TR: 3.7ms; TE: 1.6ms. T_1 mapping was performed using a 2D 3-3-5 MOdified Look-Locker Inversion recovery (MOLLI) sequence in a single short axis slice [93]. A balanced steady state free precession (bSSFP) acquisition was executed at each inversion time point with the following sequence parameters: Flip angle: 35°; image dimensions: 128x128; TR: 3.20ms; TE: 1.41ms; parallel imaging using sensitivity encoding with acceleration factor 2; FOV: 400mm; slice thickness: 5.1mm.

4.3.3 Right heart catheterisation

All patients underwent right heart catheterisation performed using a balloon-tipped 7.5 Fr thermodilution catheter (Becton-Dickinson, Franklin Lakes, NJ), typically via the internal jugular vein using a Swan-Ganz catheter. Pulmonary vascular resistance index (PVRI) was defined as (mPAP-PCWP)/CI, where CI is cardiac index, measured by thermodilution technique. Patients with right heart catheterisation within 30 days of their cardiac MRI were included in analysis of associations between right heart catheterisation metrics and myocardial T_1.

4.3.4 T_1 image registration

As has been established in Chapter 3, patients with pulmonary hypertension struggle to maintain breath hold throughout a MOLLI sequence resulting in the need to correct respiratory motion. Therefore all images underwent the image registration process described in Chapter

3, creating synthetic images using method B, which was integrated into the Matlab pixel-wise T_1 mapping algorithm previously described.

4.3.5 Image analysis

Cardiac cine MRI analysis was performed prospectively on a GE Advantage Workstation 4.1 by a radiographer with 10 years' experience, who was blinded to the patient's clinical data. Right and left endocardial and epicardial surfaces were manually traced on the short axis cine images to obtain the volumetric indices; RV end diastolic volume (RVEDV), RV end systolic volume (RVESV), LV end diastolic volume (LVEDV) and LV end systolic volume (LVESV). From the end diastolic and end systolic volumes, RV ejection fraction (RVEF) and LV ejection fraction (LVEF) were calculated. The interventricular septum was included in the LV mass. RV mass was estimated from the sum total of the myocardial slice volumes and an assumed myocardial density of 1.05g/cm^3. Ventricular mass index was calculated as VMI = RV mass / LV mass. Cardiac MR volume and mass measurements were indexed for body surface area where appropriate. Interventricular septal angle was measured by determining the angle between the mid-point of the interventricular septum and the RV insertion points at RV end systole [94]. Analysis of T_1 maps was performed by a Cardiothoracic Radiologist with 7 years cardiac MRI experience, blinded to the patient's demographic and clinical data. Regions of interest were drawn on the interventricular septum, RV insertion points and LV free wall, see Figure 4.2. Additional regions of interest were placed in the RV and LV blood pools, avoiding trabeculations. A measure of ΔT_{1RS} was used to assess elevation of T_1 in the RV insertion points, normalised to septal T_1:

$$\Delta T_{1RS} = T_1(RV\, insertion\, point) - T_1(interventricular\, septum) \tag{4.1}$$

Regions of interest were compared across pulmonary hypertension subtypes (see flowchart in Figure 4.1). All T_1 maps were analysed by both the same observer, and a second observer, who was a trained cardiac MRI researcher with 2 years of experience analysing T_1 mapping images blinded to previous results and patient data for assessment of both inter-observer and intra-observer reproducibility.

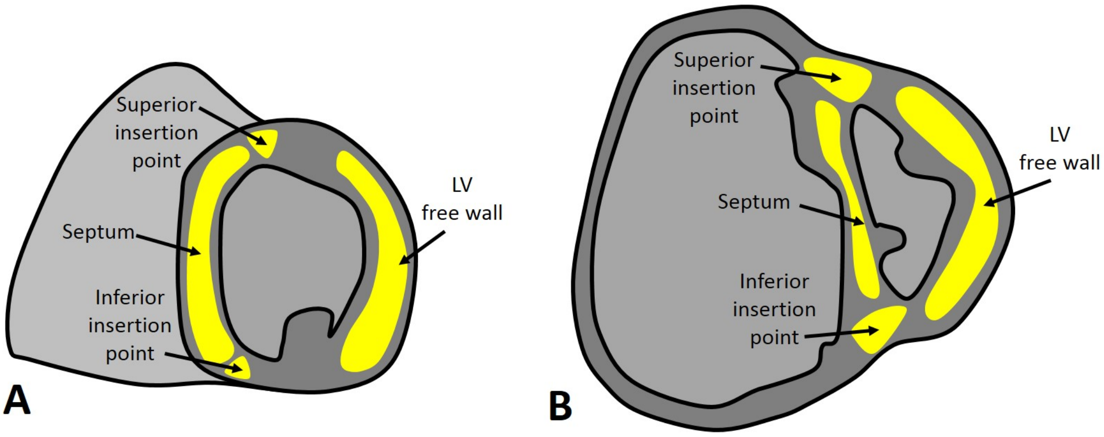

Fig. 4.2 Examples of where regions of interest would be drawn on A) a healthy volunteer and B) a patient, in the interventricular septum, interventricular insertion points and left ventricular free wall.

4.3.6 Follow up

Patients with PAH were followed up with a census date of 30.01.2018 with a mean follow-up period of 29±8 months and a median follow-up period of 30 months from MRI to death or census.

4.3.7 Statistical analysis

Statistical analysis was performed and presented using SPSS 21 (SPSS, Chicago, IL). Data is presented as mean ± standard deviation. Group comparisons were made using two-tailed ANOVA; post-hoc Bonferroni was used for multiple group corrections. Pearson's correlation coefficient was used to assess the strength of correlations. Receiver operating characteristic

(ROC) analysis was employed to assess the diagnostic accuracy of T_1 metrics with area under the curve. Inter-observer variability was assessed using the intraclass correlation coefficient (ICC); absolute values and 95% confidence intervals.

The interval from MRI until death or 01.10.2016 was regarded as the follow-up period. To control for the spatial heterogeneity of aetiology and therapy differences between the different subtypes of pulmonary hypertension, we elected to study the prognostic value of T_1 metrics in PAH alone. This controls for differences in outcome caused by factors such as severe lung disease in respiratory patients and chronic thromboembolic disease in patients undergoing pulmonary endarterectomy. Log-log plots were produced for T_1 metrics to assess proportional hazards, with variables dichotomised by median values, and prognostic value was assessed using univariate Cox proportional hazards regression analysis. Variable scaling (Z score) was performed to allow direct comparison of hazard ratios of all continuous variables by subtracting the mean from individual values and dividing by the standard deviation of the variable. Multivariate analysis with a forward stepwise approach was performed for T_1 metrics and measures of RV size and function that were significant at univariate Cox analysis ($p<0.2$). Highly correlated variables ($r>0.8$) that were significant at univariate Cox analysis were identified and the variables with the higher univariate hazard ratio were added to the model. Kaplan-Meier plots were constructed to illustrate the prognostic value of MRI volumetric measurements using median threshold values. Groups were compared using the log-rank (Mantel-Cox) test. Unless otherwise stated, a value of $p<0.05$ was considered statistically significant.

4.4 Results

All image sets underwent image registration and T_1 maps were created, see Figure 4.3. Characteristics of the study populations are given in table 4.1. Patients with pulmonary hypertension were not significantly different in age or sex than patients without pulmonary hypertension or healthy volunteers. Figure 4.3 illustrates the classification of the patients included in the study.

In patients with pulmonary hypertension, T_1 was significantly elevated at the RV insertion points when compared to healthy subjects and patients without pulmonary hypertension (patients with pulmonary hypertension, T_1 = 1065±86ms; healthy subjects, T_1 = 943±52ms, $p<0.001$; patients without pulmonary hypertension T_1 =1017±69ms, $p<0.001$). Patients with pulmonary hypertension also had elevated T_1 in the LV free wall and septum when compared to healthy subjects but not patients without pulmonary hypertension, (patients with pulmonary hypertension: LV free wall T_1 = 975±67ms, septal T_1 = 965±68ms; patients without pulmonary hypertension: LV free wall T_1 = 961±66ms, septal T_1 = 976±75ms; healthy subjects LV free wall T_1 = 913±55ms, $p<0.001$, septal T_1 = 940±56ms, $p=0.011$). See Table 4.1 and Figures 4.3 and 4.4.

Patients with pulmonary hypertension who were undergoing treatment did not have significantly different T_1 to those who were untreated (septal: $p=0.182$; RV insertion point: $p=0.977$; LV free wall: $p=0.46$). The standard deviation of T_1s within the RV insertion points was significantly higher in patients with pulmonary hypertension (SD = 62.2ms) compared to healthy subjects (SD = 36.5ms). The standard deviation of T_1s within the LV free wall and septum were not significantly different in healthy subjects when compared to patients (septal: 54.4ms, LV free wall: 42.9ms) with pulmonary hypertension (septal: 54.6ms, LV free wall: 44.6ms).

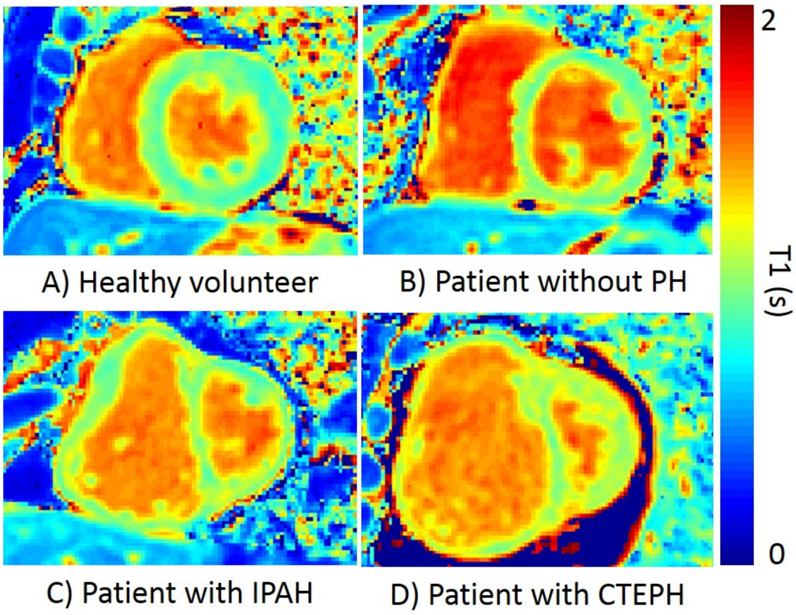

Fig. 4.3 Representative T_1 maps in cardiac short axis geometry of A) a healthy volunteer, B) a patient without pulmonary hypertension, C) a patient with IPAH and D) a patient with LHD.

Comparisons were made between pulmonary hypertension subgroups and there were no significant differences between groups. Within PAH, LV free wall T_1 was significantly higher (p=0.046) in patients with CTD than patients with CHD. There were no other significant differences between groups, see Figure 4.5.

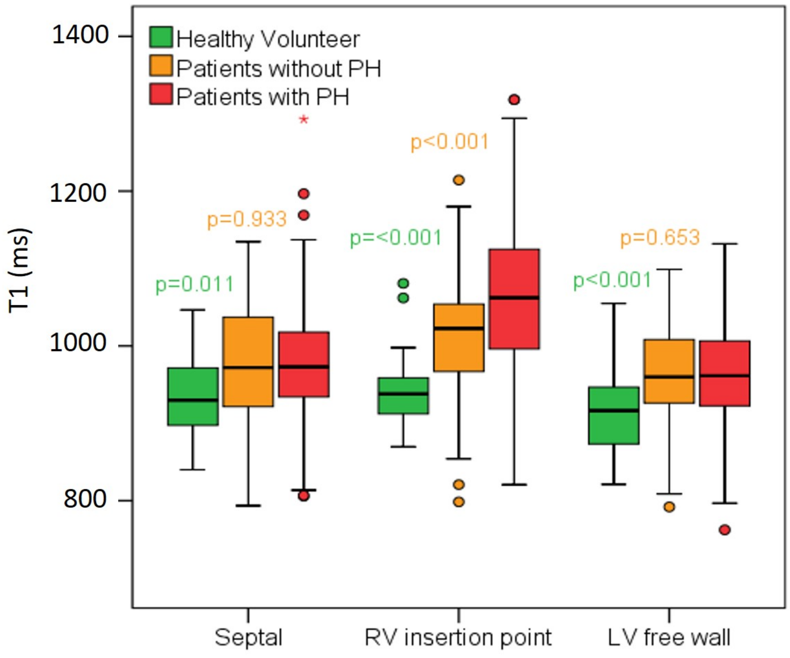

Fig. 4.4 Box plot of the mean T_1 for septal, RV insertion point and LV free wall regions. P values are given for ANOVA comparisons between patients with pulmonary hypertension and control groups above each respective control group. Circles represents outliers, * represents far outliers.

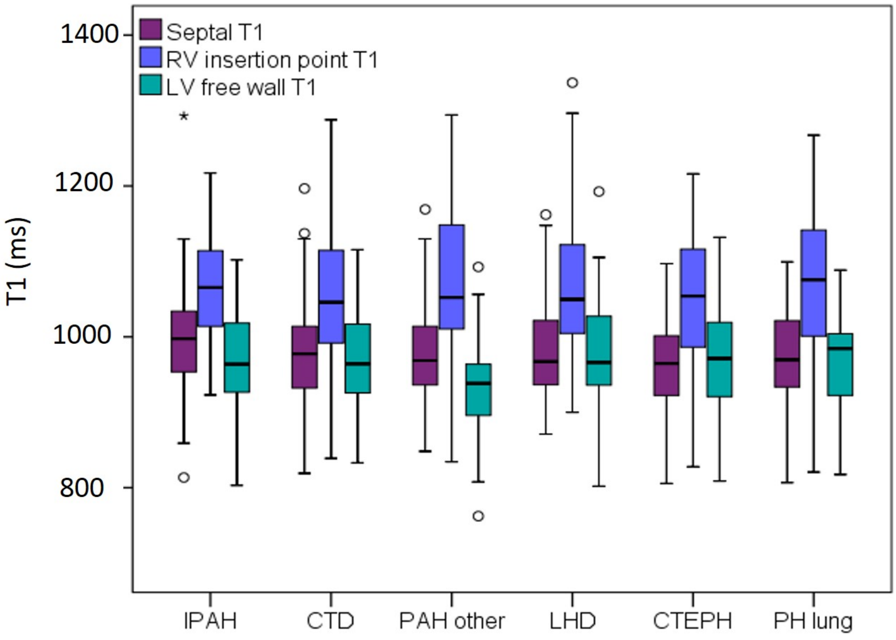

Fig. 4.5 Box plot of mean T_1 for septal, RV insertion point and LV free wall regions for pulmonary hypertension patient subtypes. Circles represent outliers, * represents far outliers.

4.4.1 Evaluation of T_1 as a diagnostic tool in pulmonary hypertension

The T_1 at the RV insertion points was the most statistically significant measurement for discriminating between volunteers and patients with pulmonary hypertension, followed by ΔT_{1RS}. However, no T_1 region was successful in discriminating between patients without pulmonary hypertension and patients with pulmonary hypertension, the most successful being ΔT_{1RS}, see Table 4.3, see Figure 4.6.

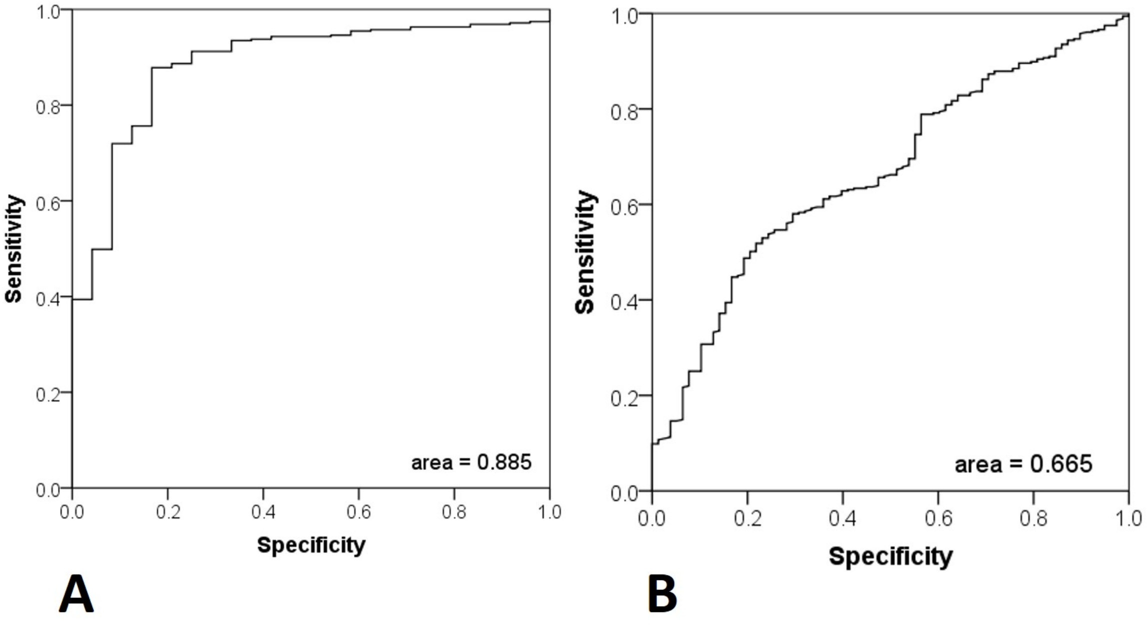

Fig. 4.6 ROC curve for RV insertion point T_1 for discriminating patients with pulmonary hypertension from A) volunteers and B) patients without pulmonary hypertension.

Table 4.2 ROC curve analysis for distinguishing patients without pulmonary hypertension and patients with pulmonary hypertension.

	Area under the curve	**Lower 95% confidence interval**	**Upper 95% confidence interval**
RV mass index	0.807	0.760	0.855
Systolic septal angle	0.850	0.809	0.892
Septal T_1	0.502	0.587	0.720
RV insertion point T_1	0.654	0.587	0.720
ΔT_{1RS}	0.675	0.612	0.738
LV free wall T_1	0.512	0.442	0.582

4.4.2 Relationship between T_1 and other MRI measures of cardiac structure and function

Across the population of pulmonary hypertension patients scanned, the RV insertion point T_1 had the strongest relationship with RV function. The mean insertion point T_1 correlated significantly with RVEDV index, RVESV index and RVEF. Additionally, the RV insertion point T_1 showed significant correlations with RV mass index, the ventricular mass index (VMI) and the systolic and diastolic septal angle, see Table 4.4. Septal T_1 and LV free wall T_1 did not correlate with any markers of RV function or LV function. However, diastolic septal angle and septal T_1 showed a positive correlation. A multivariate forward linear regression was calculated to predict RV insertion point T_1 based on all significant MRI correlators. A significant regression equation was found ($p<0.001$), with an R^2 of 0.124. RVESVI and systolic septal angle were significant predictors of RV insertion point T_1 in patients with pulmonary hypertension. In patients with LHD the RV insertion point T_1, septal T_1 and LV free wall T_1 all showed significant correlations with cine MRI metrics of RV function. ΔT_{1RS} correlated significantly with diastolic and systolic septal angle in patients with LHD.

Table 4.3 Linear regression analysis for RV insertion point T_1. Cardiac metrics from MRI are described in Table 2.4.

	Unstandardised coefficients		**Standardised coefficients**		
	B	Std. Error	Beta	t	p-value
Constant	0.845	0.073		11.609	<0.001
RVESVI	0.000623	0.000247	0.209	2.524	0.008
RVEF	-0.000213	0.0005	-0.034	-0.425	0.921
VMI	0.001	0.001	0.119	1.483	0.837
Septal angle systolic	0.001	0.0001	0.178	2.918	0.004
Relative area change	-0.001	0.001	-0.066	-0.755	0.655

4.4.3 Relationship between T_1 and right heart catheter data

228/369 patients with pulmonary hypertension also had right heart catheter within 1 month of MRI scanning, with a mean of 0 ± 1 days and a range of 15 days. The mean RV insertion point T_1 correlated significantly with the functional parameters mPAP, mRAP, and CI but not PVR, see Table 4.4. There was also a significant correlation with mixed venous oxygen saturation (SvO2). LV free wall T_1 correlated significantly with CI and SvO2, whilst septal T_1 did not correlate with any of the RHC parameters. 29/82 patients with LHD also had right heart catheter within 1 month of MRI scan, all of whom had MRI and right heart catheter on the same day. Patients with LHD also showed significant correlations between RV insertion point T_1 and mPAP, mRAP, and SVO2. Patients with LHD showed significant correlations with septal T_1 and mPAP as well as SvO2. There were no correlations between LV free wall and right heart catheter parameters.

Table 4.4 Correlations between MRI and RHC parameters in septal, RV insertion point and LV free. * indicates p<0.05, ** indicates p<0.025. Abbreviations described in Tables 2.3 and 2.4.

	Septal T_1	**RV insertion point T_1**	**LV free wall T_1**
n=369			
Age (years)	r= -0.074 p=0.159	r=0.007, p=1.000	r=-0.086, p=0.168
BSA m^2	r=0.015, p=0.771	r=0.041, p=0.444	r=-0.006, p=0.915
Heart rate (bpm)	r=0.011, p=0.836	r=-0.073, p=0.168	r=-0.086, p=0.103
RVEDVI (ml/m^2)	r=0.066, p=0.213	r=0.265**, p<0.001**	r=0.076, p=0.151
RVESVI (ml/m^2)	r=0.027, p=0.615	r=0.290, p<0.001**	r=0.088, p=0.097
RVSVI %	r=0.103, p=0.050	r=0.003, p=0.958	r=0.044, p=0.406
RVEF %	r=0.003, p=0.951	r=-0.238, p<0.001**	r=-0.080, p=0.129
LVEDVI (ml/m^2)	r=-0.035, p=0.505	r=-0.060, p=0.257	r=-0.018, p=0.734
LVESVI (ml/m^2)	r=0.005, p=0.924	r=0.011, p=0.841	r=-0.051, p=0.335
LVSVI %	r=0.051, p=0.335	r=-0.088, p=0.096	r=0.011, p=0.841
LVEF %	r=0.028, p=0.598	r=-0.066, p=0.217	r=0.050, p=0.347
Systolic septal angle (^{o})	r=0.096, p=0.069	r=0.238, p<0.001**	r=0.017, p=0.742
Diastolic septal angle (^{o})	r=0.157, p=0.003**	r=0.253, p<0.001**	r=0.017, p=0.742
n=228			
mRAP (mmHg)	r=0.074, p=0.256	r=0.160, p=0.011**	r=0.253, p<0.001**
mPAP (mmHg)	r=0.076, p=0.248	r=0.165, p=0.011**	r=0.025, p=0.706
PCWP (mmHg)	r=-0.002, p=0.9828	r=-0.053, p=0.434	r=-0.032, r=0.634
PVR (dyne/s/cm^3)	r=0.039, p=0.567	r=0.099, p=0.145	r=0.096, p=0.160
CI (l/min/m^2)	r=-0.003, p=0.964	r=-0.079, p=0.234	r=-0.166.p=0.012**
SvO2 (%)	r=-0.004, p=0.956	r=-0.152, p=0.022**	r=-0.168, p=0.011***
SaO2 (%)	r=0.119, p=0.070	r=-0.081, p=0.222	r=-0.065, p=0.322

4.4.4 Evaluation of T_1 as a prognostic tool in pulmonary hypertension

59 patients with pulmonary hypertension died during the follow up period of 29 months (standard deviation: 8 months), of which 43 had pulmonary arterial hypertension. Comparison of scaled hazard ratios showed ΔT_{RS} to be the strongest T_1 region for prediction of patient survival. See Figure 4.7. A log-rank test comparing survival in patients with pulmonary arterial hypertension with an $T_1 <$ median T_1, and $T_1 \geq$ median T_1 for each region showed that LV free wall T_1 was the strongest dichotomised predictor of patient survival, though not statistically significant (p=0.066), see Figure 4.8. Univariate Cox regression analysis of patients with PAH showed that, septal, LV free wall and RV insertion point T_1 were not associated with mortality (septal: p=0.522; LV free wall: p=0.258; RV insertion point: p=0.688), see Table 4.5. At multivariate analysis RVESVI, age diastolic septal angle were significant predictors of mortality.

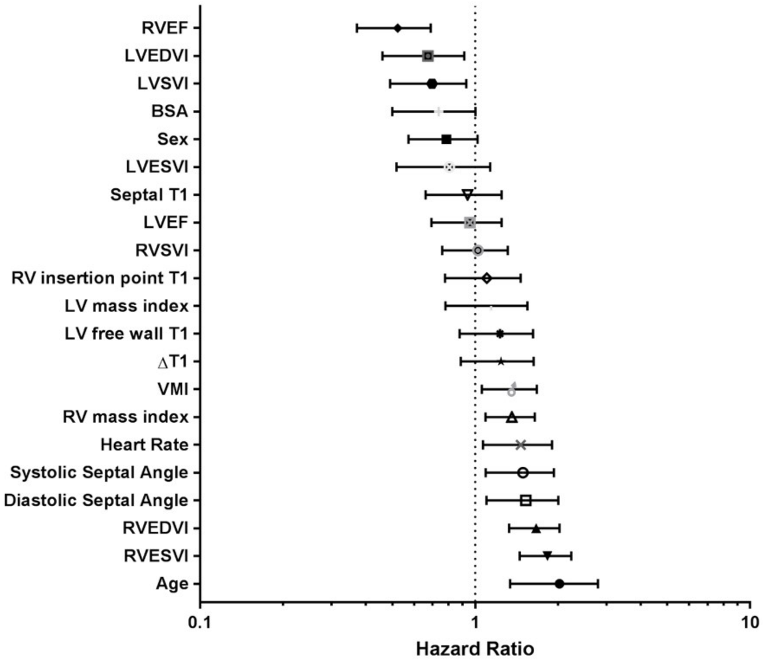

Fig. 4.7 Forest Plot of hazard ratios for patient demographics and MRI derived metrics. See tables 2.3 and 2.4 for descriptions of MRI derived metrics.

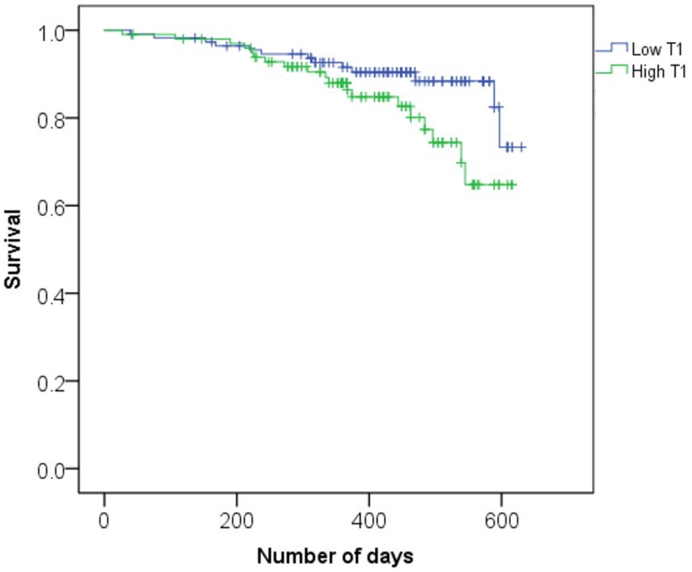

Fig. 4.8 Kaplan Meier for patient survival dichotomised by left ventricular free wall T_1 above and below median value, p=0.066.

Table 4.5 Prognostic data for patients with pulmonary arterial hypertension. Abbreviations are described in Table 2.4.

	Univariate hazard ratio	**Univariate 95% confidence interval**	**Univariate P Value**	**Multivariate Hazard Ratio**	**Multivariate 95% confidence interval**	**Multivariate p value**
Age	1.938	1.342-2.798	<0.001** †	1.279	1.396-2.248	<0.001**
Sex	0.765	0.573-1.021	0.077			
RVEDVI	1.642	1.330-2.027	<0.001** ‡			
RVEDVI	1.804	1.453-2.240	<0.001** †	1.772	1.279-2.544	<0.001**
RVEF	0.506	0.372-0.690	<0.001** †	-	-	-
Systolic septal angle	1.454	1.093-1.934	0.011** ‡			
Diastolic septal angle	1.485	1.099-2.008	0.011** †	1.556	1.108-2.186	<0.001**
RV mass index	1.341	1.091-1.649	0.018** †	-	-	-
Septal T_1	0.909	0.661-1.249	0.552			
RV insertion point T_1	1.067	0.778-1.464	0.688			
LV free wall T_1	0.195	0.879-1.624	0.258			
ΔT_{1RS}	1.205	0.888-1.634	0.237			

4.4.5 Blood T_1 in pulmonary hypertension

Blood T_1 in the LV was not significantly different between healthy subjects, patients without PH, patients with PH or patients with PH-LHD when considered together in an ANOVA. RV blood was found to differ significantly between patients with pulmonary hypertension and patients without pulmonary hypertension, p=0.049. T_1 of RV blood was significantly higher than T_1 of the LV blood in patients with pulmonary hypertension (p=0.012) and patients without pulmonary hypertension (p<0.001), this may be due a faster relaxation of spins in the LV blood pool due to paramagnetic dissolved oxygen in the highly oxygenated blood. Within patients with pulmonary hypertension, the most significant correlations (p<0.001) were between RV blood and: heart rate (r=-0.192), LVEDVI (r=-0.230), LVSVI (r=0.237) and ventricular mass index (r=-0.204). For the LV blood, the most significant correlations (p<0.001) were with heart rate (r=-0.205) and LVEDVI (r=0.196). For patients with pulmonary hypertension and right heart catheter data, the most significant correlations (p<0.001) were between RV blood and mPAP (r=-0.243) and SaO2(r=0.238).

4.4.6 Inter-observer and intra-observer reproducibility

T_1 values in the septum, RV insertion point and LV free wall were tested for absolute agreement with a random two-way model. The intraclass correlation coefficients for the interventricular septum, RV insertion points and LV free wall T_1 values respectively were: 0.841, 0.823 and 0.792 respectively. The interclass correlation coefficients for the septum, RV insertion point and LV free wall T_1 values respectively were: 0.844, 0.742 and 0.618 respectively. Intraclass reproducibility was found to be excellent in all regions in healthy volunteers, intraclass correlation coefficients for the interventricular septum, RV insertion points and LV free wall T_1 values were: 0.898, 0.934 and 0.852 respectively. The interclass correlation coefficients for the septum, RV insertion point and LV free wall T_1 values were: 0.972, 0.942 and 0.824 respectively.

4.5 Discussion

Accurate, registered T_1 maps were produced for all subjects of this study, see examples in Figure 4.3. Despite the clinical heterogeneity found in subtypes of pulmonary hypertension in the patients in this study, there were no significant differences found in myocardial

T_1 between the subtypes of this population. In particular, patients with LHD who were considered separately (due to a different aetiology and cardiac phenotype) were found to have no significant differences from patients with other forms of pulmonary hypertension, this may be because the causal mechanism of T_1 differences in pulmonary hypertension is present to some extent in all pulmonary hypertension subtypes. However, this may also be due to multiple casual mechanisms causing elevated T_1 in pulmonary hypertension due to the heterogeneity of the disease.

Patients with CTD have been previously found to have elevated T_1 compared to controls [95]. However, we did not find that patients with CTD had significantly different T_1 in any region than patients with IPAH. This indicates that any tissue changes caused by the presence of cardiac connective tissue were not detectable in this study, likely having a less significant effect than those of pulmonary hypertension itself, or patients with connective tissue disease did not have significant LV disease.

Two control groups were used to evaluate changes in the myocardium in patients with pulmonary hypertension: age matched healthy volunteers and patients without pulmonary hypertension. Patients without pulmonary hypertension had significantly higher RV insertion point T_1 when compared to healthy volunteers. Though both RV insertion point T_1 and ΔT_{1RS} were successful at differentiating healthy volunteers from patients with pulmonary hypertension, they were not successful at differentiating control patients from patients with pulmonary hypertension. ΔT_{1RS} was not significantly different between control groups which suggests regional elevation of the insertion point T_1 is characteristic of pulmonary hypertension rather than elevation of the whole myocardial T_1.

In patients with pulmonary hypertension and LHD, increase in mPAP and mRAP correlated with elevated T_1 in the RV insertion points, but not the LV free wall, indicating that T_1 in these regions is associated with elevated pulmonary pressure. It is a limitation of this study that concurrent right heart catheter and cardiac MRI data was not present for all subjects.

Patients without pulmonary hypertension had mPAP above normal and were in the borderline pulmonary hypertension diagnostic category, see Table 4.1 which may explain why this patient group has higher T_1 in the TV insertion points than healthy volunteers.

Although patients with pulmonary hypertension and higher RV insertion point native T_1 were less likely to survive than patients with pulmonary hypertension and lower RV insertion point T_1, RV insertion point T_1 was not an independent significant predictor of mortality in patients with pulmonary arterial hypertension. This conclusion is constrained by the fact that the follow up period was relatively short 85% of patients were still alive). Therefore, census at a later point may be required to provide more definitive evidence of whether RV insertion point T_1 has independent prognostic value.

Although LGE and elevated native T_1 has been observed in the interventricular septum in pulmonary hypertension [73–75] the same finding was not observed in this study. This may be because regions of interest were placed in the middle of the interventricular septum, whereas LGE imaging shows myocardial changes extending from the insertion points and therefore weakest enhancement at the central region of the septum. Further work to evaluate regions of interest at the inferior and superior portions of the interventricular septum may clarify this. Thus, the relationship between T_1 and late gadolinium enhancement in the RV insertion points were not evaluated here and further work may be warranted to evaluate this thoroughly in patients with pulmonary hypertension.

Significant differences in blood T_1 between patients with pulmonary hypertension and healthy volunteers were not found. Within patients with pulmonary hypertension significant correlations between blood (RV and LV) T_1 and parameters of left and RV function and heart rate. In addition, increased oxygen saturation of haemoglobin (SaO2) correlated significantly ($p<0.001$) with increased T_1 of RV blood. This may be because deoxygenated haemoglobin is paramagnetic, therefore as the proportion of deoxygenated haemoglobin decreases with increased oxygen saturation, blood T_1 would be expected to increase due to the oxygenation.

As patients with pulmonary hypertension were found to have significantly lower SaO2 than patients without pulmonary hypertension, any oxygenation effects in blood perfused within the myocardium would obscure T_1 changes which result from tissue changes. It has been suggested that normalising myocardium T_1 using blood T_1 results in reduced myocardial T_1 variability and sex differences [96] and our results may indicate this may be a technique relevant to patients with pulmonary hypertension.

Inter-observer and intra-observer reproducibility data was found to be in line with that previously observed in patient T_1 mapping studies [88]. The RV insertion points were found to be less reproducible than the interventricular septum. This may be due to higher T_1 heterogeneity in this region leading to greater T_1 variation when region of interest placement differs. T_1 values tended to be less reproducible in patients with PH than volunteers, which is consistent with other studies findings [70].

It may be that relatively poor breath-holding of the patient cohort contributes a greater degree of motion artefact resulting in weaker inter and intra-observer reproducibility. It has been shown previously that native T_1 mapping has good scan-scan variability over 3.6 ± 0.5 years with a coefficient of variation of 1.4%, therefore it would be of interest in future work to establish the scan-scan repeatability in patients with pulmonary hypertension, and whether native myocardial T_1 elevation changes with time in patients with pulmonary hypertension and whether this has prognostic significance.

4.5.1 Causes of elevated myocardial T_1 in patients with pulmonary hypertension

The lack of specificity of RV insertion point T_1 indicates that pathophysiological processes responsible for the elevated RV insertion point T_1 are not solely confined to patients with pulmonary hypertension. The RV insertion points were the myocardial regions with the highest T_1 and they correlated significantly with loss of RV function and RV remodelling.

Systolic septal angle and RVESVI were independent predictors of RV insertion point T_1, however these variables only predicted 12.4% of the variance seen in RV insertion point T_1 in patients with pulmonary hypertension. This may indicate that mechanisms which are not explicable solely through cardiac volume, mass and pressure changes are responsible for the tissue changes represented by T_1.

Animal models of pulmonary hypertension with increased native T_1 and LGE present in the RV insertion points have been shown to have increased interstitial collagen associated with fibre disarray, and increased connective tissue density [71]. It has been shown in two patients with PAH that fibrosis was present in the RV insertion point and it has been suggested that this is the mechanism driving LGE in PAH [69]. However, those patients also had an increase in interstitial space and a small increase of fat. A cardiac MRI case study of one patient with IPAH showed myocardial disarray with increased collagen and fat between fibre bundles in the myocardium (plexiform fibrosis). That study suggests that the cause of LGE is not pathological, and instead arises from an exaggeration of the myocardial disarray and plexiform fibrosis where fibres from the right and left ventricle cross. It is suggested this exaggeration of myocardial disarray may arise from a combination of RV hypertrophy and increased shear forces upon the interventricular septum [70]. Septal angle is a measure of deviation of the LV septum due to the high pressure in the RV, which correlated strongly with RV insertion point T_1 in patients with pulmonary hypertension and was found to be an independent linear predictor of RV insertion point T_1. Even in patients with LHD, who do not exhibit divergence of the LV septum to the same degree as other patients with pulmonary hypertension, ΔT_{1RS} correlated significantly with septal angle. However, in patients with LHD, the correlation between RV insertion point T_1 and septal angle itself was not significant (systolic: r=0.247, p=0.140; diastolic: r=0.319, p=0.054), likely due to the considerably lower patient numbers in the LHD subgroup. The T_1 value of the LV free wall, which would not experience stress/strain due to elevated ventricular pressure, was found not to show a correlation between T_1 and septal angle and was not elevated in patients with pulmonary hypertension compared to patients without pulmonary hypertension. Therefore, our data suggests that the regional elevated native T_1 in the insertion points is significantly related to the displacement of the interventricular septum in pulmonary hypertension. This supports the suggestions from histological studies that changes in myocardial T_1 and the presence of LGE may be due to exaggerated fibre disarray in the RV insertion points of the myocardium due to stress on the septum and RV insertion points in pulmonary hypertension.

4.6 Conclusions

The motion correction method developed in Chapter 3 has been shown to be effectively applied to large volumes of MOLLI data from patients with pulmonary hypertension in what we believe to be the largest study of T_1 mapping in this disease to date. The RV insertion point have been shown to be the region where T_1 changes are most significantly related to cardiac function in pulmonary hypertension. Myocardial T_1 did not differ significantly between pulmonary hypertension subtypes including LHD. The T_1 in the RV insertion point was significantly associated with RV volume and function in the patients scanned. Interventricular septal angle independently predicted RV insertion point T_1 in patients with pulmonary hypertension suggesting that regional elevation in the RV insertion point may be linked to increased stress on the interventricular septal wall. T_1 in patients with pulmonary hypertension was not found to be prognostic independent of RV size and function. Overall, T_1 mapping does not appear to predict the subtype of pulmonary hypertension, or provide additive value over RV volume in the prognostic evaluation of patients with pulmonary hypertension.

Chapter 5

Modification of registration technique for free breathing lung T1 mapping

The MRI signal from the lungs is generally weak due to a low proton density in the healthy lung, which has a tissue density of around $0.1 g/cm^3$ [97]. However, lung density varies with inflation state, with an increase in lung density to 140-180% of that of inspiration during expiration [98] [99]. This leads to a reduction in MRI signal in the lungs due to tissue density which varies with respiratory state to 10-20% of that of a typical tissue. In addition, there is a low T_2^* (0.74±0.1ms during free breathing at 3T and 2.11±0.27ms during free breathing at 1.5T [100]) due to the large magnetic susceptibility differences in the lung ($\Delta\chi = 8 ppm$). While most tissues in the body are diamagnetic, air has a very low magnetic susceptibility and dissolved oxygen and deoxyhaemoglobin in the blood are paramagnetic. Therefore, the lung experiences local magnetic field gradients due to these susceptibility differences, leading to increased T_2^* relaxation [101]. There are various methods of overcoming these difficulties in lung imaging, which usually combine a short TE with a short acquisition time in either a spin echo or gradient echo imaging sequence [97]. More recently, ultra-short gradient echo sequences (UTE) with a TE$\leq 100\mu s$ have been developed. Due to the echo time of these sequences being much less than the T_2^* of the lung, visualisation of the lung tissue is greatly enhanced. However, to determine functional information, such as lung perfusion or ventilation, additional techniques need to be employed. Pulmonary perfusion maps can be generated with injected Gadolinium paramagnetic contrast agents and a T_1 weighted, low resolution, short TR, time resolved, 3D spoiled gradient echo sequence, resulting in quantification of key lung perfusion parameters such as mean transit time and regional blood volume. The paramagnetic properties of oxygen can also be exploited as a lung contrast agent by breathing higher oxygen concentrations. Using oxygen enhancement with a T_1 weighted sequence [102], or a T_1 mapping sequence such as those described in Chapter 2.2, the signal and/or T_1 change due to the increased oxygen dissolved in the tissue and blood gives an inherent ventilation and perfusion weighting.

When using a T_1 mapping sequence, such as a Look-Locker sequence, UTE inversion recovery sequence or UTE saturation recovery sequence (see Chapter 2.2.2), the change in T_1 due to breathing 100% oxygen can be directly quantified. Difference maps between oxygen enhanced T_1 maps and T_1 maps acquired following breathing air allows the combined effect of ventilation of oxygen to the lung, and its diffusion into the blood, to be visualised and quantified. However, while it may be conceptually desirable to quantify lung ventilation and diffusion during respiration (as it removes the potential effects of the breathing manoeuvre), in clinical practice most lung imaging methods require breath hold to suppress respiratory motion. Free breathing methods have been developed using external navigators or navigator echoes to identify images which are within the same respiratory window [7] [37], however these require much longer imaging times and result in a lot of unused scanner time due to images being discarded or due to waiting for the respiratory window of choice. For example, a 2D free breathing UTE sequence requires around 2 minutes per slice [7] or a 3D free breathing interleaved saturation recovery UTE sequence requires around 10 minutes [37].

T_1 mapping sequences may be able to provide information on tissue changes within the lung. In patients with dilated cardiomyopathy, an increase of collagen content due to diffuse myocardial fibrosis is associated with an increase in native T_1 [103] and it may be that the presence of fibrosis in the lung results in a measurable change in the T_1 of the lung tissue. However, within the myocardium, it has been shown that sex differences in myocardial T_1 can be normalised using the blood pool as a reference, which may indicate that the sex differences seen in the myocardium are due to the blood content of the myocardium and it's associated sex differences (as discussed in Chapter 2.1.3.). Around half of the healthy lung mass is comprised of blood [104], therefore, like in the myocardium, the resultant lung T_1 measurement will be a combination of blood and tissue T_1. Therefore, we may expect that differences in sex, oxygenation and hemotocrit in patients will result in changes to lung T_1 *as well as* underlying tissue changes. Blood T_1 is typically longer than tissue T_1 (see Chapter 2.1.3). Fibrosis within the lung may increase the proportion of the lung comprised of tissue, therefore decreasing the net lung T_1. In patients who show heterogeneous tissue changes, regional tissue changes may be able to be visualised by T_1 mapping, which may allow regions of affected tissue to be identified from their change in T_1.

5.1 Idiopathic pulmonary fibrosis and T_1 mapping

Idiopathic pulmonary fibrosis (IPF) is a chronic and progressive lung condition where lung fibrosis occurs in heterogeneous regions of the lung. The condition effects a patients ability to breath-hold considerably, and breathlessness is a common symptom. The cause of the condition is unknown and patients with IPF have a median survival time of 2-3 years [79]. The condition has a poor outcome with a high incidence of pulmonary hypertension as the condition progresses, with 32-50% of patients in advanced stages of IPF presenting with pulmonary hypertension [105]. Assessment of the condition can include lung function tests, CT and lung biopsy. However, it remains challenging to assess disease severity and quantify disease progression in this patient group, particularly as the disease is variable and prognosis is difficult to assess [85]. If lung MRI is able to visualise disease processes (such as fibrosis or poor lung oxygenation) it may be that lung MRI methods allow monitoring of patients undergoing therapy initiation or clinical deterioration.

The presence of fibrosis in the lung causes the lung to lose elasticity and increase septal thickness, resulting in poorer diffusive oxygen exchange (due to an increase in tissue between the air and blood vessels) and decreased lung volume. In IPF the lungs develop interstitial fibrosis, areas of inflammation and cysts which may all effect the tissue T_1. These processes are heterogeneously distributed in the lung in a pattern known as honeycombing and reticulation, with discrete areas of the lung effected by fibrosis presenting next to areas of normal lung, see Figures 5.1 and 5.2.

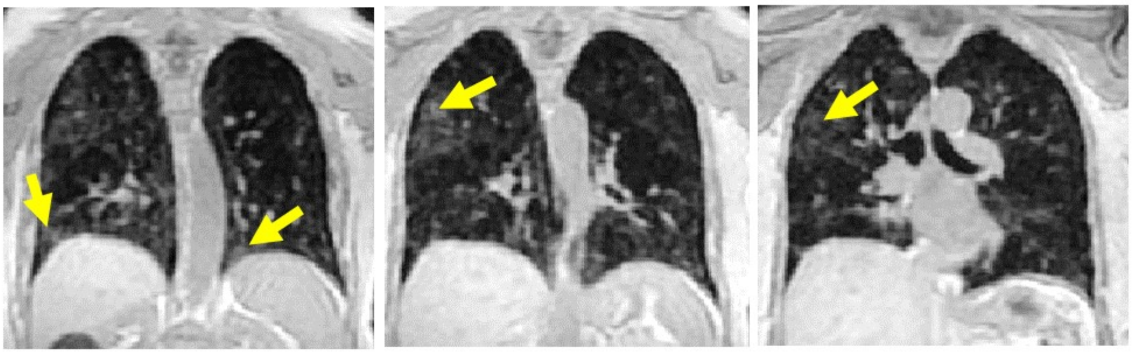

Fig. 5.1 Three coronal UTE images from a patient with IPF to demonstrate the heterogeneous regions of fibrosis characteristics of the condition. Arrows point to regions of elevated signal which may correspond to regions of fibrosis.

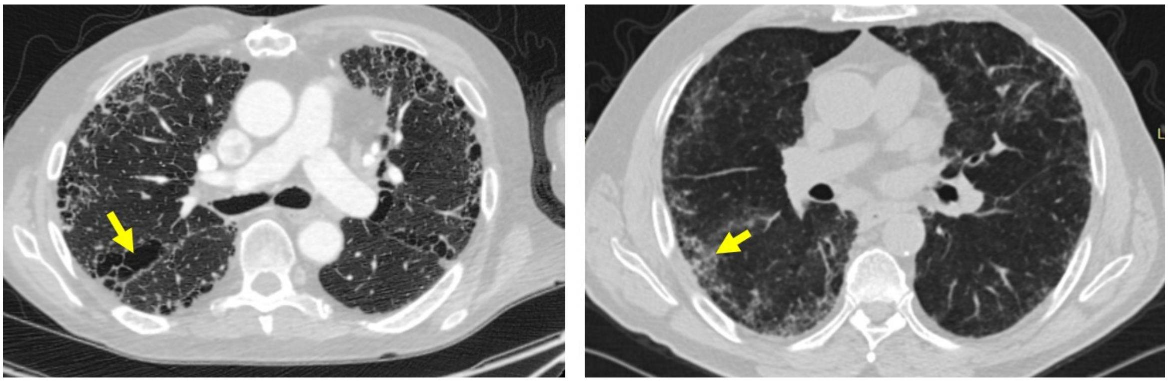

Fig. 5.2 Sagittal CT images from two patients with IPF showing ground glass and reticular changes non-specific interstitial pneumonia (right) and subpleural honeycombing (left). Arrows show areas of honey combing and ground glass reticular change respectively.

As discussed in Chapter 2.3.1, changes to the molecular environment in the body result in changes in tissue T_1. In a normal human lung, around half of the mass of the lung originates from blood, with the other half originating from tissue. Changes in the lung tissue, such as an increased collagen content due to fibrosis, will result in changes to the T_1 of the tissue in that area. In addition, the increase of thickened tissue could result in an overall lung T_1 change due to an increase of the fractional contribution of tissue versus blood. Lung perfusion is also known to change with inflation state, with expiration breath hold resulting in up to twice the perfusion levels as inspiration [52]. Increased perfusion during expiration leads to an increase in the fractional blood volume when considering the lung as a whole. As blood has a higher T_1 than tissue, this may be the cause of the elevated T_1 which has been observed in expiration breath hold when compared to inspiration breath hold in both healthy volunteers [51] and patients with IPF [84]. As discussed in Chapter 2.1.4, oxygenation can impact T_1 of blood and tissue in two ways. By binding to paramagnetic deoxyhaemoglobin or deoxymyoglobin, oxygen can increase T_1 in blood or tissue. However, at hyper-oxygenation (oxygenation >95%) excess oxygen will dissolve into the blood plasma, which decreases T_1 due to its paramagnetism [2].

Therefore, although lung T_1 mapping has the potential to detect tissue changes within the lung, it may also be significantly affected by respiratory state and other confounding physiological factors such as blood/tissue oxygenation and lung perfusion. This presents a problem to lung T_1 mapping, as it is important to understand the mechanisms behind lung T_1 changes and whether changes in T_1 are measures of tissue density change or oxygenation and/or perfusion. However, this also opens up the possibility of lung T_1 mapping being able to provide information on all of these patho-physiological effects if well understood.

When studying T_1 in the lung, the whole lung can be compared to controls, or regions of the lung affected by IPF can be compared to unaffected regions within the same patient, using CT structural changes as a guide. A MRI study with patients with IPF and healthy controls were imaged during 3T inspiration breath hold [85] and the results found pre-contrast lung T_1 was higher in patients with IPF when compared to controls and that fibrotic regions of the lung had significantly higher T_1 when compared to non-fibrotic regions of the same lung [85], indicating that regions of fibrosis may be able to be identified from MRI alone. A different study looking at whole lung T_1 in patients with IPF on a 1.5T MRI scanner during both inspiration and expiration showed net lung T_1 values lower than had been previously found by the same group in healthy volunteers [84] [51]. In addition, the study found a significant relationship between expiratory T_1 values and the total lung capacity and lung residual volume. This indicates that MRI may be useful in identifying IPF and characterising the condition.

Although patients with IPF would benefit from free breathing T_1 mapping acquisition methods, like in cardiac T_1 weighted imaging, lung T_1 weighted image contrast changes with time due to T_1 relaxation, making the acquired images difficult to automatically register. In a typical coronal lung image several tissues with different T_1s will be present, such as diaphragm, liver, lung, bone and fat. The aim of this work is to acquire free breathing lung T_1 maps, using image registration to synthetic images to correct respiratory motion. By using automated image registration for respiratory motion correction, the image acquisition time remains short, reducing scan time and increasing patient comfort.

As respiratory state of breath hold (inspiration versus expiration) is known to effect measured lung T_1 [51] [84], free breathing lung T_1 is also expected to differ from that during breath hold. In addition, the process of respiration will effect the oxygen saturation and amount of oxygen (both bound and dissolved into blood plasma) in the blood, which is expected to effect lung T_1. Patients with IPF may have lower levels of oxygen in the blood and/or higher levels of deoxyhaemoglobin in the blood, in addition to extracellular and tissue changes due to the pathophysiology of the condition.

Therefore, it is of interest to characterise the changes in lung T_1 due to free breathing acquisition, as well as confirm whether lung T_1 is significantly different in patients with IPF when compared to subjects without IPF and whether there is a larger regional variation in the lung of patients with IPF. In addition, free breathing T_1 mapping may be a comfortable and radiation free method of quantifying fibrotic areas of the lungs in patients with IPF.

5.2 Objectives

The objectives of this chapter of work are to:

i. Modify the image registration algorithm for the use in free breathing T_1 mapping in the lung using a Look-Locker sequence.

ii. Demonstrate and evaluate the effectiveness of this method in healthy volunteers and patients with IPF and assess if lung T_1 differs between these two groups.

iii. Investigate whether acquiring images in free breathing affects the measured T_1 of the lung.

iv. Investigate the affect of breathing 100% oxygen on lung T_1 during free breathing and breath hold.

5.3 Method

In order to modify the existing image registration and T_1 mapping algorithm developed in Chapter 3 for use in free breathing, the lung images which occur in the same spatial location need to be identified. In Chapter 3, the knowledge that respiratory motion due to release of breath hold tends to occur later in the image acquisition allowed the assumption that the first images acquired in the series would be best spatially aligned. This assumption held and enabled spatially aligned synthetic images to be produced. However, during free breathing, respiratory motion will be present from the beginning of the sequence and therefore this assumption can not be used. Instead, a method to determine the respiratory pattern from the time course of images themselves has been developed, such that images which occur at the same point of respiration (in 2D space) can be determined without any additional information.

5.3.1 Model for diaphragm signal changes in free breathing lung Look-Locker imaging

The basic steps involved in the image registration process are described in Figure 5.4, the relevant code is given in appendix A with accompanying flow charts of the algorithms used. Synthetic images are created using three of the acquired images which are spatially aligned. Spatially aligned images are chosen using a simple model which describes the combined effect of respiration and inversion recovery on a group of pixels at the diaphragm, as the signal of a region of interest on an image with respiratory motion is the result of a combination of inversion recovery behaviour **and** the motion of tissue in and out of the region of interest, see Figure 5.3 and appendix A.2.1. A group of pixels at the diaphragm are automatically selected based on the parameters determined from curve fitting, which will be discussed in more detail later in this chapter. The synthetic images are then used for pair-wise image registration with the acquired images, to create a set of registered images, from which a T_1 map can be produced.

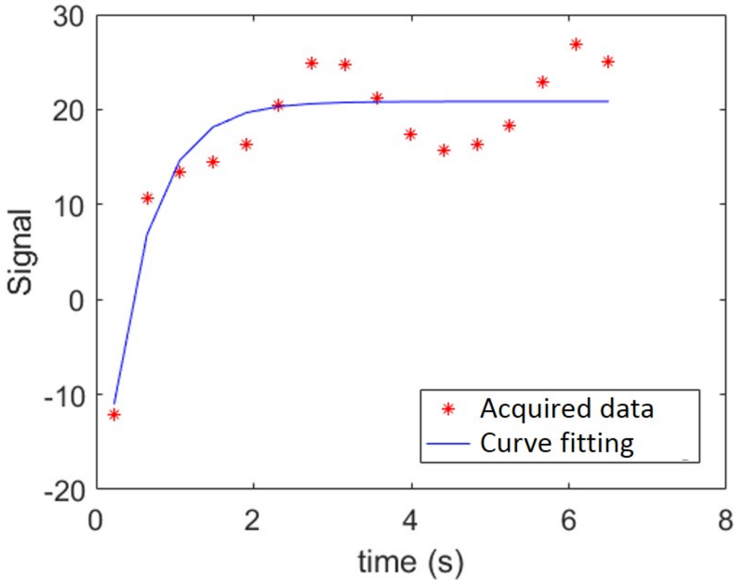

Fig. 5.3 Examples of the observed Look-Locker inversion recovery signal over time in a respiring patient from fixed pixels at the diaphragm, compared to that expected from a single compartment inversion recovery during breath hold.

The total signal from a fixed ROI in the body is effected by both the inversion recovery behaviour of the protons in this region of tissue and the changing ratio of the tissues in the ROI due to respiration, see Figure 5.3. For simplicity, consider a region of interest which represent two tissue types: tissue A and tissue B, see Figure 5.5.

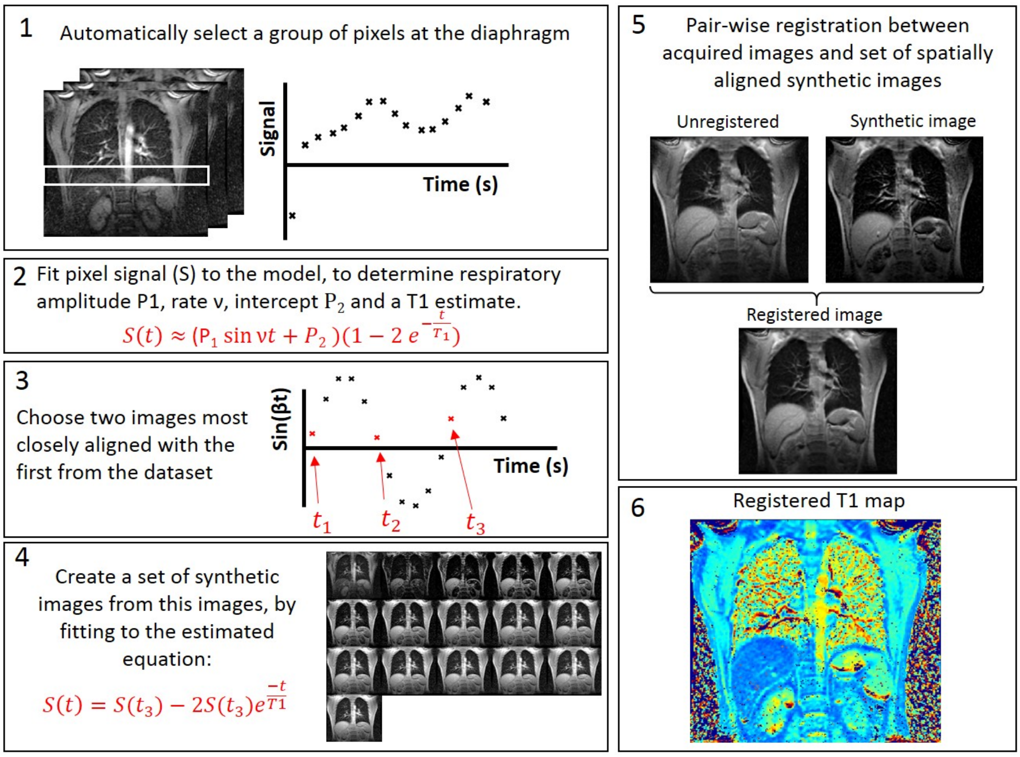

Fig. 5.4 Diagram showing the basic steps to the method of automated image registration for free breathing lung Look-Locker images. In this method S_3 acts as a surrogate for S_0.

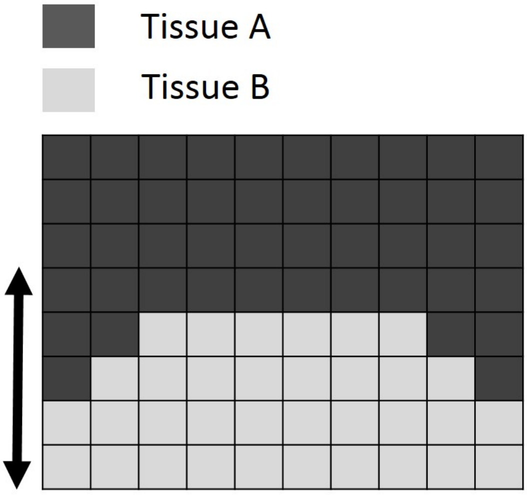

Fig. 5.5 Simplified diagram of a fixed region of pixels at the diaphragm.

The signal from these two components without respiration, can be written as:

$$S(t) = kn_A\rho_A(1-2e^{\exp^{\frac{-t}{T_{1A}}})})+kn_B\rho_B(1-2e^{\frac{-t}{T_{1B}}}) \tag{5.1}$$

Where k is a constant, n_A and n_B are the number of pixels corresponding to tissue A and B respectively, and the densities ρ_A and ρ_B are the densities of protons in each tissue per pixel. If the change in the number of pixels representing each tissue in the ROI changes according to a sinusoid, where the total number of pixels does not change:

$$n_A = \alpha\sin(\nu t+\phi)+\kappa_1, n_B = -\beta\sin(\nu t+\phi)+\kappa_2 \tag{5.2}$$

Where A and B are the two tissues in 5.5, α and β are the coefficient of the sine waves, κ_1 and κ_2 are constants and ν is the respiratory frequency, and ϕ is the respiratory phase shift. Such that

$$n_A+n_B = constant \tag{5.3}$$

Therefore, an increase in n_A results in a proportional decrease in n_B and vice versa (assuming that the tissues are incompressible), and ν is the respiratory rate. To account for time-dependant relaxation changes:

i Equation 5.2 can be substituted back into 5.1 to account for the movement of tissue A and B due to respiration

ii T_{1A} and T_{1B} become time dependent and are replaced with T'_{1A} and T'_{1B} due to possible tissue changes due to respiration, for example, oxygenation effects.

iii Two time dependant T'_2 components are included, as T_2 may also change due to respiration resulting in a time-dependency and possible T_2 weighting to the images.

iv ρ_A and ρ_A may also change with time due to tissue compression, and are written as $\rho_{A'}$ and $\rho_{B'}$.

$$S(t) = k(\alpha \sin(\nu t + \phi) + \kappa_1)\rho_A(1 - 2\exp(\frac{-t}{T'_{1A}}))\exp(\frac{T_E}{T_2 A'} + k(-\beta \sin(\nu t + \phi) + \kappa_2)\rho_B(1 - 2\exp(\frac{-t}{T'_{1B}}))\exp(\frac{T_E}{T_2 B'}) \tag{5.4}$$

The change in T_1 and T_2 due to the respiratory cycle is not necessarily known and depends on the tissue in question. Whole lung T_1 has been found to be around 10% longer during expiration breath hold compared to inspiration breath hold [51] and therefore it may be that lung T_1 varies between these extremes during respiration. However, the difference between inspiratory and expiratory breath hold volumes is expected to be more than tidal volume. During free breathing images where acquired images were dichotomised into either inspiration and expiration states, lung T_1 was found not to be significantly different between inspiration and expiration [7].

Lung T_2 has been found to decrease during inspiration due to increased magnetic susceptibility gradients across the lungs due to compression of tissue and increased presence of paramagnetic oxygen in the air in the alveoli [38] [106]. In freely breathing mouse models T_2 was shown to have a linear relationship with proton density [106] and lung T_2* was found to increase in the expiration phase of free breathing acquisition by around 4%. Liver T_1 and T_2 may also have a time dependency due to respiration, but will not be affected by the large tissue susceptibility differences seen in the lung due to air-tissue interfaces.

As respiration rate, $\nu \rightarrow 0$ (breath hold) $S(t) \rightarrow$ equation (5.1). However, equation (5.4) can be simplified by the assumptions that:

- That tissue A is lung, and therefore $\rho_{A'}$ is time dependent.
- That tissue B is incompressible.
- That the density of the lung tissue is much lower than that of the second tissue and therefore the signal from the second tissue dominates the overall $S(t)$

- That the density of the second tissue (predominantly liver) is not affected significantly by time-dependent changes in T_1 or T_2 due to oxygenation or other respiration affects.

Therefore equation 5.4 can be reduced to:

$$k(\alpha\sin(\nu t+\phi)+\kappa_1)\rho_{A'}(1-2\exp(\frac{-t}{T'_{1A}}))\exp(\frac{T_E}{T_2A'}) << k(-\beta\sin(\nu t+\phi)+\kappa_2)\rho_B(1-2\exp(\frac{-t}{T'_{1B}}))\exp(\frac{T_E}{T_2B'}) \tag{5.5}$$

and:

$$S(t) \approx k\rho_B(-\beta\sin(\nu t+\phi)+\kappa_2)(1-2\exp(\frac{-t}{T_{1B}})) \tag{5.6}$$

Which can be rewritten:

$$S(t) \approx (P_1\sin(\nu t+\phi)+P_2)(1-2\exp(\frac{-t}{T_{1B}})) \tag{5.7}$$

Where P_1 and P_2 are constant parameters to be fit to, which correspond to $-k\rho_B\beta$ and $k\rho_B\kappa_2$ respectively. The intention of these assumptions is to create a simplified model with minimal free parameters in order to allow a robust curve fitting. Equation (6.4) then has just five free parameters and can be used to determine the respiratory rate, ν, occurring within a set of inversion recovery images. $\nu t+\phi = 1$ and $\nu t+\phi = -1$ occur at inspiration and expiration respectively. Therefore, the state of respiration of the first image can be determined, and the images which minimise $sin(\nu t_1+\phi)-sin(\nu t_i+\phi)$ can be identified and used to create synthetic images spatially aligned to image 1, see Figure 5.6.

Throughout this thesis, a version of equation 5.7 without a phase shift has been erroneously used. The following work has been completed using the equation and 4 free parameters, and it is expected that further work incorportating the phase shift as an additional parameter will improve the accuracy of respiratory phase estimation and therefore improve image registration accordingly.

$$S(t) \approx (P_1 \sin(\nu t) + P_2)(1 - 2\exp(\frac{-t}{T_{1B}})) \tag{5.8}$$

This simplified model and it's associated assumptions is set in place only for the purpose of constructing synthetic images as a registration tool.

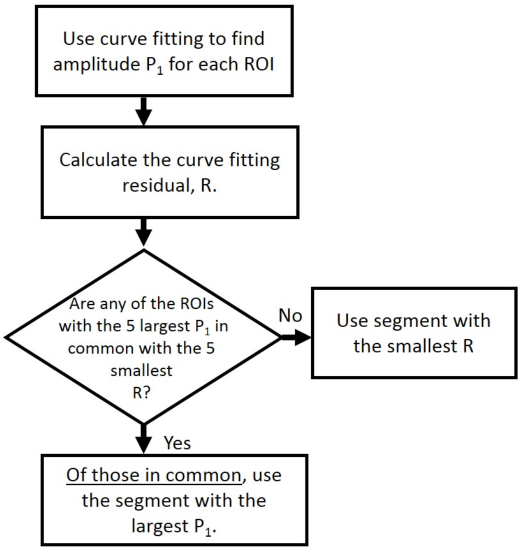

Fig. 5.6 Flow diagram to show which image segment is used to determine respiratory rate. The method aims to find a segment whose signal fits the model well (has a low curve fitting residual) but is also appreciably effected by respiratory motion (has a large coefficient P_1).

The images are segmented into horizontal ROIs of 20 pixels height, resulting in 13 sections as shown in Figure 5.7. Each strip is fitted to equation (6.4). The coefficient P_1 is maximum at a region where the effect of respiratory motion on overall signal is most significant, which is usually at the liver/stomach, see Figure 5.7. The segment used to determine respiratory rate, ν, is chosen by the algorithm shown in Figure 5.6. The method aims to choose a segment whose signal fits the model well and therefore has a low curve fitting residual, but is also appreciably effected by respiratory motion and therefore has a large coefficient P_1.

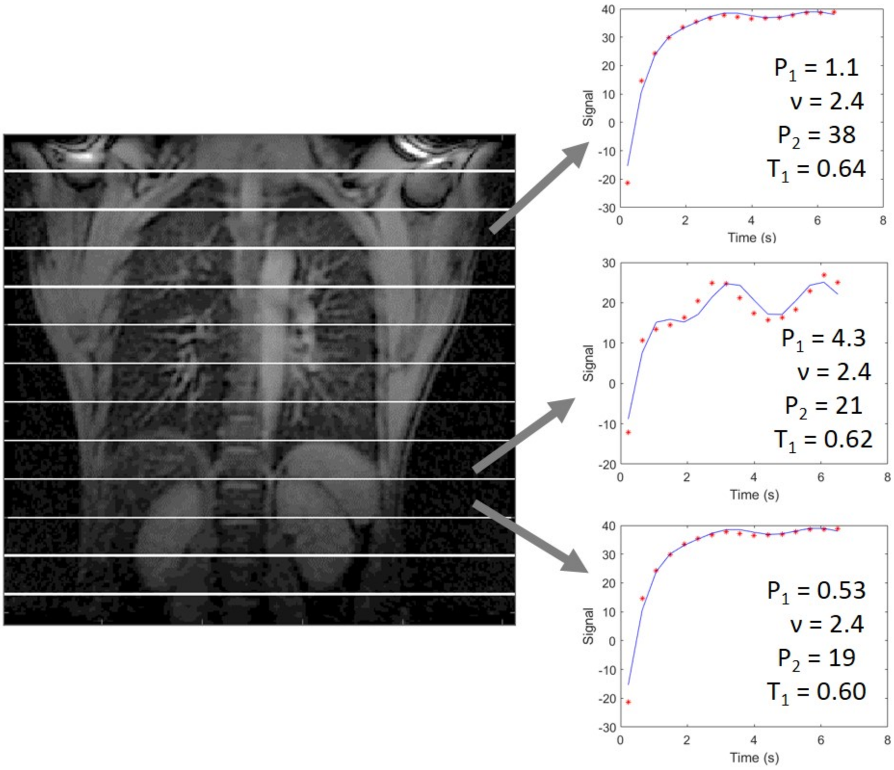

Fig. 5.7 Figure illustrating the identification of the diaphragm via the respiratory amplitude from pixel fitting horizontal segments of pixels to the combined respiratory and inversion recovery model, see equation (6.4).

Once the respiratory rate, ν, is determined, sin(ν t) can determine the state of respiration for each image, see Figure 5.6. Three input images for the synthetic image creation are then selected:

i The first image in the sequence

ii The image where $sin(\nu t_1) - sin(\nu t_i)$ is minimised.

iii Of the images which occur at least 1.5 seconds after the first image (when most tissue will have a largely recovered T_1) and which are not already chosen, the image with the smallest value of $sin(\nu t_1) - sin(\nu t_i)$.

The intention here is to choose three well aligned images, but as the third image acts as a surrogate for the fully recovered signal (S_∞), it should not occur at the beginning of a sequence. Here there is a trade-off between choosing the best aligned images and choosing images which well represent the inversion recovery signal curve. An example is shown in Figure 5.8.

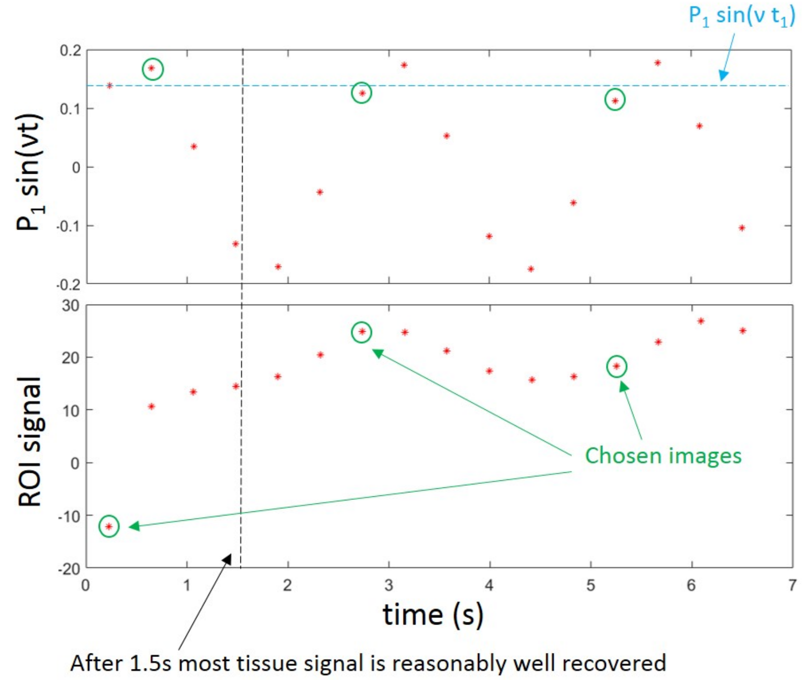

Fig. 5.8 A worked example of how the algorithm chooses images which are well aligned with image 1, and which occur later in the signal recovery curve. For this set of images, the images with the closest $P_1 sin(vt)$ to image 1 (see dashed line) are images 7, 2 and 13. However image 2 occurs within the threshold of 1.5s and is not selected. Images 7 and 13 are selected to input into the synthetic image creation.

5.3.2 Subjects

9 healthy volunteers (7/9 male, mean age 30.6±4.4 years) with no history of interstitial lung disease, were recruited as subjects to test 2D Look-Locker T_1 mapping during both inspiration breath hold and free breathing. 7/9 healthy volunteers underwent additional sequences of expiration breath hold and 4/9 underwent addition free breathing sequences whilst breathing 100% oxygen at 15L/min for 2 minutes prior to imaging to establish further whether there is an effect of O_2 inspiration upon T_1 during free breathing.

3/9 volunteers underwent additional axial plane 2D Look-Locker imaging during both inspiration and expiration to evaluate if gravitational effects are evident to lung T_1. Free breathing axial slices were not undertaken, due to the large amount of out of plane motion observed due to respiration in the axial slice. The same three volunteers underwent Look-Locker imaging with images acquired over a 10 minute period with 100% oxygen administered for the first 5 minutes and turned off for the second 5 minutes to assess the wash in and out of oxygen with time. This was performed in both inspiration breath hold and free breathing for two volunteers, and only during free breathing for the third volunteer.

11 adult patients with IPF were also recruited from a specialist interstitial lung disease clinic. Patients were excluded from the study if: they had a resting oxygen saturation below 90%; were pregnant; were on immunosuppressive treatment (not including N-acetylcysteine or prednisolone at a dose less than or equal to 20mg/day); had stage 4 or 5 chronic kidney disease; were unable to lie supine for 60 minutes; had severe coronary artery disease or angina not fully controlled by medication; had significant congestive heart failure; an allergy to gadolinium contrast; had a significant co-morbidity likely to reduce life expectancy to less than one year or had significant congestive heart failure. All IPF patients underwent 2D Look-Locker imaging in inspiration breath hold and free breathing, with the slice positioned through the descending aorta.

5.3.3 Image acquisition

A whole body, 1.5 T GE HDx scanner (GE Healthcare, Waukesha, WI) and 8-channel cardiac coil were used for Look-Locker image acquisition. Patients were positioned supine and 2D images were acquired in a coronal plane through the descending aorta. The Look-Locker sequences comprises a 180 degree inversion pulse followed by 16 gradient echo images [22] (see Figure 2.15). Imaging parameters were as follows: Inversion time (TI):

229ms; TR=3.2ms; α=7; phase x frequency: 128 x 128; slice thickness: 15mm. Breathing instructions for free breathing acquisition were to breath normally.

5.3.4 Oxygen administration

100% oxygen was administered at a flow rate of 15L/min for two minutes prior to imaging, unless otherwise specified. A simple face mask with low-flow delivery was used for oxygen delivery on the free breathing and breath held image acquisitions for 2 minutes. For image acquisitions while breathing oxygen for 5 minutes to observe the wash-in of oxygen, a non-rebreather mask was used at a flow rate of 15L/min.

5.3.5 Quantifying the efficacy of registration

Registration efficacy in free breathing lung Look-Locker images was measured using DSC to measure global lung registration, as described in Chapter 3.3.1.

Fig. 5.9 Example of segmented lungs. Guide lines are given from the upper diaphragm of the first segmented image.

The DSC was calculated for each set of segmented lung data, see Figure 5.9, pre-registration and after applying the corresponding registration maps. All images were also inspected visually as a video looping over time by an MR physicist with 4 years experience, to ensure that blood vessels and other prominent anatomical lung features were consistently aligned before calculating the lung T_1.

5.3.6 Analysis and statistics

As discussed in section 5.3.1, the acquired images will have a slight T_2 weighting due to the effect of respiration. For this chapter any changes in T_2 and T_2* with time have been assumed to be negligible compared to the change in signal from inversion recovery, and all image-processing was performed as described in Chapter 3, using custom functions written in Matlab 2016b. No images were cropped or segmented. Matlab-based non-rigid registration toolkit ShIRT [42], which was described in section 3.3.2, was integrated into the custom Matlab voxel-wise T_1 mapping algorithm for both the initial and final registrations. All computation was performed on a 64 bit Windows 10 workstation with 16GB RAM and 4 X Intel® Core™ 3.6GHz processors.

Pixel-wise T_1 maps were calculated using equations (2.26) and (2.27) and T_1 values in the lung were measured by drawing regions of interest in the entire right and left lung of the T_1 maps and calculating the mean lung T_1. T_1 of the upper and lower lung was also calculated by placing regions of interest in the upper and lower left lung. Pixel-wise standard deviation of T_1s within each lung was also measured.

Axial T_1 maps were segmented into five segments divided evenly (by eye) from anterior to posterior and mean T_1 was calculated for each segment and presented in a scatter plot. For dynamic T_1 maps mean lung T_1 was presented on a scatter plot against time.

For lung T_1 acquisitions acquired over 5 minutes of breathing 100% O_2 and 5 minutes of breathing air, mean lung T_1 from each T_1 map was plotted against time for each volunteer.

Statistical analysis was performed using SPSS 21 (SPSS, Chicago, IL). Data is presented as mean ± standard deviation. DSC before and after registration were compared using a paired t-test. T_1 values in the same region, but calculated using the two different methods described, were compared using a paired t-test. Tests for differences between T_1 values in different respiratory states were calculated using a paired t-test. Group T_1 differences were calculated using an independent t-test or an ANOVA, depending on whether two or more variables were being compared.

5.4 Results

5.4.0.1 Efficacy of registration in Look-Locker images

Image registration significantly increased overall DSC in free breathing datasets (p<0.001 for all subjects; p=0.001 volunteers only; p=0.016 patients only), see Table 5.1. When inspected visually as a video looping over time, blood vessels and lung features appeared consistently aligned post-registration in all image datasets. An example is shown in Figure 5.10.

Table 5.1 Mean lung T_1 and DSC values. The standard deviation given is the standard deviation of T_1s within both lungs. † indicates a significant improvement in DSC.

Respiratory state	N	DSC unregistered	DSC registered	T1 (ms)	Standard deviation (ms)
Healthy volunteers					
Free breathing	9	0.90±0.06	0.93±0.05†	1145±94	217
Inspiration	9	0.94±0.04	0.94±0.04	1097±53	253
Expiration	7	0.95±0.04	0.95±0.03	1179±93	200
Free breathing with oxygen	4	0.86±0.04†	0.88±0.03	1189±94	200
Patients with IPF					
Free breathing	11	0.90±0.065	0.91±0.04†	1061±59	264
Inspiration	11	0.91±0.04	0.92±0.04	1040±61	297

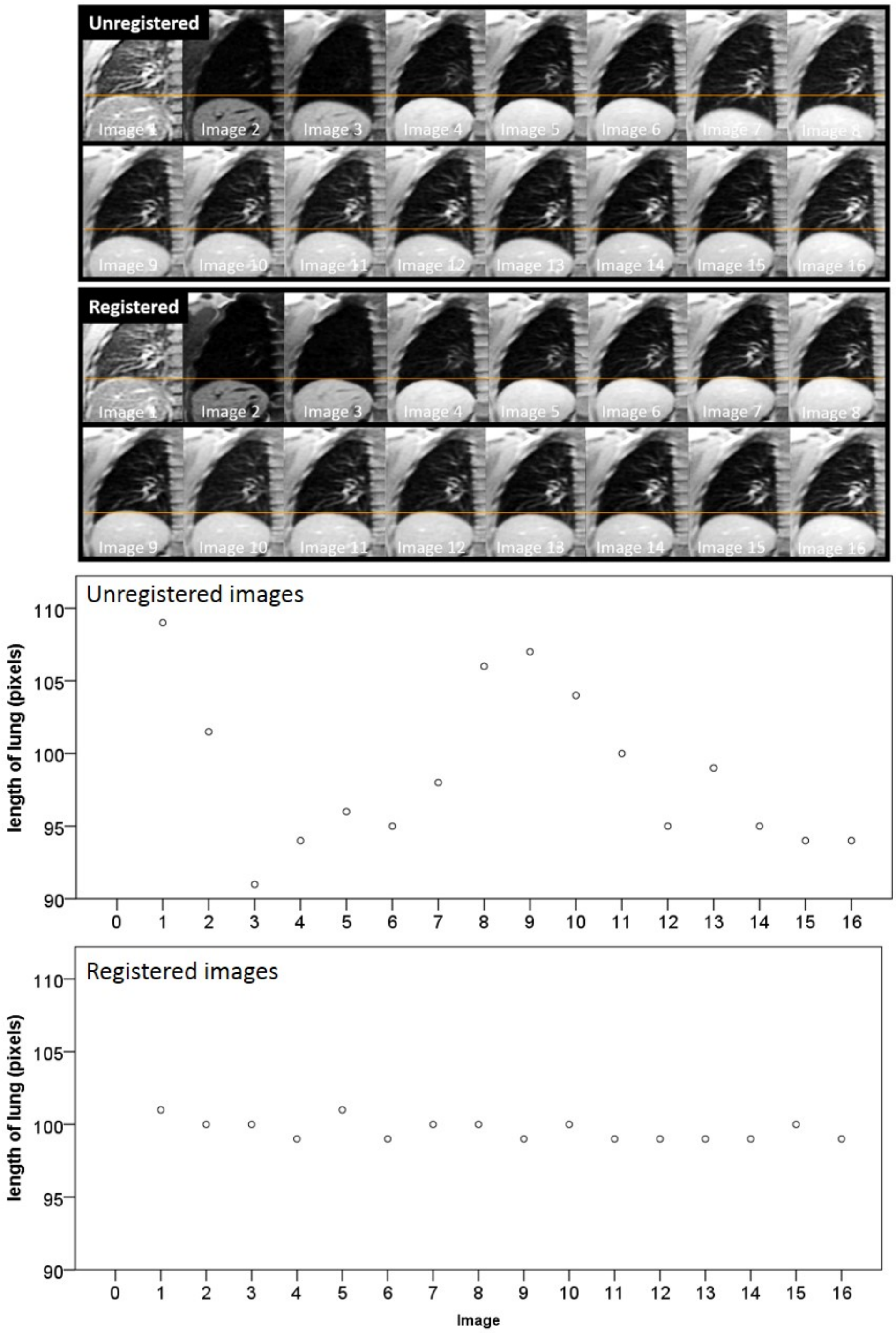

Fig. 5.10 Example of a Look-Locker dataset before and after image registration, cropped to the right lung after registration. An orange line is drawn at the diaphragm on the first image to demonstrate diaphragm motion.

DSC did not change significantly after registration in breath hold images (p=0.184 for all subjects; p=0.306 for volunteers; p=0.212 for patients). Post-registration, free breathing and breath hold images showed no significant difference in DSC (p=0.486 for all subjects; p=0.477 volunteers only; p=0.748 patients only).

5.4.0.2 Lung T_1 maps in healthy volunteers

Examples of T_1 maps in healthy volunteers are shown in Figure 5.11 and mean T_1 values are given in Table 5.1 and Figure 5.12. In healthy volunteers, inspiration breath hold T_1 was significantly lower than free breathing T_1 (p=0.031) and expiration T_1 (p=0.040). Expiration T_1 and free breathing T_1 were not significantly different (p=0.080).

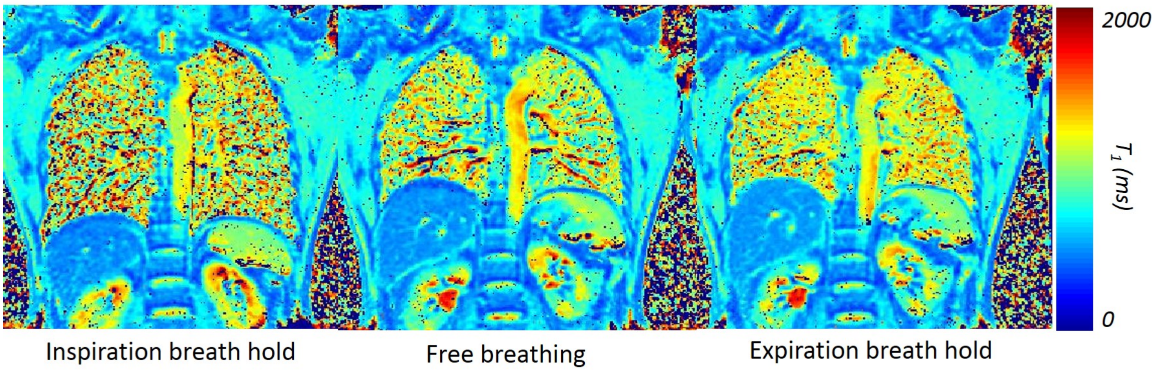

Fig. 5.11 Example T_1 maps from acquisitions made during inspiration, free breathing and expiration for a healthy volunteer.

The standard deviation of T_1 values within the lung was not significantly different in inspiration when compared to free breathing in volunteers (p=0.189).

Although the results in Table 5.1 do not show a lower in oxygen enhanced free breathing T_1, when only the sub-set of patients (n=4) who underwent both free breathing during air and free breathing during 100% oxygen were considered (n=4), lung T_1 was significantly lowered during oxygen enhanced free breathing (air: T_1=1180±30ms; 100%O_2: T_1=1120±90ms; p=0.012), see Figure 5.13.

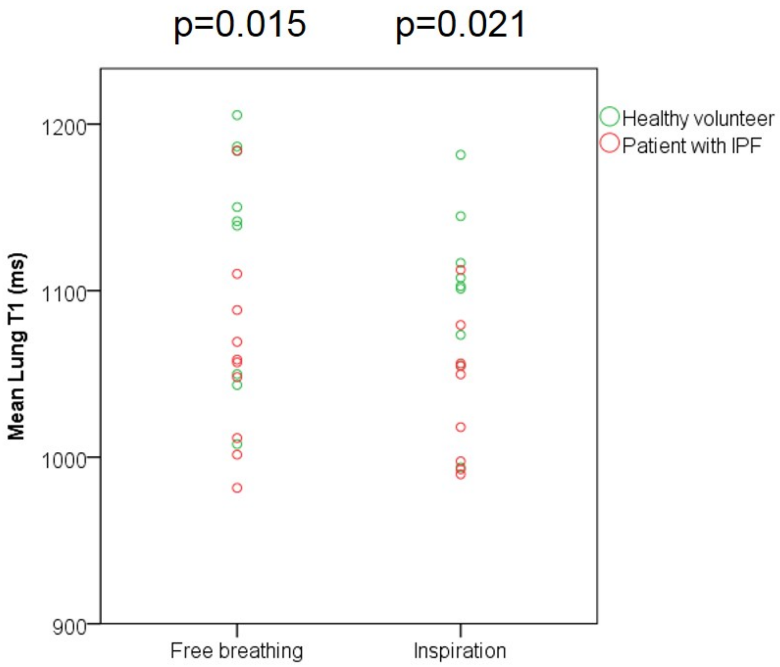

Fig. 5.12 Lung T_1 acquired during free breathing and inspiration breath hold in patients with IPF (green) and healthy volunteers (blue). P values are shown for differences in mean lung T_1 between patients with IPF and healthy volunteers.

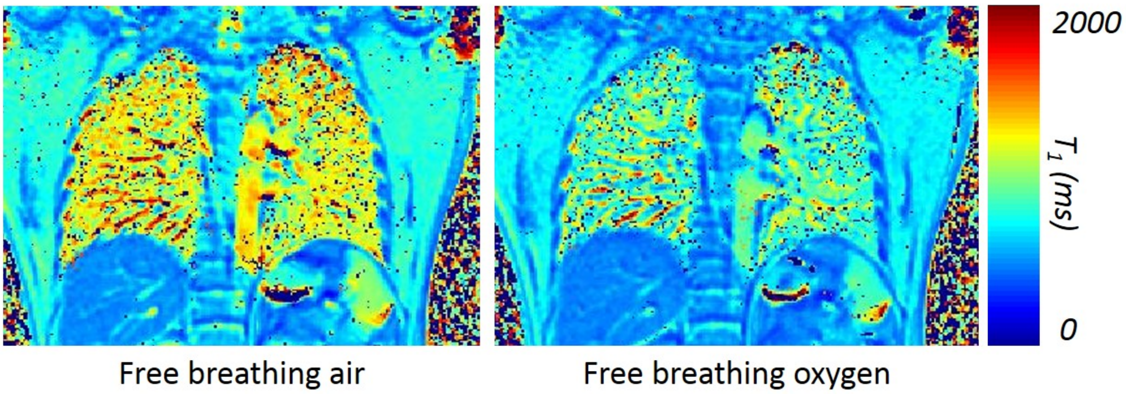

Fig. 5.13 Examples T_1 maps in a healthy volunteer during free breathing air and with oxygen enhancement.

Inspiration lung T_1 was found to have a range from anterior to posterior of 141ms, 87ms and 309ms in each volunteer. Expiration lung T_1 was found to have a range from anterior to posterior was found to have a range of 91ms, 76ms and 128ms in each volunteer. Therefore, in each volunteer, less anterior to posterior variation in T_1 was seen in expiration breath hold compared to inspiration breath hold, see Figure 5.15. In both inspiration and expiration the highest T_1 values were found in the posterior slice. An example is shown in Figure 5.15.

Table 5.2 Mean T_1 for each volunteer from all T_1 maps acquired with and without oxygen, see Figure 5.18.

	Lung T_1 breathing 100%O_2	**Lung T_1 breathing air**	**p value**
Breath hold			
Volunteer 1	1040±18	1120±18	p<0.001
Volunteer 2	1030±28	1100±18	p=0.038
Combined	1030±45	1110±30	p<0.001
Free Breathing			
Volunteer 1	1090±30	1160±40	p=0.004
Volunteer 2	1020±70	1100±90	p=0.085
Volunteer 3	1180±90	1141±30	p=0.386
Combined	1140±70	1150±80	0.020

Three volunteers underwent Look-Locker T_1 mapping over time, where oxygen was administered for 3-5 minutes and turned off for 3-5 minutes. The mean lung T_1 was signifi-

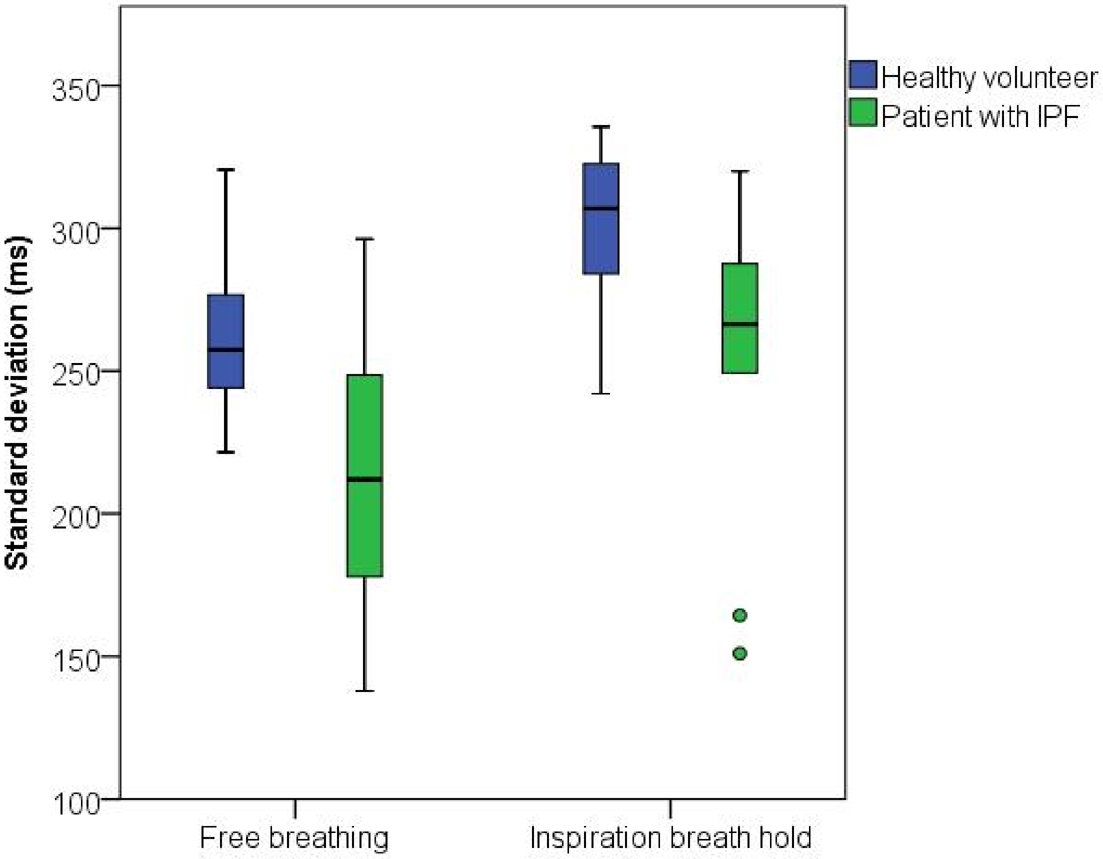

Fig. 5.14 Standard deviation of lung T_1 in free breathing and breath hold, in patients with IPF and healthy volunteers.

cantly lower when breathing 100% oxygen both during acquisition during breath hold and acquisition during free breathing, see Figures 5.17, 5.18 and Table 5.2.

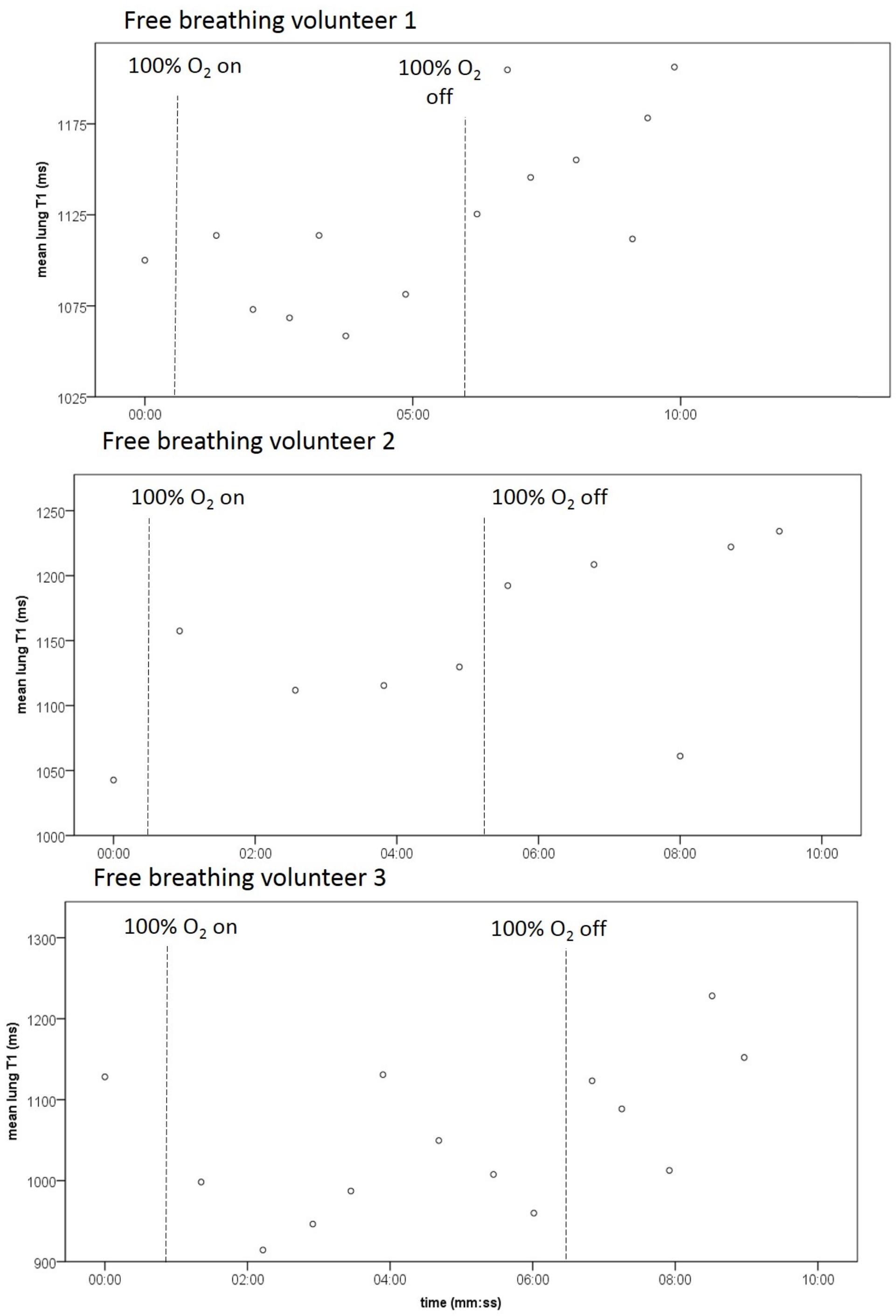

Fig. 5.17 Three volunteers underwent Look-Locker T_1 mapping over time, where oxygen was administered for 3-5 minutes and turned off for 3-5 minutes. Acquisition occurred during free breathing.

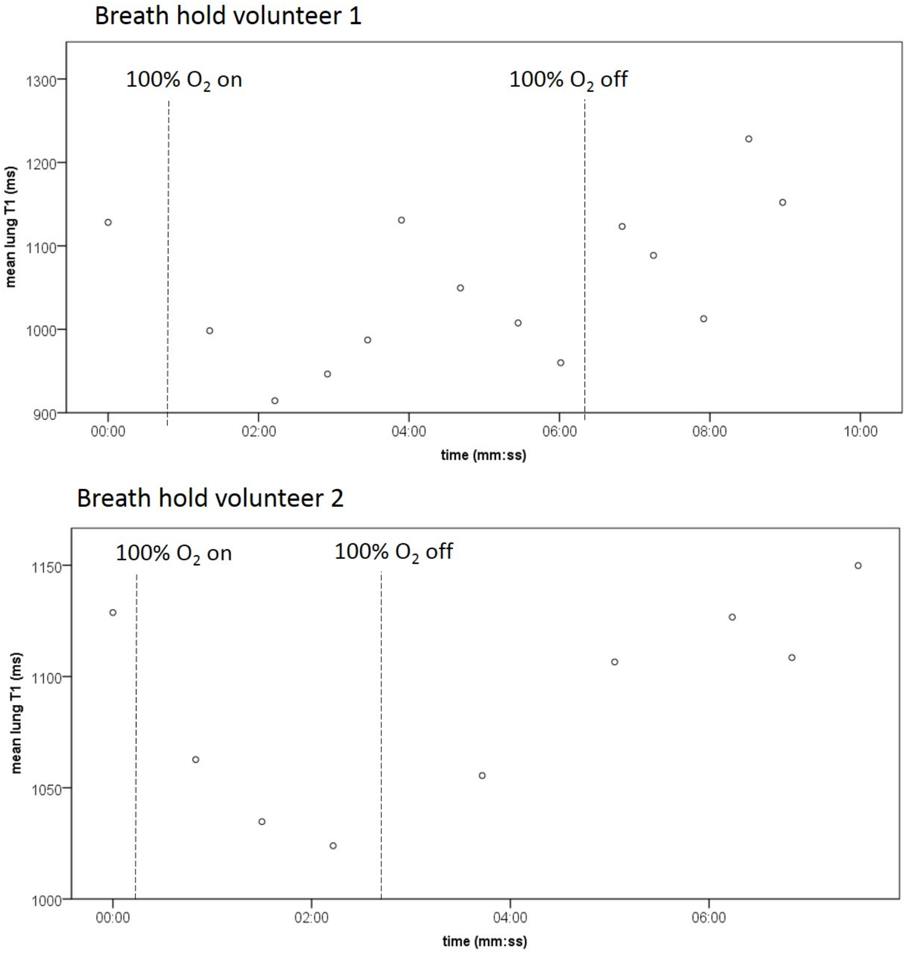

Fig. 5.18 Two volunteers underwent Look-Locker T_1 mapping over time, where oxygen was administered for 3-5 minutes and turned off for 3-5 minutes. Acquisition occurred during breath hold.

Maps of ΔT_1 were created by subtracting T_1 maps acquired during inhalation of 100% O_2 from T_1 maps acquired during breathing room air. The maps show a homogeneous distribution of oxygen enhancement which was expected for healthy volunteers.

5.4.0.3 Lung T1 maps in patients with IPF

Examples of T_1 maps in patients with IPF are shown in Figure 5.19. Lung T_1 was found to be significantly lower in patients with IPF when compared to healthy volunteers during free breathing (p=0.015) and during breath hold (p=0.021). Unlike in healthy volunteers, there was no significant difference between inspiration and free breathing lung T_1 values in patients with IPF (p=0.366), see Figure 5.12.

Table 5.3 Mean lung T_1 values in the upper and lower lung, † indicates p<0.005.

Respiratory state	**Upper Lung T_1 (ms)**	**Lower Lung T_1 (ms)**	**p value**
Healthy volunteers			
Free breathing	1099±139	1097±131	p=0.803
Inspiration	1109±62	1093±54	p=0.041†
Combined	1103±106	1095±99	p=0.082
Patients with IPF			
Free breathing	1073±68	1040±68	p=0.011†
Inspiration	1043±34	1029±41	p=0.182
Combined	1072±52	1044±54	p=0.002†

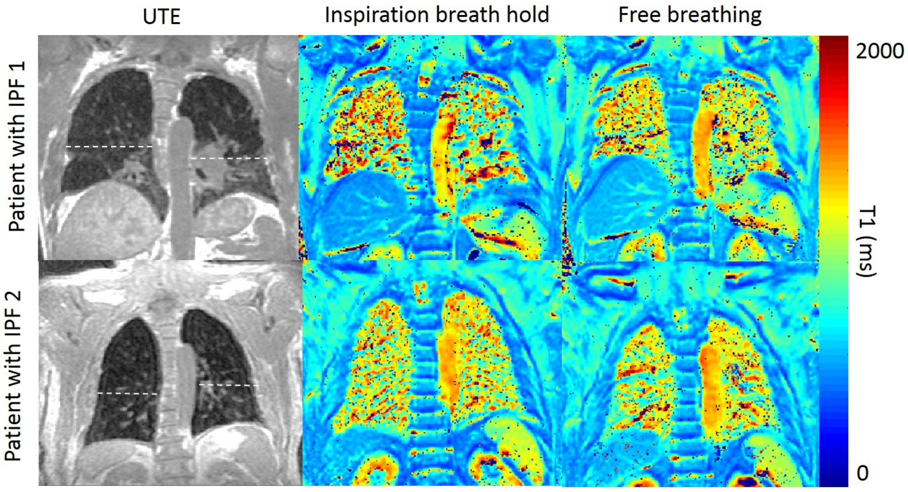

Fig. 5.19 Example T_1 maps from patients with IPF in inspiration and free breathing, with lung division into upper and lower lung shown on the two example UTE images.

The standard deviation of T_1 values within the lung was higher in patients when compared to healthy volunteers (inspiration: p=0.068; free breathing: p=0.021; both: p<0.001). A simple way of evaluating lung heterogeneity is whether there is a significant T_1 difference in the upper lung compared to the lower lung in each patient, due to the basal prevalence of fibrosis in IPF. During free breathing there was not a significant difference between upper and lower lung T_1 in healthy volunteers (p=0.803), however there was in patients with IPF (p=0.011), see Table 5.3. However, during breath hold healthy volunteers did have a significant difference between the upper and lower lungs (p=0.041) whereas patients did not have a significant difference between upper and lower lung (p=0.076). When data was combined, a paired t-test of data from both breath hold and free breathing acquisition showed patients with IPF had a significantly lower T_1 in the lower lung (p=0.002) whereas healthy volunteers did not (p=0.082), see Figure 5.20.

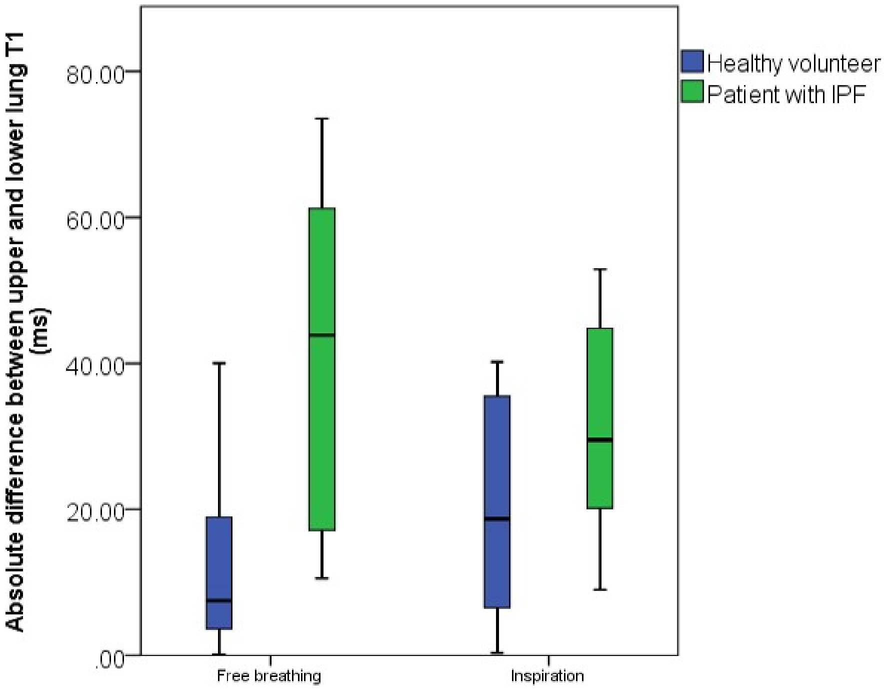

Fig. 5.20 The absolute value of the T_1 difference between upper and lower lung in free breathing and breath hold acquisitions.

5.5 Discussion

Free breathing lung T_1 mapping constituent images were significantly more aligned after registration, and there was no significant difference in alignment as measured by DSC between breath hold images and free breathing images post image registration. The method described successfully registers free breathing Look-Locker images onto a single spatial frame to allow pixel-by-pixel T_1 mapping of the lung in volunteers and patients with IPF. Mean T_1 values during inspiration in healthy volunteers were 1097±53 ms which is consistent with the results shown from a normal mean lung T_1 values at 1.5T of 1196±152ms [39].

The results in inspiration and expiration are consistent with published literature on the effect of respiratory state on lung T_1 in both healthy volunteers [51] and patients with IPF [84] [107], with expiration breath hold yielding a significantly higher T_1. The effects of breathing 100% oxygen during imaging are consistent with breath-hold data, which show a reduction in lung T_1, the free breathing data resulted in a reduction of lung T_1 by 6% compared to meta-analysis results of around 10±2.5% [39].

The range of T_1 values in the lung of healthy volunteers was found to be smaller during expiration, with higher T_1 in the posterior lung. This is consistent with previous findings which found a statistically significant T_1 variation from anterior to posterior lung in 10 healthy volunteers in inspiration, with higher T_1 found in the posterior lung [51] . This variation is consistent with an increase in fractional volume of blood towards the posterior lung due to gravitation effects. This emphasises the importance of consistency in slice choice in 2D lung T_1 mapping, as well as the potential benefits of further work into 3D lung T_1 mapping to improve anatomical specificity in future studies.

The mean lung T_1 of healthy volunteers measured with a free breathing approach was in-between the mean lung T_1 calculated during inspiration and expiration, which may suggest that the predominant mechanism causing lung T_1 changes in different respiratory states is the relative fractional volume of lung components (i.e. tissue, blood, parenchyma, air) leading to a changed apparent T_1, rather than oxygenation affects. In particular, as expiration causes an increase in pulmonary perfusion of up to twice the perfusion levels in inspiration [52], it may be that increase of the content of blood in the lungs during expiration results in a larger contribution to measured T_1 from blood resulting in an increased overall T_1. However, it is also possible that deoxygenation effects due to breath hold are also present but which are to some extent negated by the increase in fractional blood content. When free breathing with 100% oxygen the overall lung T_1 was found to lower, which is consistent with literature, due to the increased presence of dissolved paramagnetic oxygen in the pulmonary blood and tissue.

As has been previously observed that the mean lung T_1 of patients with IPF is lower than that found in healthy volunteers. In addition, during free breathing, patients with IPF were found to have a lower lung T_1. It is not possible from this work to identify whether the changes seen are due to oxygenation, perfusion or lung tissue differences between patients with IPF and healthy volunteers - as it is known all three variables can affect measured T_1. However, our results show a lower T_1 in patients with IPF and a decrease in oxygen dissolved in the blood would result in a higher T_1, and therefore it is unlikely to be a significant factor in changes in lung T_1 in these patients.

Tissue changes in patients with IPF cause heterogeneity in the lung, resulting in both heterogeneity in the tissue itself as well as heterogeneity in the ability for oxygen to dissolve into the blood in these areas. This was evaluated by comparing the standard deviation of lung T_1 values within the lung, and regional differences in the upper and lower T_1. Our results showed a higher standard deviation of T_1 within the lung in IPF, and an overall significant difference between the upper and lower lungs in patients with IPF.

Lung T_1 was significantly lowered in healthy volunteers when breathing 100% O_2 both during breath hold imaging and during free breathing. This confirms that a free breathing approach could be used during oxygen enhanced T_1 mapping to demonstrate regions where oxygen is absorbed into the blood within the lung, acting as a measure of combined ventilation and perfusion [17]. Although T_1 significantly decreased when oxygen was administered, the graphs of T_1 changes over time were not able to produce wash-in and wash-out times as seen in the work of Arnold et al., [17]. There are two likely causes for the large range of T_1 values seen: i) a conventional Look-Locker imaging sequence was used rather than a sequence with a shorter acquisition, which limited the rate of T_1 map acquisition, therefore not enough data was acquired to establish a clear pattern; ii) the type of oxygen delivery mask used is know to significantly affect the interindividual variation of lung T_1 when oxygen is administered. For this work a nontight face mask was used which has been found to yield higher variation in lung T_1 than a closed air-cushion faced mask (a "full closed face mask") [108]. In order to establish whether the potential outliers seen in Figure 5.17 are due to a physiological affect this work would need to be repeated with a closed air-cushion faced mask to remove intersubject variability.

The key limitation of this work is that the phase shift was not included in the respiratory model. Further work using the model described in equation is expected to improve the respiratory model and therefore potentially improve image registration further. Nonetheless, the results in this work show that incorporating a sinusoidal component to curve fitting allows images of similar respiratory state to be selected and used for synthetic images, resulting in significant improved image registration. In addition it is that it assumed there was no T_2 or T_2* weighting in the Look-Locker images during acquisition due to respiration. A previous study finds a variation in T_2 with respiration, with a linear relationship between respiratory state and time. It would be of interest to future work to explore whether post-processing can account for and quantify this additional parameter which influences signal in the lungs.

In addition, it is a limitation of this work that scan-scan repeatability of free breathing acquisition of the Look-Locker sequence has not been compared across breath hold manoeuvres (inspiration and expiration) and free breathing. It would be of interest to compare these methods for scan-scan repeatability in healthy volunteers prior to further work.

Furthermore, neither expiratory lung T_1 maps or oxygen enhanced T_1 maps were acquired in patients with IPF. It would be of interest to acquire this data in the future to establish how expiratory lung T_1 maps compare to free breathing lung T_1 maps in terms of differentiating patients with IPF from healthy subjects, in particular it may be that the increased blood content in the lungs results in easier identification of fibrotic tissue in the lung due to the difference in T_1 between the two components. In addition, the use of oxygen enhanced free breathing T_1 maps may show regions of poor ventilation and/or perfusion in patients with IPF.

5.6 Conclusions

Free breathing lung T_1 mapping using post-processing image registration to synthetic images created using a model of respiratory motion modulation of lung tissue signal is feasible and produces robust registration. Free breathing lung T_1 is significantly higher than breath hold T_1 in healthy volunteers, and is not significantly different to breath hold T_1 in patients with IPF. Free breathing lung T_1 was found to be significantly lower in patients with IPF compared to healthy volunteers, and patients with IPF showed a greater degree of lung heterogeneity. Free breathing lung T_1 mapping with and without admission of 100% oxygen may be a fast, comfortable method of detecting lung structure and functional changes in patients with IPF.

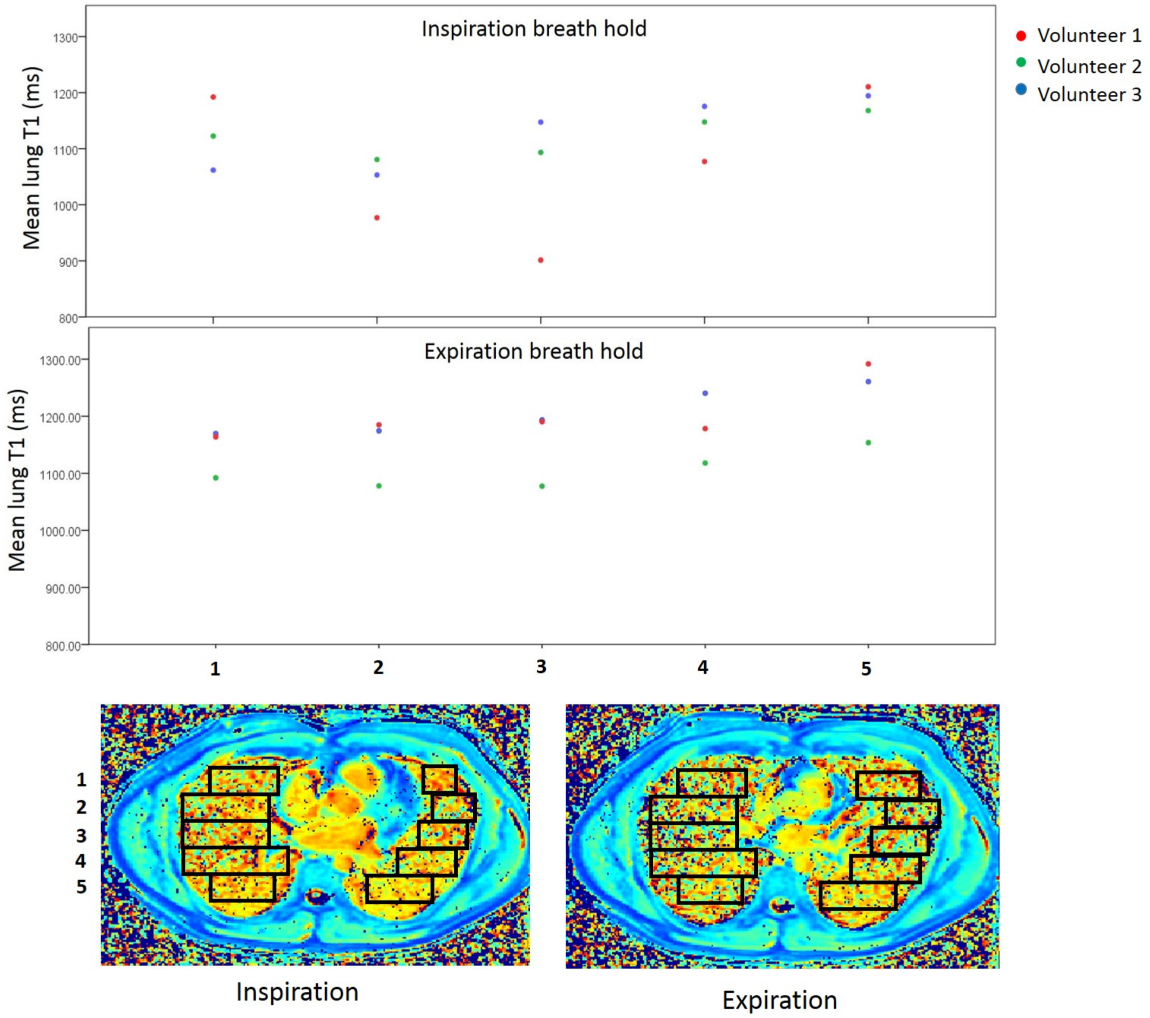

Fig. 5.15 Axial lung T_1 maps in three healthy volunteers were segmented into 5 segments from anterior (1) to posterior (5) (bottom). Mean T_1 from each region was plotted against time for inspiration and expiration breath hold (top).

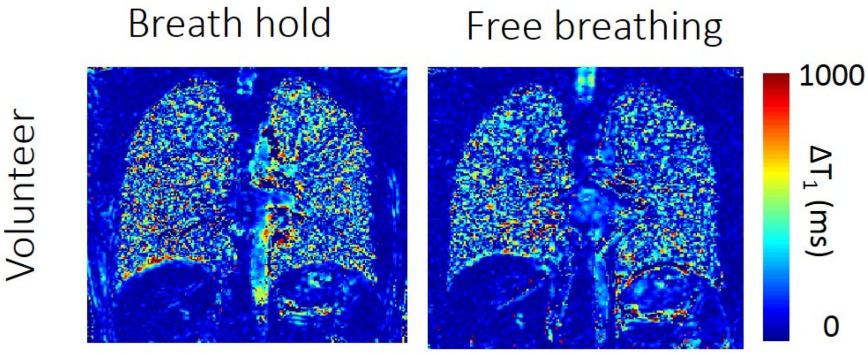

Fig. 5.16 Example maps of T_1 change due to oxygen enhancement. The T_1 map acquired prior to administration of 100% O_2 was subtracted from a T_1 map acquired 2 minutes after inhalation of O_2 in a healthy volunteer, for both breath hold and free breathing acquisitions.

Chapter 6

Image modification of registration technique for free breathing cardiac T1 mapping to incorporate respiratory motion

6.1 Introduction

6.1.1 Motivation for free breathing cardiac T_1 mapping

As discussed in Chapter 3, for patients with cardiac or pulmonary disease, breath holds can be difficult or unachievable with around 40% of some cardiac patient cohorts demonstrating cardiac motion in T_1 mapping imaging acquisitions [5]. A free breathing acquisition would increase the applicability of cardiac T_1 mapping to patient cohorts who experience shortness of breath as well as improve patient comfort. Furthermore, the limitation of sequence duration to that of a comfortable breath hold limits the precision of the calculated T_1 map as it reduces the amount of images acquired and therefore increases the uncertainty of calculated T_1 during curve fitting.

However, the free breathing acquisition alternatives discussed in Chapter 2.2.3 result in an increased acquisition time which may add to patient discomfort and examination cost, and may decrease patient through-put in a clinical imaging setting. The free breathing T_1 mapping method discussed by Weingartner et al., [8] in section 2.2 combined retrospective and prospective respiratory gating and under-sampling resulting in a 9 minute scan time for five 2D images. A similar method using a 1D NAV respiratory gating and the SASHA image acquisition sequence resulted in a 5-10 minute scan time [50] with an average scan time across 12 adult healthy subjects of 6 minutes [109]. Long scan times when using navigators may be further increased in patients with irregular respiratory patterns. In these sequences, the potential to increase T_1 precision by increasing the number of acquired images is lost due to the extended scan-time and inherent inefficiency. These scan times are generally prohibitive for routine cardiac MRI - for example, for pulmonary hypertension patient imaging in Sheffield we intent to fit all images into less than 45 minutes.

Free breathing acquisition using post processing image registration to correct respiratory motion has been performed in inversion recovery imaging for delayed-enhancement imaging of myocardial infarction [110]. The image registration algorithm required user input to define the region of the heart, and registration was applied directly to phase-sensitive inversion recovery images. Similarly, Chow et al [111] used motion correction as a tool for correcting accidental respiratory or cardiac motion in 2D SASHA T_1 mapping images. Chow simultaneously acquired additional high contrast images (to allow an easier image registration) and SASHA images during free breathing. The high contrast images were registered to one another, after which the high contrast image registration parameters were applied to the corresponding SASHA images.

However, although 3D SASHA acquisitions have higher precision than 2D acquisitions, they are still less precise than 2D MOLLI sequences (assessed using standard deviation of myocardial T_1 values) [50]. Therefore, a free breathing 2D MOLLI cardiac T_1 mapping method that uses image registration to compensate for respiratory motion may result in a more precise free breathing cardiac T_1 mapping method than the existing options. Furthermore, a free breathing 2D MOLLI cardiac T_1 mapping method that uses image registration to compensate for respiratory motion would reduce scan time and optimise scan efficiency when compared to free breathing sequences as it would not discard data.

Chapter 3 showed significant improvement in image alignment in MOLLI T_1 mapping images seen with the image registration method proposed, even in patients with considerable respiratory motion. This chapter demonstrates that the method presented in Chapter 3 can be modified for use during free breathing. Furthermore, removing the time restriction imposed by breath hold opens up the possibility for longer sequences, including three dimensional acquisitions, or for more interleaved inversions which could further improve precision of the sequence.

The predominant limitation of applying this method to 2D cardiac imaging is that it does not compensate for out-of-plane motion. The cardiac short axis plane is aligned to each subject's cardiac structure, and therefore its position with respect to the coronal, sagittal and axial planes will vary depending on the individual's anatomy and thoracic motion. Respiratory motion is predominately in the superior-inferior direction, with movement of the heart due to respiration showing an average of 9.1mm of movement in this direction, compared to 1.0mm and 1.4mm movement in the anterior-posterior and left-right directions [112]. A diagram of the short axis plane is shown in Figure 6.1 to illustrate its positioning with respect to the coronal plane. Some out of plane motion is will occur in subjects, with the amount of out-of-plane motion present depending on their anatomy and lung dynamics.

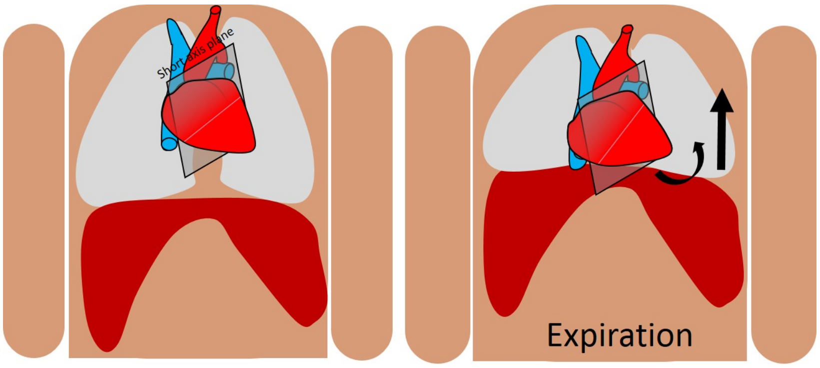

Fig. 6.1 A diagram showing the rough position of a short axis plane with respect to the body. During expiration (right) the cardiac position may move upwards and/or rotate due to the diaphragm position.

6.1.2 Objectives

The objectives of this chapter of work were to carry out preliminary studies with the aim of:

i Modifying the respiratory model based image registration algorithm described in Chapter 5 for use in free breathing T_1 mapping of the heart.

ii Demonstrate and evaluate the effectiveness of this method in volunteers.

iii Investigate whether acquiring images in free breathing effects the resultant myocardial T_1.

iv Investigate the effect of inhaled oxygen on myocardial T_1.

6.2 Method

6.2.1 Model for diaphragm signal changes in free breathing cardiac MOLLI imaging

The same method as described in Chapter 5 for free breathing lung T_1 mapping can be applied to MOLLI imaging, however cardiac T_1 imaging contributes two additional challenges. The first, as previously discussed, is that out-of-plane motion of the heart results in different planes of the myocardium may be being imaged at different time points in the sequence and this remains a challenge that will be addressed and discussed further throughout this chapter. The second challenge is that cardiac gated MOLLI images from different inversion times (t_I) are time-interleaved. Images following three separate inversions are acquired during MOLLI imaging, therefore the time, t, during acquisition and the time post-inversion, t_i, no longer have the same value. Time during the acquisition can be written as:

$$t = t_I + t_i \tag{6.1}$$

Where t is the time, t_I is the time of the inversion pulse and t_i is the time between an acquisition and the inversion pulse, see Figure 6.2.

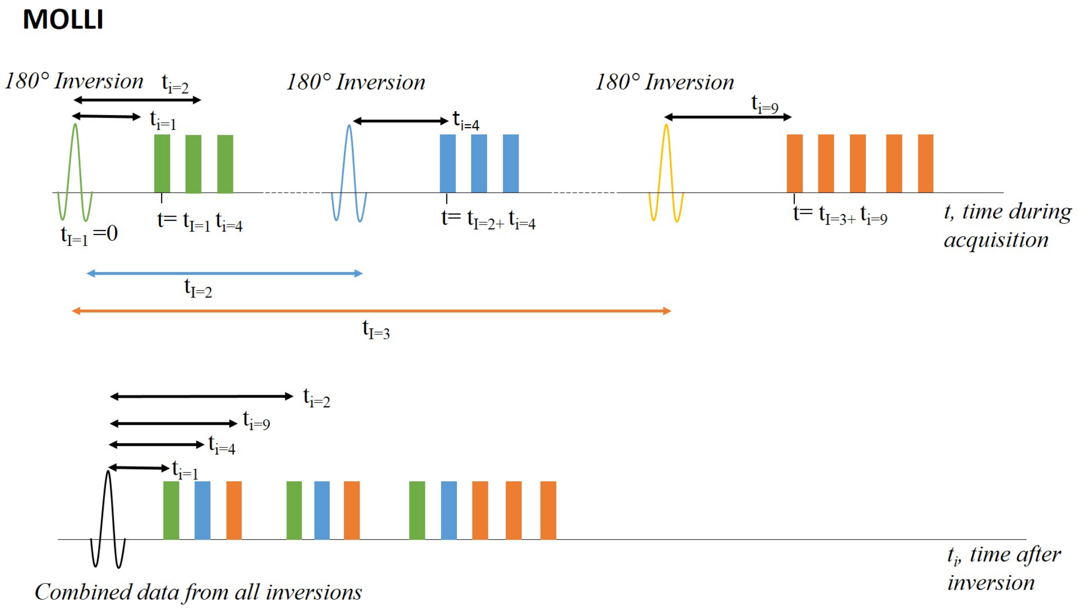

Fig. 6.2 Diagram to show the relationship between t, t_i and t_I where $t_I(1)$ is chosen as 0 for convenience.

A flow diagram showing a summary of the method for automated image registration of free breathing 2D MOLLI images using synthetic images is shown in Figure 6.3. The relevant code and accompanying flow-diagram is shown in appendix A.3.1. Where t is the time during acquisition, t_I is the time between the inversion the acquired image and the first inversion and t_i is the time between image acquisition and the inversion pulse that it follows, see Figure 6.2.

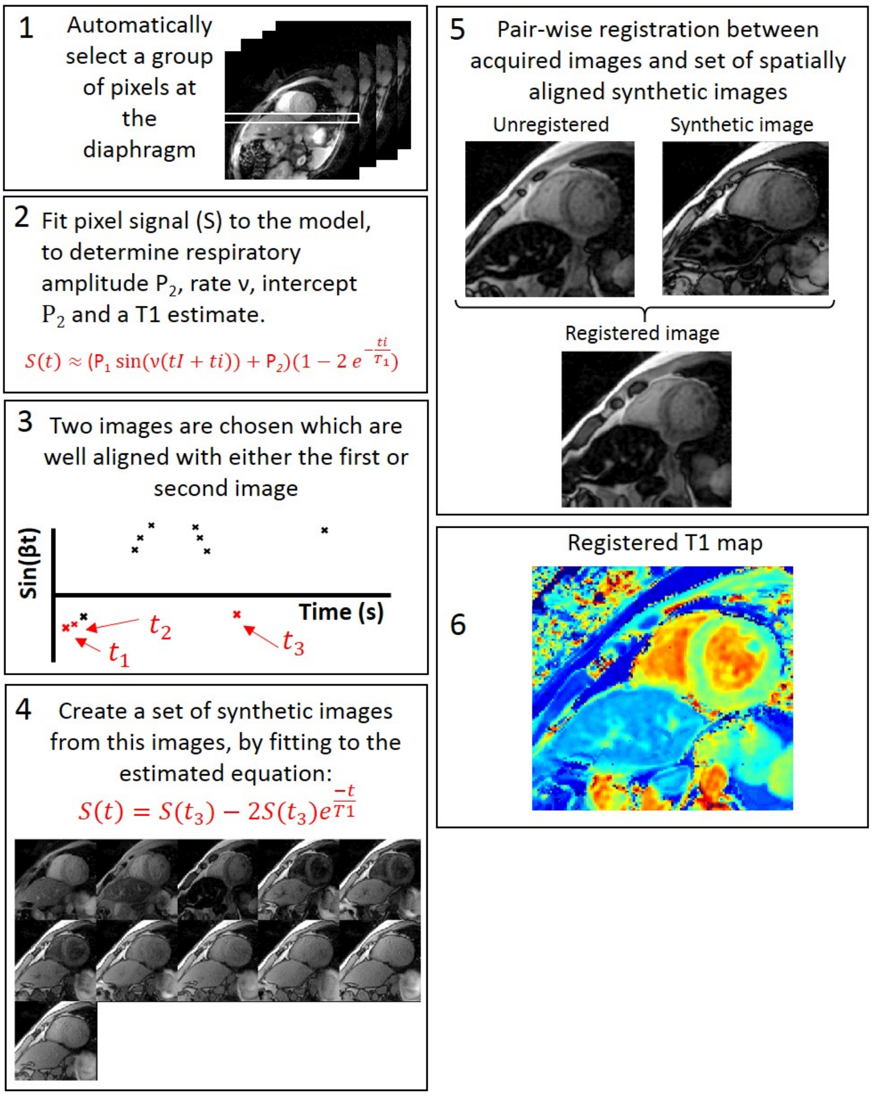

Fig. 6.3 A method diagram for automated image registration of free breathing 2D MOLLI cardiac MR images using synthetic images.

Equation 5.2 can be rewritten as:

$$n_A = \alpha \sin(v(t_I + t_i)) + \kappa_1, n_B = -\beta \sin(v(t_I + t_i)) + \kappa_2 \tag{6.2}$$

The equation (6.4) can be rewritten as:

$$S(t) \approx k\rho_A(\beta \sin(\nu(t_I + t_i)) + \kappa_2)(1 - 2\exp(\frac{-t_i}{T_1 B})) \tag{6.3}$$

Where ν is the respiratory rate, and β and κ_2 are constants. Which, following the reasoning described in Chapter 5 can be approximated as:

$$S(t) \approx (P_1 \sin(\nu(t_I + t_i)) + P_2)(1 - 2\exp(\frac{-t_i}{T_{1B}})) \tag{6.4}$$

With four free parameters to fit to during curve fitting.

t_I has three values - the time at which the three different inversion pulses occur. Rewriting time, t, in this way allows the model to describe the time dependant inversion and respiratory behaviour separately. As with Chapter 5, the images are segmented into horizontal strips of 20 pixels and the segment of the image which is chosen to fit to the respiratory model is described by Figure 6.4. In the case of an image in the short-axis cardiac plane, see Figure 6.5, the central ROIs contain either: liver and lung; myocardium and lung; or liver, myocardium and lung. Therefore tissue B represents either liver, myocardium, or both. Empirically this has not been found to affect image registration and this may be because both tissues still have a much greater density than the lung tissue and both tissues move simultaneously. The algorithm aims to choose a segment whose signal fits the model well and therefore has a low curve fitting residual, but is also appreciably effected by respiratory motion and therefore has a large coefficient P_1, which is likely to be at the diaphragm or the superior myocardium.

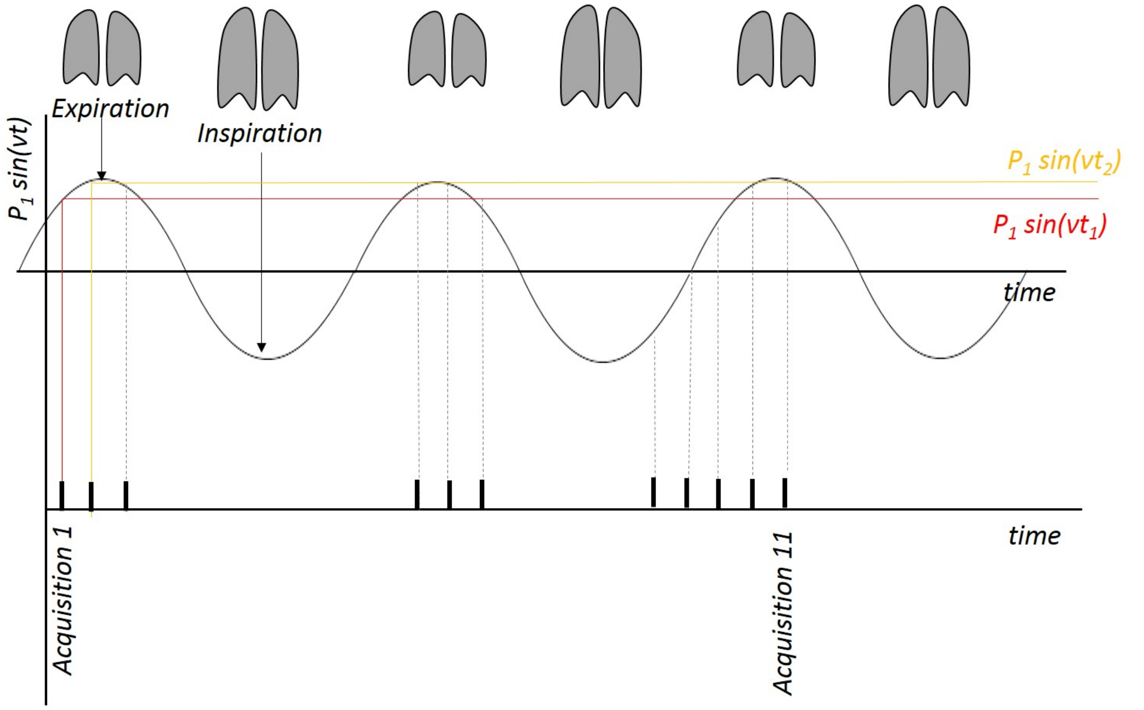

Fig. 6.4 A schematic diagram showing a case where $P_1 sin(\nu t_1)$ results in poorer alignment with images 10 and 11 than $P_1 sin(\nu t_2)$. In this case, using the second image (t_2) as the first input image would result in a better aligned set of input images (i.e. $P_1 sin(\nu t_2) - P_1 sin(\nu t_{11}) < P_1 sin(\nu t_1) - P_1 sin(\nu t_{11})$).

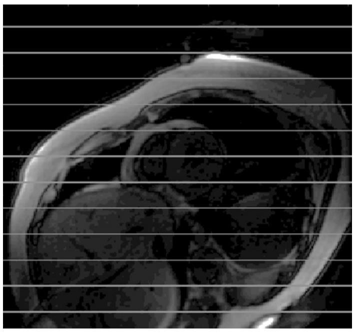

Fig. 6.5 A cardiac short axis plane image segmented into 13 horizontal ROIs.

Curve fitting to equation (6.4) is used to identify three images in the same respiratory spatial state. At least one of these chosen images must occur at $t > 1.5s$ so that it can act as a surrogate for a fully recovered image (S_∞) . However, in some instances there are not two images which are well aligned to the first image. To compensate for this, an additional step is added, where both the first and second image ($t_{i=1}$ and $t_{i=2}$) are evaluated as candidates for the first image to be input into the synthetic image model, and the three images with the lowest residual found during curve fitting are chosen. An example where using the second image as the first input image into the synthetic image model would result in a better aligned set of images to input into the model is shown in Figure 6.4.

Once the model for respiration has identified two images which occur in the same respiratory state as the first image, synthetic images can be created using exactly the same method as described in Chapter 3 for cardiac MOLLI images. Each acquired image is then co-registered to its corresponding synthetic image, as shown in Figure 5.4. The synthetic images will have similar image contrast to the acquired images but are now in an aligned spatial frame.

6.2.1.1 Image and analysis

MOLLI imaging parameters are as described in Chapter 3, with a matrix size of 128 x 128. Registration efficacy in free breathing cardiac MOLLI was measured using DSC in the left ventricle myocardium, as described in Chapter 3. The mean DSC is calculated from the DSC of each segmented image to the first or second image in the series, depending on which image was input into the synthetic image model. In addition, T_1 values were evaluated in two ways: 1) by drawing an appropriate region of interest on each acquired image, calculating the mean signal for each image, and fitting these to an inversion recovery curve to calculate a mean T_1 value; 2) ROIs were drawn on registered T_1 maps to calculate the mean T_1. This was to evaluate whether T_1 values measured on acquired images are consistent with those calculated from registered T_1 maps, to address the possibility that the registration algorithm itself was corrupting T_1 values.

In addition, regions of interest were also drawn onto a region of body fat in each T_1 map, as fat has a relatively sparse capillary bed, and therefore should be less effected by perfusion and oxygenation related T_1 changes resulting from respiration [113].

6.2.2 Subjects

10 healthy volunteers (8/10 male, mean age 29±7 years) were recruited as subjects to test the method. Each volunteer underwent 2D MOLLI both breath hold and free breathing with post-processing motion correction via registration. 4/10 volunteers also underwent 2D MOLLI breath hold acquisition imaging during inhalation of 100% oxygen after a delay of 2 minutes. 3/10 volunteers also underwent 2D MOLLI breath hold imaging during inhalation of 100% oxygen over a period of 6-9 minutes.

6.2.3 Oxygen administration

100% oxygen was administered at a flow rate of 15L/min for two minutes prior to imaging, unless otherwise specified. A simple face mask with low-flow delivery was used for oxygen delivery on the free breathing and breath held image acquisitions for 2 minutes. For image acquisitions while breathing oxygen for 6-9 minutes to observe the wash-in of oxygen, a non-re-breather mask was used at a flow rate of 15L/min.

6.3 Results

6.3.0.1 Efficacy of registration in free breathing MOLLI images

DSC significantly increased, (p<0.001) see Figure 6.7 and Table 6.1. Image registration improved in all patients, with an unregistered DSC range of 0.55-0.75 and a registered DSC range of 0.60-0.78. An example of registered free breathing images can be seen in Figure 6.8.

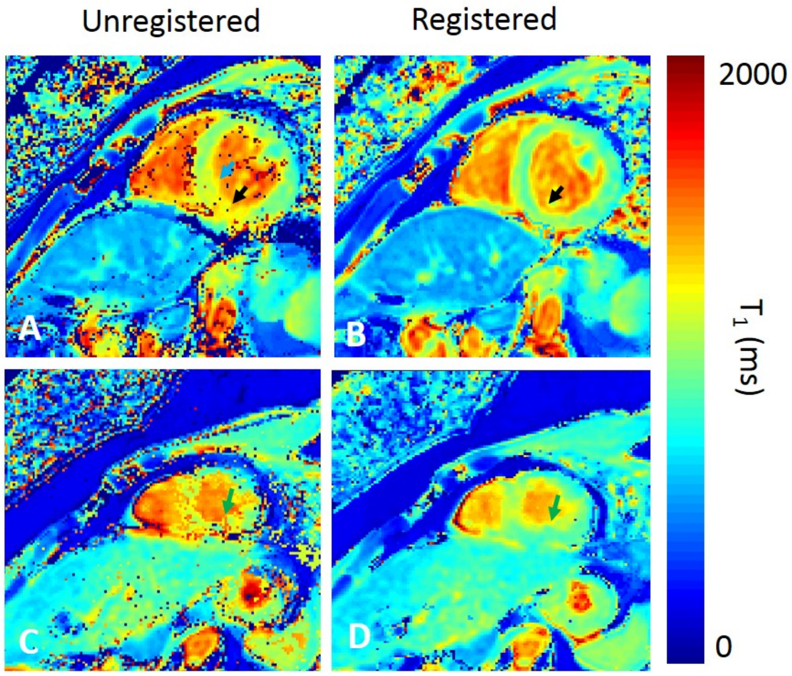

Fig. 6.6 Mean DSC from all images, calculated with respect to the first image, before and after image registration in free breathing healthy volunteers, DSC is significantly increased post registration $p<0.001$.

Examples of free breathing T_1 maps without image registration and with image registration are shown in Figure 6.6. The figure demonstrates the kinds of erroneous T_1 values you may see due to motion in MOLLI images.

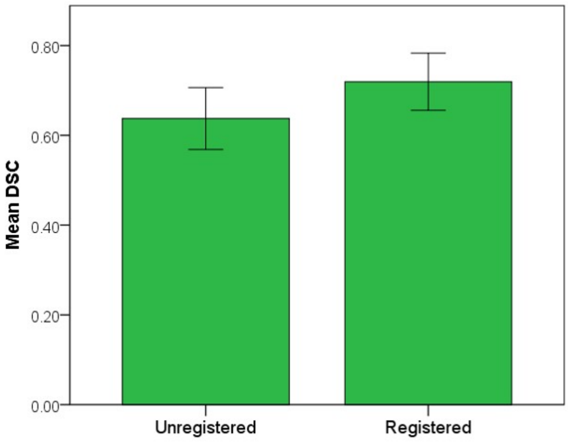

Fig. 6.7 T_1 maps before and after image registration to illustrate the improvement in T_1 maps after image registration are shown. A) Unregistered T_1 map from a free breathing healthy volunteer. Blue and black arrows indicate regions of error in the myocardium. Whereas the erroneous value in the pixel shown by the blue arrow may be easily identified, the area shown by the black arrow may be misidentified as elevated myocardial T_1. B) The registered version of the T_1 map shown in A. Black arrow shows area of erroneous T_1 in A now corrected. C) Unregistered T_1 map from a free breathing healthy volunteer. Green arrows show areas of erroneous T_1 values in the myocardium. D) The registered version of the T_1 map shown in C. Green arrow shows area of erroneous T_1 in A now corrected.

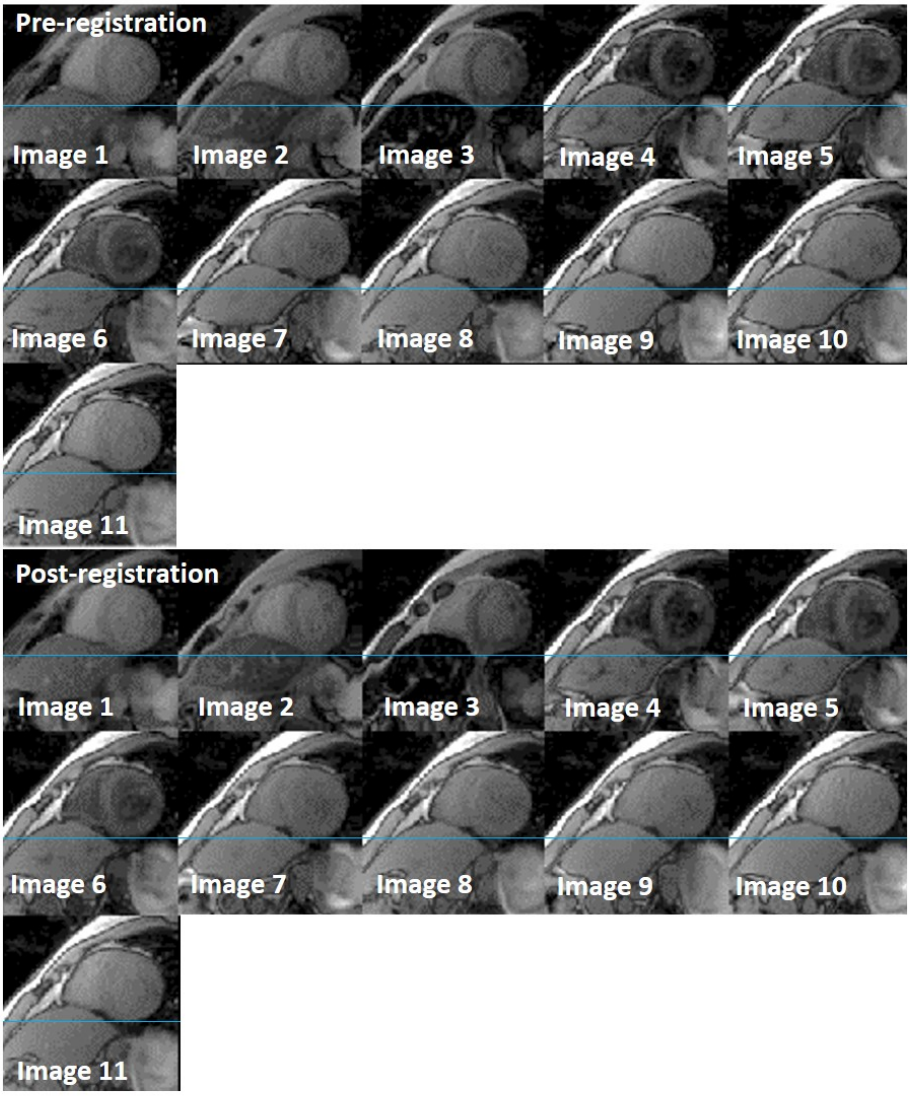

Fig. 6.8 Example cardiac MOLLI images before and after image registration, a blue line is added for reference and aligns with the bottom of the myocardium in the first image for each dataset.

Table 6.1 DSC (mean from all time points) before and after image registration.

	Unregistered DSC	**Registered DSC**	**paired t-test**
Free breathing	0.64±0.07	0.72±0.04	p<0.001
Breath hold	0.77±0.04	-	-

6.3.0.2 Effect of respiration on overall myocardial T1

In breath hold, myocardial septal T_1 was significantly lower than in free breathing (p=0.002), although LV blood T_1 was higher in free breathing it was not significantly so, see Table 6.3, Figure 6.9.

Table 6.2 Consistency of myocardial T_1 when measured directly from images and from registered T_1 maps.

	T_1 from images (ms)	**T_1 from T_1 maps (ms)**	**p-value**
Breath hold	930±45	940±50ms	p=0.142
Free breathing	1100±100ms	1000±90ms	p=0.534

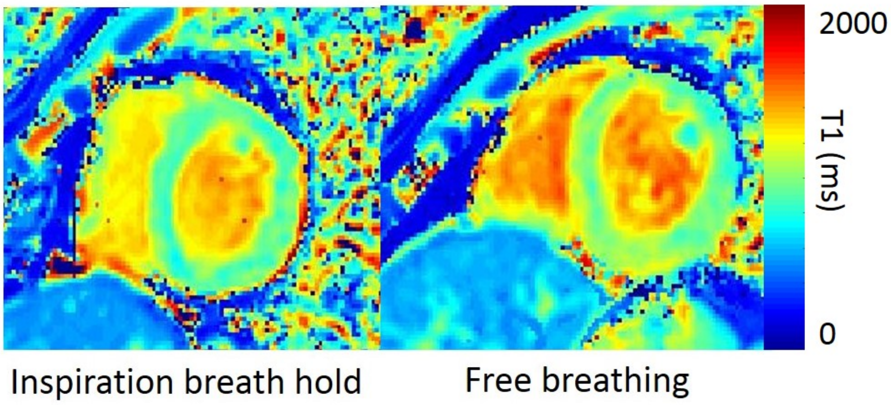

Fig. 6.9 An example of a T_1 map acquired during inspiration breath hold and acquired during free breathing with image registration using a respiratory model in a healthy volunteer.

There are no significant differences between myocardial septal T_1 values measured from registered T_1 maps compared to myocardial septal T_1 values measured from mean signal calculated from individual regions of interest drawn on MOLLI images, see Table 6.2.

Table 6.3 Effect of respiration on overall myocardial T_1

	Septal T_1(ms)	**LV blood T_1 (ms)**	**RV blood T_1 (ms)**	**Fat tissue T_1 (ms)**
Breath hold	910±120	1400±100	1400±75	200±32
Free breathing	990±160	1500±140	1500±134	200±25
Paired t-test	p=0.02**	p=0.156	p=0.212	p=0.846

6.3.0.3 Effect of respiration of 100% O_2 on overall myocardial T1

Myocardial and LV blood pool was significantly lower post inhalation of 100% O_2 during free breathing acquisitions, but there were no significant differences in the myocardium or blood pool during breath held acquisition.

Table 6.4 Effect of respiration of 100% O_2 for 2 minutes prior to acquisition of images on overall myocardial T_1. T_1 data was analysed from 8 of the volunteers, 4 of whom underwent T_1 acquisition before and after inhalation of 100% O_2 for 2 minutes with free breathing acquisitions and 4 of whom underwent T_1 acquisition before and after inhalation of 100% O_2 for 2 minutes with breath hold acquisitions.

	Myocardial septal T_1	**RV blood T_1**	**LV blood T_1**
Breath hold			
Breathing air	987±100	1260±100	1440±200
100% O_2	980±70	1190±140	1430±140
p-value	0.831	0.101	0.757*
Free breathing			
Breathing air	1030±70	1260±260	1470±60
100% O_2	940±30	1210±60	1600±40
p-value	0.035*	0.281	0.044*

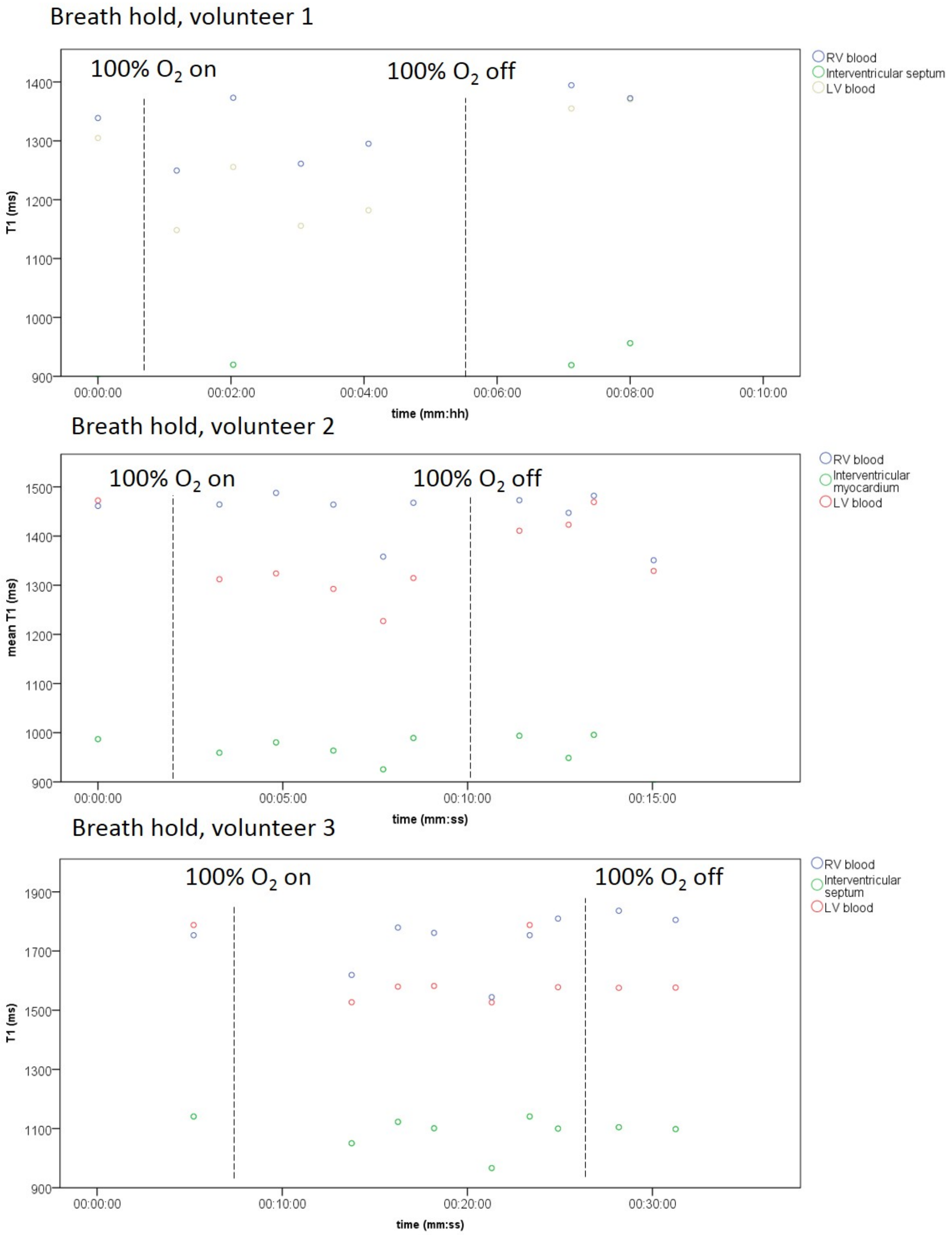

Fig. 6.10 T_1 over time for subjects breathing 100% oxygen during breath hold MOLLI imaging in the myocardium and ventricular blood pools.

A series of time resolved T_1 maps were acquired during breath hold and inhalation of 100% O_2 in three volunteers, see Figure 6.10, and Table 6.5. The mean myocardial T_1 during breathing 100%O_2 was 962±80 ms and the mean myocardial T_1 after the oxygen was switched off was 1000±70ms (p=0.156). The mean RV blood pool T_1 was significantly lower when the 100% O_2 was switched on (p=0.009).

Table 6.5 Effect of respiration of 100% O_2 on overall myocardial T_1 from three volunteers with breath hold acquisitions. N is the number of datasets included, where multiple T_1 maps were acquired for each volunteer, as shown in Figure 6.10. T_1 was grouped into T_1 measured before breathing % O_2 and during breathing 100% O_2. The values shown are mean values for all T_1 maps acquired. P-values are for a test for difference between breathing air and breathing 100% O_2.

	N	**Myocardial septal T_1**	**RV blood T_1**	**LV blood T_1**
Breathing air	3	1000±130	1500±240	1500±240
100% O_2 ON	13	960±80	1300±150	1500±190
100% O_2 OFF	16	1000±70	1500±170	1600±200
p-value		0.156	0.009**	0.226

6.4 Discussion

Myocardial alignment was significantly increased and resulted in myocardial T_1 values consistent with those determined from the mean signal from ROIs drawn on each image. This indicates the registration did not lead to erroneous T_1 values from the myocardium. Myocardial T_1 was found to be significantly higher during free breathing, and blood T_1 values were also found to be higher - but not significantly so.

During respiration, it is likely that the imaging plane will include images from slices which are anatomically positioned further towards the apex or base of the heart than other images, and therefore respiration will move the cardiac system in and out of the plane. In subjects where the myocardium may demonstrate a heterogeneous T_1 this will affect the precision of overall T_1 and therefore remains a substantial problem. This problem could be overcome by adopting the method for use in 3D imaging [50] [8] where the adjacent slices are acquired. Additionally, post-acquisition registration may be well suited to 3D T_1 mapping as it would remove the time consuming navigation or breath hold procedures otherwise required.

Although the method described in this chapter is susceptible to a lack of precision due to out of plane motion described above, this motion is unlikely to cause systematic errors resulting in an apparent elevated or lowered T_1 across a group of subjects, because the potential imprecision introduced due to the respiratory motion, the effects of which will be randomly distributed across the group (i.e. the breathing state of constituent images is essentially random). Therefore, it is unlikely that this explains the systematic differences seen in T_1 due to free breathing and breath hold acquisition. However, if the effect is due to motion rather than physiological effects, it is still relevant to the field to know that post-acquisition respiratory correction could lead to an apparent T_1 change which could be misleading or result in inaccuracies in studies where significant proportions of the study population have undergone post-acquisition motion correction.

Our study found significantly higher T_1 during free breathing acquisition when compared to inspiration breath hold. It is not clear what the mechanism of increasing T_1 during respiration is, however, it is known that myocardial perfusion and oxygenation change with breathing manoeuvres [114]. One study shows a trend of shorter breath holds decreasing myocardial oxygenation with very long breath holds having shown to result in decreased oxygenation in the LV blood pool and significantly increased myocardial oxygenation - the study suggests this may be due to increased blood flow compensating for desaturation [114]. Therefore, it may be due to a increase in paramagnetic deoxymyoglobin and deoxyhaemoglobin in the perfused myocardium during breath hold that decreases the T_1 during breath-hold.

As discussed in Chapter 5, a key limitation of this work is that the phase shift was not included in the respiratory model. Further work using the model described in equation is expected to improve the respiratory model and therefore potentially improve image registration further. Nonetheless, these results show that incorporating a sinusoidal component to curve fitting allows images of similar respiratory state to be selected and used for synthetic images, resulting in significant improved image registration.

It is a limitation of this work that scan-scan repeatability of free breathing acquisition of the MOLLI sequence has not been compared to that of a breath hold MOLLI sequence, which shows excellent scan-scan repeatability in healthy volunteers [91]. It would be of interest to compare both methods for scan-scan repeatability in healthy volunteers prior to further work.

When breathing 100% oxygen for 2 minutes prior to MOLLI imaging during free breathing, the LV blood and myocardial T_1 values significantly decreased. This is consistent with dissolved oxygen in the highly oxygenated LV blood lowering the blood T_1, due to the increase of oxygen delivery [2]. The breath hold T_1 values in the blood pool and myocardium were not significantly lower after inhalation of 100% oxygen. However, when breathing 100% oxygen followed by breath hold MOLLI imaging over a time period of 6-9 minutes, there was a significant overall lowering of T_1 seen in the RV blood pool. This indicates that the response to inhalation of 100% O_2 may be dependant on the breathing manoeuvre undertaken during imaging.

Breathing 100%O_2 during free breathing myocardial T_1 mapping has been shown to significantly decrease myocardial T_1 in healthy volunteers. This may mean that oxygen enhanced myocardial T_1 mapping can be used to visualise myocardial oxygenation - however more work with greater numbers of volunteers would be required to establish this. In addition, it has been shown that the use of a full closed air cushioned oxygen face mask for oxygen enhanced lung imaging results in higher oxygen transfer in the lung [108] and therefore repetitions of these experiments with a full closed oxygen mask may similarly result in higher oxygen transfer in the blood and myocardium.

6.5 Conclusions

Despite the limitations discussed, the method has been shown to significantly improve image registration in the short-axis plane, and indicates that there may be changes in measured myocardial T_1 due to respiration during T_1 mapping image acquisition. This indicates that respiratory state needs to be considered when evaluating T_1 values and that if a subject does not maintain breath hold it may artificially elevate their resultant myocardial T_1. The study also shows a significant decrease in free breathing T_1 after breathing 100% oxygen for 2 minutes. This emphasises that oxygenation, and any associated perfusion changes to compensate for oxygenation changes, can significantly affect myocardial T_1 and therefore, in patients with conditions associated with decreased oxygenation, there may be an associated change in measured myocardial T_1 which is not due to pathological tissue changes, but is due to blood oxygenation and/or perfusion changes. Indeed, it is worth noting that in Chapter 4 a significant negative correlation was found in patients with pulmonary hypertension with svO_2 and the myocardial T_1 in the LV free wall and RV insertion points.

In addition, this chapter demonstrates preliminary evaluation of a novel free breathing cardiac T_1 mapping technique which does not extend image acquisition time, and which could be extended to 3D acquisition to overcome the shortcomings discussed. Oxygen enhanced myocardial T_1 mapping post processing method may also be able to show oxygenation changes in the myocardium.

Chapter 7

Conclusions

The work in this thesis concerns the development and application of motion correction for cardiac and lung T_1 mapping sequences using synthetic-image based image registration methods. The thesis proposes two key methods: the first for correcting accidental motion in cardiac MOLLI images; the second for correcting motion due to respiration during free breathing acquisition of both cardiac MOLLI images and lung look locker images.

The development of a method to correct accidental motion in MOLLI images is presented in **Chapter 3**, and verified against an alternative, established motion correction method. The presented method was found to be equally as effective as the method by Xue et al [5] against which it was verified, but significantly more computationally efficient. **Chapter 3** established that a shortened acquisition sequence such as shMOLLI alone does not reduce all respiratory motion in a pulmonary hypertension cohort of patients. **Chapter 3** also found that in a cohort of patients with suspected pulmonary hypertension, neither measured T_1 nor the pixel wise standard deviation of T_1 values was significantly affected by image resolution.

This developmental work allowed a large cohort of pulmonary hypertension patients to undergo MOLLI imaging with post-processing image registration to correct accidental motion due to difficulties maintaining breath hold in this patient population. The application of this method to a pulmonary hypertension cohort of 490 patients and 25 healthy volunteers was presented in **Chapter 4**. To the authors knowledge, **Chapter 4** is the largest study of cardiac T_1 mapping in pulmonary hypertension, and the only study to consider the diagnostic and prognostic significance of T_1 mapping in pulmonary hypertension to date. Myocardial T_1 in the right ventricular insertion points was significantly higher in patients with pulmonary hypertension than in patients without pulmonary hypertension or healthy volunteers. Although there are distinctive myocardial T_1 changes with the condition, they were not found to provide diagnostic value or additive prognostic value.

Chapter 5 and **Chapter 6** modify the method described in Chapter 3 for free breathing image acquisition, with the intention of removing uncomfortable breath holds from MOLLI and Look-Locker imaging sequences without extending the time the patient is on the MRI scanner. The method was found to be successful in both cases, however, it was also found that the act of free breathing may result in significant changes to the measured T_1 in the lungs and in the myocardium. This may mean that unintended breathing during a breath-hold MOLLI or Look-Locker sequence may result in T_1 changes due to respiration.

Chapter 5 uses the image registration to correct respiratory motion in a free breathing Look-Locker acquisition in small cohort of 9 healthy volunteers and 10 patients with IPF. This work found significant differences in the free breathing lung T_1 in patients with IPF compared to healthy volunteers, with patients with IPF having a lower overall lung T_1 during free breathing and greater lung heterogeneity. These changes were significant in both breath hold and free breathing acquisition. A subset of 3 healthy volunteers also underwent T_1 mapping whilst breathing 100% O_2, which found that lung T_1 significantly reduced after administration of 100% O_2 in both breath held and free breathing acquisition.

Chapter 6 uses image registration to correct respiratory motion in a free breathing MOLLI acquisition in a small cohort of 10 healthy volunteers. The registration method significantly improved image registration in the short-axis plane and indicates that there may be changes in measured myocardial T_1 due to respiration during T_1 mapping image acquisition. The chapter also shows that a significant decrease in breath hold and free breathing myocardial T_1 after administration of 100% O_2 for 2 minutes prior to imaging, which indicates that blood oxygenation affects measured myocardial T_1, although future work with larger subject numbers is required to fully establish this association. **Chapter 6** describes cardiac T_1 mapping in 2D which is affected by out-of-plane motion, and it would be of interest in future work to look at 3D cardiac T_1 mapping with image registration to correct motion. This would overcome the issues concerning out-of-plane motion and confirm whether breathing manoeuvres affect myocardial T_1.

7.1 Future work

Chapter 4 presented the largest study of cardiac T1 mapping in pulmonary hypertension, and the only study to consider the diagnostic and prognostic significance of T1 mapping in pulmonary hypertension to date. The study found significantly elevated myocardial T_1 in the RV insertion points compared to both control groups - however the study did not find diagnostic or prognostic significance to native myocardial T_1. The discussion in Chapter 4 highlights that normalising myocardial T_1 values using blood T_1 values in order to remove effects due to hematocrit, oxygenation or perfusion changes in the myocardium may be a useful technique in this patient population, and this is strengthened by the data in Chapter 6 which shows that oxygenation can affect myocardial T_1. In particular, it would therefore be of interest to look at whether normalising myocardial T_1 data with each patients blood T_1 shows greater differences between patients with pulmonary hypertension and patients without pulmonary hypertension. In addition, it would be of interest in future work to establish: the scan-scan repeatability in patients with pulmonary hypertension; whether native myocardial T_1 elevation changes with time in patients with pulmonary hypertension and whether any T_1 changes over time have prognostic significance.

This thesis has described the development and application of methods for free breathing cardiac and lung T_1 mapping using post-processing image registration. These methods have the potential to provide a clinically applicable free breathing T_1 mapping for patients with cardiac and respiratory disease, however, there remains several areas of developmental work required to establish the methods are robust, repeatable and to correctly interpret their results.

For the free breathing lung T_1 mapping method developed in **Chapter 5** a phase term would need to be incorporated into the respiratory model as discussed in Chapter 5 before any future work. I would like to acknowledge the examiners for this thesis for highlighting this error. It is expected that a phase term will improve the accuracy of the respiratory model which will further improve the success of the image registration based motion correction. It would also be a priority to understand the scan-scan repeatability in healthy volunteers during free breathing and breath hold. In addition, it would be of interest to extend the oxygen enhanced lung T_1 mapping methods undertaken in **Chapter 5** to patients with IPF, as ΔT_1 between T_1 maps acquired whilst breathing room air compared to breathing $100\%\ O_2$ may be able to visualise regions of poor ventilation and/or perfusion in patients with IPF. If data were acquired alongside CT images it would also be possible to explore whether any oxygenation deficits are associated with regions of fibrosis. Furthermore, if the increased lung T_1 in expiration (compared to inspiration) is due to increased lung perfusion, co-registration of inspiration and expiration lung T_1 maps using synthetic images may allow a contrast-free visualisation of lung perfusion. This could be explored by comparison with contrast enhanced lung perfusion scans.

Redeveloping the method discussed in **Chapter 6** to compensate for out-of-plane motion would overcome the key limitation of this method. One way of achieving this may be to use a 3D MOLLI acquisition during free breathing with image registration in all three dimensions. It may also be beneficial to calculate inspiration and expiration T_1 maps from a free breathing acquisition, using only the images which occur in inspiratory and expiratory states (and are therefore within the same plane). The differences between inspiration (and expiration) T_1 maps in breath hold and during free breathing acquisition will show how much of the T_1 changes are breathing manoeuvre dependent (i.e. dependent on the oxygenation and perfusion effects of breath holding rather than the changes to the fractional components of tissue within the lung). This could be implemented by interleaving the only the inspiratory and expiratory components of several MOLLI scans acquired during free breathing. In addition, it would be a priority to do scan-scan repeatability testing comparisons between free breathing and breath held MOLLI acquisitions. It would also be interesting to explore whether myocardial T_1 changes due to oxygen enhancement would enable oxygenation mapping of the myocardium.

References

[1] N. Bloembergen, E. M. Purcell, and R. V. Pound, “Relaxation effecs in nuclear magnetic resonance absorption,” *Physical Review*, vol. 78, pp. 697–710, 1948.

[2] M. J. Silvennoinen, M. I. Kettunen, and R. A. Kauppinen, “Effects of hematocrit and oxygen saturation level on blood spin-lattice relaxation,” *Magnetic Resonance in Medicine*, vol. 49, no. 3, pp. 568–571, 2003.

[3] R. Damadian, “Tumor detection by nuclear magnetic resonance.,” *Physiol Chem and Phys*, vol. 171, pp. 1151–3, 1971.

[4] P. Lauterbur, “Image formation by induced local interactions: Examples employing nuclear magnetic resonance,” *Nature*, vol. 242, pp. 190–191, 1973.

[5] H. Xue, S. Shah, A. Greiser, C. Guetter, A. Littmann, M.-P. . Jolly, and P. Kellman, “Motion correction for myocarial t1 mapping using image registration with synthetic image estimation,” *Magnetic Resonance in Medicine*, vol. 67, pp. 1644–55, 2012.

[6] Q. Tao, P. van der Tol, F. Berendsen, P. E.H.M., H. Lamb, and R. van der Geest, “Robust motion correction for myocardial t1 and extracellular volume mapping by principle component analysis-based groupwise image registration,” *Journal of Magnetic Resonance Imaging*, vol. 47, no. 5, pp. 1397–1405, 2018.

[7] S. Triphan, B. F.A., D. Gensler, K. Hans-Ulrich, and P. M., “Oxygen enhanced lung mri by simultaneous measurement of t1 and t2* during free breathing using ultrashort te,” *Journal of Magnetic Resonance Imaging*, vol. 41, no. 6, pp. 1708–1714, 2014.

[8] S. Weingartner, M. Akcakaya, S. Roujol, T. Basha, C. Stehning, K. Kissinger, B. Goddu, S. Berg, W. Manning, and R. Nezafat, “Free-breathing post-contrast three-dimensional t1 mapping: Volumetric assessment of myocardial t1 values.,” *Magnetic Resonance in Medicine*, vol. 73, pp. 214–222, 2015.

[9] M. H. Levitt, *spin dynamics*. Wiley, 2009.

[10] E. Haacke, R. W. Brown, M.R.Thompson, and R. Venkatesan, *Magnetic Resonance Imaging: Physical Principles and Sequence Design*. Wiley, 1999.

[11] F. Bloch, “Nuclear induction,” *Physical Review*, vol. 70, p. 4604–73, 1946.

[12] W. G. Murphy, “The sex difference in haemoglobin levels in adults — mechanisms, causes, and consequences,” *Blood Reviews*, vol. 28, no. 2, pp. 41 – 47, 2014.

[13] X. Zhang, E. T. Petersen, E. Ghariq, J. B. Vis, A. G. Webb, W. M. Teeuwisse, J. Hendrikse, and M. J. P. Osch, "In vivo blood t1 measurements at 1.5 t, 3 t, and 7 t," *Magnetic Resonance in Medicine*, vol. 70, no. 4, pp. 1082–1086, 2013.

[14] U. Reiter, G. Reiter, K. Dorr, A. Greiser, R. Maderthaner, and M. Fuchsjäger, "Normal diastolic and systolic myocardial t1 values at 1.5-t mr imaging: Correlations and blood normalization," *Radiology*, vol. 271, p. 365–72, 2013.

[15] G. Chiarotte, G. Christiani, and L. Guilotto, "Proton relaxation in pure liquids and in liquids containing paramagnetic gases in solution.," *Il Nuovo Cimento*, vol. 1, pp. 863–873, 1955.

[16] U. Ohno, H. Hatabu, D. Takenaka, M. Cauteren, M. Fuji, and K. Sugimura, "Dynamic oxygen-enhanced mri reflects diffusing capacity of the lung," *Magnetic resonance in medicine*, vol. 47, pp. 1139–1144, 2002.

[17] J. Arnold, F. Fidler, T. Wang, E. Pracht, M. Schmidt, and P. Jakob, "Imaging lung function using rapid dynamic acquisition of t1-maps during oxygen enhancement.," *MAGMA*, vol. 16, pp. 246–253, 2004.

[18] S. K. Piechnik, V. M. Ferreirak, A. J. Lewandowskik, N. A. Ntusik, R. Banerjeek, C. Hollowayk, M. B. Hofmank, D. M. Sadok, V. Maestrinik, S. K. Whitek, M. Lazdamk, T. Karamitsosk, J. C. Moonk, S. Neubauerk, P. Leeson, and M. D. Robson, "Determining the longitudinal relaxation time (t1) of blood at 3.0 tesla," *Magnetic Resonance in Medicine*, vol. 52, pp. 679–82, 2004.

[19] P. Jakob, T. Wang, G. Schultz, H. Hebestreit, A. Hebestreit, and D. Hahn, "Assessment of human pulmonary function using oxygen-enhanced t(1) imaging in patients with cystic fibrosis.," *Magnetic resonance in medicine*, vol. 51, pp. 1009–1016, 2004.

[20] R. R. Ernst, "Application of fourier transform spectroscopy to magnetic resonance," *Review of Scientific Instruments*, vol. 37, 1966.

[21] P. Kellman and M. Hansen, "T1-mapping in the heart: accuracy and precision.," *Journal of cardiovascular magnetic resonance*, vol. 16, p. 2, 2014.

[22] D. C. Look and D. R. Locker, "Time saving in measurement of nmr and epr relaxation times.," *Review of Scientific Instruments*, vol. 41, pp. 250–251, 1970.

[23] D. R. Messroghli, A. Radjenovic, S. Kozerke, D. Higgins, M. Sivananthan, and J. Ridgway, "Modified look-locker inversion recovery (molli) for high-resolution t1 mapping of the heart.," *Magnetic Resonance in Medicine*, vol. 52, pp. 141–6, 2004.

[24] S. Roujol, S. Weingärtner, M. Foppa, K. Chow, K. Kawaji, L. Ngo, P. Kellman, W. Manning, T. R.B., and R. Nezafat, "Accuracy, precision, and reproducibility of four t1 mapping sequences: a head-to-head comparison of molli, shmolli, sasha, and sapphire.," *Radiology*, vol. 272, pp. 683–9, 2014.

[25] K. Chow, J. Flewitt, J. Green, J. Pagano, M. Friedrich, and R. Thompson, "Saturation recovery single-shot acquisition (sasha) for myocardial t(1) mapping.," *Journal of cardiovascular magnetic resonance*, vol. 71, pp. 2082–95, 2014.

[26] P. Kellman, A. Arai, and H. Xue, “T1 and extracellular volume mapping in the heart: estimation of error maps and the influence of noise on precision.,” *Journal of cardiovascular magnetic resonance*, vol. 15, p. 56, 2013.

[27] G. Slavin and J. Stainsby, “Comparing the accuracy and precision of smart1map, sasha and molli.,” *Journal of cardiovascular magnetic resonance*, vol. 16, p. 11, 2014.

[28] D. Messroghli, A. Greiser, M. Frohlich, R. Dietz, and J. Schulz-Menger, “Optimization and validation of a fully-integrated pulse sequence for modified look-locker inversion-recovery (molli) t1 mapping of the heart.,” *Journal of cardiovascular magnetic resonance*, vol. 26, pp. 1081–6, 2007.

[29] F. von Knobelsdorff-Brenkenhoff, M. Prothmann, M. Dieringer, R. Wassmuth, A. Greiser, C. Schwenke, T. Niendorf, and J. Schulz-Menger, “Myocardial t1 and t2 mapping at 3t: reference values, influencing factors and implications.,” *Journal of cardiovascular magnetic resonance*, vol. 15, p. 53, 2013.

[30] S. Piechnik, V. Ferreira, E. Dall’Armellina, L. Cochlin, A. Greiser, S. Neubauer, and M. Robson, “Shortened modified look-locker inversion recovery shmolli for clinical myocardial t1-mapping at 1.5 and 3t within a 9 heartbeat breathhold,” *Magnetic Resonance in Medicine*, vol. 12, p. 69, 2010.

[31] S. Weingartner, M. Akcakaya, S. Berg, W. J. Manning, and R. Nezafat, “Heart-rate independent myocardial t1-mapping using combined saturation and inversion preparation pulses,” *Journal of Cardiovascular Magnetic resonance*, vol. 15, p. 46, 2013.

[32] D. Dabir, N. Child, A. Kalra, T. Rogers, R. Gebker, A. Jabbour, S. Plein, C.-Y. Yu, J. Otton, A. Kidambi, A. McDiarmid, D. Broadbent, D. M. Higgins, B. Schnackenburg, L. Foote, C. Cummins, E. Nagel, and V. O. Puntmann, “Reference values for healthy human myocardium using a t1 mapping methodology: results from the international t1 multicenter cardiovascular magnetic resonance study,” *Journal of Cardiovascular Magnetic Resonance*, vol. 16, p. 69, 2014.

[33] H. Bulluck, J. Bryant, J. Tan, Y. Go, T. Le, R. Tan, T. Lim, H. Tang, N. Lath, A. Low, C. Chin, S. Cook, and D. Hausenloy, “Gender differences in native myocardial t1 in a healthy chinese volunteer cohort.,” *Cardiovasc Imaging Asia.*, vol. 1, pp. 110–115, 2017.

[34] S. Rosmini, H. Bulluck, G. Captur, T. A. Treibel, A. Abdel-Gadir, A. N. Bhuva, V. Culotta, A. Merghani, M. Fontana, V. Maestrini, A. S. Herrey, K. Chow, R. B. Thompson, S. K. Piechnik, P. Kellman, C. Manisty, and J. C. Moon, “Myocardial native t1 and extracellular volume with healthy ageing and gender,” *European Heart Journal - Cardiovascular Imaging*, vol. 19, no. 6, pp. 615–621, 2018.

[35] C. Roy, A. Slimani, C. de Meester, M. Amzulescu, A. Pasquet, D. Vancraeynest, J.-L. Vanoverschelde, A.-C. Pouleur, and B. L. Gerber, “Age and sex corrected normal reference values of t1, t2 t2* and ecv in healthy subjects at 3t cmr,” *Journal of Cardiovascular Magnetic Resonance*, vol. 19, 2017.

[36] P. M. Jakob, C. M. Hillenbrand, T. Wang, G. S. andDietbert Hahn, and A. Haase, “Rapid quantitative lung 1h t1 mapping,” *Journal of magnetic resonance imaging*, vol. 14, 2001.

[37] N. D. Gai, A. A. Malayeri, and D. A. Bluemke, “Three-dimensional t1 and t2* mapping of human lung parenchyma using interleaved saturation recovery with dual echo ultrashort echo time imaging (itsr-dute),” *Journal of Magnetic Resonance Imaging*, vol. 45, no. 4, pp. 1097–1104, 2017.

[38] S. M. F. Triphan, B. J. Jobst, A. Anjorin, O. Sedlaczek, U. Wolf, M. Terekhov, C. Hoffmann, S. Ley, C. Düber, J. Biederer, H.-U. Kauczor, P. M. Jakob, and M. O. Wielpütz, “Reproducibility and comparison of oxygen-enhanced t1 quantification in copd and asthma patients,” *Plos one*, vol. 12, 2017.

[39] O. Dietricha, T. Gaass, M. F, and Reiser, “T1 relaxation time constants, influence of oxygen, and the oxygen transfer function of the human lung at 1.5 t—a meta-analysis,” *European Journal of Radiology*, vol. 87, no. 1, pp. 60–66, 2019.

[40] M. Wyawahare, P. Patil, and H. Abhyankar, “Image registration techniques: An overview,” *International Journal of Signal Processing, Image Processing and Pattern Recognition*, vol. 2, pp. 11–22, 2009.

[41] J. Maintz and M. A. Viergever, “A survey of medical image registration,” *Medical Image Analysis*, vol. 2, pp. 140–144, 1997.

[42] D. Barber and D. Hose, “Automatic segmentation of medical images using image registration: diagnostic and simulation applications,” *Journal of Medical Engineering Technology*, vol. 29, pp. 53–63, 2005.

[43] R. H. Ireland, K. E. Dyker, D. C. Barber, S. M. Wood, M. B. Hanney, W. B. Tindale, N. Woodhouse, N. Hoggard, J. Conway, , and M. H. Robinson, “Nonrigid image registration for head and neck cancer radiotherapy treatment planning with pet/ct.,” *Int J Radiat Oncol Biol Phys*, vol. 68, pp. 952–957, 2007.

[44] K. H. Zou, S. K. Warfield, A. Bharatha, C. M. C. Tempany, M. R. Kaus, S. J. . Haker, and . . h.-.-. Kikinis, R. (2004). Statistical Validation of Image Segmentation Quality Based on a Spatial Overlap Index: Scientific Reports. Academic Radiology, “Statistical validation of image segmentation quality based on a spatial overlap index.,” *Academic radiology*, vol. 11, pp. 178–89, 2004.

[45] H. Xue, A. Greiser, S. Zuehlsdorff, M.-P. Jolly, J. Guehring, A. E. Arai, and P. Kellman, “Phase-sensitive inversion recovery for myocardial t1 mapping with motion correction and parametric fitting,” *Magnetic Resonance in Medicine*, vol. 69, pp. 1408–20, 2013.

[46] V. M. Ferreira1, S. K. Piechnik, E. Dall’Armellina, T. D. Karamitsos, J. M. Francis, N. Ntusi, C. Holloway, R. P. Choudhury, A. Kardos, M. D. Robson, M. G. Friedrich, and S. Neubauer, “Native t1-mapping detects the location, extent and patterns of acute myocarditis without the need for gadolinium contrast agents.,” *Journal of cardiovascular magnetic resonance*, vol. 16, p. 36, 2014.

[47] K. Hong and D. Kim, "Molli and air t1 mapping pulse sequences yield different myocardial t1 and ecv measurements.," *NMR in biomedicine*, vol. 27, pp. 1419–26, 2014.

[48] N. Kawel, M. Nacif, Zavodni, J. Jones, S. Lui, and D. Bluemke, "T1 mapping of the myocardium: Intra-individual assessment of the effect of field strength, cardiac cycle and variation by myocardial region.," *Journal of cardiovascular magnetic resonance*, vol. 14, p. 27, 2012.

[49] P. Lai, A. C. Larson, X. Bi, R. Jerecic, and D. Li, "A dual-projection respiratory self-gating technique for whole-heart coronary mra," *Journal of Magnetic Resonance Imaging*, vol. 28, pp. 612–20, 2008.

[50] N. Giovanna, H. Markus, C. Amedeo, V. A. D.M., S. Torben, and B. R. M., "3d myocardial t1 mapping using saturation recovery," *Journal of Magnetic Resonance Imaging*, vol. 46, no. 1, pp. 218–227, 2017.

[51] A. Stadler, P. Jakob, M. Griswold, M. Barth, and A. Bankier, "T1 mapping of the entire lung parenchyma: Influence of the respiratory phase in healthy individuals.," *Journal of magnetic resonance imaging*, vol. 21, pp. 759–764, 2005.

[52] J. J. Cao, Y. Wang, W. Schapiro, J. McLaughlin, J. Cheng, M. Passick, N. Ngai, P. Marcus, and N. Reichek, "Effects of respiratory cycle and body position on quantitative pulmonary perfusion by mri," *Journal of Magnetic Resonance Imaging*, vol. 34, no. 1, pp. 225–230, 2011.

[53] S. Rosenkranz and I. R. Preston, "Right heart catheterisation: best practice and pitfalls in pulmonary hypertension," *European Respiratory Review*, vol. 24, no. 138, pp. 642–652, 2015.

[54] D. G. Kiely, C. A. Elliot, I. Sabroe, and R. Condliffe, "Pulmonary hypertension: diagnosis and management," *BMJ*, vol. 346, p. 346, 2013.

[55] E. M. Moreira, H. Gall, M. J. G. Leening, L. Lahousse, D. W. Loth, B. P. Krijthe, and J. F. ... Felix, "Prevalence of pulmonary hypertension in the general population: The rotterdam study.," *PLoS ONE*, vol. 10, no. 6, 2015.

[56] A. J. Swift, J. M. Wild, S. K. Nagle, A. Roldán-Alzate, C. J. François, S. Fain, and M. L. ... Schiebler, "Quantitative mr imaging of pulmonary hypertension: A practical approach to the current state of the art.," *Journal of Thoracic Imaging*, vol. 29, no. 2, 2014.

[57] G. D'Alonzo, R. Barst, S. Ayres, E. Bergofsky, B. Brundage, and e. a. Detre K.M., "Survival in patients with primary pulmonary hypertension. results from a national prospective registry," *Annals of Internal Medicine*, vol. 115, pp. 343–9, 1991.

[58] S. A. van Wolferen, J. T. Marcus, A. L. Boonstra, K. M. J. Marques, J. G. F. Bronzwaer, M. D. Spreeuwenberg, P. E. Postmus, and A. Vonk-Noordegraaf, "Prognostic value of right ventricular mass, volume, and function in idiopathic pulmonary arterial hypertension.," *European Heart J*, vol. 28, pp. 1250–7, 2007.

[59] B. H. Freed, M. Gomberg-Maitland, S. Chandra, V. Mor-Avi, S. Rich, S. L. . Archer, and A. R. Patel, “Late gadolinium enhancement cardiovascular magnetic resonance predicts clinical worsening in patients with pulmonary hypertension.,” *Journal of Cardiovascular Magnetic Resonance*, vol. 14, p. 11, 2012.

[60] R. R. Vanderpool, M. R. Pinsky, D. hc, R. Naeije, C. Deible, V. . Kosaraju, and M. A. Simon, “Rv-pulmonary arterial coupling predicts outcome in patients referred for pulmonary hypertension.,” *Heart*, vol. 101, pp. 37–43, 2015.

[61] A. Swift, S. Rajaram, M. Campbell, J. Hurdman, S. Thomas, D. Capener, C. Elliot, R. Condliffe, J. Wild, and D. Kiely, “Prognostic value of cardiovascular magnetic resonance imaging measurements corrected for age and sex in idiopathic pulmonary arterial hypertension.,” *Circulation Cardiovascular imaging*, vol. 7, pp. 100–6, 2014.

[62] M. C. van de Veerdonk, T. Kind, J. T. Marcus, G.-J. Mauritz, M. W. Heymans, H.-J. Bogaard, A. Boonstra, K. M. Marques, N. Westerhof, and A. Vonk-Noordegraaf, “Progressive right ventricular dysfunction in patients with pulmonary arterial hypertension responding to therapy,” *Journal of the American College of Cardiology*, vol. 58, no. 24, pp. 2511 – 2519, 2011.

[63] A. Maceira, J. Parsad, M. Khan, and D. Pennell, “Reference right ventricular systolic and diastolic function normaliz to age,gender and body surface area from steady state free precession cardivascular magnetic resonance,” *Journal of Magnetic Resonance Imaging*, vol. 196, no. 2, p. 228–239, 2017.

[64] C. S. Johns, J. M. Wild, S. Rajaram, E. Tubman, D. Capener, C. Elliot, R. Condliffe, A. Charalampopoulos, D. G. Kiely, and A. J. Swift, “Identifying at-risk patients with combined pre- and postcapillary pulmonary hypertension using interventricular septal angle at cardiac mri,” *Radiology*, vol. 289, 2018.

[65] A. J. Swift, D. Capener, C. Johns, N. Hamilton, A. Rothman, C. . Elliot, and D. G. Kiely, “Magnetic resonance imaging in the prognostic evaluation of patients with pulmonary arterial hypertension.,” *Journal of Magnetic Resonance Imaging*, vol. 196, no. 2, p. 228–239, 2017.

[66] A. J.Swift, S. Rajaram, D. Capener, C. Elliot, R. Condliffe, J. M. Wild, and D. G. Kiely, “Lge patterns in pulmonary hypertension do not impact overall mortality.,” *JACC Cardiovascular imaging*, vol. 7, pp. 1209–17, 2014.

[67] K. G. Blyth, B. A. Groenning, T. N. Martin, J. E. Foster, P. B. Mark, H. J. Dargie, and A. J. Peacock, “Contrast enhanced-cardiovascular magnetic resonance imaging in patients with pulmonary hypertension,” *European Heart Journal*, vol. 26, no. 19, pp. 1993–1999, 2005.

[68] van Spreeuwel A and B. C. Bax N, “The relevance of extracellular matrix structure and composition in engineering the diseased cardiac microenvironment.,” *OA Tissue Engineering*, vol. 18, p. 2, 2014.

[69] G. McCann, C. Gan, A. Beek, H. Niessen, A. Vonk Noordegraaf, and A. van Rossum, “Extent of mri delayed enhancement of myocardial mass is related to right ventricular dysfunction in pulmonary artery hypertension.,” *American journal of roentgenology*, vol. 188, pp. 349–55, 2007.

[70] W. Bradlow, R. Assomull, P. Kilner, J. Gibbs, M. Sheppard, and R. Mohiaddin, "Understanding late gadolinium enhancement in pulmonary hypertension.," *Circulatory cardiovascular imaging*, vol. 3, pp. 501–3, 2010.

[71] A. García-Álvarez, I. García-Lunar, D. Pereda, R. Fernández-Jimenez, J. Sánchez-González, J. G. Mirelis, M. Nuño-Ayala, D. Sánchez-Quintana, L. Fernández-Friera, J. M. García-Ruiz, G. Pizarro, J. Agüero, P. Campelos, M. Castellá, M. Sabaté, V. Fuster, J. Sanz, and B. Ibañez, "Association of myocardial t1-mapping cmr with hemodynamics and rv performance in pulmonary hypertension.," *JACC Cardiovascular imaging*, vol. 8, pp. 76–82, 2015.

[72] S. K. Soma, V. Goyal, V. K. Rathi, M. Doyle, S. Murali, D. A. Vido, R. Benza, G. Sokos, and R. W. Biederman1, "Late gadolinium enhancement in pulmonary hypertension predicts clinical events," *Journal of Cardiovascular Magnetic Resonance.*, vol. 14, p. 86, 2012.

[73] R. F. C., C. Wiedenroth, A. Breithecker, C. Liebetrau, E. Mayer, C. Schneider, A. Rolf, C. Hamm, and G. A. Krombach, "Native t1 mapping and extracellular volume fraction measurement for assessment of right ventricular insertion point and septal fibrosis in chronic thromboembolic pulmonary hypertension.," *European Radiology*, vol. 27, p. 1980–1991, 2016.

[74] S. O.A., L. Vissers, H. Bogaard, M. Hofman, A. Vonk-Noordegraaf, and J. Marcus, "Increased native t1-values at the interventricular insertion regions in precapillary pulmonary hypertension.," *International Journal of Cardiovascular Imaging*, vol. 32, pp. 451–9, 2016.

[75] U. Reiter, G. Reiter, G. Kovacs, G. Adelsmayr, A. Greiser, H. Olschewski, and M. Fuchsjäger, "Native myocardial t1 mapping in pulmonary hypertension: correlations with cardiac function and hemodynamics.," *European Radiology*, vol. 27, pp. 157–66, 2017.

[76] J. Wang, H. Zhao, Y. Wang, H. C. Herrmann, W. Witschey, and Y. Han, "Native t1 and t2 mapping by cardiovascular magnetic resonance imaging in pressure overloaded left and right heart diseases.," *Journal of thoracic disease*, vol. 10, pp. 2968–2975, 2018.

[77] G. Raghu, D. Weycker, J. Edelsberg, W. Bradford, and G. Oster, "Incidence and prevalence of idiopathic pulmonary fibrosis.," *American journal of respiratory and critical care medicine*, vol. 17, pp. 810–6, 2006.

[78] V. Taskar and D. Coultas, "Is idiopathic pulmonary fibrosis an environmental disease?," *Proceedings of the American Thoracic Society*, vol. 3, pp. 293–8, 2006.

[79] H. Robbie, C. Daccord, F. Chua, and A. Devaraj, "Evaluating disease severity in idiopathic pulmonary fibrosis," vol. 26, no. 145, p. 145, 2017.

[80] N. I. for Health and C. Excellence, "Idiopathic pulmonary fibrosis in adults," *NICE Guideline*, vol. QS79, 2015.

[81] G. Raghu, H. R. Collard, J. J. Egan, F. J. Martinez, J. Behr, K. K. Brown, T. V. Colby, J. F. Cordier, K. R. Flaherty, J. A. Lasky, D. A. Lynch, J. H. Ryu, J. J. Swigris, A. U. Wells, J. Ancochea, D. Bouros, C. Carvalho, U. Costabel, M. Ebina, D. M. Hansell, T. Johkoh, D. S. Kim, T. E. King, Y. Kondoh, J. Myers, N. L. Müller, A. G. Nicholson, L. Richeldi, M. Selman, R. F. Dudden, B. S. Griss, S. L. Protzko, and H. J. Schünemann, "Ats/ers/jrs/alat committee on idiopathic pulmonary fibrosis (2011). an official ats/ers/jrs/alat statement: idiopathic pulmonary fibrosis: evidence-based guidelines for diagnosis and management.," *Journal of Magnetic Resonance Imaging*, vol. 183, no. 6, pp. 788–824, 2011.

[82] C. HR, K. TE, B. BB, V. JS, S. MI, and B. KK, "Changes in clinical and physiologic variables predict survival in idiopathic pulmonary fibrosis," *American journal of respiratory and critical care medicine*, vol. 168, pp. 538–42, 2003.

[83] S. L. Schmidt, N. Tayob, M. K. Han, C. Zappala, D. Kervitsky, S. Murray, A. U. Wells, K. K. Brown, F. J. Martinez, and K. R. Flaherty, "Predicting pulmonary fibrosis disease course from past trends in pulmonary function," *Chest*, vol. 145, no. 3, pp. 579 – 585, 2014.

[84] A. Stadler, P. Jakob, M. Griswold, L. Stiebellehner, M. Barth, and A. Bankier, "T1 mapping of the entire lung parenchyma: Influence of respiratory phase and correlation to lung function test results in patients with diffuse lung disease," *Magnetic resonance in medicine*, vol. 59, pp. 96–101, 2005.

[85] S. Mirsadraee, M. Tse, L. Kershaw, S. Semple, N. Schembri, C. Chin, and E. J. R. van Beek, "T1 characteristics of interstitial pulmonary fibrosis on 3t mri—a predictor of early interstitial change?," *Quantitative Imaging in Medicine and Surgery*, vol. 6, 2016.

[86] A. Taylor, M. Salerno, R. Dharmakumar, and M. Jerosch-Herold, "T1 mapping: Basic techniques and clinical applications.," *JACC Cardiovascular Imaging*, vol. 9, pp. 67–81, 2016.

[87] N. Kawel, E. B. , Turkbey, J. J. Carr, J. Eng, A. S. Gomes, W. G. Hundley, and D. A. Bluemke, "Normal left ventricular myocardial thickness for middle aged and older subjects with ssfp cardiac mr: The multi-ethnic study of atherosclerosis," *Circulation Cardiovascular imaging.*, vol. 5, no. 4, pp. 500–508, 2012.

[88] T. Rogers, D. Dabir, I. Mahmoud, T. Voigt, T. Schaeffter, E. Nagel, and V. Puntmann, "Standardization of t1 measurements with molli in differentiation between health and disease – the consept study.," *Journal of Cardiovascular Magnetic Resonance*, vol. 15, no. 1, p. 78, 2013.

[89] V. Puntmann, A. Isted, R. Hinojar, L. Foote, G. Carr-White, and E. Nagel, "T1 and t2 mapping in recognition of early cardiac involvement in systemtic sarcoidosis," *Radiology*, vol. 285, pp. 63–72, 2017.

[90] E. Tahir, M. Sinn, S. Bohnen, M. Avanesov, D. Säring, C. Stehning, B. Schnackenburg, C. Eulenburg, J. Wien, U. K. Radunski, S. Blankenberg, G. Adam, C. B. Higgins, M. Saeed, K. Muellerleile, and G. K. Lund, "Acute versus chronic myocardial infarction: Diagnostic accuracy of quantitative native t1 and t2 mapping

versus assessment of edema on standard t2-weighted cardiovascular mr images for differentiation," *Radiology*, vol. 285, p. 83=91, 2017.

[91] F. aus dem Siepen, C. Baumgärtner, M. Müller-Henessen, F. André, D. Messroghli, M. Ochs, J. Riffel, E. Giannitsis, H. A. Katus, M. G. Friedrich, and S. J. Buss, "Variability of cardiovascular magnetic resonance (cmr) t1 mapping parameters in healthy volunteers during long-term follow-up," vol. 5, no. 1, 2018.

[92] T. J. W. Dawes, A. de Marvao, W. Shi, T. Fletcher, G. M. J. Watson, J. Wharton, C. J. Rhodes, L. S. G. E. Howard, J. S. R. Gibbs, D. Rueckert, S. A. Cook, M. R. Wilkins, and D. P. O'Regan, "Machine learning of three-dimensional right ventricular motion enables outcome prediction in pulmonary hypertension: A cardiac mr imaging study.," *Radiology*, vol. 283, pp. 381–90, 2017.

[93] E. C. e. a. Hurdman J, Condliffe R, "Aspire registry: assessing the spectrum of pulmonary hypertension identified at a referral centre.," *The European Respiratory Journal*, vol. 283, pp. 945–55, 2012.

[94] J. Hurdman, R. Condliffe, C. Elliot, C. Davies, C. Hill, J. W. ..., and D. Kiely, "Noninvasive estimation of pa pressure, flow, and resistance with cmr imaging: derivation and prospective validation study from the aspire registry.," *JACC Cardiovascular Imaging*, vol. 6, pp. 1036–47, 2013.

[95] A. Mayr, D. Kitterer, J. Latus, H. Steubing, J. Henes, F . Vecchio, and S. Greulich, "Evaluation of myocardial involvement in patients with connective tissue disorders: a multi-parametric cardiovascular magnetic resonance study.," *JCMR*, vol. 18, p. 67, 2016.

[96] U. Reiter, G. Reiter, K. Dorr, A. Greiser, R. Maderthaner, and M. Fuchsjäger, "Normal diastolic and systolic myocardial t1 values at 1.5-t mr imaging: Correlations and blood normalization," *Radiology*, vol. 271, pp. 365–72, 2013.

[97] J. Wild, H. Marshall, L. J. P. Bock, M.and Schad, M. . Puderbach, and J. Biederer, "Mri of the lung (1/3): methods.," *Insights into Imaging*, vol. 3(4), p. 345–353, 2012.

[98] J. V. Dyk, T. Keane, and W. Rider, "Lung density as measured by computerized tomography: implications for radiotherapy," *International Journal of Radiation Oncology, Biology, Physics*, vol. 8, no. 8, pp. 1363 – 1372, 1982.

[99] H. B. Robert, A. W. Robert, G. Kirk, M. B. Drummond, and W. Mitzner, "Lung density changes with growth and inflation.," *Ches*, vol. 148, pp. 995–1002, 2015.

[100] J. Yu, Y. Xue, , and H. K. Song, "Comparison of lung t2* during free-breathing at 1.5t and 3.0t with ultrashort echo time (ute) imaging," *Magnetic resonance in medicine*, vol. 66, p. 248–254, 2011.

[101] D. W. McRobbie, E. A. Moore, M. J. Graves, and M. R. Prince, *MRI from Picture to Proton*. Cambridge University Press, 2006.

[102] R. R. Edelman, H. Hatabu, E. Tadamura, W. Li, and P. V. Prasad, "Noninvasive assessment of regional ventilation in the human lung using oxygen–enhanced magnetic resonance imaging," *Nature Medicine*, vol. 2, p. 1236–1239, 1996.

[103] S. Nakamori, K. Dohi, M. Ishida, Y. Goto, K. Imanaka-Yoshida, T. Omori, I. Goto, N. Kumagai, N. Fujimoto, Y. Ichikawa, K. Kitagawa, N. Yamada, H. Sakuma, and M. Ito, "Native t1 mapping and extracellular volume mapping for the assessment of diffuse myocardial fibrosis in dilated cardiomyopathy," *JACC: Cardiovascular Imaging*, vol. 11, pp. 48 – 59, 2018.

[104] J. Armstrong, E. Gluck, R. Crapo, H. Jones, and J. Hughes, "Lung tissue volume estimated by simultaneous radiographic and helium dilution methods.," *Thorax*, vol. 37, p. 76–679, 1982.

[105] S. Collum, J. Amione-Guerra, A. Cruz-Solbes, A. DiFrancesco, A. Hernandez, A. Hanmandlu, K. Youker, A. Guha, , and H. Karmouty-Quintana, "Pulmonary hypertension associated with idiopathic pulmonary fibrosis: Current and future perspectives," *Canadian Respiratory Journal*, vol. 12, p. 1430350, 2017.

[106] L. Olsson and P. Hockings, "In vivo measurements of t2 relaxation time of mouse lungs during inspiration and expiration," *PLoS ONE*, vol. 11, 2016.

[107] A. Stadler, L. Stiebellehner, P. M. Jakob, J. F. T. Arnold, E. Eisenhuber, I. von Katzler, and A. A. Bankier, "Quantitative and o2 enhanced mri of the pathologic lung: Findings in emphysema, fibrosis, and cystic fibrosis," *Int J Biomed Imaging*, vol. 22, 2007.

[108] J. Renne, P. Lauermann, J. Hinrichs, C. Schönfeld, S. Sorrentino, M. Gutberlet, P. Jakob, F. Wacker, and J. Vogel-Claussen, "Clinical use of oxygen-enhanced t1 mapping mri of the lung: Reproducibility and impact of closed versus loose fit oxygen delivery system," *Journal of Magnetic Resonance Imaging*, vol. 41, no. 1, pp. 60–66, 2015.

[109] R. Guo, Z. Chen, Y. Wang, D. A. Herzka, J. Luo, and H. Ding, "Three-dimensional free breathing whole heart cardiovascular magnetic resonance t1 mapping at 3 t," *Journal of Cardiovascular Magnetic Resonance*, vol. 20, p. 64, 2018.

[110] P. Kellman, A. C. Larson, L.-Y. Hsu, Y.-C. Chung, O. P. Simonetti, E. R. McVeigh, and A. E. Arai1, "Motion-corrected free-breathing delayed enhancement imaging of myocardial infarction," *Magnetic resonance in medicine*, vol. 53, pp. 194–200, 2005.

[111] K. Chow, Y. Yang, P. Shaw, C. M. Kramer, and M. Salerno, "Robust free-breathing sasha t1 mapping with high-contrast image registration," *Journal of Cardiovascular Magnetic Resonance*, vol. 18, p. 47, 2016.

[112] G. Kovalski, O. Israel, Z. Keidar, A. Frenkel, J. Sachs, , and H. A. 1, "Correction of heart motion due to respiration in clinical myocardial perfusion spect scans using respiratory gating," *The Journal of Nuclear Medicine*, vol. 48, pp. 630–636, 2007.

[113] I. Gersh and M. A. Still, "Blood vessels in fat tissue. relation to problems of gas exchange.," *The Journal of Experimental Medicine*, vol. 81, p. 219–232, 1945.

[114] D. P. Guensch, K. Fischer, J. A. Flewitt, J. Yu, R. Lukic, J. A. Friedrich, and M. G. Friedrich, "Breathing manoeuvre-dependent changes in myocardial oxygenation in healthy humans," *European Heart Journal - Cardiovascular Imaging*, vol. 15, no. 4, pp. 409–414, 2014.

Appendix A

Appendix

The following appendix shows the relevant code for this thesis, with accompanying flow charts describing the algorithm for each section of code.

A.1 Matlab code for Chapter3

Each step of the algorithm in Figure A.1 is described in the following section, with an accompanying flow chart describing each section of code further.

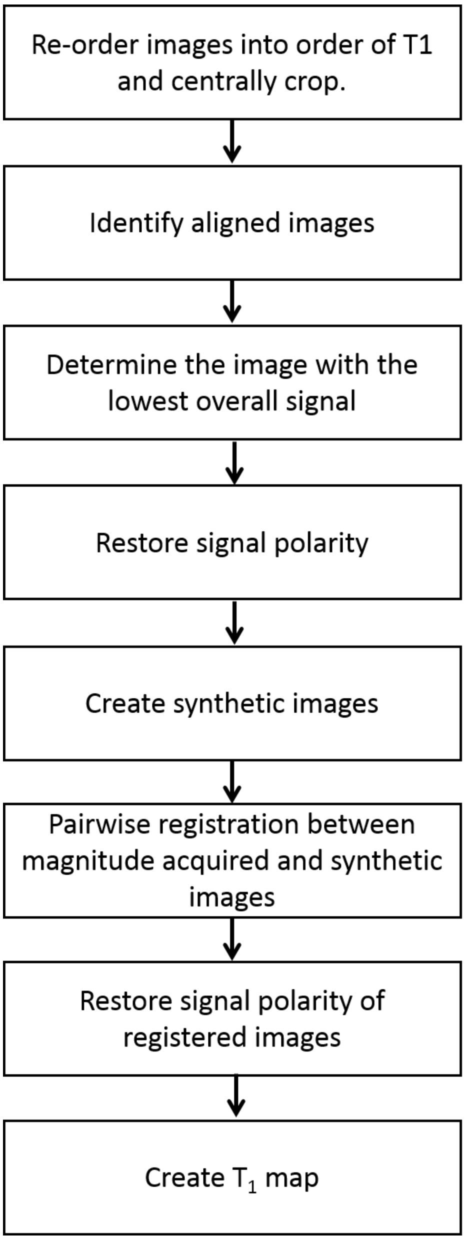

Fig. A.1 Flow chart to show the relevant sections of code and their ordering for Chapter 3.

A.1.1 Reorder images

The purpose of this section of code is to reorder the MOLLI images according to their time post-inversion (TI). The steps of the algorithm, as well as input and output information, are outlined in Figure A.2.

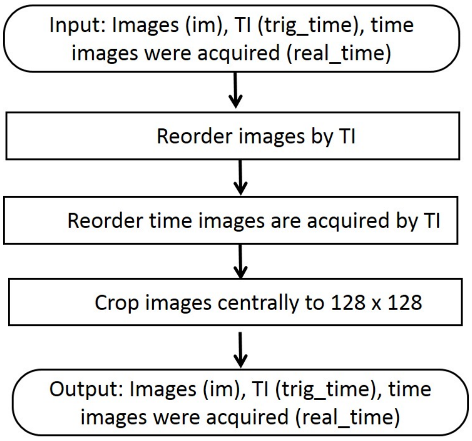

Fig. A.2 Flow chart to demonstrate following code. The code reorders and centrally crops the images.

```
[pixelx, pixely, series_size]=size(im);
[trig_time, index_trig]=sort(trig_time/1000);
for i=1:series_size
IM(:,:,i)=im(:,:,index_trig(i));
real_time2(i)=real_time(index_trig(i));
end
real_time=real_time2/1000;
for i=1:series_size
IMc(:,:,i)=imcrop(IM(:,:,i), [64 64 128 128]);
end
```

A.1.2 Code to determine the image of lowest overall signal

The purpose of this section of code is to determine the MOLLI image with the lowest overall signal, to later provide information on curve steepness during the creation of synthetic images. The steps of the algorithm, as well as input and output information, are outlined in Figure A.3.

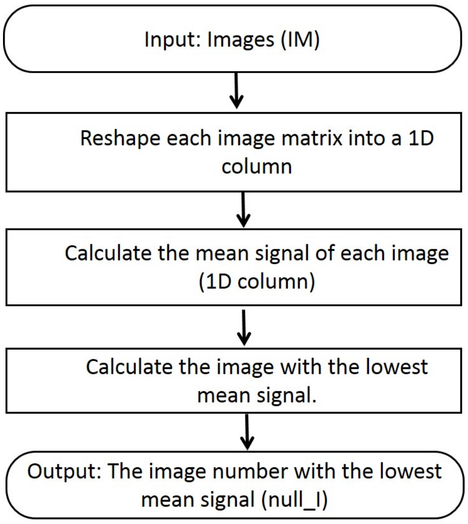

Fig. A.3 Flow chart to demonstrate following code. The code determines the image with the lowest overall signal.

```
imcc=IM(:,:,series_size);
tempor=reshape(IMc, [129*129,series_size]);
meanval=nanmean(tempor)';
[¬,null_I]=min(meanval);
```

A.1.3 Code for initial registration

The purpose of this section of code is to determine whether the input images for synthetic image creation require initial registration, and to register them if so. The steps of the algorithm, as well as input and output information, are outlined in Figure A.4.

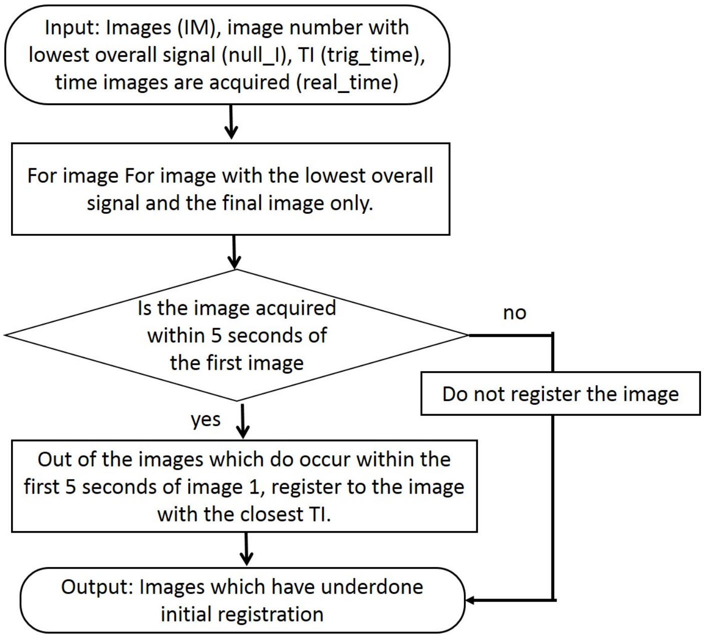

Fig. A.4 Flow chart to demonstrate following code which determines whether or not images need to undergo an initial registration.

```
function imgs=reg_approx(imgs, null_I, time_trig, time_real)
[¬,¬, z] = size(imgs);
for i=[ null_I, z]
if (time_real(i)-time_real(1))>5
realtimediff=abs(time_real(1)-time_real);
trigtimediff=abs(time_trig(i)-time_trig);
for k=1:z
if (realtimediff(k)>5 || realtimediff(k)==0 )
trigtimediff(k)=NaN ;
end
end
[¬, I]=min(trigtimediff);
A = image_object(imgs(:,:,I));
B = image_object(imgs(:,:,i));
```

```
C = register_image(A,B,[],'NS 4');
imgs(:,:,i)=C.Data;
end
end
end
```

A.1.4 Code to restore signal polarity pixel-wise

The purpose of this section of code is to restore signal polarity to a set of inversion recovery images. The steps of the algorithm, as well as input and output information, are outlined in Figure A.5.

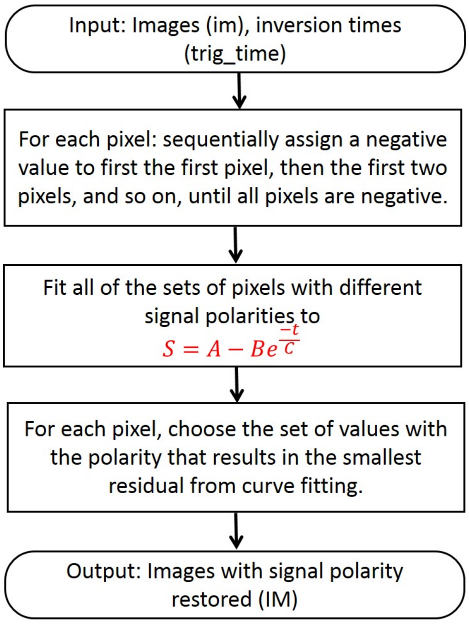

Fig. A.5 Flow chart to demonstrate following code. The code restores signal polarity for a set of inversion recovery images.

```
[pixelx, pixely, series_size]=size(im);
for i=1:pixelx
```

```
for j=1:pixely
for k=1:series_size
if IM(i,j,k)>0
IM(i,j,k)=-IM(i,j,k);
end
arraytest{k}=IM(i,j,:);
opts = optimset('Display','off');
x = lsqcurvefit(@myfun, [IM(i,j,series_size), ...
    IM(i,j,series_size)*2, 0.8], trig_time', squeeze(IM(i,j,:)), ...
    [], [], opts);
y = x(1) - x(2) * exp ( -trig_time / x(3));
xyvalues{k,1}=x;
xyvalues{k,2}=y;
residu2(k)=sum(   (squeeze(IM(i,j,:))  -y').^2 ./ y'    );
end
[¬, I] = min(abs(residu2));
IM(i,j,:)=arraytest{I};
end
end

function f=myfun(x,xdata)
f =(x(1)-x(2)*exp(-xdata/x(3)));
end
```

A.1.5 Code to create synthetic images

The purpose of this section of code is to create synthetic images via curve fitting to a simplified inversion recovery model, from the three chosen input images. The steps of the algorithm, as well as input and output information, are outlined in Figure A.6.

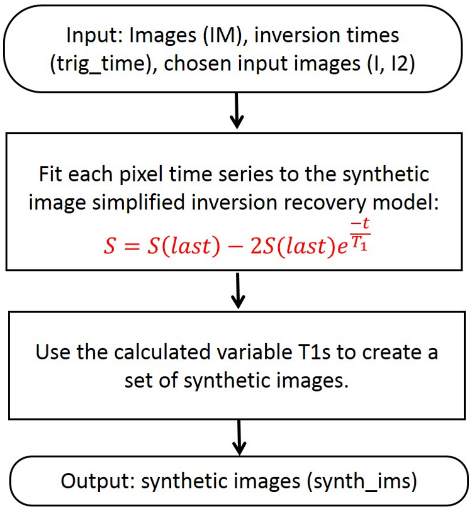

Fig. A.6 Flow chart to demonstrate following code. The code creates synthetic images for a set of inversion recovery images.

```
[pixelx, pixely, series_size]=size(IM);
for i=1:pixelx
for j=1:pixely
y_real =  double([IM(i,j,1), IM(i,j,I), IM(i,j,I2)]);
t_real=[trig_time(1), trig_time(I), trig_time(I2)];
ymax = IM(i,j,I2);
global ymax;
opts = optimset('Display','off');
X=lsqcurvefit(@myfun_synth, 1, t_real, y_real, [], [], opts); % ...
    fit to just signal for 1,4 and 11
Y = abs(y_real(3) - 2 * y_real(3)* exp ( -trig_time / X(1)));
synth_ims(i,j,1:series_size)=Y(1:series_size);
end
end

function f =  myfun_synth (x, xdata)
```

```
global ymax;%
f =(ymax-2*ymax*exp(-xdata/x(1)));
end
```

A.1.6 Code for image registration

The purpose of this section of code is perform pair-wise final image registration between the acquired images and the synthetic images. The steps of the algorithm, as well as input and output information, are outlined in Figure A.7.

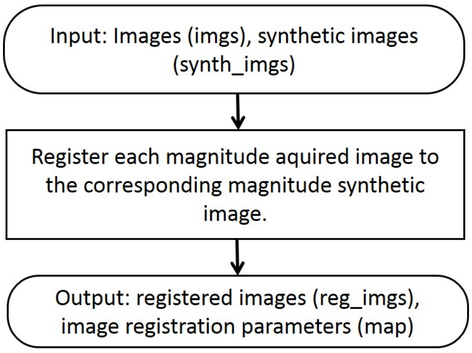

Fig. A.7 Flow chart to demonstrate following code. The code creates registers acquired images to synthetic images using toolkit ShIRT.

```
function [reg_imgs, map]= final_reg(imgs, synth_imgs)

IRLab;
[¬,¬, z] = size(imgs);

reg_imgs=imgs;
for i=1:z
A = image_object(synth_imgs(:,:,i));
B = image_object(imgs(:,:,i));
```

```
C = register_image(A,B,[],'NS 1');
reg_imgs(:,:,i)=C.Data;
map{i}=C;
end

end
```

A.1.7 Code for T1 map creation

The purpose of this section of code is perform the T_1 mapping on the registered images. The steps of the algorithm, as well as input and output information, are outlined in Figure A.8.

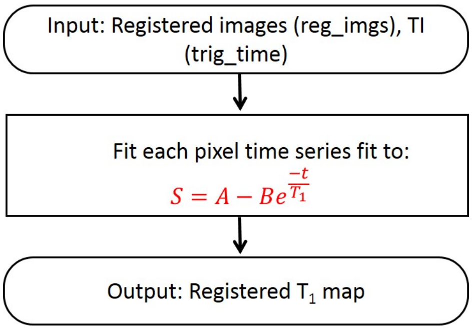

Fig. A.8 Flow chart to demonstrate following code. The code creates the final registered T_1 maps.

```

[pixelx, pixely, series_size]=size(im);

for i=1:pixelx
for j=1:pixely

regtemp=reg_imgs(i,j,:);
opts = optimset('Display','off');
```

```
x= lsqcurvefit(@myfun,[regtemp(series_size), ...
    regtemp(series_size)*2, 1], ...
trig_time(1,:), regtemp(1,:), [], [], opts); % x(1) is A, x(2) is ...
    B, x(3) is T1*
y = x(1) - x(2) * exp ( -trig_time / x(3));
T1_matrix(i,j) = x(3) * (x(2)/x(1) - 1); % x(1) is A, x(2) is B ...
    and x(3) is C/T1*]
residu(i,j)=sum( ((regtemp(1,: )-y).^2) ./abs(regtemp(1,: )) ;

end

end


function f=myfun(x,xdata)
f =(x(1)-x(2)*exp(-xdata/x(3)));
end
```

A.2 Matlab code for Chapter 5

Each step of the algorithm in Figure A.9 is described either in the previous section (for steps which are in common with the previous chapter), or in the following section (for new or altered steps) with an accompanying flow chart describing each section of code further.

A.2.1 Code to determine aligned images for synthetic image creation

The purpose of this section of code is to determine three aligned images to use for creating synthetic images. These images are determined using a combined inversion recovery and respiratory model. Regions of interest are fit to the combined model to determine respiratory rate and therefore, images which occur in the same respiratory state.

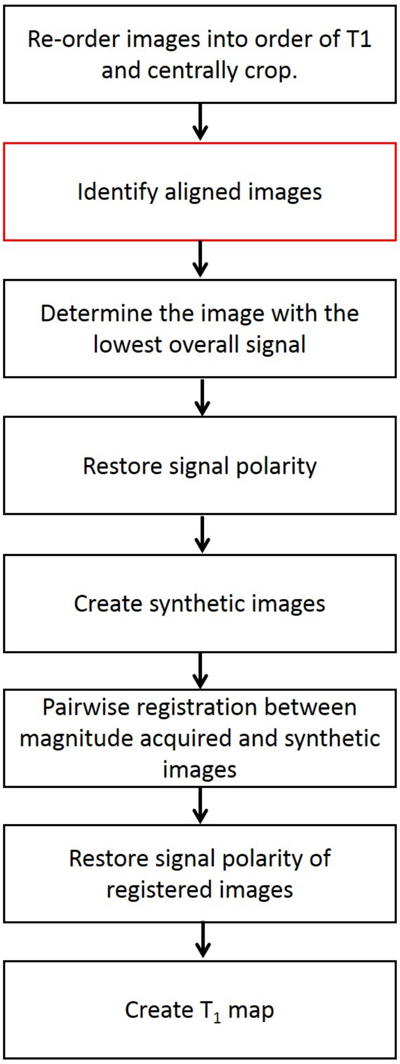

Fig. A.9 Flow chart to show the relevant sections of code and their ordering for Chapter 5. Sections that are different to that described in Chapter 3 are highlighted in red.

The steps of the algorithm, as well as input and output information, are outlined in Figure A.10.

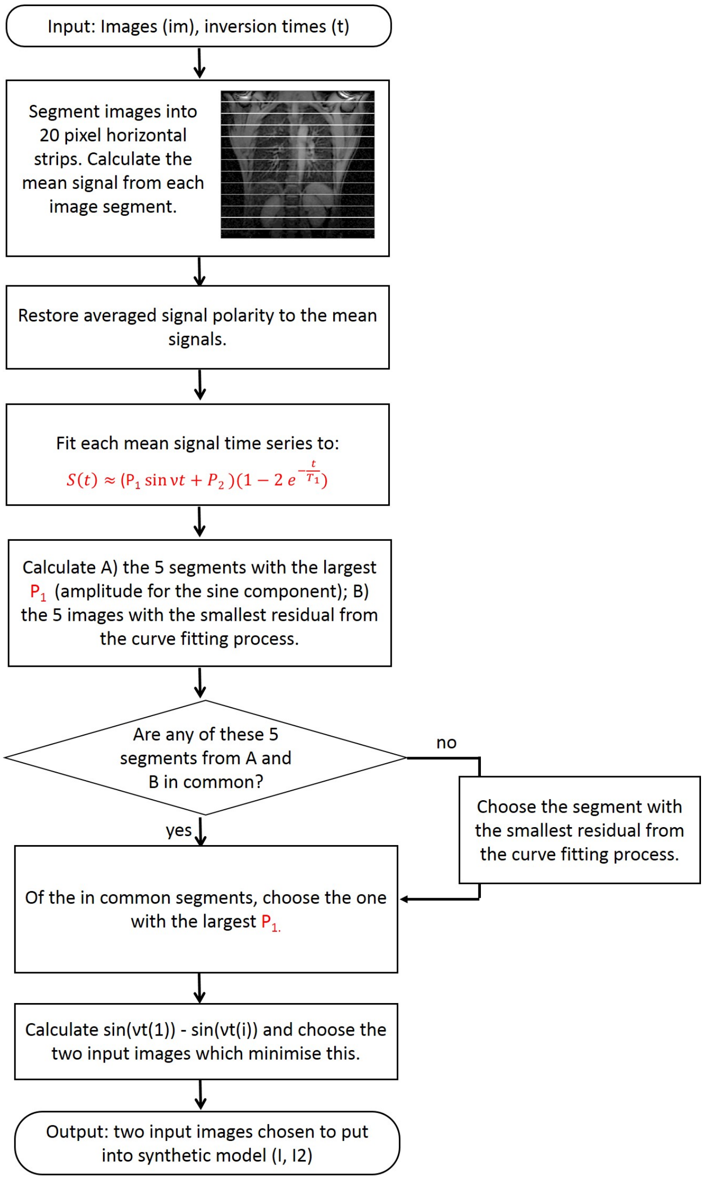

Fig. A.10 Flow chart to demonstrate following code. The code determines aligned images for synthetic image creation.

```
function [I1, I2, model]=lung_t1analysis(im, t)
[x ,y ,z] = size(im);
Q=20;
N=round(y/Q);
```

```

for k=1:N

for j=1:z
imc(:,:,j)=imcrop(im(:,:,j), [0 (k-1)*Q x Q] ) ;
meansig(j)=sum(sum(imc(:,:,j)))/(x*Q);
end
meansig1=meansig;
meansig1A=meansig;
meansig1B=meansig;
diaphragm_test{k}=imc;
clear imc
[ Im, minm]=min(meansig1);
meansig1A(1:minm)=-meansig1(1:minm);
meansig1B(1:(minm-1))=-meansig1(1:(minm-1));
global ymax
ymax = max(meansig1);

guess= [ ymax/4, 1.75, ymax ,0.2];
opts = optimset('Display','off');
xA = lsqcurvefit(@myfun7, guess, t,  meansig1A, [], [], opts);
xB = lsqcurvefit(@myfun7, guess, t,  meansig1B, [], [], opts);

A=[1 4 7];
B=[2 5 8];
C=[ 3 6 9 10 11];
global invtime

yA(A) = ...
    (xA(1)*sin(xA(2)*(t(A)+invtime(1)))+xA(3)).*(1-2*exp(-t(A)/xA(4))) ...
    ;
```

```
yA(B) = ...
    (xA(1)*sin(xA(2)*(t(B)+invtime(2)))+xA(3)).*(1-2*exp(-t(B)/xA(4))) ...
    ;
yA(C) = ...
    (xA(1)*sin(xA(2)*(t(C)+invtime(3)))+xA(3)).*(1-2*exp(-t(C)/xA(4))) ...
    ;

yB(A) = ...
    (xB(1)*sin(xB(2)*(t(A)+invtime(1)))+xB(3)).*(1-2*exp(-t(A)/xB(4))) ...
    ;
yB(B) = ...
    (xB(1)*sin(xB(2)*(t(B)+invtime(2)))+xB(3)).*(1-2*exp(-t(B)/xB(4))) ...
    ;
yB(C) = ...
    (xB(1)*sin(xB(2)*(t(C)+invtime(3)))+xB(3)).*(1-2*exp(-t(C)/xB(4))) ...
    ;

residuA(k,:)=sum(    ( squeeze(yA(1,:))   - meansig1A(:)'    ).^2 ./ ...
    meansig1A(:)');
residuB(k,:)=sum(    ( squeeze(yB(1,:))   - meansig1B(:)'    ).^2 ./ ...
    meansig1B(:)');


if residuA<residuB
Xvalues(k,:)=xA;
residu(k,:)=residuA(k,:);
else
Xvalues(k,:)=xB;
residu(k,:)=residuB(k,:);
end

end
```

```

[chosen_segment,pos]=max(abs(Xvalues(:,1)));

model=sin(Xvalues(pos,2)*t )+ Xvalues(pos,3);

model_1=model(1)-model(1:11); model_1(1)=NaN;
model_2=model(2)-model(1:11); model_2(2)=NaN;

model_1=abs(model_1); model_2=abs(model_2);

sum1= abs(min(model_1(1:6)))+abs(min(model_1(7:11)));
sum2= abs(min(model_2(1:6)))+abs(min(model_2(7:11)));

if sum1<sum2
[¬, I1]=min(abs(model_1(1:6)));
[¬, I2]=min(abs(model_1(7:11)));
I2=I2+6;
model=1;

else
[¬, I1]=min(abs(model_2(1:6)));
[¬, I2]=min(abs(model_2(7:11)));
I2=I2+6;
model=2;
end

end


function f=myfun7(x,xdata)

f = (x(1)*sin(x(2)*xdata+x(5))+x(3)).*(1-2*exp(-xdata/x(4))) ;
```

```
end
```

A.3 Matlab code for Chapter 6

Each step of the algorithm in Figure A.11 is described either in the previous sections (for steps which are in common with the previous chapters), or in the following section (for new or altered steps) with an accompanying flow chart describing each section of code further.

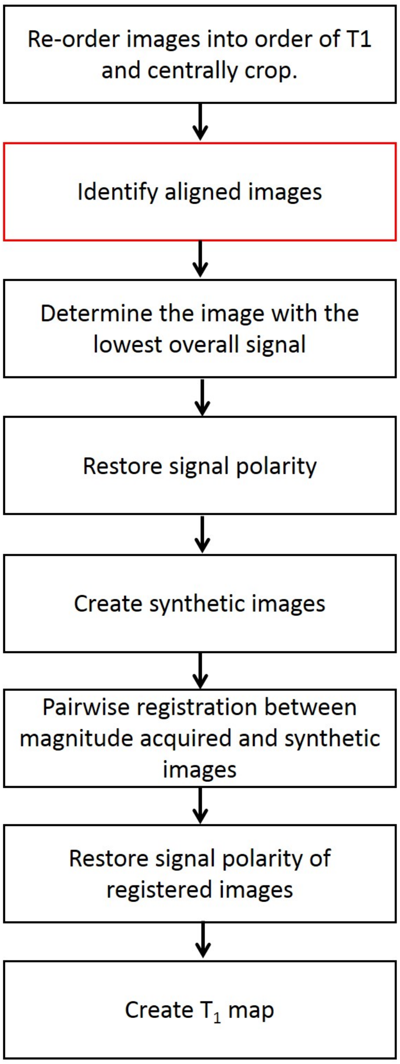

Fig. A.11 Flow chart to show the relevant sections of code and their ordering for Chapter 6. Sections that are different to that described in Chapter 5 or Chapter 3 are highlighted in red.

A.3.1 Code to determine aligned images for synthetic image creation

The purpose of this section of code is to determine three aligned images to use for creating synthetic images for cardiac images with images interleaved from multiple inversions. These images are determined using a combined inversion recovery and respiratory model. Regions of interest are fit to the combined model to determine respiratory rate and therefore, images which occur in the same respiratory state.

The steps of the algorithm, as well as input and output information, are outlined in Figure A.12.

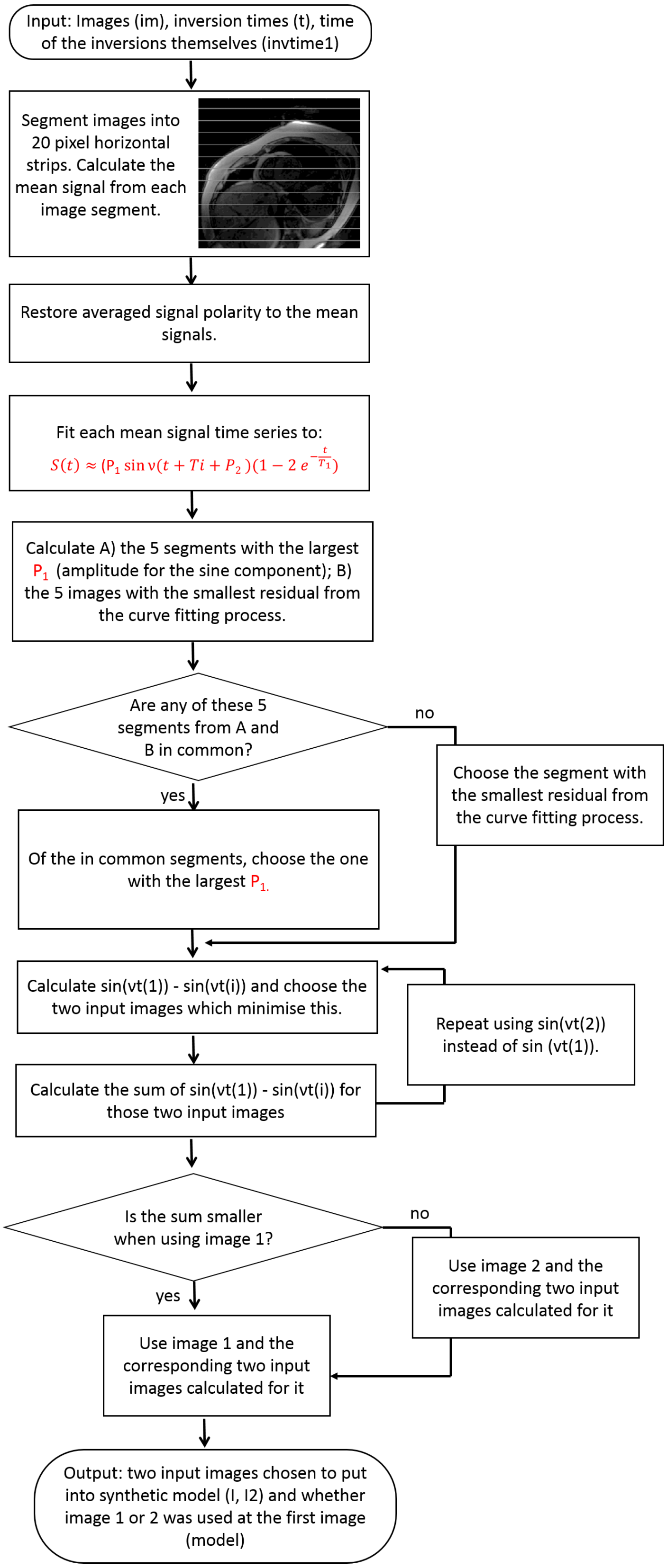

Fig. A.12 Flow chart to demonstrate following code. The code determines aligned images for synthetic image creation.

```

function [I1, I2, model]=cardiac_t1analysis(im, t)
[x ,y ,z] = size(im);
Q=20;

N=round(y/Q);
clear imc;

for k=1:N

for j=1:z
imc(:,:,j)=imcrop(im(:,:,j), [0 (k-1)*Q x Q] ) ;
meansig(j)=sum(sum(imc(:,:,j)))/(x*Q);
end
meansig1=meansig;
meansig1A=meansig;
meansig1B=meansig;
diaphragm_test{k}=imc;

clear imc
[ Im, minm]=min(meansig1);
meansig1A(1:minm)=-meansig1(1:minm);
meansig1B(1:(minm-1))=-meansig1(1:(minm-1));
global ymax
ymax = max(meansig1);

guess= [ ymax/4, 1.75, ymax ,0.2, 0];
opts = optimset('Display','off');
xA = lsqcurvefit(@myfun1, guess, t,  meansig1A, [], [], opts);
```

```
xB = lsqcurvefit(@myfun1, guess, t,  meansig1B, [], [], opts);

A=[1 4 7];
B=[2 5 8];
C=[ 3 6 9 10 11];
global invtime

yA(A) = ...
    (xA(1)*sin(xA(2)*(t(A)+invtime(1))+xA(5))+xA(3)).*(1-2*exp(-t(A)/xA(4))) ...
    ;
yA(B) = ...
    (xA(1)*sin(xA(2)*(t(B)+invtime(2))+xA(5))+xA(3)).*(1-2*exp(-t(B)/xA(4))) ...
    ;
yA(C) = ...
    (xA(1)*sin(xA(2)*(t(C)+invtime(3))+xA(5))+xA(3)).*(1-2*exp(-t(C)/xA(4))) ...
    ;

yB(A) = ...
    (xB(1)*sin(xB(2)*(t(A)+invtime(1))+xB(5))+xB(3)).*(1-2*exp(-t(A)/xB(4))) ...
    ;
yB(B) = ...
    (xB(1)*sin(xB(2)*(t(B)+invtime(2))+xB(5))+xB(3)).*(1-2*exp(-t(B)/xB(4))) ...
    ;
yB(C) = ...
    (xB(1)*sin(xB(2)*(t(C)+invtime(3))+xB(5))+xB(3)).*(1-2*exp(-t(C)/xB(4))) ...
    ;

residuA(k,:)=sum(    ( squeeze(yA(1,:))  - meansig1A(:)'   ).^2 ./ ...
    meansig1A(:)');
residuB(k,:)=sum(    ( squeeze(yB(1,:))  - meansig1B(:)'   ).^2 ./ ...
    meansig1B(:)');

```

```

if residuA<residuB
Xvalues(k,:)=xA;
residu(k,:)=residuA(k,:);
else
Xvalues(k,:)=xB;
residu(k,:)=residuB(k,:);
end

figure, plot(t, meansig1A, '*', t,  yA, 'r-');
end

[chosen_segment,pos]=max(abs(Xvalues(:,1)));

model=sin(Xvalues(pos,2)*t +Xvalues(pos,5))  + (Xvalues(pos,3));

model_1=model(1)-model(1:11); model_1(1)=NaN;
model_2=model(2)-model(1:11); model_2(2)=NaN;

model_1=abs(model_1); model_2=abs(model_2);

sum1= abs(min(model_1(1:6)))+abs(min(model_1(7:11)));
sum2= abs(min(model_2(1:6)))+abs(min(model_2(7:11)));

if sum1<sum2
[¬, I1]=min(abs(model_1(1:6)));
[¬, I2]=min(abs(model_1(7:11)));
I2=I2+6;
model=1;

else
[¬, I1]=min(abs(model_2(1:6)));
```

```
[¬, I2]=min(abs(model_2(7:11)));
I2=I2+6;
model=2;
end

end
```

Appendix B

Permissions

Copyright permission for Figure 2.11: License Number 4545861279931. License date Mar 11, 2019. Licensed Content Publisher: John Wiley and Sons. Licensed Content Publication: Magnetic Resonance in Medicine. Licensed Content Title: Effects of hematocrit and oxygen saturation level on blood spin-lattice relaxation. Licensed Content Author: M. Johanna Silvennoinen, Mikko I. Kettunen, Risto A. Kauppinen. Licensed Content Date: Mar 18, 2003. Licensed Content Volume: 49. Licensed Content Issue: 3. Licensed Content Pages: 4. Type of use: Dissertation/Thesis.

Copyright permission for Figure 2.11: License Number RNP/19/MAR/012762. License date Mar 11, 2019. Licensed Content Publisher:American Physical Society. Licensed Content Publication: Physical Review. Licensed Content Title: Relaxation Effects in Nuclear Magnetic Resonance Absorption. Licensed Content Author: N. Bloembergen, E. M. Purcell, and R. V. Pound. Licensed Content Date: 1 April 1948. Licensed Content Volume: 73. Licensed Content Pages: 679. Type of use: Dissertation/Thesis.